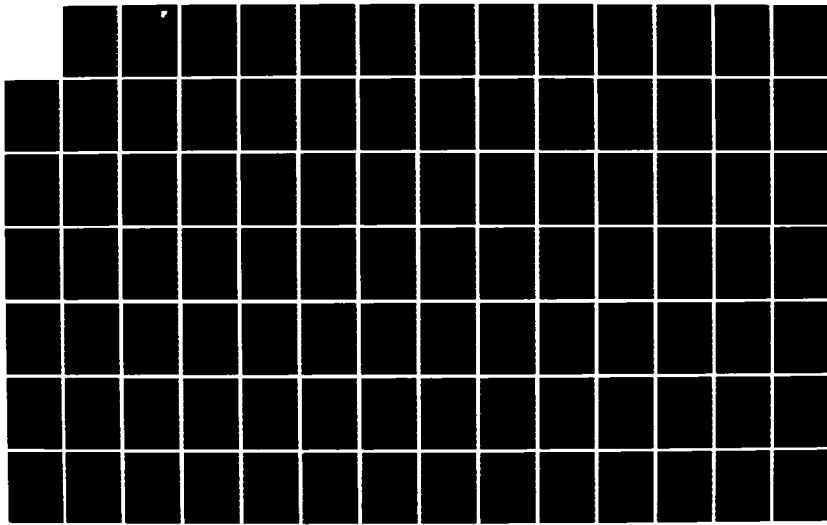
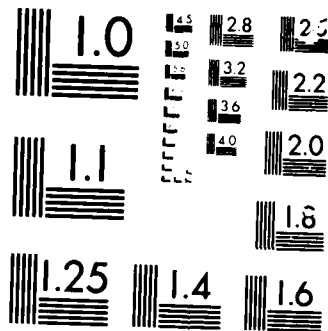


AD-A169 011 A STUDY OF MICROSTRIP ANTENNAS FOR MULTIPLE BAND AND 1/4
HIGH FREQUENCY OPERA. (U) ILLINOIS UNIV AT URBANA DEPT
OF ELECTRICAL AND COMPUTER ENGIN. Y T LO ET AL.

UNCLASSIFIED MAR 86 UILU-EM-84-15 RADC-TR-86-8 F/G 9/5 NL





MICROCOM

AD-A169 011

RADC-TR-86-8
Final Technical Report
March 1986



12

A STUDY OF MICROSTRIP ANTENNAS FOR MULTIPLE BAND AND HIGH FREQUENCY OPERATIONS

University of Illinois

**Y. T. Lo
S. M. Wright
W. F. Richards
B. F. Wang**

DTIC
SELECTED
S JUN 30 1986 D
B

APPROVED FOR PUBLIC RELEASE; DISTRIBUTION UNLIMITED

**ROME AIR DEVELOPMENT CENTER
Air Force Systems Command
Griffiss Air Force Base, NY 13441-5700**

REVIEWED AND APPROVED BY THE DIRECTOR OF THE RADAR AND ELECTRONIC SYSTEMS GROUP (R&ES) AND
THE DIRECTOR OF THE ELECTRONIC SYSTEMS DIVISION (ESD) OF THE RADAR AND ELECTRONIC SYSTEMS GROUP (R&ES).

RADC-TR-69-6 has been reviewed and is approved for publication.

APPROVED:

Charles J. Drane

CHARLES J. DRANE
Project Engineer

APPROVED:

Allan C. Schell

ALLAN C. SCHELL
Chief, Electromagnetic Sciences Division

FOR THE COMMANDER:

John A. Ritz

JOHN A. RITZ
Plans & Programs Division

If your address has changed or if you wish to be removed from the RADC mailing list, or if the addressee is no longer employed by your organization, please notify RADC (EEAA) Hanscom AFB MA 01731-5000. This will assist us in maintaining a current mailing list.

Do not return copies of this report unless contractual obligations or notices on a specific document requires that it be returned.

UNCLASSIFIED

SECURITY CLASSIFICATION OF THIS PAGE

REPORT DOCUMENTATION PAGE

1a. REPORT SECURITY CLASSIFICATION UNCLASSIFIED		1b. RESTRICTIVE MARKING N/A AD-A169011			
2a. SECURITY CLASSIFICATION AUTHORITY N/A		3. DISTRIBUTION/AVAILABILITY OF REPORT Approved for public release; distribution unlimited.			
2b. DECLASSIFICATION/DOWNGRADING SCHEDULE N/A		5. MONITORING ORGANIZATION REPORT NUMBER(S) RADC-TR-86-8			
4. PERFORMING ORGANIZATION REPORT NUMBER(S) EM 84-15		7a. NAME OF MONITORING ORGANIZATION Rome Air Development Center (EEAA)			
6a. NAME OF PERFORMING ORGANIZATION University of Illinois		6b. OFFICE SYMBOL (if applicable)	7b. ADDRESS (City, State, and ZIP Code) Dept of Electrical & Computer Engineering 1406 W. Green Street Urbana IL 61801		
8a. NAME OF FUNDING/SPONSORING ORGANIZATION Rome Air Development Center		8b. OFFICE SYMBOL (if applicable) EEAA	9. PROCUREMENT INSTRUMENT IDENTIFICATION NUMBER F19628-82-K-0005		
8c. ADDRESS (City, State, and ZIP Code) Hanscom AFB MA 01731-5000		10. SOURCE OF FUNDING NUMBERS			
		PROGRAM ELEMENT NO 61102F	PROJECT NO 2305	TASK NO J3	WORK UNIT ACCESSION NO 34
11. TITLE (Include Security Classification) A STUDY OF MICROSTRIP ANTENNAS FOR MULTIPLE BAND AND HIGH FREQUENCY OPERATIONS					
12. PERSONAL AUTHOR(S) Y. T. Lo, S. M. Wright, W. F. Richards, B. F. Wang					
13a. TYPE OF REPORT Final	13b. TIME COVERED FROM Nov 81 TO Sep 84		14. DATE OF REPORT (Year, Month, Day) March 1986	15. PAGE COUNT 306	
16. SUPPLEMENTARY NOTATION N/A					
17. COSATI CODES			18. SUBJECT TERMS (Continue on reverse if necessary and identify by block number) Microstrip Antennas Microstrip Antenna Arrays Circularly Polarized Antennas Printed-Dipole Arrays Dual-Frequency Antennas (See Reverse)		
19. ABSTRACT (Continue on reverse if necessary and identify by block number) This report consists of four parts. Part I is on an "Efficient Analysis of Infinite Microstrip Arrays on Electrically Thick Substrates". The emphasis is placed on a numerically <u>efficient</u> method. The analysis also includes the case of infinite arrays with printed dipoles. Some experiments, using the waveguide simulators, have been performed to verify the theoretical results. For microstrip antenna arrays the experiment is found difficult to realize due to the feed problems.					
Part II is an extension of the previous work on multiple port microstrip antennas. Experiments were carried out, which showed that this improved theory could predict the loading effect at the second port at the resonant frequency of the input port very accurately. The analysis also showed the changes in magnetic current distribution around the edges of the patch due to leading.					
20. DISTRIBUTION/AVAILABILITY OF ABSTRACT <input checked="" type="checkbox"/> UNCLASSIFIED/UNLIMITED <input type="checkbox"/> SAME AS RPT <input type="checkbox"/> DTIC USERS			21. ABSTRACT SECURITY CLASSIFICATION UNCLASSIFIED		
22a. NAME OF RESPONSIBLE INDIVIDUAL Charles J. Drane			22b. TELEPHONE (Include Area Code) (617) 861-2051	22c. OFFICE SYMBOL RADC (EEAA)	

DD FORM 1473, 84 MAR

83 APR edition may be used until exhausted
All other editions are obsoleteSECURITY CLASSIFICATION OF THIS PAGE
UNCLASSIFIED

UNCLASSIFIED

Part III is devoted to the theory and experiment of single element dual-frequency microstrip antennas. The main objective is to achieve a dual-frequency operation for the same linear polarization with a single element fed at one port. To make the devices more useful it is desirable to have some means to vary the two frequency ratios over a wide range. In this work it is shown that by cutting slots and/or inserting shorting pins in the patch, the ratio can be varied from 3 to 1.3. For some other applications, such as GPS, a smaller ratio is required. It is found that by using a C-shaped slot, the ratio can be reduced to 1.05. This is discussed in Part IV.

18. SUBJECT TERMS (Continued)

Periodic Green's Functions
Multipole-Port Microstrip Antennas

UNCLASSIFIED

TABLE OF CONTENTS

- PART I. EFFICIENT ANALYSIS OF INFINITE MICROSTRIP ANTENNA ARRAYS ON ELECTRICALLY THICK SUBSTRATES BY S. M. WRIGHT AND Y. T. LO

PART II. THEORETICAL AND EXPERIMENTAL INVESTIGATION OF A MICROSTRIP RADIATOR WITH MULTIPLE LUMPED LINEAR LOADS BY W. F. RICHARDS AND Y. T. LO

PART III. MICROSTRIP ANTENNAS FOR DUAL-FREQUENCY OPERATION BY B. F. WANG AND Y. T. LO

PART IV. FURTHER STUDY OF DUAL-FREQUENCY MICROSTRIP ANTENNAS BY B. F. WANG AND Y. T. LO

(Each part has its own pagination.)

- PART V. PERSONNEL

PART VI. OTHER PUBLICATIONS RESULTING FROM CONTRACT SPONSORSHIP

PART VII. REPORTS RESULTING FROM CONTRACT SPONSORSHIP

DTIC
SELECTED
JUN 30 1986
S B D

✓ A-1

PART I

EFFICIENT ANALYSIS OF INFINITE
MICROSTRIP ANTENNA ARRAYS ON ELECTRICALLY
THICK SUBSTRATES

BY

S. M. WRIGHT

AND

Y. T. LO

ABSTRACT

Infinite arrays of microstrip antennas on electrically thick substrates are analyzed using an efficient moment method solution. The computation of the matrix elements, ordinarily very time-consuming, is performed efficiently using series acceleration techniques. Because the Green's function for the dielectric slab is used, the solution is not restricted to thin substrates. In addition, the efficient computation of the matrix elements allows large numbers of basis functions to be used with reasonable execution times, providing the basis for a general solution technique.

The method is applied to the analysis of infinite arrays of microstrip dipoles. In an attempt to further improve the efficiency of the solution, several thin-wire approximations are made, and their range of validity is discussed. It is found that the approximations significantly improve the efficiency of the solution, but are only valid for dipoles with widths less than approximately $0.02\lambda_0$. A series of waveguide simulator experiments were conducted which demonstrated the validity of the theory. Several arrays were modeled, both with and without radomes. Because the effects of surface waves are included through the use of the Green's function for the grounded dielectric substrate and the infinite array formulation, blind angles in the array scan performance are accurately predicted.

An initial analysis of arrays of microstrip patches on thick substrates is discussed. Because of the lack of published results and the complexity of a suitable experiment, the theory was initially tested by treating the array of patches as a scatterer. Good agreement with independently computed current distributions on single plate scatterers is observed if the array spacing is several times the plate size and for similar separations from the ground plane. Based on this agreement and the success of the dipole results, several examples are presented for probe-fed microstrip patches, using a simplified feed model commonly used in the analysis of patches on very thin substrates.

TABLE OF CONTENTS

	Page
1. INTRODUCTION.	1
2. FORMULATION	11
2.1. Integral Equation for the Total Patch Current.	11
2.2. Periodic Green's Function.	14
2.2.1. Plane wave spectrum technique	14
2.2.2. Fields of a current sheet	18
2.2.3. Fields of an arbitrary periodic current distribution. . .	26
2.3. Method of Solution of the Integral Equation.	30
2.4. Numerical Evaluation of the Solution	34
3. EVALUATION OF INNER PRODUCTS.	42
3.1. Introduction to the Acceleration Technique	43
3.2. Application of the Acceleration Technique to Two-dimensional Sums	51
3.2.1. General formulation	52
3.2.2. Spectral sum.	53
3.2.3. Spatial sum	57
3.3. Examples of Inner Product Evaluation	62
3.3.1. Electric field periodic Green's function.	62
3.3.2. Rooftop basis functions and linear testing functions	78
3.4. Parameters Affecting the Numerical Evaluation of Inner Products.	91
4. INFINITE ARRAYS OF MICROSTRIP DIPOLES	97
4.1. Evaluation of the Matrix Elements.	99
4.1.1. Choice of basis and testing functions	99
4.1.2. Evaluation of the impedance matrix.	102
4.1.3. Use of symmetry	107
4.1.4. Evaluation of the excitation matrix	109
4.2. Numerical Results.	110
4.2.1. Convergence and the effect of various parameters.	111
4.2.2. Experimental verification	128
4.2.3. Theoretical results	139
4.2.4. Discussion.	166

	Page
5. INFINITE ARRAYS OF MICROSTRIP PATCHES.	167
5.1. Evaluation of the Matrix Elements	167
5.1.1. The impedance matrix	167
5.1.2. The excitation matrix.	170
5.1.3. The voltage matrix	172
5.2. Numerical Results	174
5.2.1. Scattering from square plates.	174
5.2.2. Arrays of microstrip patches	179
6. CONCLUSION	194
REFERENCES	197

LIST OF TABLES

TABLE	Page
2.1 COMPONENTS \tilde{G}_{ij} AND \tilde{G}_{ij}^H FOR THE PERIODIC GREEN'S FUNCTION OF A SINGLE LAYER GDS.	24
2.2 COMPONENTS \tilde{G}_{ij} AND \tilde{G}_{ij}^H FOR THE PERIODIC GREEN'S FUNCTION OF A TWO LAYER GDS	27
2.3 COMPUTATION TIME AND RATE OF CONVERGENCE OF EQUATION (2.4-7).	39
3.1 COEFFICIENTS OF ASYMPTOTIC EXPANSIONS THROUGH κ^{-5}	56
3.2 COMPONENTS OF THE ASYMPTOTIC GREEN'S FUNCTION IN THE SPECTRAL DOMAIN.	58
3.3 COMPONENTS OF THE ASYMPTOTIC GREEN'S FUNCTION IN THE SPATIAL DOMAIN.	68
3.4 A SHORT TABLE OF SINGULAR INTEGRALS ASSOCIATED WITH THE BASIS AND TESTING FUNCTIONS USED IN THIS REPORT	86
3.5 FUNCTIONS USED TO EVALUATE THE SINGULAR INTEGRALS IN TABLE 3.4.	88
4.1 THE EFFECT OF VARIOUS PARAMETERS ON THE INPUT IMPEDANCE OF A DIPOLE IN AN INFINITE ARRAY. (METHOD 1: EDGE MODES)	115
4.2 THE EFFECT OF VARIOUS PARAMETERS ON THE INPUT IMPEDANCE OF A DIPOLE IN AN INFINITE ARRAY. (METHOD 2: ROOFTOP FUNCTIONS).	116
4.3 CONVERGENCE FOR UNACCELERATED COMPUTATION OF INNER PRODUCTS (METHOD 1: EDGE MODES)	119
4.4 CONVERGENCE FOR UNACCELERATED COMPUTATION OF INNER PRODUCTS (METHOD 2: ROOFTOP FUNCTIONS).	121
4.5 COMPARISON OF ROOFTOP BASIS FUNCTION SOLUTION TO RESULT FROM METHOD 1 FOR DIFFERENT WIDTH STRIPS	127
5.1 CONVERGENCE AND EXECUTION TIMES FOR MOMENT METHOD SOLUTION OF MICROSTRIP PATCH ARRAY, USING THREE DIFFERENT INTEGRATION TECHNIQUES	182

LIST OF FIGURES

Figure	Page
1.1 Section of an infinite array of microstrip patches.	2
1.2 Illustration of transmission line model (from [5]).	4
2.1a Spatial or "direct" lattice	15
2.1b Spectral or "reciprocal" lattice.	15
2.2a Single layer grounded dielectric substrate (GDS).	19
2.2b Double layer grounded dielectric substrate.	19
3.1 Convergence of the first infinite sum in Equation (3.1-10) for level 0, 1, 3 and 5 accelerations, with $u = 0.5$ and $b = 0.75$	49
3.2 Effect of the parameter u on the convergence of the first infinite sum in Equation (3.1-10) with $L = 3$ and $b = 0.75$	50
3.3 Approach of the unaccelerated evaluation of G_{yy} to the value from the fifth order acceleration as the observation point approaches the array plane $z = t$	70
3.4 Convergence of the spectral sum of $G_{yy}(\vec{\rho} - \vec{\rho}')$ for level 1, 3, and 5 accelerations, with $u = 0.5$ β_{av} , obs. pt. = $0.02\vec{S}_1 + 0.02\vec{S}_2$	71
3.5 Convergence of the spatial sum of $G_{yy}(\vec{\rho} - \vec{\rho}')$ for level 1, 3, and 5 accelerations, with $u = 0.5$ β_{av} , obs. pt. = $0.02\vec{S}_1 + 0.02\vec{S}_2$	73
3.6 Convergence of the spectral sum of $G_{yy}(\vec{\rho} - \vec{\rho}')$ for level 1, 3, and 5 accelerations, with $u = 0.5$ β_{av} , obs. pt. = $0.3\vec{S}_1 + 0.3\vec{S}_2$	74
3.7 Convergence of the spatial sum of $G_{yy}(\vec{\rho} - \vec{\rho}')$ for level 1, 3, and 5 accelerations, with $u = 0.5$ β_{av} , obs. pt. = $0.3\vec{S}_1 + 0.3\vec{S}_2$	75
3.8 Effect of the parameter u on the convergence of the spectral sum of $G_{yy}(\vec{\rho} - \vec{\rho}')$ with level 5 acceleration and observation point $0.3\vec{S}_1 + 0.3\vec{S}_2$	76

Figure	Page
3.9 Effect of the parameter u on the convergence of the spatial sum of $G_{yy}(\vec{p} - \vec{p}')$ with level 5 acceleration and observation point $0.3\vec{S}_1 + 0.3\vec{S}_2$	77
3.10 Illustration of the spatial domain summation procedure.	84
4.1 Section of an infinite array of microstrip dipoles.	98
4.2 Basis function layout on microstrip dipoles	103
4.3a Convergence of the input resistance of a microstrip dipole in an infinite array. Square lattice, $S_1 = S_2 = 0.6 \lambda_0$, $t = 0.15 \lambda_0$, $\epsilon_r = 2.55$, $b = 0.35 \lambda_0$	113
4.3b Convergence of the input reactance of a microstrip dipole in an infinite array. square lattice, $S_1 = S_2 = 0.6 \lambda_0$, $t = 0.15 \lambda_0$, $\epsilon_r = 2.55$, $b = 0.35 \lambda_0$	114
4.4 Transverse current distribution on a $0.35 \lambda_0$ dipole with $a = 0.0002 \lambda_0$	122
4.5 Transverse current distribution on a $0.35 \lambda_0$ dipole with $a = 0.002 \lambda_0$	123
4.6 Transverse current distribution on a $0.35 \lambda_0$ dipole with $a = 0.02 \lambda_0$	124
4.7 Transverse current distribution on a $0.35 \lambda_0$ dipole with $a = 0.05 \lambda_0$	125
4.8 Waveguide simulator experimental set-up.	129
4.9 Waveguide simulator array fixture.	130
4.10a Waveguide simulator results for a dipole array on a single layer substrate $a = 1\text{mm}$, $b = 95\text{mm}$, $t = 25.4\text{mm}$, $\epsilon_r = 1.03$	133
4.10b Waveguide simulator results for a dipole array on a single layer substrate $a = 1\text{mm}$, $b = 95\text{mm}$, $t = 25.4\text{mm}$, $\epsilon_r = 1.03$	134
4.11a Waveguide simulator results for a dipole array on a single layer substrate $a = 1\text{mm}$, $b = 84\text{mm}$, $t = 25.4\text{mm}$, $\epsilon_r = 2.53$	135
4.11b Waveguide simulator results for a dipole array on a single layer substrate $a = 1\text{mm}$, $b = 84\text{mm}$, $t = 25.4\text{mm}$, $\epsilon_r = 2.53$	136
4.12a Waveguide simulator results for a dipole array on a single layer substrate $a = 1\text{mm}$, $b = 54\text{mm}$, $t = 19.1\text{mm}$, $\epsilon_r = 6.0$	137

Figure	Page
4.12b Waveguide simulator results for a dipole array on a single layer substrate $a = 1\text{mm}$, $b = 54\text{mm}$, $t = 19.1\text{mm}$, $\epsilon_r = 6.0$	138
4.13a Waveguide simulator results for a dipole array on a multi-layer substrate $a = 1\text{mm}$, $b = 54\text{mm}$, $t_3 = 19.1\text{mm}$, $\epsilon_{r3} = 6.0$, $t_2 = 25.4\text{mm}$, $\epsilon_{r2} = 2.53$	140
4.13b Waveguide simulator results for a dipole array on a multi-layer substrate $a = 1\text{mm}$, $b = 54\text{mm}$, $t_3 = 19.1\text{mm}$, $\epsilon_{r3} = 6.0$, $t_2 = 25.4\text{mm}$, $\epsilon_{r2} = 2.53$	141
4.14a Waveguide simulator results for a dipole array on a multi-layer substrate $a = 1\text{mm}$, $b = 95\text{mm}$, $t_3 = 25.4\text{mm}$, $\epsilon_{r3} = 1.03$, $t_2 = 25.4\text{mm}$, $\epsilon_{r2} = 2.53$	142
4.14b Waveguide simulator results for a dipole array on a multi-layer substrate $a = 1\text{mm}$, $b = 95\text{mm}$, $t_3 = 25.4\text{mm}$, $\epsilon_{r3} = 1.03$, $t_2 = 25.4\text{mm}$, $\epsilon_{r2} = 2.53$	143
4.15 Spectral lattice, with visible regions superimposed (grating lobe lattice)	145
4.16 Alternate construction of spectral or grating lobe lattice	148
4.17 Scan performance of an infinite dipole array on a rectangular lattice. $a = 0.001 \lambda_0$, $b = 0.36 \lambda_0$, $t = 0.15 \lambda_0$, $\epsilon_r = 2.55$, $S_1 = 0.575 \lambda_0$, $S_2 = 0.5 \lambda_0$	149
4.18 Surface wave circle diagram for array in Figure 4.17	150
4.19 Scan performance of an infinite dipole array with a radome on a rectangular lattice. $a = 0.001 \lambda_0$, $b = 0.36 \lambda_0$, $t = 0.15 \lambda_0$, $\epsilon_r = 2.55$, $t = 0.1 \lambda_0$, $\epsilon_r = 2.55$, $S_1 = 0.575 \lambda_0$, $S_2 = 0.5 \lambda_0$	152
4.20 Surface wave circle diagram for array in Figure 4.19	153
4.21 Scan performance of an infinite dipole array on a hexagonal lattice. $a = 0.001 \lambda_0$, $b = 0.36 \lambda_0$, $t = 0.15 \lambda_0$, $\epsilon_r = 2.55$, $S_1 = S_2 = 0.5774 \lambda_0$	155
4.22 Surface wave circle diagram for array in Figure 4.21	156
4.23 Scan performance of an infinite dipole array on a rectangular lattice. $a = 0.002 \lambda_0$, $b = 0.1546 \lambda_0$, $t = 0.08 \lambda_0$, $\epsilon_r = 12.8$, $S_1 = 0.5 \lambda_0$, $S_2 = 0.4 \lambda_0$	157
4.24 Surface wave circle diagram for array in Figure 4.23	158
4.25 Reflection coefficient versus frequency for three microstrip dipole arrays (zero scan.) $a = 2.0\text{mm}$, $b = 115\text{mm}$, $\epsilon_r = 2.53$, $S_1 = S_2 = 166.7\text{mm}$	160

Figure	Page
4.26 Impedance of a dipole in an infinite array in free space as a function of lattice spacing. $a = 0.002 \lambda_0$, $b = 0.5 \lambda_0$, $t = 0.25 \lambda_0$, $\epsilon_r = 1$	162
4.27 Resistance of a microstrip dipole in an infinite array as a function of lattice spacing. $a = .0002 \lambda_0$, $b = 0.317 \lambda_0$, $t = 0.1016 \lambda_0$, $\epsilon_r = 3.25$	164
4.28 Reactance of a microstrip dipole in an infinite array as a function of lattice spacing. $a = .0002 \lambda_0$, $b = 0.317 \lambda_0$, $t = 0.1016 \lambda_0$, $\epsilon_r = 3.25$	165
5.1 Basis function layout on microstrip patches.	169
5.2a \hat{y} component of current induced on a $0.15 \lambda_0$ square plate in an infinite array by a normally incident plane wave ($S_1 = S_2 = 3.1 \lambda_0$)	175
5.2b \hat{x} component of current induced on a $0.15 \lambda_0$ square plate in an infinite array by a normally incident plane wave ($S_1 = S_2 = 3.1 \lambda_0$)	176
5.3a \hat{y} component of current induced on a $0.15 \lambda_0$ square plate in an infinite array by a normally incident plane wave ($S_1 = S_2 = 2.2 \lambda_0$)	177
5.3b \hat{x} component of current induced on a $0.15 \lambda_0$ square plate in an infinite array by a normally incident plane wave ($S_1 = S_2 = 2.2 \lambda_0$)	178
5.4a \hat{y} component of current induced on a $1.0 \lambda_0$ square plate in an infinite array by a normally incident plane wave ($S_1 = S_2 = 3.1 \lambda_0$)	180
5.4b \hat{x} component of current induced on a $1.0 \lambda_0$ square plate in an infinite array by a normally incident plane wave ($S_1 = S_2 = 3.1 \lambda_0$)	181
5.5a \hat{y} component of current distribution on a probe fed microstrip patch.	184
5.5b \hat{x} component of current distribution on a probe fed microstrip patch.	185
5.6 Impedance of an element in an infinite rectangular array of microstrip patches on a thick substrate ($Z_0 = 50\Omega$) $t = 26.7\text{mm}$, $\epsilon_r = 2.53$, $S_1 = S_2 = 167\text{mm}$, $a = b = 100\text{mm}$	187

Figure	Page
5.7 Impedance of an element in an infinite rectangular array of microstrip patches on a thick substrate ($Z_0 = 50\Omega$) $t = 33.3\text{mm}$, $\epsilon_r = 2.53$, $S_1 = S_2 = 167\text{mm}$, $a = b = 100\text{mm}$	188
5.8 Current density induced on a microstrip patch in an infinite array by a normally incident plane wave. $S_1 = S_2 = 167\text{mm}$, $\epsilon_r = 2.53$, $a = b = 100\text{mm}$, $t = 13.3\text{mm}$	190
5.9 Current density induced on a microstrip patch in an infinite array by a normally incident plane wave. $S_1 = S_2 = 167\text{mm}$, $\epsilon_r = 2.53$, $a = b = 100\text{mm}$, $t = 26.6\text{mm}$	191
5.10 Q factor for an infinite microstrip patch array obtained from scattering current distribution. $S_1 = S_2 = 167\text{mm}$, $\epsilon_r = 2.53$, $a = b = 100\text{mm}$	192

CHAPTER 1

INTRODUCTION

One of the most active areas of research in the antenna field in recent years has been microstrip antennas. Recently, there has been a great deal of interest in arrays made of microstrip antennas, as their printed circuit constructions make them well-suited for use in large scanning arrays. A section of a microstrip patch array is illustrated in Figure 1.1. One major disadvantage of the microstrip antenna is its low bandwidth. It is well-known that increased bandwidth can be obtained by increasing the thickness of the substrate on which the microstrip antenna is printed. While the compact size of these antennas is one of their major advantages, in many applications one will accept the increased thickness for the gain in bandwidth. In addition, millimeter-wave arrays can be built on substrates which can be electrically thick, but still physically thin. Unfortunately, many analysis techniques employ approximations which are valid only for thin substrates. Other more general approaches suffer from a lack of computational efficiency, which in practice can restrict their usefulness due to high computational costs. This report uses a general moment method [1] approach to analyze infinite arrays of microstrip dipoles and patches on thick substrates. A summation technique [2-4] is used to significantly improve the computational efficiency of the solution compared to the approach commonly used, discussed below.

Many techniques, using different levels of approximation, are available to analyze a variety of microstrip antennas. An excellent

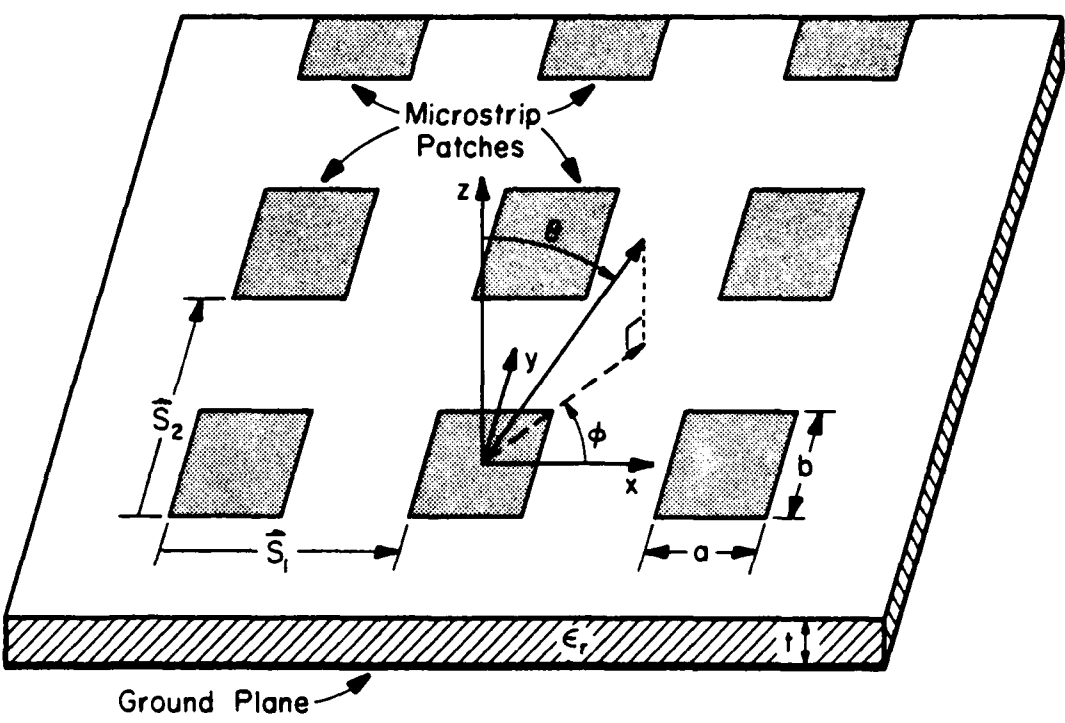


Figure 1.1. Section of an infinite array of microstrip patches.

review of theoretical and practical design techniques is contained in a paper by Carver and Mink [5]. In addition, Mailloux, McIlvenna and Kernweis [6] authored a companion paper on microstrip array technology. These papers cover the development of the subject until early 1981. No attempt will be made to update these reviews here, but several of the recent developments will be mentioned, along with a brief discussion of two of the more widely used of the earlier techniques. The analysis of individual microstrip antennas is discussed first, continuing with a discussion of array analysis techniques.

Using microstrip patches as radiators was first reported thirty years ago by Deschamps [7]. However, only in the last ten years has much theoretical analysis been done. One simple technique to analyze rectangular patches is the transmission line model [8]. A microstrip fed patch, as shown in Figure 1.2, is modeled by two narrow slots radiating into a half space. The impedance of the antenna is simply given as the impedance of slot A in parallel with the transformed impedance of slot B. The patch simply acts as a low impedance microstrip transmission line. The impedance of each slot is easily determined [9, page 183], and the transformation down the transmission line is straightforward. This model is restricted to analysis of patches on thin substrates, primarily for rectangular patches fed at the edge.

A more complete theory was reported by Lo, Richards and Solomon [10,11] in which the area under the patch is modeled as a cavity bounded by perfect electric conducting (PEC) walls on the top and bottom and perfect magnetic conducting (PMC) walls on the four sides. This model is founded in three simple observations [10], which are approximately true

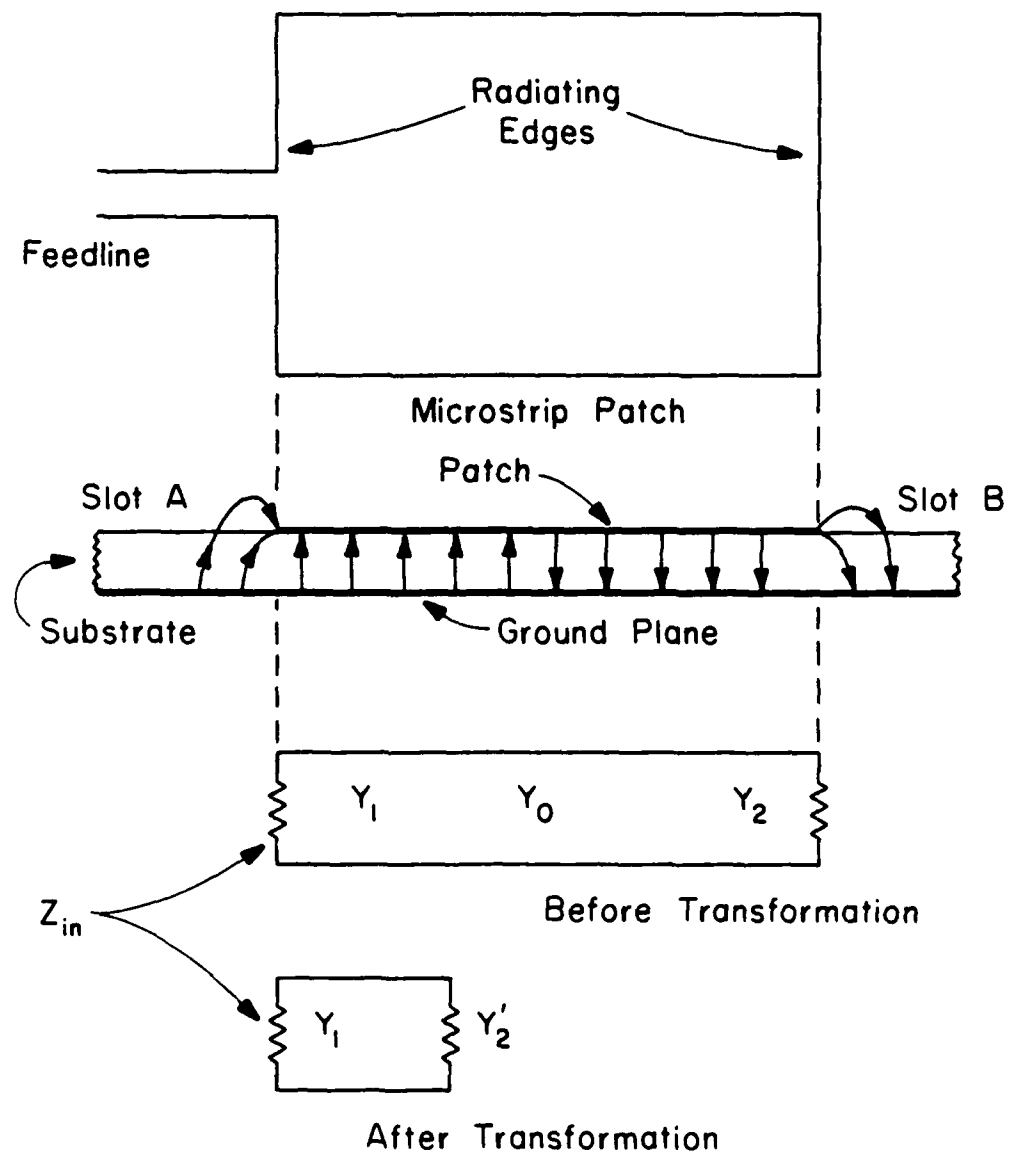


Figure 1.2. Illustration of transmission line model (from [5]).

for thin substrates:

- (1) The electric field under the patch has only a z component, and the magnetic field has only x and y components (z is normal to the patch).
- (2) The fields under the patch are independent of z .
- (3) The normal component of the electric current on the patch normal to the edge goes to zero at the edge. Hence, there is no tangential component of the H field at the sides of the cavity, to the degree that the above conditions are satisfied.

As long as these conditions are approximately true, the cavity model can be used. The analysis proceeds by expanding the fields inside the cavity in a complete set of cavity expansion modes. The coefficient of each mode is found from the particular feed used, and the internal fields of the cavity are found by summing all of the modal fields. Equivalent magnetic currents on the PMC walls are found, and finally the radiation of the antenna is found from these currents.

This model provides excellent results for patches on thin substrates. It is equally applicable to rectangular, elliptical and circular patches, indeed any patch configuration for which the cavity modes can be found, and thus is general enough to allow treatment of dual-frequency and circular-polarization antennas.

The final approximate technique to be discussed is a moment method approach used by Newman and Tulyathan [12]. In their approach the dielectric substrate is replaced by volume equivalence currents, and the

ground plane is removed by image theory. They then solve the new free space problem with standard surface patch techniques. Newman and Tulyathan calculated results for rectangular patches, with results which were comparable to the more simple cavity model. Their approach requires extremely precise evaluation of the impedance matrix elements due to the close proximity of the patch and its image. This model does not appear to have any significant advantage over the cavity model except for its applicability to patches of more general shape.

In order to improve upon these approximate techniques, several authors have attempted to solve an integral equation for the current on the antenna using the method of moments and employing the exact Green's function for the grounded dielectric substrate. The use of the rigorous Green's function is particularly important when analyzing arrays in order to include the effects of surface waves, which can cause severe mismatch at certain scan angles in large arrays, or scan blindness in infinite arrays [13]. Most of these authors use entire domain basis and testing functions best suited to the geometry of the patch they are analyzing [14-17]. Others, however, use a more general approach employing subsectional basis and testing functions [18-22], which is the approach used in this work. All of these authors use a spectral domain moment method formulation [23], which requires the evaluation of Sommerfeld integrals to evaluate the elements of the generalized impedance matrix. The evaluation of these integrals can consume a great deal of computer time, thus, in practice can reduce the number of basis functions used to represent the unknown current distribution, restricting the generality of the solution. Alexopoulos and Rana [21,22] have used an acceleration

technique to improve the computational efficiency of their solution for microstrip dipoles, but they have not as yet extended their solution to microstrip patches, or large arrays of dipoles or patches. Still, the agreement with experimental results for thin microstrip antennas is very good using this method. In principle, the method is extendable to the analysis of patches on thick substrates. However, as shown in Chapter 5, the complicated current distribution in the feed region requires either the use of more basis functions as is done here, or a separate treatment of the feed region currents as done by Chew and Kong [15] for the circular patch.

The analysis of antenna arrays requires one to include the effects of mutual impedances between antenna elements. One approach to this problem, called the element-by-element approach [24], is to individually calculate the mutual impedance between elements. Several authors have successfully used the spectral domain moment method approach to compute the mutual impedance between microstrip dipoles [22] and microstrip patches [18,20]. Recently, this technique has been applied to the analysis of finite linear arrays [25,26]. However, this approach also requires the evaluation of Sommerfeld integrals, and can require the solution of prohibitively large matrix equations to analyze large arrays.

A more computationally efficient approach to the analysis of large arrays is the infinite array approach [27]. Assuming certain other conditions are met, this approach is useful for arrays large enough that the central elements can be considered to be operating in an infinite array environment. Aside from its computational advantages, the chief advantages of this approach are that the mutual coupling effects are built

in and that it is only necessary to determine the current on one element in the array. Floquet's theorem [28] ensures that the current on any other element differs only by a phase shift, determined by the array excitation. While the minimum size of the array for which such an approach can be used for the central elements depends on several factors including beam scan angle and element geometry, this is a widely used approach and certainly applicable to the analysis of scanning arrays with hundreds of elements [29-31]. In addition, to this condition, the array has to be periodic and uniformly excited with only a constant incremental phase shift between elements. Several references contain detailed discussions of this approach [24,28,31].

The analysis of an infinite array of antennas using the infinite array approach is very similar to the analysis of a single element using the spectral domain moment method. The major difference between the formulations of the two methods is that the integrand of the Sommerfeld integrals, which arise in the single element problem, becomes discrete in the array problem, leading to an infinite summation instead of an infinite integral. In fact, as pointed out by Munk and Burrell [32], averaging the impedance of an element in an infinite array over all scan angles in real space gives the impedance of the single element. They refer to this technique as the array scanning method. Unfortunately, as a direct result of the similarity between the two problems, the infinite summations which replace the Sommerfeld integrals of the single element problem are slowly convergent, resulting in the same practical limitations due to computational cost and time.

This technique has been used by many authors, and is the approach used in this report. Recently, Pflug and Schuman [33] have used it to analyze infinite arrays of microstrip patches on very thin substrates. Their approach solves for the equivalent magnetic current loops around the exterior of the patch. This approach allows them to handle a wide variety of problems, but it is currently limited to the analysis of arrays of patches on thick substrates. Infinite arrays of microstrip dipoles have also been analyzed using this technique, by the author [34,35] and simultaneously and independently by Pozar and Schaubert [36,37]. The major difference between the two approaches is the improved computational efficiency obtained here by applying the series acceleration methods discussed in Chapter 3. Finally, Rubin and Bertoni have applied the infinite array approach to analyze plane-wave scattering by a periodically perforated plate and several other problems [38-40]. While this work is not directly applicable to the microstrip problem, it is of interest here because of the similar approach.

This work extends previous work in two areas. First, results are obtained for infinite arrays of microstrip dipoles and patches on thick substrates. As mentioned previously, Pozar and Schaubert have also successfully analyzed arrays of dipoles since this project was begun. Perhaps more importantly, the application of series acceleration techniques to the microstrip array problem has significantly improved the computational efficiency of the standard infinite array formulation.

The remainder of Part I is divided into five chapters. The formulation of the problem is discussed in Chapter 2. The formalism of the periodic Green's function is used to express the fields of periodic

current distributions, and use of the method of moments to obtain an approximate solution for the patch current distribution is discussed. The numerical evaluation of the generalized impedance matrix is discussed in Chapter 3. The techniques used to improve the efficiency of these calculations are discussed in detail, along with several examples in one and two dimensions. In Chapter 4, infinite arrays of microstrip dipoles are analyzed, and both theoretical and experimental results are given. Chapter 5 is similarly devoted to results for infinite arrays of microstrip patches. One important restriction to the theory which should be mentioned is that an analysis of the feed region was not included in this report, in that the geometry of the feed was not included in the boundary conditions of the integral equation for the patch current. A simple feed model commonly used by other authors to model a coaxial probe feed for patches on thin substrates was used. It is expected that a more accurate feed model will be the next step in this work. Finally, some conclusions are given in Chapter 6, along with a discussion of some directions for possible improvement in the future.

Throughout this report a basic understanding of phased array theory and terminology is assumed. As mentioned above, many excellent references discuss phased arrays in detail [24,28,31]. The conventions and theorems in Fourier analysis used follow Papoulis [41].

CHAPTER 2

FORMULATION

In order to determine various properties of an antenna or scatterer, the currents on the structure, or a suitable set of equivalent currents, must be determined. While several formulations have been proposed for the microstrip antenna, the total patch current formulation will be used in this report. In this formulation, the sum of the currents flowing on the top and the bottom of the patch is determined. These are the currents that actually radiate, neglecting the feed region currents. As mentioned previously, the patch will be considered to be infinitely thin and perfectly conducting.

Four basic steps in the solution for the patch current will be discussed. First, an integral equation is written which enforces the boundary condition on the tangential electric field on the surface of the patch. Second, an expression for the tangential electric field produced by a current distribution on the patch must be developed. Third, having developed the expression for the tangential electric field, an approach for solving the integral equation must be selected, and the solution formulated. Typically, an approximate technique is chosen, as only a few simple problems have analytical solutions. The method of moments [1] will be used here. Fourth, and most difficult, the solution must be cast into a form which can be solved on a computer, both accurately and efficiently.

2.1. Integral Equation for the Total Patch Current

Many references cover in detail the formulation of the integral equations for electromagnetic scattering problems [9, 42]. In one

approach to the antenna problem, the antenna is treated as a scatterer, with the excitation being due to the feed region rather than an incoming plane wave. In so doing, one formulation is valid for both arrays of antennas and scatterers. Briefly, an integral equation for the total patch current is written which enforces the boundary condition that the total tangential electric field on the surface of the patch is zero. In this report the boundary condition is not enforced on the surface of the feed probe. Such an approach assumes that the patch current is the dominant characteristic of the antenna and that the effect of the feed currents can be accounted for with a simple approximation. Recall from Chapter 1 that due to the periodicity of the problem Floquet's theorem states that the patch current in each unit cell differs from that in any other cell only by a linear phase shift, determined by the excitation. Therefore, enforcing the boundary condition in one unit cell assures the satisfaction of the boundary condition on all patches.

In its simplest form the integral equation can be written

$$\underline{E}_{\tan}^{\text{scat}}(\vec{p}) + \underline{E}_{\tan}^{\text{inc}}(\vec{p}) = 0 \quad (2.1-1)$$

where the equation is enforced over the metallic patch in one unit cell. $\underline{E}_{\tan}^{\text{scat}}$ denotes the tangential component of the electric field produced by the currents on the patch, and $\underline{E}_{\tan}^{\text{inc}}$ denotes the tangential component of the incident field. For the microstrip antenna problem the incident field is usually due to a coaxial probe or a microstrip feed. In the case of a scatterer, the incident field is often an incoming plane wave. The scattered field is found by convolving the current on one patch with the

periodic Green's function, to be derived in the next section. The electric field periodic Green's function for this problem is defined as the electric field produced by an infinite periodic array of point sources in the array plane. In the case of the geometry in Figure 1.1, this would be at the air-dielectric interface. Denoting the dyadic periodic Green's function by $\underline{\underline{G}}$, the integral equation for the patch current becomes

$$\int_{\text{u.c.}} \underline{\underline{G}}(\vec{p} - \vec{p}') \underline{J}(\vec{p}') d\vec{p}' = -\underline{\underline{E}}_{\text{tan}}^{\text{inc}}(\vec{p}) \quad (2.1-2)$$

where u.c. denotes one unit cell. The next step is to derive the periodic Green's function, but first some conventions used in this report will be noted.

1. $e^{j\omega t}$ time variation is assumed throughout.
2. The magnitude of a vector is denoted by leaving off the vector symbol. For example,

$$|\vec{\beta}| = \beta$$

3. A summation sign without limits is assumed to have limits $-\infty$ to ∞ .
4. If the meaning remains clear, the argument of a function will often be suppressed for brevity.
5. For generality, when discussing the Green's function and other quantities with multiple components, the notation G_{ij} will often be used, where i and j can be x , y or z .

6. The terms of a summation will often be given the arguments $\vec{\rho}$ and $\vec{\rho}'$ for a spectral and a spatial summation, respectively. The dependence of $\vec{\rho}$ and $\vec{\rho}'$ on the summation indices is assumed.

2.2. Periodic Green's Function

The fields of a periodic array of an arbitrary current distribution can be obtained by solving for the field of each source explicitly and adding the contribution of each. However, a more natural approach that follows from the plane-wave spectrum technique [43] is to find the fields due to an array of point sources with the same periodicity and convolve the result with the current distribution in one cell. The first step is to find the field of the infinite array of point sources.

2.2.1. Plane-wave spectrum technique

Consider an infinite array of \vec{y} directed, unit amplitude point sources

$$\underline{J}(\vec{\rho}) = \vec{y} \sum_{mn} \delta(\vec{\rho} - \vec{\rho}' - \vec{S}_{mn}) \delta(z) \quad (2.2-1)$$

(From now on the delta function in z will be dropped.) The location of these point sources in space defines a spatial domain lattice shown in Figure 2.1a. The periodicity is defined by the lattice vectors \vec{S}_1 and \vec{S}_2 . Each lattice point is defined by a vector $\vec{S}_{mn} = m\vec{S}_1 + n\vec{S}_2$. The Fourier series for $\underline{J}(\vec{\rho})$ can be found by an extension of standard two-dimensional Fourier series to non-orthogonal lattices. To do so, the "reciprocal

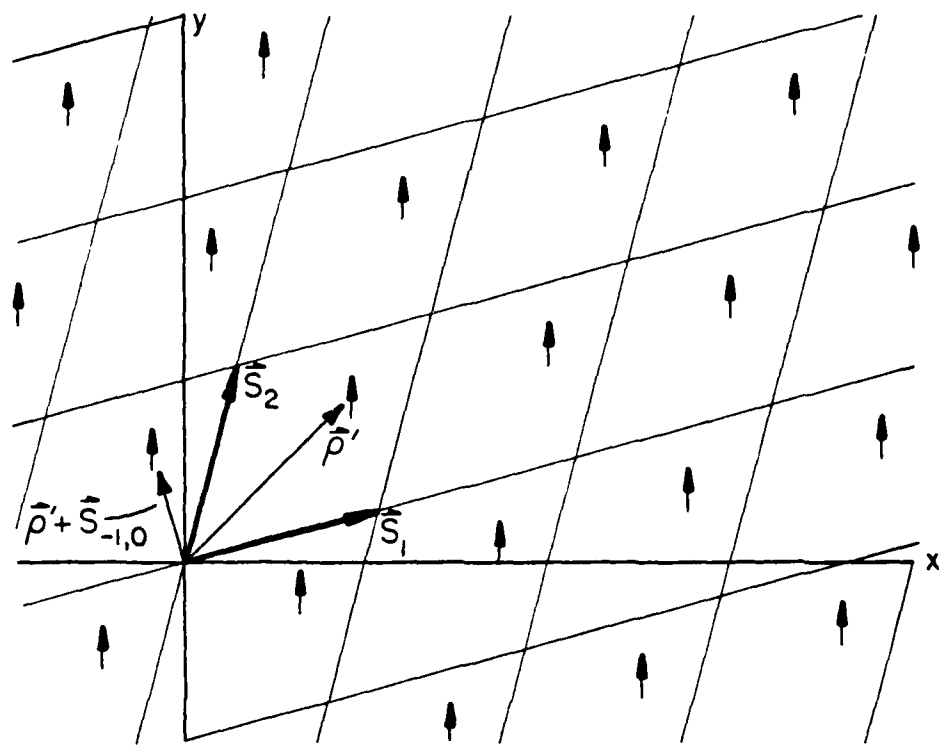


Figure 2.1a. Spatial or "direct" lattice.

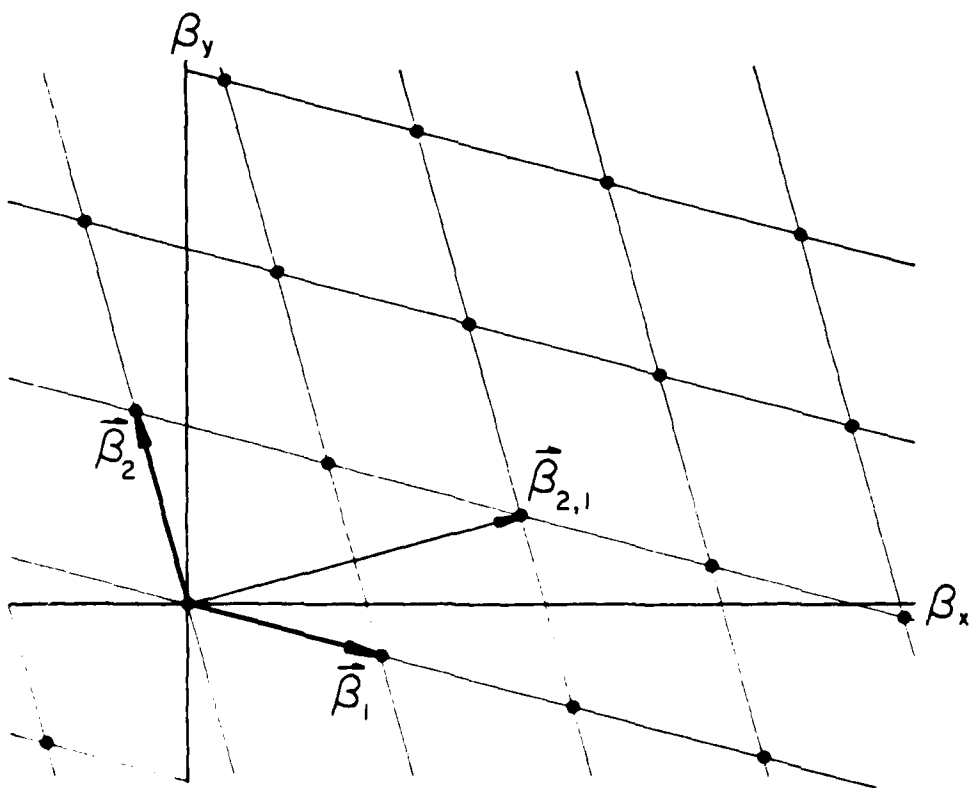


Figure 2.1b. Spectral or "reciprocal" lattice.

lattice" [44] is needed. The reciprocal lattice is defined by the lattice vectors $\vec{\beta}_1$ and $\vec{\beta}_2$, as shown in Figure 2.1b, and describes the periodicity in the spectral domain. $\vec{\beta}_1$ and $\vec{\beta}_2$ are easily found by enforcing the orthogonality required for the Fourier series,

$$\begin{aligned}\vec{\beta}_1 \cdot \vec{s}_1 &= 2\pi & \vec{\beta}_2 \cdot \vec{s}_1 &= 0 \\ \vec{\beta}_1 \cdot \vec{s}_2 &= 0 & \vec{\beta}_2 \cdot \vec{s}_2 &= 2\pi\end{aligned}\tag{2.2-2}$$

which lead to the definitions

$$\vec{\beta}_1 = -\frac{2\pi}{A} (\vec{n} \times \vec{s}_2) \quad \vec{\beta}_2 = \frac{2\pi}{A} (\vec{n} \times \vec{s}_1) \tag{2.2-3}$$

A is the area of a unit cell in the direct lattice, and is defined by $A = \vec{n} \cdot (\vec{s}_1 \times \vec{s}_2)$ where \vec{n} is the normal from the array plane containing \vec{s}_1 and \vec{s}_2 . In this report $\vec{n} = \vec{z}$. Finally, on these lattices, the Fourier series of a function $f(\vec{\rho})$ is defined

$$f(\vec{\rho}) = \sum \alpha_{mn} e^{j\vec{\beta}_{mn} \cdot \vec{\rho}} \tag{2.2-4}$$

where

$$\alpha_{mn} = \frac{1}{A} \iint_{u.c.} f(\vec{\rho}') e^{-j\vec{\beta}_{mn} \cdot \vec{\rho}'} d\vec{\rho}' \tag{2.2-5}$$

$$\hat{\beta}_{mn} = m\hat{\beta}_1 + n\hat{\beta}_2 \quad (2.2-6)$$

Using this definition, $J(\vec{\rho})$ can be expressed in a Fourier series

$$\underline{J}(\vec{\rho}) = \hat{y} \sum_{mn} e^{j\hat{\beta}_{mn} \cdot (\vec{\rho} - \vec{\rho}')} \quad (2.2-7)$$

To treat the general case, an applied phase shift must be included in the current distribution

$$\underline{J}(\vec{\rho}) = \hat{y} \sum_{mn} \delta(\vec{\rho} - \vec{\rho}' - \hat{\beta}_{mn}) e^{j\hat{\beta}_0 \cdot (\vec{\rho} - \vec{\rho}')} \quad (2.2-8)$$

The applied phase shift is given by $\hat{\beta}_0$, where $\hat{\beta}_0 = m_0\hat{\beta}_1 + n_0\hat{\beta}_2$. Note that this is referenced so that the $m = 0, n = 0$ unit cell will have no phase shift. m_0 and n_0 can uniquely assume values from -1 to 1. The Fourier series expression for this current distribution is found to be

$$\underline{J}(\vec{\rho}) = \hat{y} \sum_{mn} e^{jk_{mn} \cdot (\vec{\rho} - \vec{\rho}')} \quad (2.2-9)$$

where

$$\hat{k}_{mn} = \hat{b}_{mn} + \hat{b}_0 = (m + m_0) \hat{b}_1 + (n + n_0) \hat{b}_2 \quad (2.2-10)$$

For convenience the notation

$$e_{mn}(\vec{p} - \vec{p}') = e^{jk_{mn} \cdot (\vec{p} - \vec{p}')} \quad (2.2-11)$$

will be used.

The form of Equation (2.2-9) suggests an approach to finding the electric field of the array of point sources. Let the array of point sources be placed at the array plane of the grounded dielectric substrate (GDS) shown in Figure 2.2a or 2.2b. Each $e_{mn}(\vec{p} - \vec{p}')$ is a current sheet in the array plane with a different phase variation. While the fields of a single point source at this interface involve Sommerfeld integrals, and are difficult to compute [45 - 47], the fields of a current sheet are easily found. Hence, the fields of each current sheet component of $\mathbf{J}(\vec{p})$ are summed to find the total fields of the array of sources, the periodic Green's function.

2.2.2. Fields of a current sheet

The solution for the fields of a current sheet in free space is discussed in several texts [9, 48], and can be easily extended to layered geometries. Only a general outline will be given here. Consider a \hat{y} directed current sheet $\hat{y}e_{mn}(\vec{p} - \vec{p}')$ at the air-dielectric interface of Figure 2.1a. The solution for the \hat{x} directed sheet follows immediately. In the region $z > 0$, but excluding the source plane $z = t$, the electromagnetic fields satisfy Maxwell's equations

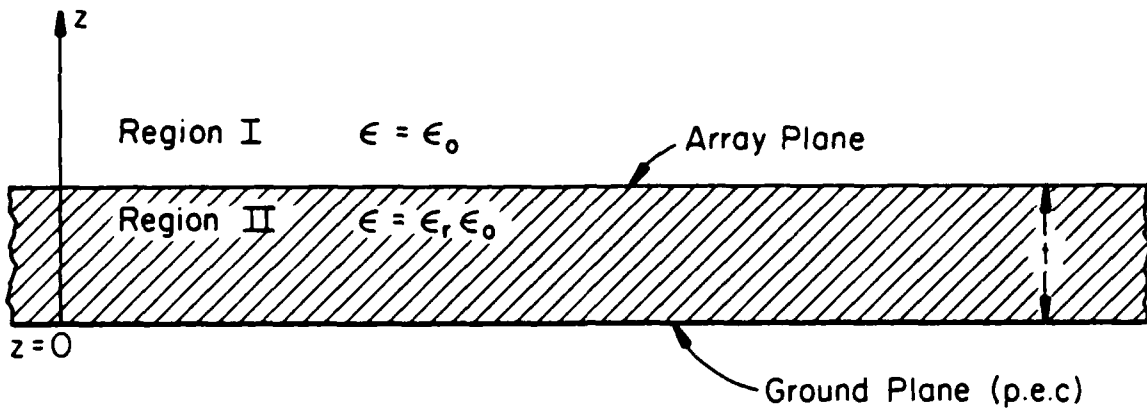


Figure 2.2a. Single layer grounded dielectric substrate (GDS).

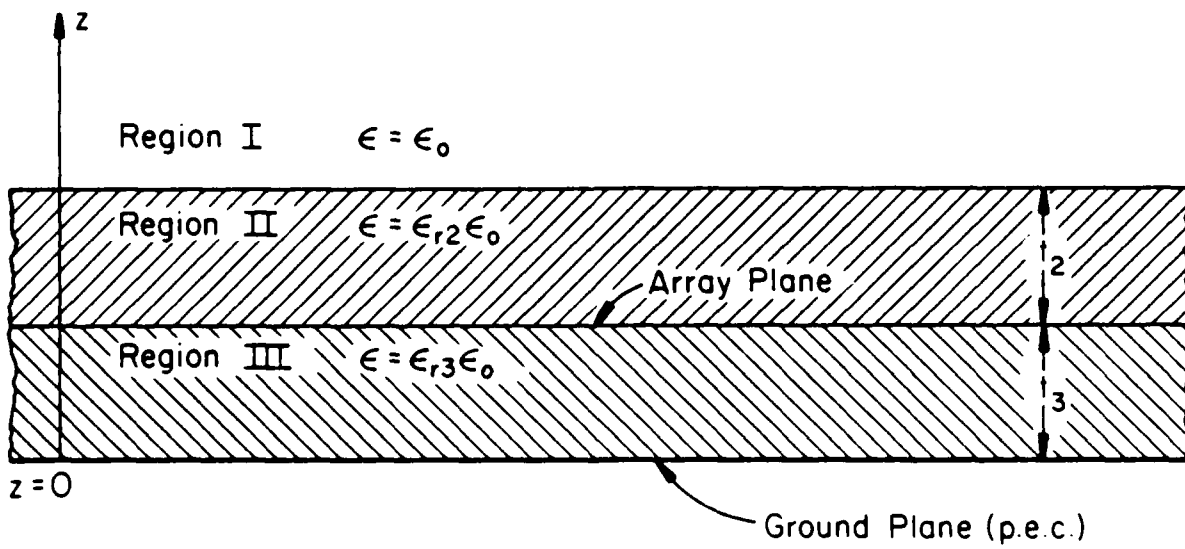


Figure 2.2b. Double layer grounded dielectric substrate.

$$\begin{aligned}\bar{\nabla} \times \underline{E} &= -j\omega\mu \underline{H} & \bar{\nabla} \cdot \underline{H} &= 0 \\ \bar{\nabla} \times \underline{H} &= j\omega\epsilon \underline{E} & \bar{\nabla} \cdot \underline{E} &= 0\end{aligned}\tag{2.2-12}$$

Because \underline{H} is divergenceless due to the lack of magnetic charge, it can be defined as the curl of a magnetic vector potential \underline{A} , and \underline{E} can be expressed in terms of \underline{A} through the Lorentz gauge [49]

$$\begin{aligned}\underline{H} &= \bar{\nabla} \times \underline{A} \\ \underline{E} &= -j\omega\mu\underline{A} + \frac{1}{j\omega\epsilon} \bar{\nabla}(\bar{\nabla} \cdot \underline{A})\end{aligned}\tag{2.2-13}$$

\underline{A} must satisfy the Helmholtz equation in both regions $z < t$, and $z > t$

$$\bar{\nabla}^2 \underline{A} + K^2 \underline{A} = 0\tag{2.2-14}$$

Note that because the source free Maxwell's equations and Helmholtz equation are used the fields will be strictly valid only outside the source region. This is done deliberately in order to avoid a discussion of the evaluation of the Green's function singularity in the source region. This subject has been discussed in detail by several authors [50 - 52], but is not a factor here. Because the tangential electric fields are continuous at the source region except at a source discontinuity, the value of the electric field at the source plane can be determined by taking the limit as z approaches t . In general, the limit can be taken simply by substituting in the value $z = t$. However, for certain current distributions the resulting expression does not converge. A technique to overcome this problem will be discussed in Chapter 3.

Equations (2.2-12) through (2.2-14) can be solved by taking their Fourier transforms and applying the boundary conditions in the spectral domain. Note that because the fields of each current sheet vary in the x-y plane only by a linear phase variation, the boundary conditions at $z = 0$ and $z = t$ can be applied equally well to the fields and their Fourier transforms. The Fourier transform pair used in this report is

$$\tilde{f}(\vec{\beta}) = \int_{-\infty}^{\infty} \int_{-\infty}^{\infty} f(\vec{\rho}) e^{-j\vec{\beta} \cdot \vec{\rho}} d\vec{\rho} \quad (2.2-15)$$

$$f(\vec{\rho}) = \frac{1}{4\pi^2} \int_{-\infty}^{\infty} \int_{-\infty}^{\infty} \tilde{f}(\vec{\beta}) e^{j\vec{\beta} \cdot \vec{\rho}} d\vec{\beta}$$

An alternative approach to solving the fields of a current sheet is to employ a transmission line analogy [14]. This method is particularly useful for multilayer problems such as illustrated in Figure 2.2b, as is needed for a microstrip problem with a radome. Using either of these techniques, the fields for $z > t$ of a single current sheet $\hat{y}e_{mn}(\vec{\rho} - \vec{\rho}')$ located at the air-dielectric interface of Figure 2.2a are

$$E_i(\vec{\rho}) = \hat{i} \tilde{G}_{iy}(\vec{k}_{mn}) e_{mn}(\vec{\rho} - \vec{\rho}') \quad (2.2-16)$$

where $i = x, y$ or z , and

$$\tilde{G}_{xy}(\vec{k}_{mn}) = \frac{\beta_x \beta_y D_3 e^{-js(z-t)}}{\omega \epsilon_0 D_1 D_2} \quad (2.2-17a)$$

$$\tilde{G}_{yy}(\vec{k}_{mn}) = \frac{(s_y^2 D_3 - k_o^2 D_1) e^{-js(z-t)}}{\omega \epsilon_o D_1 D_2} \quad (2.2-17b)$$

$$\tilde{G}_{zy}(\vec{k}_{mn}) = \frac{-\beta_y s'}{\omega \epsilon_o D_1} e^{-js(z-t)} \quad (2.2-17c)$$

and with the unit vectors $\hat{\beta}_x$ and $\hat{\beta}_y$,

$$\beta_x = \vec{k}_{mn} \cdot \hat{\beta}_x, \quad \beta_y = \vec{k}_{mn} \cdot \hat{\beta}_y$$

$$k_o = 2\pi/\lambda_o$$

$$\left. \begin{array}{l} s = (k_o^2 - k_{mn}^2)^{1/2} \\ s' = (\epsilon_r k_o^2 - k_{mn}^2)^{1/2} \end{array} \right\} \begin{array}{l} + \text{root, if real} \\ - \text{root, if imaginary} \end{array} \quad (2.2-18)$$

$$D_1 = s' - js \epsilon_r \cot s' t$$

$$D_2 = s - js' \cot s' t$$

$$D_3 = s' - js \cot s' t$$

Of course, the fields of the \hat{x} directed source can be obtained by a simple rotation of coordinates. Note that \tilde{G}_{xy} , \tilde{G}_{yy} and \tilde{G}_{zy} are the Fourier transforms of the standard Green's function, the electric field of a single point source in the array plane.

The field of each current sheet is a plane wave, either homogeneous or inhomogeneous, depending on \vec{k}_{mn} . The standard notation for the phase variation of a plane wave with $e^{j\omega t}$ time convention is, (for $z > 0$)

$$e^{-j\vec{k} \cdot \vec{r}} = e^{-jk_x x} e^{-jk_y y} e^{-jk_z z} \quad (2.2-19)$$

which has a direction of propagation given by the vector $\hat{\vec{k}} = \hat{k_x} \hat{u_x} + \hat{k_y} \hat{u_y} + \hat{k_z} \hat{u_z}$. In this report, due to the Fourier transform pair used, the phase variation of a plane wave is written as $e^{j\vec{k}_{mn} \cdot \vec{p}} e^{-jsz}$. Thus, \vec{k}_{mn} is in the negative direction of propagation of the wave projected into the x-y plane, and $\beta_x = -k_x$, $\beta_y = -k_y$ and $s = k_z$. This notation should be kept in mind when comparing the results here to other work, but within this report it only affects the sign of the z components of the Green's function and the beam steering constants m_o and n_o .

As discussed above, the periodic Green's function is easily derived from the solution for a single current sheet by summing the fields due to all of the component current sheets of an array of point sources, as indicated by Equation (2.2-9). In this manner the periodic Green's function for the GDS of Figure 2.2a is obtained

$$\underline{G}_{ij}(\vec{p} - \vec{p}') = \frac{i}{A} \sum_{mn} \widetilde{G}_{ij}(\vec{k}_{mn}) \underline{e}_{mn}(\vec{p} - \vec{p}') \quad (2.2-20)$$

where the components \widetilde{G}_{ij} for both $0 \leq z \leq t$ and $z \geq t$ are found in Table 2.1. For completeness the magnetic field periodic Green's function is

$$\underline{G}_{ij}^H(\vec{p} - \vec{p}') = \frac{i}{A} \sum_{mn} \widetilde{G}_{ij}^H(\vec{k}_{mn}) \underline{e}_{mn}(\vec{p} - \vec{p}') \quad (2.2-21)$$

where the components \widetilde{G}_{ij}^H are also found in Table 2.1. Finally, the

TABLE 2.1

COMPONENTS \tilde{G}_{ij} AND \tilde{G}_{ij}^H FOR THE PERIODIC GREEN'S FUNCTION
OF A SINGLE LAYER GDS

Region I $z \geq t$

$$\tilde{G}_{xy} = \tilde{G}_{yx} = \frac{\beta_x \beta_y D_3 e^{-js(z-t)}}{\omega \epsilon_0 D_1 D_2}$$

$$\tilde{G}_{yy} = [\tilde{G}_{xx}]_{x \leftrightarrow y} = \frac{(\beta_y^2 D_3 - k_0^2 D_1)}{\omega \epsilon_0 D_1 D_2} e^{-js(z-t)}$$

$$\tilde{G}_{zy} = [\tilde{G}_{zx}]_{x \leftrightarrow y} = \frac{-s' \beta_y}{\omega \epsilon_0 D_1} e^{-js(z-t)}$$

$$\tilde{G}_{xy}^H = -[\tilde{G}_{yx}^H]_{x \leftrightarrow y} = \frac{(s D_1 - j \beta_y^2 (\epsilon_r - 1) \cot s't)}{D_1 D_2} e^{-js(z-t)}$$

$$\tilde{G}_{yy}^H = -\tilde{G}_{xx}^H = \frac{(j \beta_x \beta_y (\epsilon_r - 1) \cot s't)}{D_1 D_2} e^{-js(z-t)}$$

$$\tilde{G}_{zy}^H = -[\tilde{G}_{zx}^H]_{x \leftrightarrow y} = \frac{\beta_x}{D_2} e^{-js(z-t)}$$

TABLE 2.1 (Cont.)

Region II $0 \leq z \leq t$

$$\tilde{G}_{xy} = \tilde{G}_{yx} = \frac{\beta_x \beta_y D_3}{\omega \epsilon_0 D_1 D_2} \frac{\sin s'z}{\sin s't}$$

$$\tilde{G}_{yy} = [\tilde{G}_{xx}]_{x \leftrightarrow y} = \frac{\beta_y^2 D_3 - k_0^2 D_1}{\omega \epsilon_0 D_1 D_2} \frac{\sin s'z}{\sin s't}$$

$$\tilde{G}_{zy} = [\tilde{G}_{zx}]_{x \leftrightarrow y} = \frac{-js\beta_y \cos s'z}{D_1 \sin s't}$$

$$\tilde{G}_{xy}^H = -[\tilde{G}_{yx}^H]_{x \leftrightarrow y} = \frac{j(s'D_1 - \beta_y^2(\epsilon_r - 1))}{D_1 D_2} \cdot \frac{\cos s'z}{\sin s't}$$

$$\tilde{G}_{yy}^H = -\tilde{G}_{xx}^H = \frac{j\beta_x \beta_y (\epsilon_r - 1)}{D_1 D_2} \cdot \frac{\cos s'z}{\sin s't}$$

$$\tilde{G}_{zy}^H = -[\tilde{G}_{zx}^H]_{x \leftrightarrow y} = \frac{\beta_x \sin s'z}{D_2 \sin s't}$$

Note: 1) \tilde{G}_{ij} and \tilde{G}_{ij}^H are all functions of k_{mn} .
 2) $[\cdot]_{x \leftrightarrow y}$ means replace x with y, y with x.

periodic Green's function for the two layer problem of Figure 2.2b is also expressed by Equations (2.2-20) and (2.2-21). The components for the two layer Green's function are found in Table 2.2. The results in Table 2.2 are valid in the source plane only, but can be easily extended for all z . The Green's function in the source plane for many different cases can be obtained from Table 2.2 by deriving \tilde{Z}_0^e and \tilde{Z}_0^h for the geometry, as described in [14]. For example, with $Y_{TE} = s/\omega\mu_0$ and $Y_{TM} = \omega\epsilon_0/s$, the single layer Green's function of Table 2.1 (for $z = t$) can be obtained by substituting

$$\tilde{Z}_0^e = \frac{ss'}{\omega\epsilon_0 D_1} \quad \tilde{Z}_0^h = \frac{\omega\mu_0}{D_2} \quad (2.2-22)$$

and the free-space Green's function by using

$$\tilde{Z}_0^e = \frac{s}{2\omega\epsilon_0} \quad \tilde{Z}_0^h = \frac{\omega\mu_0}{2s} \quad (2.2-23)$$

2.2.3. Fields of an arbitrary periodic current distribution

The final step in the solution of the fields of a general periodic source is to convolve the source distribution in one unit cell with the periodic Green's function

$$\underline{E}(\vec{\rho}) = \underline{G}(\vec{\rho}) * \underline{J}(\vec{\rho}) \quad (2.2-24)$$

From now on, $\underline{J}(\vec{\rho})$ indicates a general current distribution in one unit cell. Considering only a \hat{y} directed source, and retaining only the

TABLE 2.2

COMPONENTS \tilde{G}_{ij} AND \tilde{G}_{ij}^H FOR THE PERIODIC
GREEN'S FUNCTION OF A TWO LAYER GDS

$$\tilde{G}_{xy} = \tilde{G}_{yx} = (\tilde{z}_o^h - \tilde{z}_o^e) \frac{\beta_x \beta_y}{\beta_x^2 + \beta_y^2}$$

$$\tilde{G}_{yy} = [\tilde{G}_{xx}]_{x \leftrightarrow y} = - \frac{(\tilde{z}_o^e \beta_y^2 + \tilde{z}_o^h \beta_x^2)}{\beta_x^2 + \beta_y^2}$$

$$\tilde{G}_{zy} = [\tilde{G}_{zx}]_{x \leftrightarrow y} = - \frac{\tilde{z}_o^e \beta_y}{\beta_z}$$

$$\tilde{G}_{xy}^H = -[\tilde{G}_{yx}^H]_{x \leftrightarrow y} = \frac{\tilde{z}_o^h Y_{TE} \beta_x^2 + \tilde{z}_o^e Y_{TM} \beta_y^2}{\beta_x^2 + \beta_y^2}$$

$$\tilde{G}_{yy}^H = -\tilde{G}_{xx}^H = (\tilde{z}_o^h Y_{TE} - \tilde{z}_o^e Y_{TM}) \frac{\beta_x \beta_y}{\beta_x^2 + \beta_y^2}$$

$$\tilde{G}_{zy}^H = -[\tilde{G}_{zx}^H]_{x \leftrightarrow y} = \frac{\tilde{z}_o^h \beta_x}{\omega \mu_0}$$

Note: 1) \tilde{G}_{ij} and \tilde{G}_{ij}^H are all functions of \vec{k}_{mn} .
2) $[\cdot]_{x \leftrightarrow y}$ means replace x with y, y with x.

TABLE 2.2 (Cont.)

where:

$$\hat{Z}_o^e = \frac{s_2 s_3 D_7}{\omega \epsilon_0 (\epsilon_2 s_3 D_6 - j \epsilon_3 s_2 D_7 \cot s_3 t_3)}$$

$$\hat{Z}_o^h = \frac{\omega \mu_0 D_5}{(s_2 D_4 - j s_3 D_5 \cot s_3 t_3)}$$

$$Y_{TE} = \frac{s_2}{\omega \mu_0}, \quad Y_{TM} = \frac{\omega \epsilon_0 \epsilon_2}{s_2}$$

$$s_r = \sqrt{k_0^2 \epsilon_r - \beta_x^2 - \beta_y^2} \quad (+ \text{ root, if real}) \quad (- \text{ root, if imag.})$$

$$D_4 = s_2 - j s_1 \cot s_2 t_2$$

$$D_5 = s_1 - j s_2 \cot s_2 t_2$$

$$D_6 = \epsilon_2 s_1 - j s_2 \cot s_2 t_2$$

$$D_7 = s_2 - j \epsilon_2 s_1 \cot s_2 t_2$$

tangential components of the fields, Equation (2.2-24) becomes

$$\begin{aligned} \underline{E}_{tan}(\vec{\rho}) = & \iint_{u.c.} \left[\frac{\hat{x}}{A} \sum_{mn} \tilde{G}_{xy}(\vec{K}_{mn}) e_{mn}(\vec{\rho} - \vec{\rho}') J_y(\vec{\rho}') \right. \\ & \left. + \frac{\hat{y}}{A} \sum_{mn} \tilde{G}_{yy}(\vec{K}_{mn}) e_{mn}(\vec{\rho} - \vec{\rho}') J_y(\vec{\rho}') \right] d\vec{\rho}' \end{aligned} \quad (2.2-25)$$

Noting that \tilde{G}_{xy} and \tilde{G}_{yy} do not depend on $\vec{\rho}'$, and recognizing that

$$\begin{aligned} e_{mn}(\vec{\rho} - \vec{\rho}') &= e_{mn}(\vec{\rho}) e_{mn}(-\vec{\rho}') \\ &= e_{mn}(\vec{\rho}) e^{-jk\vec{K}_{mn} \cdot \vec{\rho}'} \end{aligned} \quad (2.2-26)$$

one obtains after interchanging the order of integration and summation

$$\begin{aligned} \underline{E}_{tan}(\vec{\rho}) = & \frac{\hat{x}}{A} \sum_{mn} \tilde{G}_{xy}(\vec{K}_{mn}) e_{mn}(\vec{\rho}) \iint_{u.c.} J_y(\vec{\rho}') e^{-jk\vec{K}_{mn} \cdot \vec{\rho}'} d\vec{\rho}' \\ & + \frac{\hat{y}}{A} \sum_{mn} \tilde{G}_{yy}(\vec{K}_{mn}) e_{mn}(\vec{\rho}) \iint_{u.c.} J_y(\vec{\rho}') e^{-jk\vec{K}_{mn} \cdot \vec{\rho}'} d\vec{\rho}' \end{aligned} \quad (2.2-27)$$

The integration is recognized to be the Fourier transform of the current distribution, resulting in the final form for the fields of an arbitrary current distribution

$$\begin{aligned} \underline{E}_{tan}(\vec{\rho}) = & \frac{\hat{x}}{A} \sum_{mn} \tilde{G}_{xy}(\vec{K}_{mn}) \tilde{J}_y(\vec{K}_{mn}) e_{mn}(\vec{\rho}) \\ & + \frac{\hat{y}}{A} \sum_{mn} \tilde{G}_{yy}(\vec{K}_{mn}) \tilde{J}_y(\vec{K}_{mn}) e_{mn}(\vec{\rho}) \end{aligned} \quad (2.2-28)$$

This result could have been obtained more directly by simply using the Fourier series for the periodic current distribution. This expresses

the periodic current distribution directly in terms of current sheets, the fields of which can be summed to give the desired total fields. However, it is felt that the formalism of the periodic Green's function provides a somewhat better insight into the problem.

2.3. Method of Solution of the Integral Equation

Using the above results for the field of an arbitrary current distribution, the integral equation for the patch current becomes dual algebraic equations

$$\sum_{mn} \tilde{G}_{xx}(\vec{k}_{mn}) \tilde{J}_x(\vec{k}_{mn}) \frac{e_{mn}(\vec{\rho})}{A} + \sum_{mn} \tilde{G}_{xy}(\vec{k}_{mn}) \tilde{J}_y(\vec{k}_{mn}) \frac{e_{mn}(\vec{\rho})}{A} = - E_x^{inc}(\vec{\rho})$$

(2.3-1)

$$\sum_{mn} \tilde{G}_{yx}(\vec{k}_{mn}) \tilde{J}_x(\vec{k}_{mn}) \frac{e_{mn}(\vec{\rho})}{A} + \sum_{mn} \tilde{G}_{yy}(\vec{k}_{mn}) \tilde{J}_y(\vec{k}_{mn}) \frac{e_{mn}(\vec{\rho})}{A} = - E_y^{inc}(\vec{\rho})$$

The solution to this equation will be the desired total patch current, or more accurately, its Fourier transform. An approximate solution for the equation can be obtained using the method of moments [1, 53, 54]. This technique takes advantage of the linearity of the Green's function to reduce the coupled equations into a set of simultaneous equations which can be solved by matrix techniques. Briefly, to solve the equations with the method of moments, a set of linearly independent basis functions is chosen to represent the unknown current. To obtain the exact solution, the basis functions must span the domain of possible solutions to the current distributions. Ideally, a complete set of basis functions is chosen, as a general solution is desired and very little is known about the actual

current distribution. Now the current distribution can be represented as a sum of components from the set of basis functions

$$\underline{J}(\vec{\rho}) = \hat{x} \sum_{p=0}^{\infty} a_p J_{xp}(\vec{\rho}) + \hat{y} \sum_{q=0}^{\infty} b_q J_{yq}(\vec{\rho}) \quad (2.3-2)$$

or using the linearity of the Fourier Transform,

$$\underline{\tilde{J}}(\vec{\beta}) = \hat{x} \sum_{p=0}^{\infty} a_p \tilde{J}_{xp}(\vec{\beta}) + \hat{y} \sum_{q=0}^{\infty} b_q \tilde{J}_{yq}(\vec{\beta}) \quad (2.3-3)$$

Using the notation

$$E_{ij}^p = \sum_{mn} \tilde{G}_{ij}(\vec{k}_{mn}) \tilde{J}_{jp}(\vec{k}_{mn}) \frac{e_{mn}(\vec{\rho})}{A} \quad (2.3-4)$$

Equations (2.3-3) and (2.3-1) combine to give a new expression for the patch current equation

$$\sum_{p=0}^{\infty} a_p E_{xx}^p + \sum_{q=0}^{\infty} b_q E_{xy}^q = -E_x^{inc}(\vec{\rho}) \quad (2.3-5)$$

$$\sum_{p=0}^{\infty} a_p E_{yx}^p + \sum_{q=0}^{\infty} b_q E_{yy}^q = -E_y^{inc}(\vec{\rho})$$

To reduce Equation (2.3-5) into a set of simultaneous equations, a set of testing functions is chosen, $\sum_{r=0}^{\infty} T_{xr}(\vec{\rho})$, $\sum_{s=0}^{\infty} T_{ys}(\vec{\rho})$, often the same as the set of basis functions. Again, for an exact solution, the set of

testing functions must span the range of the operator, the periodic Green's function, on the current. As usual, the assumption is made that a denumerable set of testing functions can span the range of the operator. Physically, the set of testing functions must be able to represent the tangential electric field. Defining the inner product as

$$\langle \underline{f}(\vec{\rho}), \underline{g}(\vec{\rho}) \rangle = \int_{-\infty}^{\infty} \int_{-\infty}^{\infty} \underline{f}(\vec{\rho}) \cdot \underline{g}(\vec{\rho}) d\vec{\rho} \quad (2.3-6)$$

the inner product is formed with each member of the set of testing functions

$$\langle T_{xr}, \sum_{p=0}^{\infty} a_p E_{xx}^p + \sum_{q=0}^{\infty} b_q E_{xy}^q + E_x^{\text{inc}}(\vec{\rho}) \rangle = 0 \quad r = 1, 2, \dots, \infty \quad (2.3-7)$$

$$\langle T_{ys}, \sum_{p=0}^{\infty} a_p E_{yx}^p + \sum_{q=0}^{\infty} b_q E_{yy}^q + E_y^{\text{inc}}(\vec{\rho}) \rangle = 0 \quad s = 1, 2, \dots, \infty$$

The inner product of orthogonal quantities is zero, and has been dropped from Equation (2.3-7).

Each inner product requires that the error in the solution be orthogonal to that testing function. As successive inner products are taken, the answer gets progressively better. Theoretically, if a complete set is used for both the basis and testing functions, the exact answer can be obtained. Unfortunately, this generally requires an infinite number of functions, resulting in an infinite set of equations which can be solved in only a few special cases. Hence to make the problem tractable, a

finite set of basis and testing functions is generally chosen. A good choice of these functions is one which has some physical basis and, because efficiency is important, numerical convenience. In this report, subsectional basis and testing functions with closed-form Fourier transforms are used. Each subsectional basis function exists only over a finite section of the patch. Thus the current distribution is now approximately represented with a finite set of basis functions

$$\underline{J}(\vec{\rho}) \approx \hat{x} \sum_{p=0}^P a_p J_{xp}(\vec{\rho}) + \hat{y} \sum_{q=0}^Q b_q J_{yq}(\vec{\rho}) \quad (2.3-8)$$

and the set of equations to be solved becomes

$$\sum_{p=0}^P a_p \langle T_{xr}, E_{xx}^p \rangle + \sum_{q=0}^Q b_q \langle T_{xr}, E_{xy}^q \rangle = \langle T_{xr}, -E_x^{\text{inc}}(\vec{\rho}) \rangle \quad r = 1, 2, \dots, R \quad (2.3-9)$$

$$\sum_{p=0}^P a_p \langle T_{ys}, E_{yx}^p \rangle + \sum_{q=0}^Q b_q \langle T_{ys}, E_{yy}^q \rangle = \langle T_{ys}, -E_y^{\text{inc}}(\vec{\rho}) \rangle \quad s = 1, 2, \dots, S$$

which can be solved for the current coefficients. Typically, the number of testing functions and basis functions is equal, i.e., $P = S$ and $Q = R$, resulting in a set of equations of order $P + Q$, which can be conveniently represented in matrix form

$$\begin{bmatrix} Z_{RP}^{xx} & Z_{RQ}^{xy} \\ \hline Z_{SP}^{yx} & Z_{SQ}^{yy} \end{bmatrix} \begin{bmatrix} a_p \\ b_q \end{bmatrix} = \begin{bmatrix} v_{xR} \\ v_{yS} \end{bmatrix} \quad (2.3-10)$$

where Z_{RP}^{xx} , Z_{RQ}^{xy} , Z_{SP}^{yx} and Z_{SQ}^{yy} are all matrices of the form

$$Z_{RP}^{xx} = \begin{bmatrix} \langle T_{x1}, E_{xx}^1 \rangle & \langle T_{x1}, E_{xx}^2 \rangle & \dots & \langle T_{x1}, E_{xx}^P \rangle \\ \langle T_{x2}, E_{xx}^1 \rangle & \langle T_{x2}, E_{xx}^2 \rangle & \dots & \langle T_{x2}, E_{xx}^P \rangle \\ \vdots & \ddots & & \vdots \\ \vdots & \ddots & & \vdots \\ \vdots & \ddots & & \vdots \\ \langle T_{xR}, E_{xx}^1 \rangle & \langle T_{xR}, E_{xx}^2 \rangle & \dots & \langle T_{xR}, E_{xx}^P \rangle \end{bmatrix} \quad (2.3-11)$$

and the other matrices are

$$[a_p] = [a_1, a_2, \dots, a_p]^T, [b_Q] = [b_1, b_2, \dots, b_Q]^T$$

$$[v_R] = [\langle T_{x1}, -E_x^{inc}(\rho) \rangle, \langle T_{x2}, -E_x^{inc}(\rho) \rangle, \dots, \langle T_{xR}, -E_x^{inc}(\rho) \rangle]^T \quad (2.3-12)$$

$$[v_S] = [\langle T_{y1}, -E_y^{inc}(\rho) \rangle, \langle T_{y2}, -E_y^{inc}(\rho) \rangle, \dots, \langle T_{yS}, -E_y^{inc}(\rho) \rangle]^T$$

This matrix equation can easily be solved for the unknown current coefficients once inner products have been evaluated. It is this task which is at the heart of any moment method solution, and must be examined more closely.

2.4. Numerical Evaluation of the Solution

Equation (2.3-10) is of the form $Zx = v$. The Z matrix, or the impedance matrix, and the right-hand side, the incident field matrix, both consist of inner products which can be difficult to evaluate. For the purposes of this chapter only the Z matrix will be considered. In

general, the V matrix is either very simple to evaluate or is very similar in evaluation to the Z matrix. The incident field for each class of problem will be considered in the section dealing with that problem.

Examining one equation in the set and expanding the expression for the scattered field give

$$\begin{aligned}
 & \sum_{p=0}^P a_p \int_{-\infty}^{\infty} \int_{-\infty}^{\infty} T_{xr}(\vec{\rho}) \sum_{mn} \tilde{G}_{xx}(\vec{k}_{mn}) \tilde{J}_{xp}(\vec{k}_{mn}) \frac{e_{mn}}{A}(\vec{\rho}) d\vec{\rho} \\
 & + \sum_{q=0}^Q b_q \int_{-\infty}^{\infty} \int_{-\infty}^{\infty} T_{xr}(\vec{\rho}) \sum_{mn} \tilde{G}_{xy}(\vec{k}_{mn}) \tilde{J}_{yq}(\vec{k}_{mn}) \frac{e_{mn}}{A}(\vec{\rho}) d\vec{\rho} \quad (2.4-1) \\
 & = \langle T_{xr}(\vec{\rho}), -E_x^{\text{inc}}(\vec{\rho}) \rangle
 \end{aligned}$$

Interchanging the order of summation and integration and removing from under the integral those functions which do not depend on the spatial variable, the integral is again recognized as the Fourier transform integral with a sign change in the kernel. The integral results in the complex conjugate of the testing function, denoted T_{xr}^* and T_{ys}^* .

Performing the integration results in

$$\begin{aligned}
 & \sum_{p=0}^P a_p \sum_{mn} \tilde{G}_{xx} \tilde{J}_{xp} T_{xr}^* + \sum_{q=0}^Q b_q \sum_{mn} \tilde{G}_{xy} \tilde{J}_{yq} T_{xr}^* \\
 & = \langle T_{xr}, -E_x^{\text{inc}} \rangle \quad (2.4-2)
 \end{aligned}$$

where the arguments have been dropped. Finally, in this report all members of the basis and testing sets are identical to all others except for a linear translation, and all are even functions. For example, if $J_x(\vec{\rho})$ denotes the general form of the basis functions, the members of the basis set can be expressed

$$J_{xp}(\vec{\rho}) = J_x(\vec{\rho} - \vec{\rho}_p) \quad (2.4-3)$$

Then the transform of a member in the basis set becomes

$$\tilde{J}_{xp}(\vec{\beta}) = \tilde{J}_x(\vec{\beta}) e^{-j\vec{\beta} \cdot \vec{\rho}_p} \quad (2.4-4)$$

Hence denoting the unshifted testing and expansion functions and their transforms as J_x , T_x and \tilde{J}_x , and \tilde{T}_x , Equation (2.4-2) can be expressed as

$$\sum_{p=0}^P a_p \sum_{mn} \tilde{G}_{xx} \tilde{J}_x \tilde{T}_x e_{mn}(\vec{\rho}_r - \vec{\rho}_p) + \sum_{q=0}^Q b_q \sum_{mn} \tilde{G}_{xy} \tilde{J}_y \tilde{T}_x e_{mn}(\vec{\rho}_r - \vec{\rho}_q) = \langle T_{xr}, -E_x^{\text{inc}} \rangle \quad (2.4-5)$$

where $\vec{\rho}_p$, $\vec{\rho}_q$ and $\vec{\rho}_r$ are the vectors from the origin to the p th and q th basis functions and the r th testing function, respectively.

Up to this point, only two approximations have been made: casting the physical problem into an idealized mathematical model, and using a finite set of basis and expansion functions. Unfortunately, another approximation must enter at this point. The infinite summations in Equation (2.4-5) must necessarily be truncated at some finite number of terms. Assuming for the moment that the expressions do converge, the question of how many terms need to be summed to achieve sufficient accuracy is a difficult one. In addition, for some choices of basis and testing functions, such as the commonly used pulse expansion and point matching functions,

$$\begin{aligned}
 J_1(\vec{\rho}) &= 1 & |x| \leq a, \quad |y| \leq b \\
 &= 0 & \text{otherwise}
 \end{aligned} \tag{2.4-6}$$

$$T_1(\vec{\rho}) = \delta(\vec{\rho})$$

The summations required in some inner products do not converge at all under a straightforward summation of terms. (The terms do not approach zero as m and n approach infinity.)

In practice, basis and testing functions with sufficient smoothness to ensure convergence of all terms in the Z matrix are chosen, and as in common practice, a numerical test for convergence is used. In particular, m and n are increased until the change in the partial sums is only evident beyond a chosen number of digits. The required tolerance in the matrix elements depends on the desired accuracy in the final answer. Because of the oscillating nature of the terms of the series, m and n need to be increased beyond the point where tolerance first appears to be met to ensure that the tolerance has indeed been satisfied. Unfortunately, as the parameters of the problem are varied, such as the size of the patch, the array spacing, and the relative location of the basis and testing functions, the required upper limits on m and n can vary greatly.

The problem in truncating the sum is further complicated by the slow convergence of the sum. Consider the inner product which arises from the following choices of J_x and T_x

$$\begin{aligned}
 J_x(\vec{\rho}) &= (1 - |x|/a) & |x| \leq a, \quad |y| \leq b \\
 &= 0 & \text{otherwise}
 \end{aligned}
 \tag{2.4-7}$$

$$\begin{aligned}
 T_x(\vec{\rho}) &= \delta(y) & |x| \leq a/2 \\
 &= 0 & \text{otherwise}
 \end{aligned}$$

The transforms of these functions are found to be

$$\begin{aligned}
 \tilde{J}_x(\vec{\beta}) &= \frac{4 \sin^2(\beta_x a/2)}{\beta_x^2 a} \cdot \frac{2 \sin(\beta_y b)}{\beta_y} \\
 &
 \end{aligned}
 \tag{2.4-8}$$

$$\tilde{T}_x(\vec{\beta}) = \frac{2 \sin(\beta_x a/2)}{\beta_x}$$

This set of basis functions, known as rooftop functions due to their shape [54], and testing functions are commonly used, both for single element problems [54] and array problems [38 - 40]. A term in the Z matrix takes the form

$$z_{rp}^{xx} = \frac{1}{A} \sum_{mn} \tilde{G}_{xx} \tilde{J}_x \tilde{T}_x e_{mn}(\vec{\rho}_r - \vec{\rho}_p) \tag{2.4-9}$$

and can be shown to converge as $(mn\sqrt{m^2 + n^2})^{-1}$. While this does converge, it does so fairly slowly. Consider an array with lattice spacing $\$_1 = \$_2 = 0.5\lambda_0$, thickness $t = 0.1\lambda_0$, and relative permittivity $\epsilon_r = 2.55$. For the basis functions in Equation (2.4-7), with $a = 0.03\lambda_0$ and $b = 0.01\lambda_0$, Table 2.3 shows the partial sums for three typical matrix

TABLE 2.3

COMPUTATION TIME AND RATE OF CONVERGENCE
OF EQUATION (2.4-7)

Upper limit on m,n	Magnitude of partial sum			Execution time (sec.)	
	$(\vec{p}_r - \vec{p}_q)$				
	$0.0\vec{s}_1 + 0.0\vec{s}_2$	$0.3\vec{s}_1 + 0.0\vec{s}_2$	$0.5\vec{s}_1 + 0.5\vec{s}_2$		
10	456.602445	9.446813	0.731649	0.3	
20	623.542342	4.712036	0.676901	0.9	
30	558.282397	2.661585	0.674685	1.8	
40	548.478539	0.931113	0.676388	3.2	
50	554.964071	2.414094	0.674967	4.9	
60	551.076179	2.952526	0.675325	6.9	
70	554.695405	2.234459	0.674922	9.3	
80	561.559123	2.387653	0.674983	12.2	
90	556.348143	2.749048	0.674845	15.3	
100	551.758663	2.423449	0.674967	18.9	
110	555.884998	2.260668	0.674909	22.7	
120	558.338015	2.484901	0.674976	26.9	
130	555.769395	2.434351	0.674964	31.5	
140	555.104160	2.286058	0.675000	36.4	
150	555.707834	2.420648	0.674967	41.7	
160	555.130869	2.498604	0.674986	47.4	

elements each with different vectors ($\vec{p}_r - \vec{p}_q$), along with the execution time on a CDC 6600. These times do not take advantage of the symmetry which exists in the sum, which can reduce the execution time by as much as a factor of 4 for a rectangular array with no element-to-element phase shift. However, in the general problem where a phase shift exists there is no symmetry, and the times in Table 2.3 would be representative of a general program used to compute all the required inner products. It is evident that many terms are required to get several digits of accuracy. From this example a rough estimate of the time required to solve a problem can be made. Assume that 10 basis functions in both the \hat{x} and \hat{y} directions are used on a patch, for both the \hat{x} and \hat{y} components of the current. As will be shown later, for a problem with no phase shift this leads to 200 distinct elements of the Z matrix. Even if the summations are truncated at M and $N = 50$ (summing all terms for $|m| < M$ and $|n| < N$), approximately 5 seconds of computer time are required per matrix element at a cost of 17 cents a second (roughly the cost on the University of Illinois CDC 6600). The total cost per problem is then 1000 seconds of execution time, or \$170. Using even less tolerance and truncating the series at $M = 2S_1/a$, $N = S_1/b$ as Rubin and Bertoni suggest [15], which results in truncating the series at $M=33$, $N=50$, require approximately 3 seconds per inner product, or \$100 per problem. Of course, the execution times in Table 2.3 are representative of only one computer program, but nevertheless indicate that the required computer time is a major obstacle to a general solution for periodic scatterers and arrays using this technique.

In order to overcome this problem, a series acceleration procedure has been developed which significantly accelerates the convergence of the infinite summations [2] - [4]. This technique, the subject of the next

chapter, should have wide application to periodic electromagnetic problems, such as the microstrip arrays considered here, frequency selective surfaces, and waveguide and cavity problems.

CHAPTER 3

EVALUATION OF INNER PRODUCTS

In general, the analysis of periodic problems requires the summation of infinite series. This is true whether analyzing arrays of scatterers or arrays of antennas in the space or spectral domain, or analyzing cavities or waveguides using image or modal techniques, to name just a few examples. Unfortunately, the evaluation of infinite summations can be quite time-consuming, particularly for sums which are infinite in two or more indices.

Recall from Chapter 2 the basic form of a term in the Z matrix:

$$z_{rp}^{ij}(\vec{k}_{mn}) = \frac{1}{A} \sum_{mn} \tilde{G}_{ij}(\vec{k}_{mn}) \tilde{J}_j(\vec{k}_{mn}) \tilde{T}_i(\vec{k}_{mn}) e_{mn}(\vec{\rho}_r - \vec{\rho}_p) \quad (3.0-1)$$

As in the last chapter, the dependence on \vec{k}_{mn} will often be suppressed. This sum has two properties of particular importance in its evaluation. First, as discussed earlier, it is usually very slowly convergent. Second, a singularity exists in the terms for certain values of the parameters involved. D_1 and D_2 in the denominator of \tilde{G}_{ij} are the equations for the TM and TE surface wave poles of the grounded dielectric slab [55]. As will be discussed later, these singularities can lead to blind angles in infinite arrays and stop bands in frequency selective surfaces.

Much work has been done on techniques to accelerate the convergence of summations or to evaluate them in closed form. Two of the most common

acceleration techniques are Poissons' summation formula (PSF) and Kummer's transformation of series, more generally referred to as the subtraction or comparison technique.

Recently, a general method was reported [2, 3] which embodies both of these techniques in an acceleration technique which allows for efficient evaluation of the infinite summations derived in Chapter 2. This technique has been used to efficiently analyze arrays of dipoles in free space [4] and arrays of microstrip dipoles [34, 35]. Section 3.1 will introduce the method by application to a simple one-dimensional sum, and a more comprehensive explanation of the application to the two-dimensional sums in the inner products of Equation (2.3-10) will be given in Section 3.2. The remainder of the chapter will discuss the application of the technique to two examples of interest.

3.1. Introduction to the Acceleration Technique

Consider the one-dimensional sum

$$F(b) = \sum_n \frac{1}{n^2 - b^2} \quad (3.1-1)$$

the terms of which are given by the function $f(x) = (x^2 - b^2)^{-1}$ evaluated at the points $x = 0, \pm 1, \pm 2, \pm 3, \dots$. A common practice throughout this chapter when discussing infinite summations will be to refer to the continuous function which defines the terms of the sum by evaluating the function at discrete values of the continuous variable. The sum in Equation (3.1-1) has both of the important properties of the two-dimensional sum in Equation (3.0-1) discussed above: it converges slowly, in

this case as n^{-2} , and a singularity exists in $f(x)$ for $x = \pm b$. This sum will be used to introduce the acceleration technique because of its simplicity, its similarity to the sums of interest here, and because it can be summed in closed form with the well-known result:

$$\sum_n \frac{1}{n^2 - b^2} = -\frac{\pi}{b} \cot(\pi b) \quad (3.1-2)$$

As mentioned previously, this method incorporates two common acceleration techniques, the Poisson summation formula and Kummer's transformation of series.

In its simplest form the Poisson summation formula (PSF) can be stated [41]:

$$\sum_n f(n) = \sum_n \tilde{f}(2\pi n) \quad (3.1-3)$$

The usefulness of this formula is based upon the property that the Fourier transform of a smooth, slowly decaying function is a rapidly decaying function. In this report, the term decaying means approaching zero. Unfortunately, because of the singularity in $f(x)$, the PSF is not directly applicable to its summation.

Kummer's transformation of series, more commonly known as the subtraction or the comparison technique, can be stated [56]:

$$\sum_n f(n) = \sum_n [f(n) - f_a(n)] + \sum_n f_a(n) \quad (3.1-4)$$

where $f_a(n)$ is a function which is asymptotic to $f(n)$ for large n . This technique is related to the singularity subtraction technique for

evaluating singular integrals. As in that technique, the trick is to select a suitable function to subtract and add; in this case a function which can be efficiently summed by the PSF is needed.

The most obvious choice for $f_a(x)$ in this case might be $f_a(x) = x^{-2}$. However, while x^{-2} is asymptotic to $(x^2 - b^2)^{-1}$ for large x , it is singular at $x = 0$ and thus is not suitable for acceleration by the PSF because its transform does not decay rapidly. Instead, choose

$$f_a(x) = \frac{1}{x^2 + u^2} \quad (3.1-5)$$

where u is a real, arbitrary constant. Now $f_a(x)$ is asymptotic to $f(x)$ and has no real singularities, and can be efficiently summed with the PSF. Substituting Equation (3.1-5) into Equation (3.1-4) and applying the PSF formula to the second summation results in

$$F(b) = \sum_n \left(\frac{1}{n^2 - b^2} - \frac{1}{n^2 + u^2} \right) + \frac{\pi}{u} \sum_n e^{-2\pi n} \quad (3.1-6)$$

The second sum in Equation (3.1-6) converges very rapidly, and the first sum can be shown to converge as n^{-4} . While this may be adequate in some cases, more rapid convergence may be needed, particularly for sums in two or more indices. The first sum can be made to converge arbitrarily fast by subtracting as many terms as needed of the asymptotic expansion of $f(x)$ in powers of x^{-1} . An asymptotic expansion of a function $f(x)$ is a series which satisfies the equation:

$$f(x) - \sum_{\ell=0}^L c_\ell x^{-\ell} = o(x^{-L}) \quad \text{as } x \rightarrow \infty \quad (3.1-7)$$

where $f_{a\ell}(x)$ is the ℓ th term of the asymptotic expansion, and $f(x) = o(g(x))$ as $x \rightarrow x_0$ if $f(x)/g(x) \rightarrow 0$ as $x \rightarrow x_0$ [57]. A suitable choice for the asymptotic expansion is one for which each term can be summed efficiently by the PSF (or any other technique). After deriving an asymptotic expansion and applying the PSF to the sums of the terms of the asymptotic expansion, Equation (3.1-4) becomes

$$\sum f(n) = \left[f(n) - \sum_{\ell=0}^L f_{a\ell}(n) \right] + \sum_{\ell=0}^L \sum \tilde{f}_{a\ell}(2\pi n) \quad (3.1-8)$$

Now the terms of the first sum on the right-hand side of Equation (3.1-8) will behave asymptotically as n^{-L-1} or better, from Equation (3.1-7). Of course, the number of terms in the subtracted asymptotic expansion can not be increased indefinitely without paying a price; as L increases, the PSF results in a sum which converges increasingly slowly. This behavior is expected from the previous discussion of the PSF. A suitable expansion for $f_a(x)$ is to use the first few terms of a Taylor series expansion. For the reasons discussed above, an expansion in powers of x^{-1} is not suitable. Instead the substitution $(x^2 - b^2) = (x^2 + u^2) - (b^2 + u^2)$ is made. Denoting $(x^2 + u^2) = \kappa^2$ and $(b^2 + u^2) = \alpha^2$, the Taylor series expansion of $f(x)$ in powers of κ^{-1} is

$$f(x) = \frac{1}{\kappa^2(x) - \alpha^2} = \frac{1}{\kappa^2(x)} \left(1 + \left(\frac{\alpha}{\kappa(x)} \right)^2 + \left(\frac{\alpha}{\kappa(x)} \right)^4 + \dots \right) \alpha^2 < \kappa^2(x) \quad (3.1-9)$$

From now on, the dependence of κ on the continuous variable x or the summation index will be understood. The individual terms in Equation

(3.1-9) are smooth functions and are therefore amenable to an application of the PSF. Hence, if one chooses the first L terms of the above series as the asymptotic expansion in Equation (3.1-8), $F(b)$ becomes

$$F(b) = \sum_n \left[\frac{1}{n^2 - b^2} - \sum_{\ell=1}^L \frac{\alpha^{2\ell-2}}{\kappa^{2\ell}} \right] + \sum_n \sum_{\ell=1}^L (b^2 + u^2)^{\ell-1} \left(\frac{u}{n} \right)^{1/2} \left(\frac{n\pi}{u} \right)^\ell \frac{K_{\ell-1/2}(2n\pi u)}{(\ell-1)!} \quad (3.1-10)$$

The Fourier transform pair [58]

$$F\{(x^2 + u^2)^{-v-1/2}\} = \left(\frac{y}{2u} \right)^v \frac{\sqrt{\pi}}{\Gamma(v + 1/2)} K_v(uy) \quad (3.1-11)$$

has been used to obtain Equation (3.1-10). Γ is the gamma function, and K_v is the modified Bessel function of order v . As usual, F and F^{-1} denote Fourier and inverse Fourier transformations, respectively.

Equations (3.1-1), (3.1-2) and (3.1-10) give three different methods to evaluate the same number. Equation (3.1-2) is actually an acceleration procedure in itself, as the cotangent would be computed using a rapidly convergent series, an approximating polynomial, or some other technique which is usually transparent to the user. Both Equations (3.1-1) and (3.1-2) are generally considered exact representations of the same number, as the result can be computed to arbitrary accuracy if enough terms of the sum are taken. The accelerated formula of Equation (3.1-10) is also exact in this sense. If enough terms of the two rapidly convergent sums in this equation are taken, arbitrary accuracy can be achieved, because even though the asymptotic form of the terms has been subtracted, the sum of these terms is added back by the second infinite sum, resulting in an exact expression which can be summed to arbitrary precision.

The effectiveness of the acceleration method is demonstrated in Figure 3.1. Using Equation (3.1-2) for the exact answer, the absolute error in percent is plotted versus the number of terms summed of the first sum (in n) in Equation (3.1-10), for $L = 0, 1, 3$ and 5 , where $L = 0$ is the direct or unaccelerated summation. In the figures, level ℓ means $L = \ell$. To obtain the data for these plots, the second sum in Equation (3.1-10) was first summed to machine accuracy, approximately 14 digits, on a CDC 6600. Then the percent relative error after summing $M = 2N+1$ terms of the first sum is plotted (symmetric partial sums about $n = 0$, where N is the upper limit on n). In all the examples $b = 0.75$. Clearly the acceleration procedure is a distinct improvement over the unaccelerated sum. Even after summing 1000 terms, the unaccelerated sum, $L = 0$ in Equation (3.1-10), has a relative error of 0.1 percent. With only a first-order acceleration ($L = 1$), a comparable accuracy is realized with only 15 terms ($M = 15$), and with the fifth-order acceleration the relative error is 0.00047 percent after only 9 terms. As expected, as the level of acceleration is increased, the number of terms required for a given relative error decreases. Unfortunately, the opposite is true of the second infinite sum in Equation (3.1-10). For $L = 1$ in Figure 3.1, 23 terms were required to sum the second sum to machine accuracy, and 7 terms ($M = 7$) were required for 5 digits of accuracy. For $L = 3$, the number of terms required were 25 and 9, and for $L = 5$, they were 27 and 9, respectively. Obviously there is a trade-off here which prevents the order of acceleration from being increased indefinitely.

Finally, Figure 3.2 demonstrates the effect of varying the parameter u . In each curve in Figure 3.2, $L = 3$ and $b = 0.75$. As in Figure 3.1,

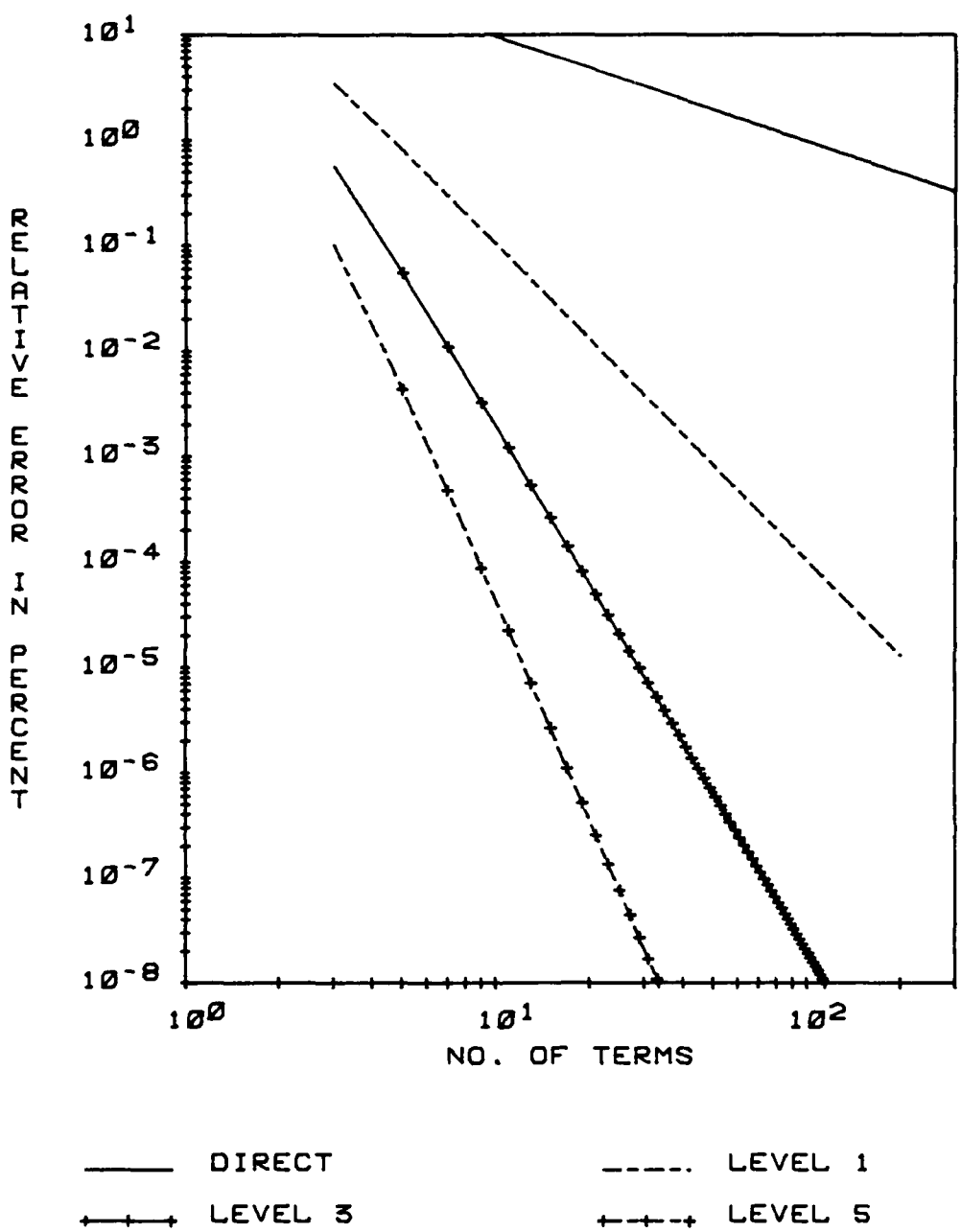


Figure 3.1. Convergence of the first infinite sum in Equation (3.1-10) for level 0, 1, 3 and 5 accelerations, with $u = 0.5$ and $b = 0.75$.

50

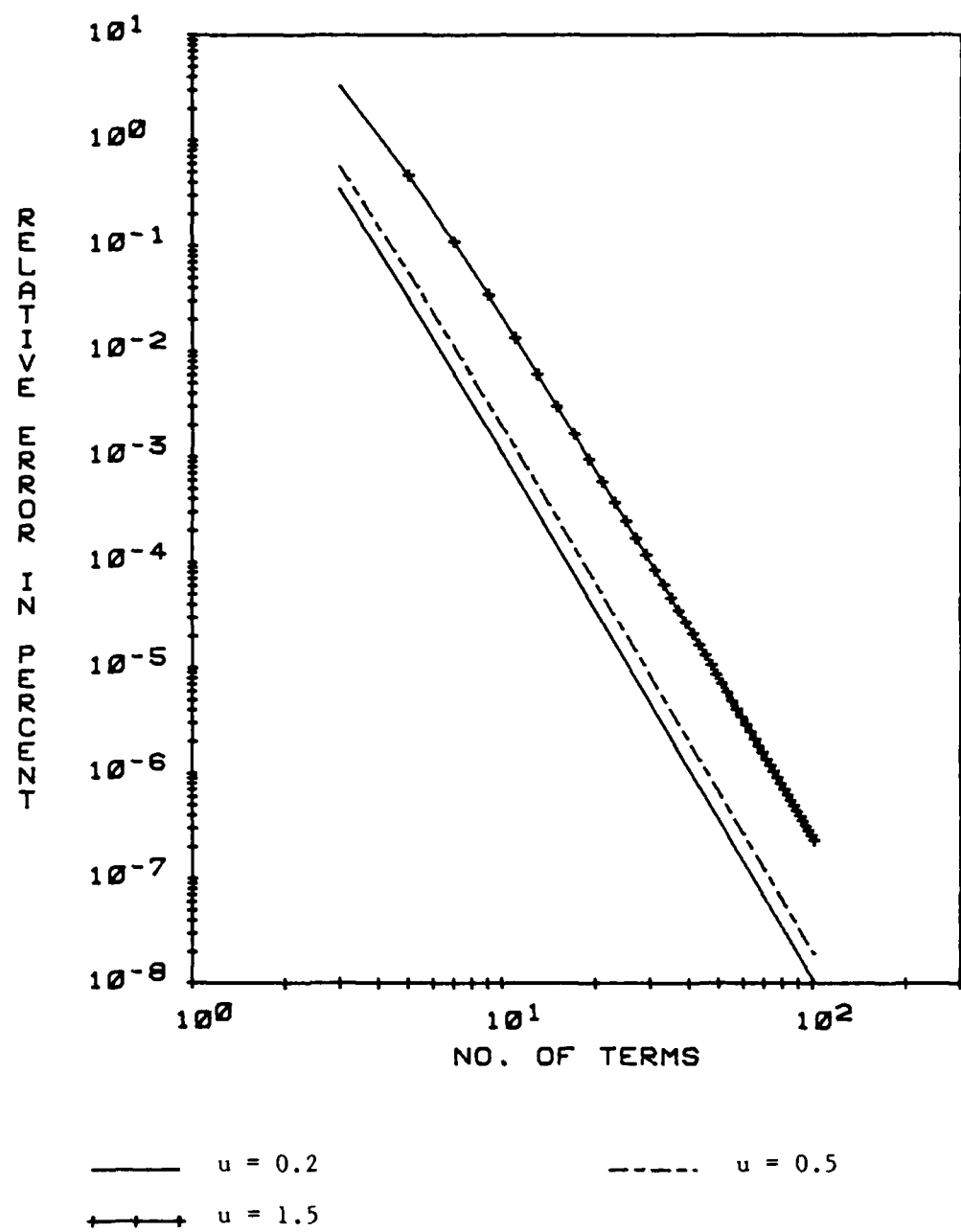


Figure 3.2. Effect of the parameter u on the convergence of the first infinite sum in Equation (3.1-10) with $L = 3$ and $b = 0.75$.

the second sum was summed to machine accuracy, and the relative error in percent after summing M terms of the first sum of Figure (3.1-10) is plotted. It is evident that as u decreases fewer terms of the first sum are required for a given level of accuracy. However, the opposite is again true for the second sum. The number of terms required in the second sum for machine precision and 5 digits of accuracy, respectively, were 9 and 3 for $u = 1.5$, 25 and 9 for $u = 0.5$, and 61 and 21 for $u = 0.2$. Obviously, one would not want to choose u too small. The optimum choice of u will depend on the particular problem, but it is not particularly critical and, of course, does not affect the final answer if enough terms of both sums are taken.

To summarize the acceleration method, given a slowly convergent sum of terms $f(n)$, one or more terms of the asymptotic expansion $f_a(n)$ in inverse powers of the smoothed parameter $\kappa = (n^2+u^2)^{-1/2}$ are derived. The original sum is then expressed as the sum of two new infinite summations in the form of Equation (3.1-8). The terms of the first sum, $f(n)-f_a(n)$, approach zero asymptotically no worse than x^{-L-1} , where L is the power of the last term in the asymptotic expansion $f_a(n)$; hence, the first sum can generally be made to converge satisfactorily. The second sum, with terms $f_a(n)$, can be efficiently summed by an application of the PSF, due to the expansion in powers of the smoothed parameter κ .

3.2. Application of the Acceleration Technique to Two-dimensional Sums

As discussed earlier, the application of the acceleration technique to the two-dimensional summations such as given in Equation (3.1) is somewhat more detailed due to the more complicated functions involved and

the additional difficulty of applying the PSF on a general two-dimensional lattice. The ability to use a general lattice instead of only a rectangular lattice is required to analyze the important case of a hexagonal array. In this section, a general procedure will be developed, noting in particular the steps required to change the Green's function to one for another problem and to incorporate different basis and testing functions. The steps required to obtain the two infinite summations on the right-hand side of Equation (3.1-8), infinite in two indices from now on, will be discussed. As an example, the asymptotic expansion of one component of the periodic Green's function will be derived. Next, the application of the PSF to two-dimensional sums on non-orthogonal lattices will be discussed. In Section 3.3 the technique is applied to two examples of interest, and a brief discussion of some of the parameters affecting the numerical evaluation of the infinite sums is contained in Section 3.4.

3.2.1. General formulation

The inner products that must be evaluated to fill the Z and V matrices derived in Section 2.3 are all of the form

$$Z_{rp}^{ij} = \frac{1}{A} \sum_{mn} \tilde{G}_{ij} \tilde{J}_j \tilde{T}_i e_{mn} (\vec{\rho}_r - \vec{\rho}_p) \quad (3.2-1)$$

Again, $(\vec{\rho}_r - \vec{\rho}_p)$ is the vector from the p th basis function to the r th testing function. To apply the acceleration technique, the asymptotic expansion is derived for \tilde{G}_{ij} only. While this is not the only possibility, it is a convenient approach. Denoting the asymptotic expansion of \tilde{G}_{ij} as \tilde{G}_{ij}^a , Z_{rp}^{ij} can be expressed as:

$$\begin{aligned}
 z_{rp}^{ij} = & \frac{1}{A} \sum_{mn} (\tilde{G}_{ij}^a - \tilde{G}_{ij}^a) \tilde{J}_j \tilde{T}_i e_{mn} (\vec{\rho}_r - \vec{\rho}_p) \\
 & + \frac{1}{A} \sum_{mn} \tilde{G}_{ij}^a \tilde{J}_j \tilde{T}_i e_{mn} (\vec{\rho}_r - \vec{\rho}_p)
 \end{aligned} \tag{3.2-2}$$

The first two-dimensional sum in Equation (3.2-2) will be referred to as the spectral sum and denoted S_β because its terms are functions of the spectral variable $\beta = \beta_x \beta_x + \beta_y \beta_y$. The second sum is accelerated by the PSF, which results in a sum whose terms are a function of the spatial variable $\vec{\rho}$. It will be referred to as the spatial sum and denoted S_ρ .

3.2.2. Spectral sum

The derivation and evaluation of the spectral sum are fairly straightforward. The Fourier transforms of the basis and testing functions will generally be available in closed form, and the only remaining step in the derivation is to obtain \tilde{G}_{ij}^a . Following the procedure outlined in Section 3.1, a Taylor series expansion of \tilde{G}_{ij}^a is derived, but as before, instead of using powers of K_{mn}^{-1} , where $K_{mn} = |\vec{K}_{mn}|$, a Taylor series is derived in powers of a smoothed parameter κ^{-1} , where now, similar to the definition in Section 3.1, $\kappa^2 = (K_{mn}^2 + u^2)$. This procedure is entirely general and should apply to the Green's function for any problem. This report is concerned with the Green's function for a grounded dielectric slab, given in Equation (2.2-20). As an example, consider \tilde{G}_{xy} , given in Table 2.1.

Because only the asymptotic form of the Green's function is of interest, \tilde{G}_{xy} can be more conveniently expressed as

$$\tilde{G}_{xy}(\vec{k}_{mn}) = \frac{j\beta_x \beta_y (\gamma' + \gamma \coth \gamma' t) e^{-\gamma(z-t)}}{\omega \epsilon_0 (\gamma + \gamma' \coth \gamma' t)(\gamma' + \epsilon_r \gamma \coth \gamma' t)} \quad (3.2-3)$$

where

$$\gamma = \sqrt{k_{mn}^2 - k_o^2} = js$$

$$\gamma' = \sqrt{k_{mn}^2 - \epsilon_r k_o^2} = js'$$

In order to derive the asymptotic expansion in powers of κ^{-1} , γ and γ' are written as

$$\gamma = \sqrt{(k_{mn}^2 + u^2) - (k_o^2 + u^2)} = \sqrt{\kappa^2 - \alpha^2} \quad (3.2-4)$$

$$\gamma' = \sqrt{(k_{mn}^2 + u^2) - (\epsilon_r k_o^2 + u^2)} = \sqrt{\kappa^2 - \beta^2}$$

where $\alpha^2 = k_o^2 + u^2$ and $\beta^2 = k_o^2 \epsilon_r + u^2$. The dependence of κ on m and n is understood. This β only occurs in the coefficients of the asymptotic expansions and should cause no confusion with the magnitude of the spectral variable, β . Next, the asymptotic expansions of parts of \tilde{G}_{xy} are found and the results combined to give \tilde{G}_{xy}^a .

The term $\coth(\gamma' t)$ arises due to the dielectric slab, and does not appear in the free-space Green's function. The asymptotic expansion of this term in powers of κ^{-1} can be shown to be 1; therefore this term can be neglected in the asymptotic expansion. Unfortunately, for thin substrates many terms may be required before 1 is a good approximation to $\coth(\gamma' t)$, which can increase the number of terms required for adequate numerical convergence of the spectral sum. This

will not be a problem here because this report is concerned with thick substrates. Other theories are available to analyze microstrip antennas on thin substrates.

The exponential term $\exp -\gamma(z-t)$ can be expanded by expressing it as

$$e^{-\gamma(z-t)} = e^{-\kappa(z-t)} e^{(\kappa-\gamma)(z-t)} \quad (3.2-5)$$

An asymptotic expansion for the latter exponential can be derived, while the multiplying exponential is left intact to be handled by the PSF. However, if the testing function is at $z = t$, in the source plane, as is generally the case, this term becomes 1. An expansion of Equation 3.2-5 is needed only if a component of the periodic Green's function in which it appears needs to be evaluated outside the array plane. This case does not arise in this report.

The only remaining term for which an asymptotic expansion is needed is $(\gamma' + \epsilon_r \gamma)$. This is easily obtained by adding the Taylor series expansions (in powers of κ^{-1} , of course) of γ and γ' . The first few terms of the expansion for $(\gamma' + \epsilon_r \gamma)$ are:

$$(\gamma' + \epsilon_r \gamma) \sim (1 + \epsilon_r) \kappa \sum_{\ell=1}^5 a_{1,\ell} \kappa^{-\ell} \quad (3.2-6)$$

where the coefficients $a_{1,\ell}$ are found in Table 3.1. Using Equation (3.2-6), the asymptotic expansion of \tilde{G}_{xy} is obtained:

$$\tilde{G}_{xy}^a = \frac{j\beta_x \beta_y}{\omega \epsilon_0 (1 + \epsilon_r)} \sum_{\ell=1}^N c_{2,\ell} \kappa^{-\ell} \quad (3.2-7)$$

TABLE 3.1

COEFFICIENTS OF ASYMPTOTIC EXPANSIONS THROUGH κ^{-5}

coefficient	ℓ	1	2	3	4	5
$a_{1,\ell}$	1	0	$-\frac{(\beta^2 + \epsilon_r \alpha^2)}{2(1 + \epsilon_r)}$	0	$-\frac{(\beta^4 + \epsilon_r \alpha^4)}{8(1 + \epsilon_r)}$	
$c_{1,\ell}$	1	0	$\frac{1}{4}(\alpha^2 + \beta^2)$	0	$\frac{(\alpha^4 + \beta^4 + \alpha^2 \beta^2)}{8}$	
$c_{2,\ell}$	1	0	$\frac{(\beta^2 + \epsilon_r \alpha^2)}{2(1 + \epsilon_r)}$	0	$\frac{(\epsilon_r \alpha^4 - 2\epsilon_r \alpha^4 + 2\epsilon_r^2 \alpha^2 \beta^2 - \beta^4)}{4(1 + \epsilon_r)}$	
$c_{3,\ell}$	0	0	1	0	$\frac{\alpha^2(1 + 3\epsilon_r) + \beta^2(5 + 3\epsilon_r)}{4(1 + \epsilon_r)}$	

$$\alpha^2 = k_0^2 + u^2 \quad \beta^2 = \epsilon_r k_0^2 + u^2$$

where the coefficients $C_{2,\ell}$ are also found in Table 3.1.

In the same manner, one obtains asymptotic expansions for the other components \tilde{G}_{ij} , and for convenience these are listed in Table 3.2. The coefficients can be found in Table 3.1.

This completes the derivation of the spectral sum, S_β . In summary, each term of the spectral sum consists of the term from the original series, as in Equation (3.2-1), minus the asymptotic expansion of all or part of the original term, as discussed above. For the inner products of interest here, this results in the first double summation in Equation (3.2-2), which is more rapidly convergent than the original sum. In this report, an asymptotic expansion is derived for the Green's function only, transforms of the basis and testing functions being handled by the PSF. The asymptotic expansion is straightforward to derive, and the expansions of the Green's function for a single layer GDS are all tabulated in Table 3.2. The treatment of the spatial sum, to be discussed next, is somewhat more detailed.

3.2.3. Spatial sum

The first step in the acceleration procedure is to subtract from the terms of the original sum their asymptotic form, resulting in a more rapidly convergent sum. This sum is the spectral sum discussed above. To complete the procedure, the asymptotic terms subtracted in the previous step must be summed and added to the spectral sum. Because of the form of the terms of the asymptotic expansion, this second sum can be efficiently summed by using the PSF. This sum, denoted the spatial sum due to its final form, has the general form:

$$S_{\rho} = \frac{1}{A} \sum_{mn} \tilde{G}_{ij}^a \tilde{J}_j \tilde{T}_i e_{mn} (\vec{\rho}_r - \vec{\rho}_p) \quad (3.2-8)$$

The application of the PSF is made clearer by noting that the PSF is derived from an application of Parseval's theorem [41], which can be stated

$$\int_{-\infty}^{\infty} \int_{-\infty}^{\infty} \tilde{f}_1(\vec{\beta}) \tilde{f}_2(\vec{\beta}) d\beta_x d\beta_y = 4\pi^2 \int_{-\infty}^{\infty} \int_{-\infty}^{\infty} f_1(-\vec{\rho}) f_2(\vec{\rho}) dx dy \quad (3.2-9)$$

The PSF is obtained by choosing as $f_2(\vec{\rho})$ a two-dimensional impulse train, or comb function. A comb function has as its Fourier transform another comb function. Integrating the comb functions on each side of the equation against the continuous functions $f_1(\vec{\rho})$ and $\tilde{f}_1(\vec{\beta})$ results in two infinite summations, and the equality gives the PSF.

To use Parseval's theorem to obtain the PSF acceleration of S_{ρ} , one expresses S_{ρ} as

$$S_{\rho} = \frac{1}{A} \int_{-\infty}^{\infty} \int_{-\infty}^{\infty} \tilde{G}_{ij}^a(\vec{\beta}) \tilde{J}_j(\vec{\beta}) \tilde{T}_i(\vec{\beta}) \sum_{mn} \delta(\vec{\beta} - \vec{k}_{mn}) e^{j\vec{\beta} \cdot (\vec{\rho}_r - \vec{\rho}_p)} d\beta_x d\beta_y \quad (3.2-10)$$

This is then separated into the two functions $\tilde{f}_1(\vec{\beta})$ and $\tilde{f}_2(\vec{\beta})$

$$\tilde{f}_1(\vec{\beta}) = \tilde{G}_{ij}^a(\vec{\beta}) \tilde{J}_j(\vec{\beta}) \tilde{T}_i(\vec{\beta}) \quad (3.2-11)$$

$$\tilde{f}_2(\vec{\beta}) = \frac{1}{A} \sum_{mn} \delta(\vec{\beta} - \vec{k}_{mn}) e^{j\vec{\beta} \cdot (\vec{\rho}_r - \vec{\rho}_p)} \quad (3.2-12)$$

An unshifted comb function on the spectral lattice shown in Fig. 2.1-b

has as a transform pair the comb function defined by the spatial lattice of Figure 2.1-a. Using shifting theorems [41], $f_2(\vec{p})$ is found to be

$$f_2(\vec{p}) = \frac{A}{4\pi^2} \sum_{mn} \delta(\vec{p} + (\vec{p}_r - \vec{p}_p) - \vec{s}_{mn}) e^{j\vec{\beta}_0 \cdot (\vec{p} + (\vec{p}_r - \vec{p}_p))} \quad (3.2-13)$$

With this result, the general form of the spatial sum becomes

$$S_p = \sum_{mn} f_1(\vec{p}_r - \vec{p}_p - \vec{s}_{mn}) e^{j2\pi(m\vec{m}_0 + n\vec{n}_0)} \quad (3.2-14)$$

where

$$f_1(\vec{p}) = F^{-1}\{\tilde{G}_{ij}^a(\vec{\beta}) \tilde{J}_j(\vec{\beta}) \tilde{T}_i(\vec{\beta})\} \quad (3.2-15)$$

and the relation $\vec{\beta}_0 \cdot \vec{s}_{mn} = 2\pi(m\vec{m}_0 + n\vec{n}_0)$ has been used; $\vec{\beta}_0$ is the element-to-element phase shift for beam steering, as discussed in Section 2.2.

With the evaluation of S_p , the original unaccelerated inner product of Equation (3.2-1) can be expressed as the sum of two rapidly convergent sums, given by Equation (3.2-2). The evaluation of $f_1(\vec{p})$ is the most difficult part of applying the acceleration procedure. A computer program written to evaluate the spectral sum requires only minor alterations to use different basis and testing functions, assuming the transforms of these functions are available in closed form. Even changing the Green's function in order to solve problems in free space or on multilayered dielectrics, for example, is generally not difficult, usually requiring only a line or two to evaluate the Green's function and requiring

different coefficients for the asymptotic form. The evaluation of $f_1(\rho)$ can vary in difficulty depending on the smoothness of the basis and testing functions, as will be shown by the examples of the next section. First an observation about the acceleration technique is in order. The general foundations for this technique, namely Kummer's transformation of series and the PSF, are widely known and used. As such, techniques similar to this one abound in the literature, and a few examples from the antenna literature deserve mentioning.

Chang [59] combined the subtraction technique with the PSF in an analysis of dipole arrays. However, he only subtracted one term, unlike the approach used here. Butler and Keshavamurthy use a similar approach to evaluate infinite series in analyses of radial, parallel-plate waveguides [60] and circular-disk microstrip antennas [61]. Another example is a technique used by Alexopolous and Rana to evaluate Sommerfeld integrals [22]. In that reference, the tail of the integral is approximated by several asymptotic terms, and each term is integrated in closed form. The fact that they are dealing with integrals is unimportant, because these techniques apply equally well to integrals as series. However, they are approximating the tail of the integral and do not develop an asymptotic expansion in the smoothed parameter κ^{-1} . Brittingham, Miller and Okada [46] use a technique very similar to this one, also to evaluate Sommerfeld integrals. They begin by deriving the same asymptotic expansion as done here, but then use it as an approximation to the original integrand (terms of the summation in this case). This is equivalent to ignoring the spectral sum and is a valid approximation if the observation point is very close to the source

point. Undoubtedly there are other similar applications, but these three demonstrate some of the most common approaches.

3.3. Examples of Inner Product Evaluation

Because current distributions in different problems can have very different characteristics, the ability to change basis and testing functions easily is desirable in a moment method code. In this section the evaluation of the spectral and spatial sums will be examined for two different choices of basis and testing functions. Most of the attention is given to the details of evaluating the spatial sum, as the spectral sum is easily altered and evaluated when changing functions. All of the examples will use the Green's function of the GDS of Figure 2.1a.

3.3.1. Electric field periodic Green's function

One example of particular interest, perhaps more academic than practical, is the evaluation of the periodic Green's function for the GDS. To evaluate the Green's function, one may choose impulses as basis and testing functions

$$J_j(\vec{\rho}') = \delta(\vec{\rho}'), \quad T_i(\vec{\rho}) = \delta(\vec{\rho}) \quad (3.3-1)$$

Transforms of the unshifted versions of these functions are simply 1, and the formula for the periodic Green's function is obtained by substituting 1 for \tilde{J}_j and \tilde{T}_i in Equation (3.2-2)

$$\begin{aligned} G_{ij}(\vec{\rho} - \vec{\rho}') &= \frac{1}{A} \sum_{mn} (\tilde{G}_{ij}(\vec{k}_{mn}) - \tilde{G}_{ij}^a(\vec{k}_{mn})) e_{mn}(\vec{\rho} - \vec{\rho}') \\ &+ \sum_{mn} f_1(\vec{\rho} - \vec{\rho}' - \vec{s}_{mn}) e^{j2\pi(m\vec{m}_0 + n\vec{n}_0)} \end{aligned} \quad (3.3-2)$$

The spectral sum is evaluated by choosing \tilde{G}_{ij} from Table 2.1, and \tilde{G}_{ij}^a from

Table 3.2, and substituting into the first summation in Equation (3.2-2). The evaluation of the spatial sum is somewhat more complicated. The inverse Fourier transformation required to find $f_1(\vec{\rho})$ can be performed in closed form only for special cases, as in this example. In Section 3.3.2 an example will be given where $f_1(\vec{\rho})$ can not be evaluated in closed form, as is the case in general. In all cases, the evaluation of $f_1(\vec{\rho})$ is at the heart of the application of the acceleration technique.

In this example $f_1(\vec{\rho})$ involves only \tilde{G}_{ij}^a , and will be denoted G_{ij}^a .

$$f_1(\vec{\rho}) = F^{-1}\{\tilde{G}_{ij}^a(\vec{\beta})\} = G_{ij}^a(\vec{\rho}) \quad (3.3-3)$$

As discussed in Chapter 2, \tilde{G}_{ij}^a is the Fourier transform of the \hat{G}_{ij}^a component of the dyadic electric field Green's function for a point source on a GDS. The inverse transform of \tilde{G}_{ij}^a leads to Sommerfeld integrals and is difficult to evaluate. G_{ij}^a , however, can be computed easily and in closed form. As an example, consider the \hat{G}_{yy}^a component from Table 3.1.

G_{yy}^a is

$$G_{yy}^a(\rho) = \frac{j}{\omega\epsilon_0} \sum_{\ell=1}^N \left[\frac{C_{2,\ell}}{1 + \epsilon_r} F^{-1}\{\beta_y^2 \kappa^{-\ell}\} - \frac{k_0^2}{2} C_{1,\ell} F^{-1}\{\kappa^{-\ell}\} \right] \quad (3.3-4)$$

The inverse Fourier transforms of $\kappa^{-\ell}$ and $\beta_y^2 \kappa^{-\ell}$ are needed. Switching to polar notation $\vec{\beta} = \beta \angle \theta$, $\vec{\rho} = \rho \angle \theta$, the inverse transform of $\kappa^{-\ell}$ is

$$g_\ell(\rho) = F^{-1}\{\kappa^{-\ell}\} = \frac{1}{2\pi} \left[\frac{\rho}{2u} \right]^{\frac{\ell}{2} - 1} \frac{K_{\ell/2} - 1}{\Gamma(\ell/2)} \quad (3.3-5)$$

For all cases in this report, only $\ell = 1, 3$ and 5 have been used, with the results

$$g_1(\vec{\rho}) = \frac{e^{-u\rho}}{2\pi\rho} \quad (3.3-6a)$$

$$g_3(\vec{\rho}) = \frac{e^{-u\rho}}{2\pi u} \quad (3.3-6b)$$

$$g_5(\vec{\rho}) = \frac{e^{-u\rho}(u\rho + 1)}{6\pi u^3} \quad (3.3-6c)$$

The functions $g_\ell(\vec{\rho})$ will be referred to as the asymptotic Green's function. When used to evaluate different components of the periodic Green's function, these terms will be multiplied by different constants, and one or more terms can be used, depending on the level of acceleration. However, the relation of $g_\ell(\vec{\rho})$ to the free-space Green's function $\exp(-jk_0\rho)/\rho$ is obvious, and because the terms are used together, the term asymptotic Green's function will apply to them all. This relation has important consequences to the evaluation of $f_1(\vec{\rho})$ in some cases and will be discussed later.

Next, the inverse transforms of $\beta_y^2 e^{-\ell}$ must be evaluated. In rectangular form these transforms, denoted by $g_\ell^{yy}(\vec{\rho})$, are

$$g_\ell^{yy}(\vec{\rho}) = \frac{1}{4\pi^2} \int_{-\infty}^{\infty} \int_{-\infty}^{\infty} \frac{\beta_y^2 e^{j\vec{\beta} \cdot \vec{\rho}}}{(\beta_x^2 + u^2)^{\ell/2}} d\beta_x d\beta_y \quad (3.3-7)$$

Unfortunately this integral representation is divergent for $\ell = 1$, but can

be evaluated by a limiting or regularization procedure. For example, the condition $z = t$, which caused the exponential term in z to drop out, can be relaxed. Since the electric field, the Green's function, is finite in the $z = t$ plane, excluding source points, and the integral is convergent for $z \neq t$, a limit can be taken as $z \rightarrow t$. This difficulty is due to the singularity in the Green's function in the source plane, as discussed earlier. A better way to evaluate the inverse transforms is to recognize that

$$g_\ell^{yy}(\vec{\rho}) = \frac{1}{4\pi^2} \int_{-\infty}^{\infty} \int_{-\infty}^{\infty} -\frac{\partial^2}{\partial y^2} \left(\frac{e^{j\beta \cdot \vec{\rho}}}{(\beta^2 + u^2) \ell/2} \right) d\beta_x d\beta_y \quad (3.3-8)$$

which is just an application of the differentiation theorem from Fourier analysis [41]. In this manner, one obtains the result

$$g_\ell^{yy}(\vec{\rho}) = F^{-1}\{\beta_y^2 \kappa^{-\ell}\} = -\frac{\partial^2}{\partial y^2} g_\ell(\vec{\rho}) \quad (3.3-9)$$

For $\ell = 1, 3$ and 5 , this gives

$$g_1^{yy}(\vec{\rho}) = -\frac{e^{-up}}{2\pi\rho} \left[\left(u^2 + \frac{2u}{\rho} + \frac{2}{\rho^2} \right) \sin^2 \phi \left(-\frac{u}{\rho} + \frac{1}{\rho^2} \right) \cos^2 \phi \right] \quad (3.3-10a)$$

$$g_3^{yy}(\vec{\rho}) = -\frac{e^{-up}}{2\pi\rho} (up \sin^2 \phi - \cos^2 \phi) \quad (3.3-10b)$$

$$g_5^{yy}(\vec{\rho}) = -\frac{e^{-up}}{6\pi u} (up \sin^2 \phi - 1) \quad (3.3-10c)$$

Now the functions $g_\ell^{yy}(\vec{\rho})$ are singular only at the source point $\vec{\rho} = 0$, not

at all points in the plane $z = t$, as before. This will be discussed in more detail shortly, but first the functions needed to complete the derivation of the spatial sum of the other components of the Green's function will be derived.

For the other components of the Green's function, the inverse transforms of $\beta_x^{2\kappa-\ell}$, $\beta_x \beta_y^{\kappa-\ell}$, $\beta_y^{\kappa-\ell}$ and $\beta_x^{\kappa-\ell}$ are needed. The transforms of $\beta_x^{2\kappa-\ell}$ are obtained from Equations (3.3-10a-c) by interchanging $\sin \phi$ and $\cos \phi$. In a similar process to the above, these transforms can be found from the differentiation theorem,

$$g_\ell^{ij}(\vec{\rho}) = F^{-1}\{\beta_i \beta_j^{\kappa-\ell}\} = -\frac{\partial^2}{\partial i \partial j} g_\ell(\vec{\rho}) \quad (3.3-11)$$

$$g_\ell^i(\vec{\rho}) = F^{-1}\{\beta_i^{\kappa-\ell}\} = -j \frac{\partial}{\partial i} g_\ell(\vec{\rho})$$

The functions $g_\ell^{xy}(\vec{\rho})$ then equal $g_\ell^{yx}(\vec{\rho})$, and for $\ell = 1, 3$ and 5 are

$$g_1^{xy}(\vec{\rho}) = -\sin \phi \cos \phi \frac{e^{-up}}{2\pi\rho} \left[u^2 + \frac{3u}{\rho} + \frac{3}{\rho^2} \right] \quad (3.3-12a)$$

$$g_3^{xy}(\vec{\rho}) = -\sin \phi \cos \phi \frac{e^{-up}}{2\pi\rho} (up + 1) \quad (3.3-12b)$$

$$g_5^{xy}(\vec{\rho}) = -\sin \phi \cos \phi \frac{e^{-up}}{6\pi u^2} \left[u^2 \rho + up + 1 - u - \frac{1}{\rho} \right] \quad (3.3-12c)$$

And finally, the transforms of $\beta_y^{\kappa-\ell}$ and $\beta_x^{\kappa-\ell}$ are found to be

$$g_1^y(\vec{\rho}) = j \sin \phi \frac{e^{-up}}{2\pi\rho} \left[u + \frac{1}{\rho} \right] \quad (3.3-13a)$$

$$g_3^y(\vec{\rho}) = j \sin \phi \frac{e^{-up}}{2\pi} \quad (3.3-13b)$$

$$g_5^y(\vec{\rho}) = \frac{j \sin \phi \rho e^{-u\rho}}{6\pi u} \quad (3.3-13c)$$

where $g_5^x(\vec{\rho})$ is obtained by replacing $\sin \phi$ with $\cos \phi$.

At this point the $\hat{G}_{ij}^y(\vec{\rho} - \vec{\rho}')$ component of the periodic Green's function can be accelerated, and in addition all of the functions needed to evaluate the other components of the periodic Green's function in Table 2.1 have been derived. The result is

$$\begin{aligned} G_{ij}^y(\vec{\rho} - \vec{\rho}') &= \frac{1}{A} \sum_{mn} (\tilde{G}_{ij}^y(\vec{k}_{mn}) - \tilde{G}_{ij}^{a,y}(\vec{k}_{mn})) e_{mn}(\vec{\rho} - \vec{\rho}') \\ &+ \sum_{mn} G_{ij}^{a,y}(\vec{\rho} - \vec{\rho}' - \vec{s}_{mn}) e^{j2\pi(m\omega_0 + n\omega_0)} \end{aligned} \quad (3.3-14)$$

where $\tilde{G}_{ij}^y(\vec{k}_{mn})$ is found in Table 2.1, $\tilde{G}_{ij}^{a,y}(\vec{k}_{mn})$ is found in Table 3.2, and $G_{ij}^{a,y}(\vec{\rho})$ is found in Table 3.3. In these tables $[x] \leftrightarrow y$ indicates the interchange of x and y , as usual.

Before demonstrating the effectiveness of the acceleration technique with some numerical results, the question of convergence should be discussed further. Without any acceleration, the terms of $\tilde{G}_{yy}^y(\vec{k}_{mn})$ behave for large m and n as

$$\frac{n^2}{\sqrt{m^2 + n^2}} e^{-\sqrt{m^2 + n^2} (z-t)} \quad (3.3-15)$$

and $G_{yy}^y(\vec{\rho} - \vec{\rho}')$ does not converge if $z = t$. The same behavior is true of all the other components. This is due to the use of source-free equations in the formulation and is not physical. One of the initial boundary

TABLE 3.3

COMPONENTS OF THE ASYMPTOTIC GREEN'S
FUNCTION IN THE SPATIAL DOMAIN

$$G_{yy}^a(\vec{\rho}) = \frac{j}{\omega \epsilon_0} \sum_{\ell=1}^L \left[\frac{c_{2,\ell}}{1 + \epsilon_r} g_{\ell}^{yy}(\vec{\rho}) - \frac{k_0^2}{2} c_{1,\ell} g_{\ell}(\vec{\rho}) \right]$$

$$G_{xy}^a(\vec{\rho}) = \frac{j}{\omega \epsilon_0 (1 + \epsilon_r)} \sum_{\ell=1}^L c_{2,\ell} g_{\ell}^{xy}(\vec{\rho})$$

$$G_{zy}^a(\vec{\rho}) = \frac{1}{\omega \epsilon_0 (1 + \epsilon_r)} \sum_{\ell=1}^L \left[\frac{k_0^2}{2} ((1 - \epsilon_r) c_{3,\ell} - c_{2,\ell}) \right] g_{\ell}^y(\vec{\rho})$$

$$G_{xx}^a(\vec{\rho}) = \frac{j}{\omega \epsilon_0} \sum_{\ell=1}^L \left[c_{2,\ell} g_{\ell}^{xx}(\vec{\rho}) - \frac{k_0^2}{2} c_{1,\ell} g_{\ell}(\vec{\rho}) \right]$$

$$G_{yx}^a(\vec{\rho}) = G_{xy}^a(\vec{\rho})$$

$$G_{zx}^a(\vec{\rho}) = \frac{1}{\omega \epsilon_0 (1 + \epsilon_r)} \sum_{\ell=1}^L \left[\frac{k_0^2}{2} ((1 - \epsilon_r) c_{3,\ell} - c_{2,\ell}) \right] g_{\ell}^x(\vec{\rho})$$

conditions used was the continuity of the tangential electric field at the source plane, excluding source points. To evaluate $G_{yy}(\vec{\rho} - \vec{\rho}')$ as formulated in Chapter 2, one could, as stated above, take the limit as z approaches t , but this is very expensive as the sum is very slowly convergent for z close to t . Fortunately, the accelerated version of $G_{yy}(\vec{\rho} - \vec{\rho}')$, given by Equation (3.3-14), is convergent when $z = t$.

Figure 3.3 demonstrates the approach of the unaccelerated (direct) sum to a limiting value at $z = t$. In this example, the $\hat{y}\hat{y}$ component of the periodic Green's function for a square lattice with $\hat{S}_1 = \hat{S}_2 = 0.5 \lambda_0$ on a GDS with $t = 0.1 \lambda_0$ and $\epsilon_r = 2.55$ was evaluated with no phase shift and an observation point $(\vec{\rho} - \vec{\rho}') = 0.3 \hat{S}_1 + 0.3 \hat{S}_2$. First, what will be called the "exact" answer was obtained using a fifth-order acceleration ($L = 5$), with the constant $u = 0.5 \beta_{av}$, where $\beta_{av} = (\beta_1 + \beta_2)/2$. Next, the value of the direct sum was computed for values of z approaching t , and the relative error in percent from the "exact" value plotted versus $z - t$. It is seen that as z approaches t the relative error approaches zero. Since the field is continuous through the source plane, one would expect the error to continue asymptotically to zero as z approaches t . The limit was not taken further because of the extremely slow convergence of the direct sum. This simple example, while not a proof, demonstrates the convergence of the direct sum in the limit as z approaches t to the value obtained from the accelerated sum. The remaining examples demonstrate the effectiveness of the acceleration procedure and address the choice of u and L .

Figure 3.4 shows the relative error in percent after summing N terms of the spectral sum. $N = (2M+1)^2$ is the number of terms in a partial sum

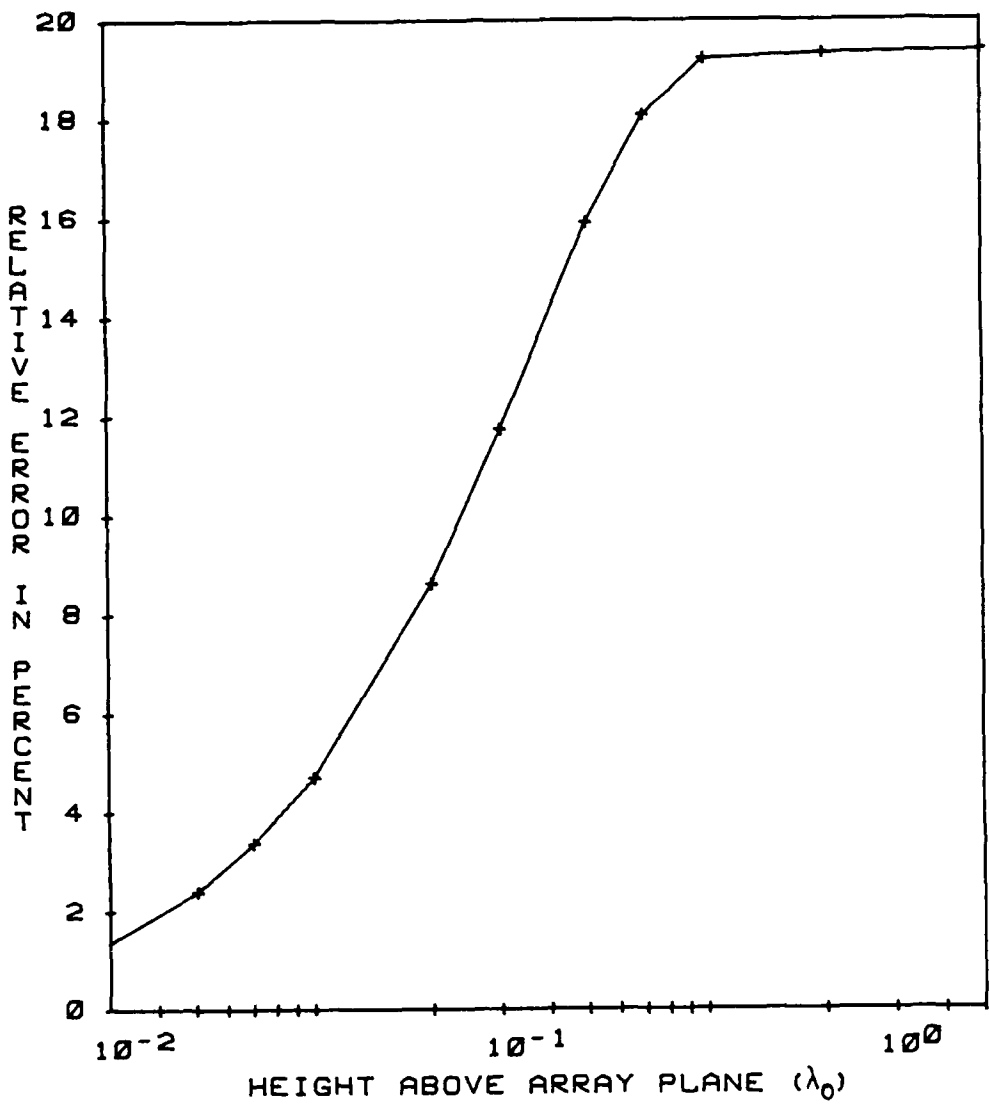


Figure 3.3. Approach of the unaccelerated evaluation of G_{yy} to the value from the fifth order acceleration as the observation point approaches the array plane $z = t$.

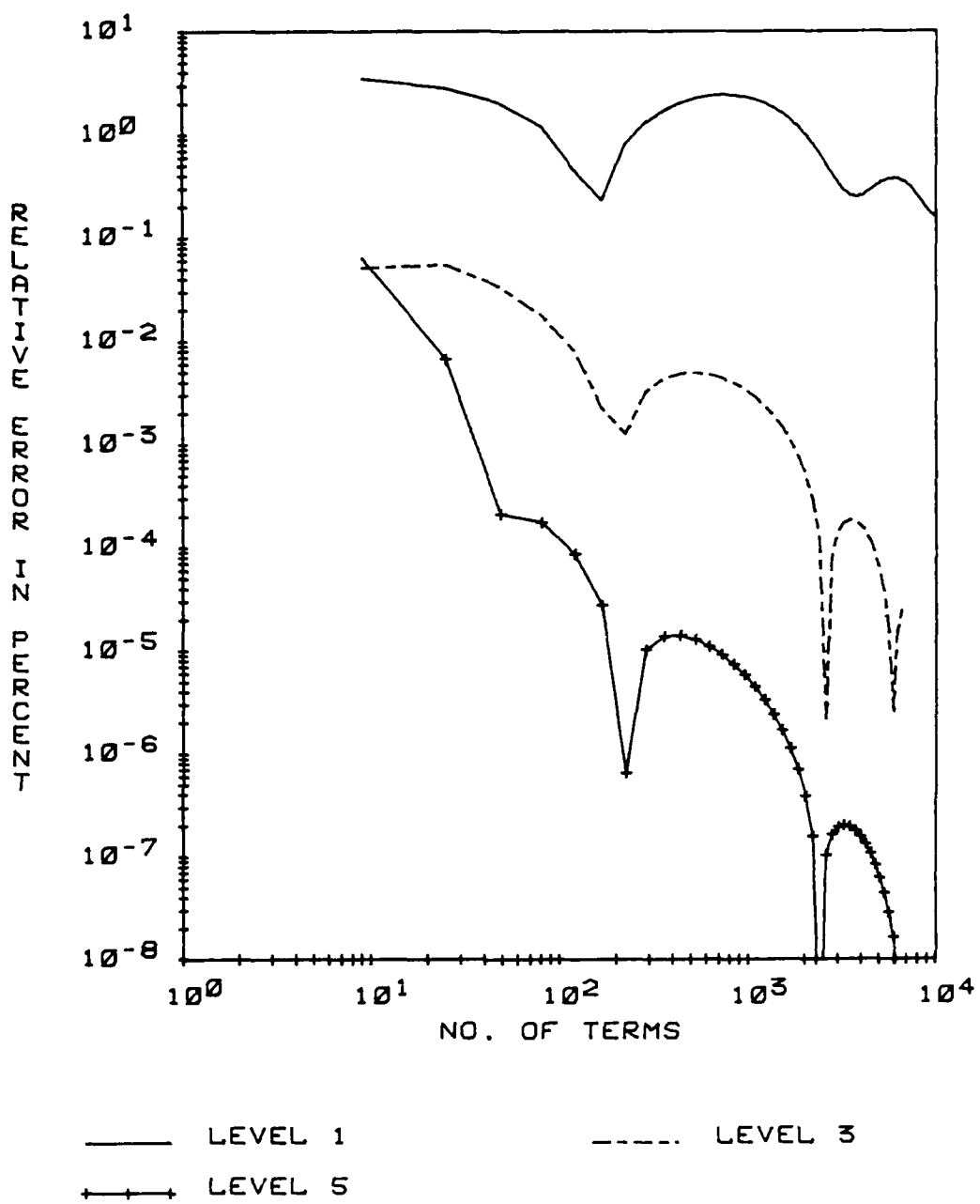


Figure 3.4. Convergence of the spectral sum of $G_{yy}(p - p')$ for level 1, 3, and 5 accelerations, with $u = 0.5 \beta_{av}$, obs. pt. = $0.02\vec{S}_1 + 0.02\vec{S}_2$.

including all terms for which $|m|$ and $|n|$ are less than M . As in Figure 3.1 the exact answer was initially computed with a fifth-order acceleration summed to very high accuracy. Again, in the figures, level ℓ means $L = \ell$. The lattice vectors \vec{S}_1 and \vec{S}_2 and the GDS are the same as in Figure 3.3, and again there was no phase shift. The observation point is at $(\vec{p} - \vec{p}') = 0.02 \vec{S}_1 + 0.02 \vec{S}_2$. As expected, the higher the order of acceleration the lower the error for a given number of terms. The oscillation is due to the phase variation in the terms, which was not present in the example in Figure 3.1. Figure 3.5 also shows the relative error, but for the spatial sum. While it converges very rapidly, it is seen that increasing L increases the error for a given number of terms, in opposition to the spectral sum.

Figures 3.6 and 3.7 repeat the results of Figures 3.4 and 3.5, except that the observation point is moved to $(\vec{p} - \vec{p}') = 0.3 \vec{S}_1 + 0.3 \vec{S}_2$. The behavior is similar to the corresponding plots in the previous example. In Figures 3.8 and 3.9, the effect of the parameter u on the convergence of the spectral and spatial sums is shown for the same case as in Figures 3.6 and 3.7. The results for three values of u are plotted, $u = 0.2 \beta_{av}$, $0.5 \beta_{av}$ and $3.0 \beta_{av}$. In all cases, $L = 5$. From Figure 3.8, it is apparent that too high a value of u is undesirable, and a lower value is better in general. As expected, the error decreases at the same rate in all three cases, as they are all the same order of acceleration. In Figure 3.9, the opposite behavior is seen in the spatial sum. When $u = 3.0 \beta_{av}$, only 10^{-6} terms are required for a relative error of better than 10^{-6} percent, and the error for a given number of terms increases as u decreases.

From these examples $u = 0.5 \beta_{av}$ seems to be a good value. In general, this value gives good results for array spacings and dielectric

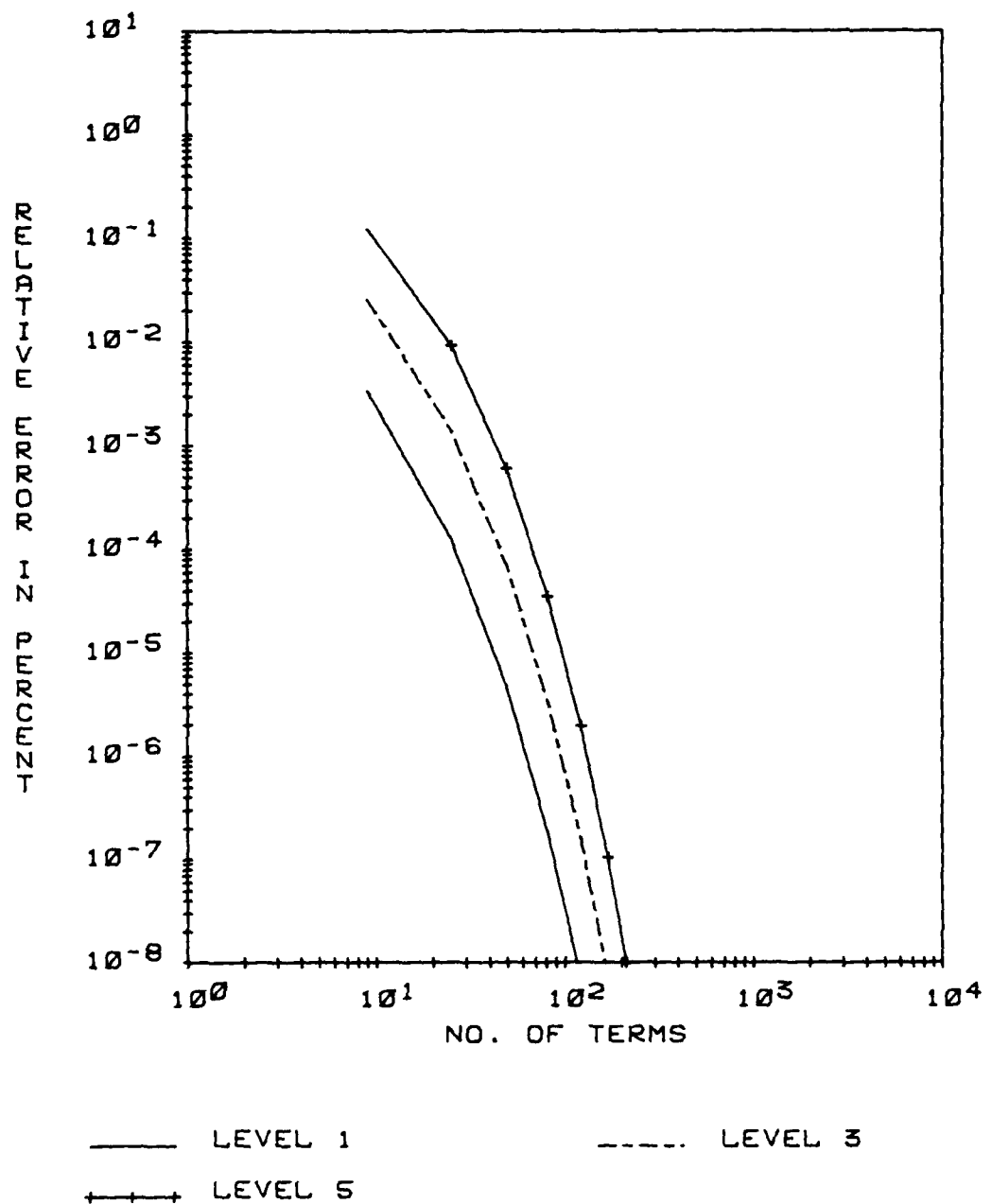


Figure 3.5. Convergence of the spatial sum of $G_{yy}(\vec{\rho} - \vec{\rho}')$ for level 1, 3, and 5 accelerations, with $u = 0.5 \beta_{av}$, obs. pt. = $0.02\vec{S}_1 + 0.02\vec{S}_2$.

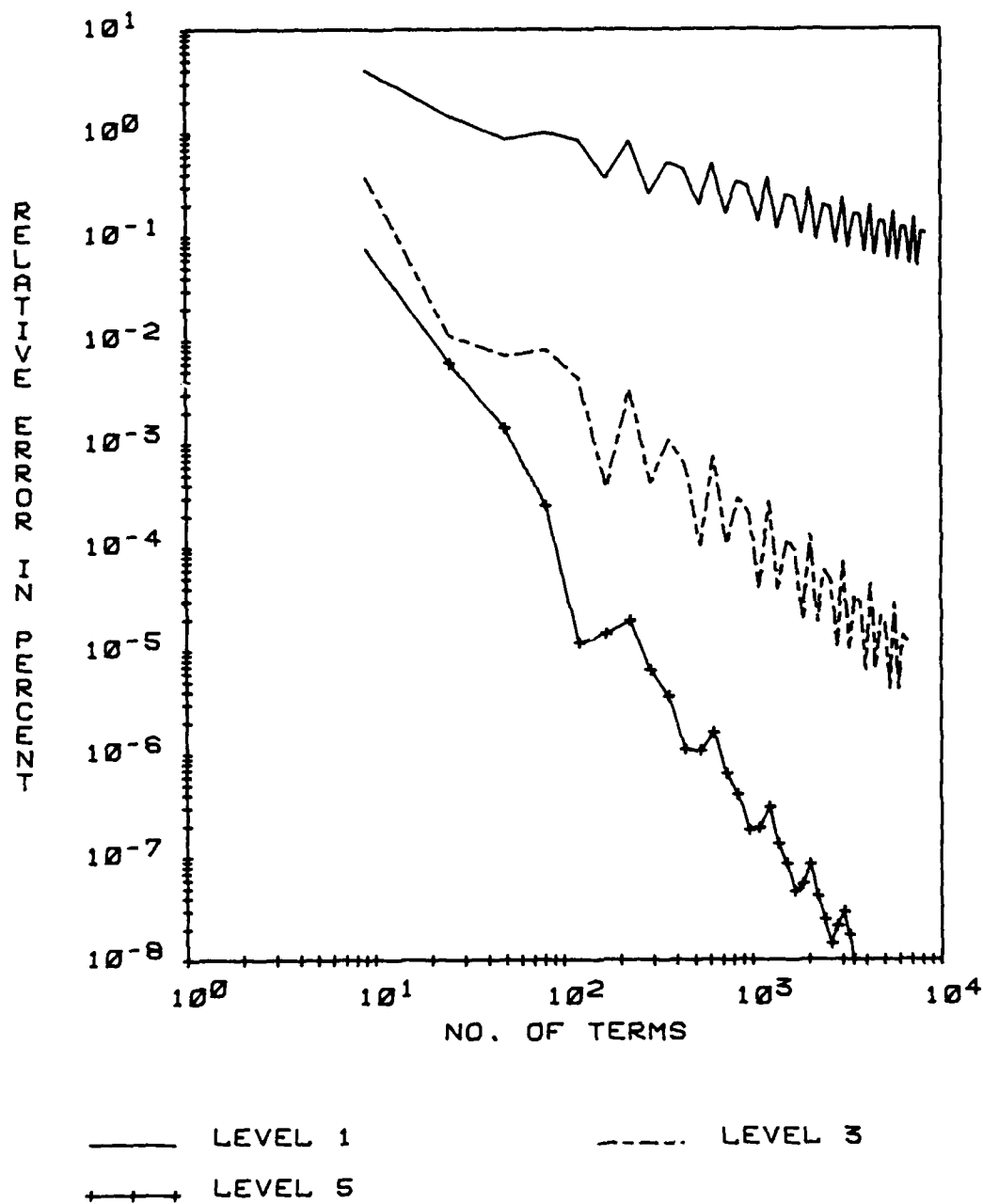


Figure 3.6. Convergence of the spectral sum of $G_{yy}(\vec{\rho} - \vec{\rho}^*)$ for level 1, 3, and 5 accelerations, with $u = 0.5 \beta_{av}$, obs. pt. = $0.3\vec{S}_1 + 0.3\vec{S}_2$.

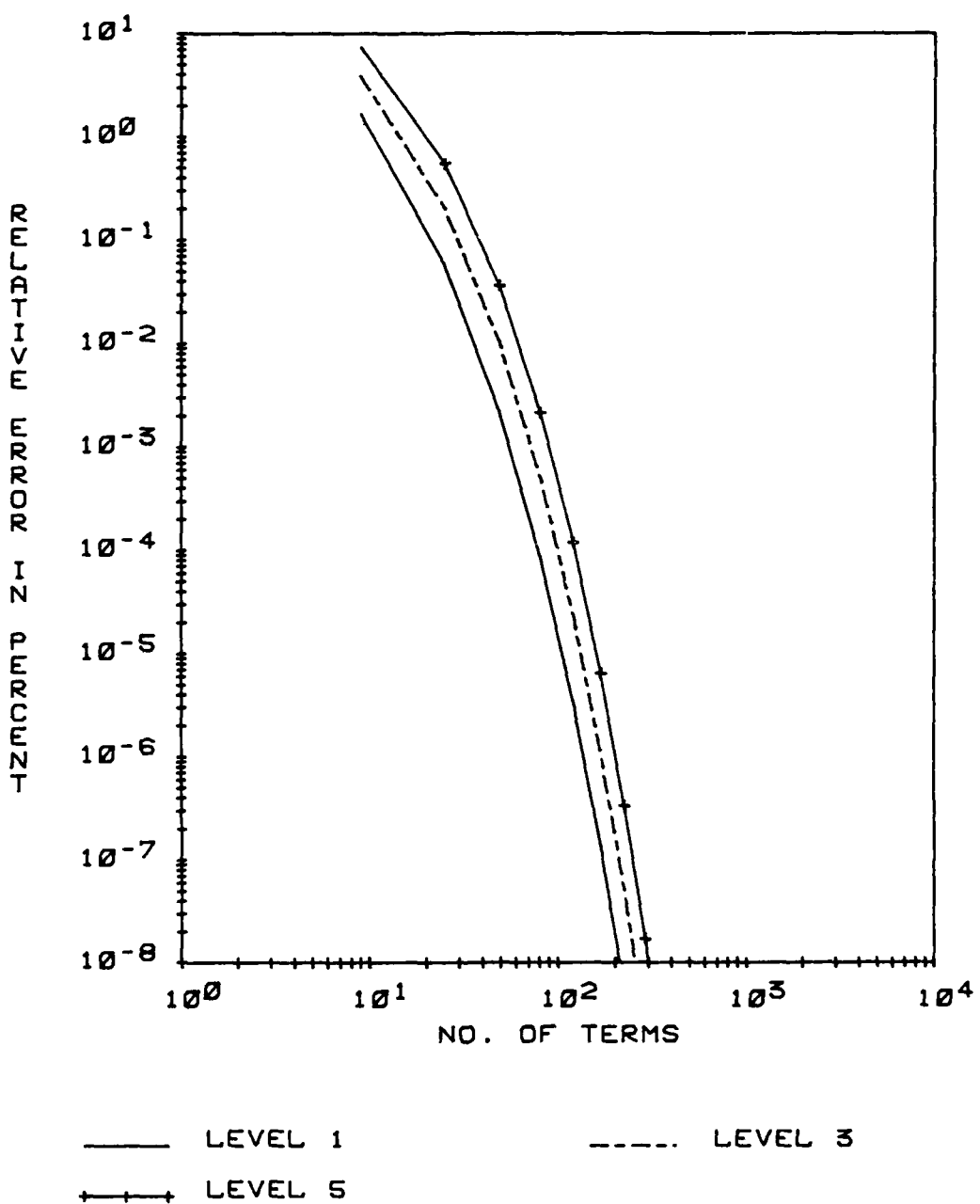


Figure 3.7. Convergence of the spatial sum of $G_{yy}(\vec{\rho} - \vec{\rho}')$ for level 1, 3, and 5 accelerations, with $u = 0.5 \vec{\beta}_{av}$, obs. pt. = $0.3\vec{S}_1 + 0.3\vec{S}_2$.

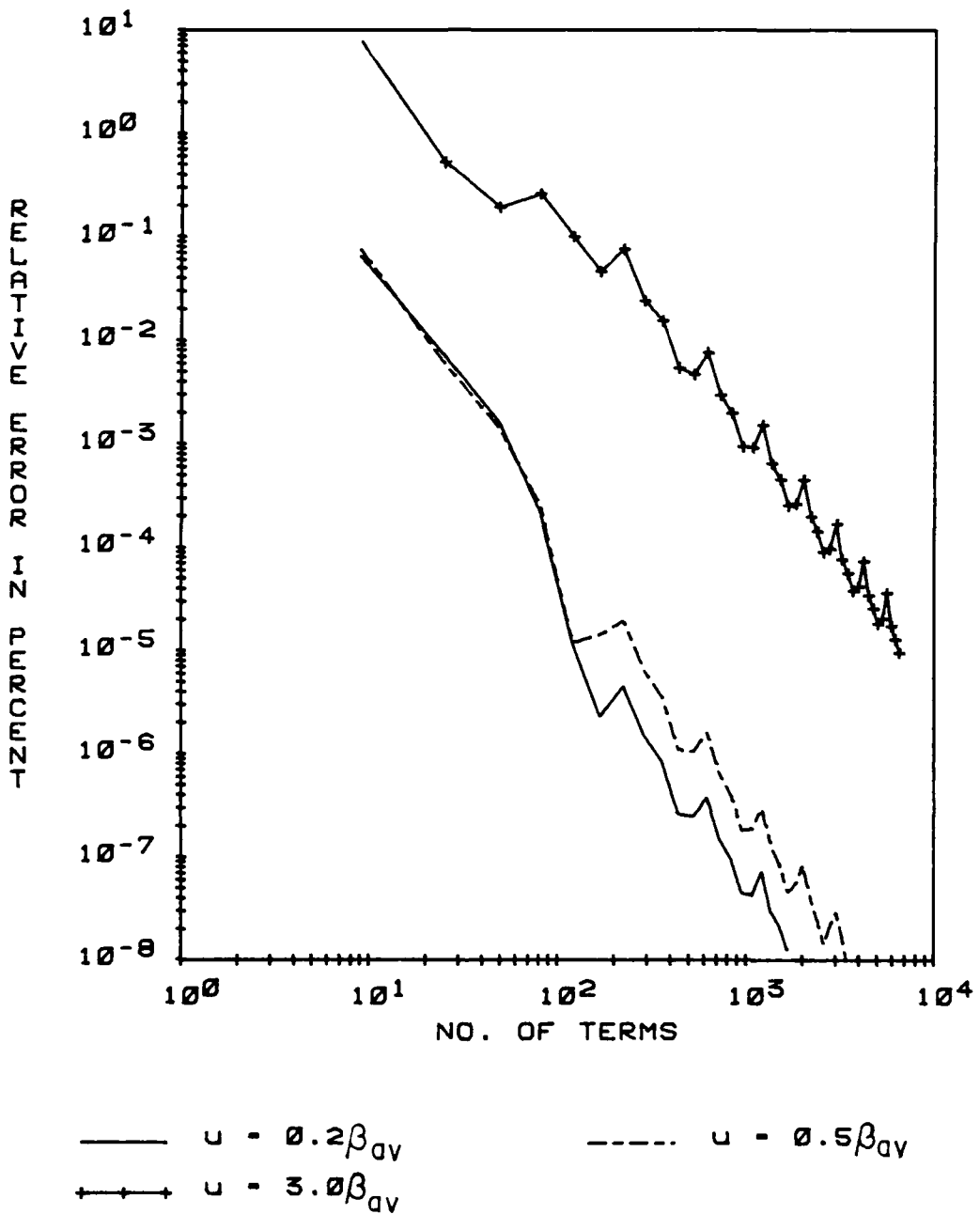


Figure 3.8. Effect of the parameter u on the convergence of the spectral sum of $G_{yy}(\vec{\rho} - \vec{\rho}')$ with level 5 acceleration and observation point $0.3\vec{S}_1 + 0.3\vec{S}_2$.

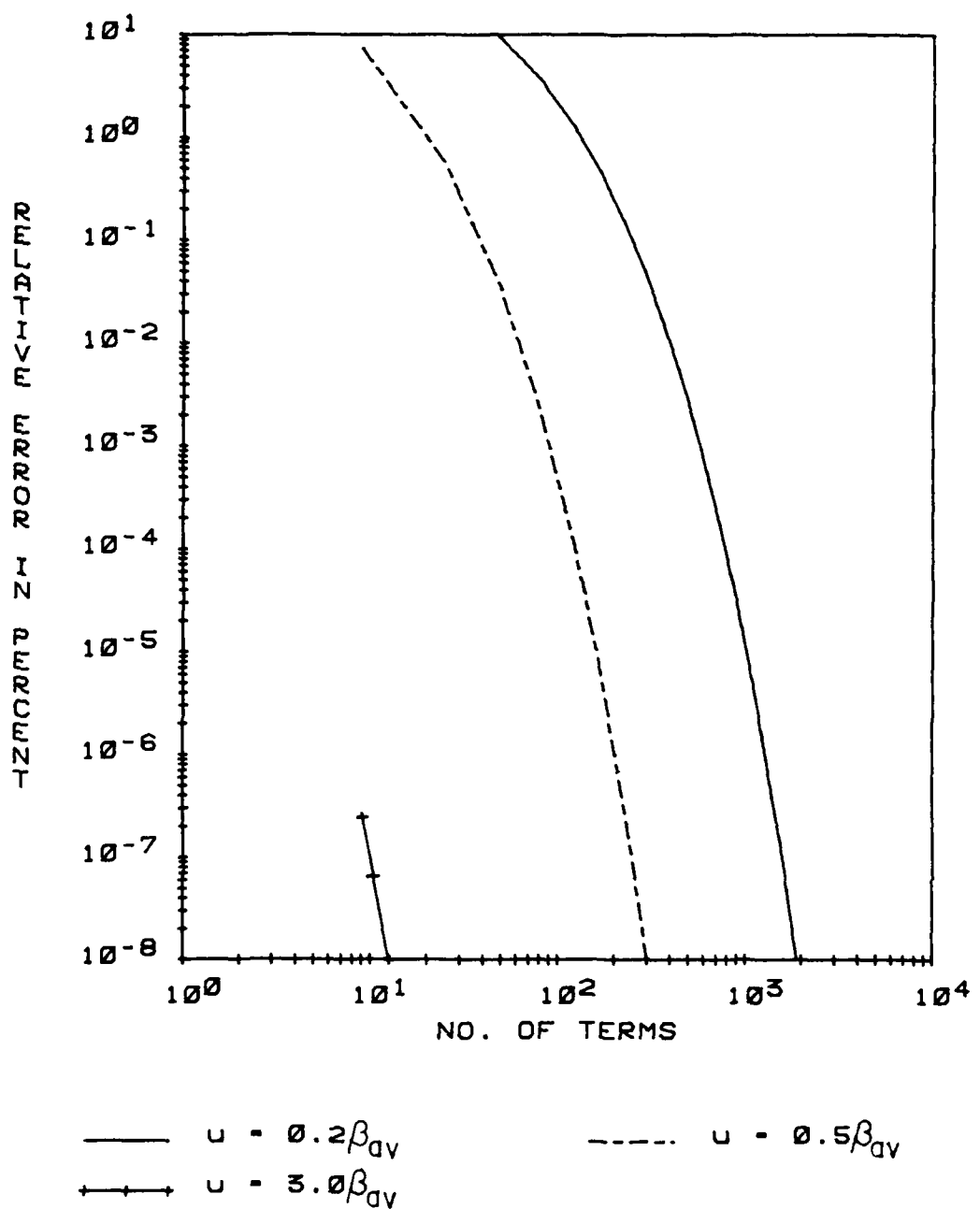


Figure 3.9. Effect of the parameter u on the convergence of the spatial sum of $G_{yy}(p - p')$ with level 5 acceleration and observation point $0.3S_1 + 0.3S_2$.

thicknesses like those used in these examples. For particular problems, however, one may want to choose u so as to decrease the number of terms required in either the spectral or spatial sum.

In this example, the periodic Green's function was straightforward to compute because all terms could be computed in closed form. Most choices of basis and testing functions do not lead to results quite this simple, as will be demonstrated in the next example.

3.3.2. Rooftop basis functions and linear testing functions

The evaluation of $f_1(\vec{p})$ is not as straightforward in general as in the previous example. A final example will demonstrate the evaluation of $f_1(\vec{p})$ for more typical basis and testing functions. In this example, a component of the Z_{SQ}^{yy} matrix will be evaluated with rooftop basis and linear testing functions. These functions are denoted

$$\begin{aligned} J_{yq} &= q(L_y; y - y_q) p(w_x; x - x_q) \\ T_{ys} &= q(L_y; y - y_s) \delta(x - x_s) \end{aligned} \quad (3.3-16)$$

where

$$\begin{aligned} q(a; i - i_p) &= 1 - \frac{|i - i_p|}{a} & |i - i_p| \leq a \\ &= 0 & \text{otherwise} \\ p(a; i - i_p) &= 1 & |i - i_p| \leq a \\ &= 0 & \text{otherwise} \end{aligned} \quad (3.3-17)$$

The transforms of the unshifted basis and testing functions are needed, and are denoted

$$\tilde{J}_y = \tilde{q}(L_y; y) \tilde{p}(w_x; x), \quad \tilde{T}_y = \tilde{q}(L_y; y) \quad (3.3-18)$$

where

$$\tilde{q}(a; i) = \frac{4 \sin^2(\beta_y a/2)}{\beta_y^2 a} \quad (3.3-19a)$$

$$\tilde{p}(a; i) = \frac{2 \sin(\beta_y a)}{\beta_y} \quad (3.3-19b)$$

From Equation (3.2-2) the spectral sum becomes

$$S_\beta = \frac{1}{A} \sum_{mn} \{ \tilde{G}_{yy}^a - \tilde{G}_{yy}^a \} \tilde{J}_y \tilde{T}_y e_{mn} (\vec{\rho}_s - \vec{\rho}_q) \quad (3.3-20)$$

where $(\vec{\rho}_s - \vec{\rho}_q)$ is the vector from the qth basis function to the sth testing function. As in the last example, the spectral sum is straightforward to compute.

The spatial sum is given by Equation (3.2-14), which was

$$S_\rho = \sum_{mn} f_1 (\vec{\rho}_s - \vec{\rho}_q - \vec{s}_{mn}) e^{j2\pi(m m_o + n n_o)} \quad (3.3-21)$$

where

$$f_1(\vec{\rho}) = F^{-1} \{ \tilde{G}_{yy}^a \tilde{J}_y \tilde{T}_y \} \quad (3.3-22)$$

Note that \tilde{G}_{yy}^a consists of two terms. One term will be referred to as the scalar potential term because it corresponds to the scalar potential term in the usual spatial domain formulation of the Green's function. Under

in the Lorentz gauge, the scalar potential term is proportional to two differentiations of the magnetic vector potential \underline{A} in Equation (2.2-13), resulting in a factor of β_y^2 in the numerator of this term. The other term in \tilde{G}_{yy}^a corresponds directly to the magnetic vector potential and will be referred to as the vector potential term. Separating the terms, $f_1(\vec{\rho})$ can be written

$$f_1(\rho) = \frac{j}{\omega\epsilon_0(1+\epsilon_r)} f_s(\vec{\rho}) - \frac{jk_0^2}{2\omega\epsilon_0} f_v(\vec{\rho}) \quad (3.3-23)$$

where $f_s(\vec{\rho})$ and $f_v(\vec{\rho})$ denote the scalar potential term and the vector potential term, respectively, and are given explicitly as

$$f_s(\vec{\rho}) = F^{-1} \left\{ \sum_{\ell=1}^L c_{2,\ell} \kappa^{-\ell} \beta_y^2 \tilde{q}^2(L_y; y) \tilde{p}(w_x; x) \right\} \quad (3.3-24a)$$

$$f_v(\vec{\rho}) = F^{-1} \left\{ \sum_{\ell=1}^L c_{1,\ell} \kappa^{-\ell} \tilde{q}^2(L_y; y) \tilde{p}(w_x; x) \right\} \quad (3.3-24b)$$

The evaluation of $f_s(\vec{\rho})$ will be considered first.

After substituting Equation (3.3-19) into (3.3-24a), and cancelling the factor β_y^2 , $f_s(\vec{\rho})$ becomes

$$f_s(\vec{\rho}) = F^{-1} \left\{ \sum_{\ell=1}^L c_{2,\ell} \kappa^{-\ell} \frac{4}{L_y} \sin^2(\beta_y L_y/2) \tilde{q}(L_y; y) \tilde{p}(w_x; x) \right\} \quad (3.3-25)$$

The factor $\sin^2(\beta_y L_y/2)$ is handled by successive applications of the shifting theorem, and application of the convolution theorem and use of Equation (3.3-5) result in

$$f_s(\vec{\rho}) = -\frac{1}{L_y} \left\{ \sum_{\ell=1}^{L_y} C_{2,\ell} [g_\ell(\vec{\rho}_1) - 2g_\ell(\vec{\rho}_2) + g_\ell(\vec{\rho}_3)] q(L_y; y) p(w_x; x) \right\}. \quad (3.3-26)$$

where $\vec{\rho}_1 = \vec{\rho} - L_y \hat{y}$, $\vec{\rho}_2 = \vec{\rho}$ and $\vec{\rho}_3 = \vec{\rho} + L_y \hat{y}$

Before discussing the evaluation of Equation (3.3-26), the remaining term $f_v(\vec{\rho})$ will be examined. Applying the convolution theorem to Equation (3.3-24b), one similarly obtains

$$f_v(\vec{\rho}) = \left\{ \sum_{\ell=1}^{L_y} C_{1,\ell} g_\ell(\vec{\rho}) \right\} * (q(L_y; y) * q(L_y; y) p(w_x; x)) \quad (3.3-27)$$

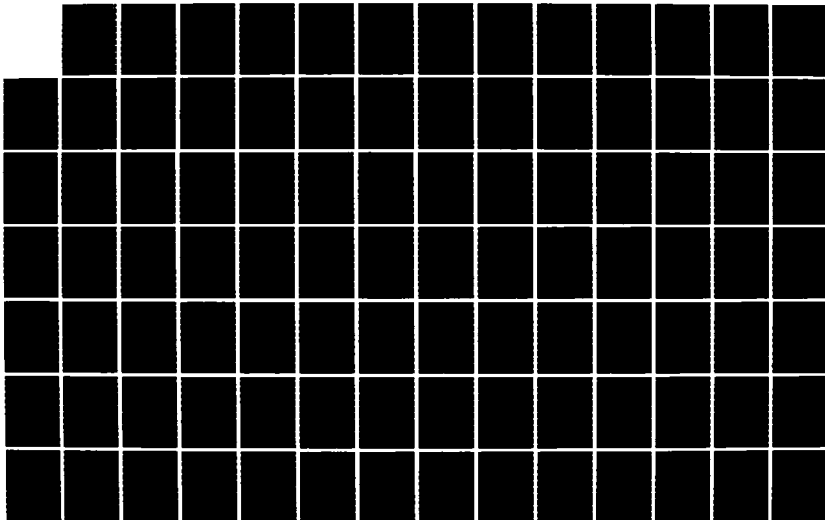
Unlike the scalar potential term where the β_y^2 in the numerator led to a simplification of the convolution integral, two factors of $q(L_y; y)$ appear in Equation (3.3-27). This prevents the convolution integrals required for $f_s(\vec{\rho})$ and $f_v(\vec{\rho})$ from being evaluated simultaneously. In addition, the integral in Equation (3.3-27) is fairly complicated, more so than Equation (3.3-26). Because computational efficiency is important in most situations, an approximation can be made which will allow these two integrals to be evaluated simultaneously. This approximation, which has been used successfully by Glisson and Wilton [54], is based on the following observation. Whenever ρ , the magnitude of $\vec{\rho} = (\vec{\rho}_s - \vec{\rho}_q - \vec{s}_{mn})$, is comparable to the support of J and T , as in the diagonal and the near-diagonal terms of the Z^{ij} matrices, the scalar potential term is dominant. These terms are often referred to as the self and near-mutual terms, respectively. When ρ is large compared to the support of J and T , $f_v(\vec{\rho})$ is relatively insensitive to the shape of J , depending more on the

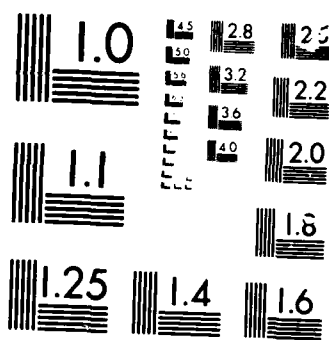
AD-A169 811 A STUDY OF MICROSTRIP ANTENNAS FOR MULTIPLE BAND AND 2/4
HIGH FREQUENCY OPERA. (U) ILLINOIS UNIV AT URBANA DEPT
OF ELECTRICAL AND COMPUTER ENGIN. Y T LO ET AL.

UNCLASSIFIED MAR 86 UILU-EM-84-15 RADC-TR-86-8

F/B 9/5

ML





MICROCOPIER

moment (the same is true for T). With this in mind, the rooftop basis function is replaced by a two-dimensional pulse function of equal moment, $J = p(L_y/2; y)p(w_x; x)$, where $p(a; i)$ was defined in Equation (3.3-17). In a similar manner, the linear testing function T is replaced by an equal moment pulse function, $T = p(L_y/2; y)$. As with J , this approximation is valid for large ρ (compared to the support of T and J), and is not important for small ρ , where the scalar potential term is dominant.

With these approximations, and noting that

$$p\left(\frac{L_y}{2}; y\right) * p\left(\frac{L_y}{2}; y\right) = L_y q(L_y; y) \quad (3.3-28)$$

$f_v(\vec{\rho})$ becomes

$$f_v(\vec{\rho}) = \left(L_y \sum_{\ell=1}^N c_{1,\ell} g_\ell(\vec{\rho}) \right) * (q(L_y; y) p(w_x; x)) \quad (3.3-29)$$

which is in the same form as Equation (3.3-26). Now, with proper care to ensure that the constants are all correctly accounted for, the integrations of Equations (3.3-26) and (3.3-29) can be performed simultaneously, improving the computational efficiency.

The evaluation of convolution integrals of this type is straightforward, but a few comments will be made here. Recall the general form of the spatial sum S_ρ

$$S_\rho = \frac{1}{A} \sum_{mn} f_1(\vec{\rho} - \vec{s}_{mn}) e^{j2\pi(m m_o + n n_o)} \quad (3.3-30)$$

where $\vec{\rho} = \vec{\rho}_s - \vec{\rho}_q$ is again the vector from the q th basis function to the

sth testing function. The form of Equation (3.3-30) is directly analogous to the spatial domain moment method solution for an infinite array of antennas, the primary difference being in the Green's function. Each of the convolution integrals in $f_1(\vec{\rho})$ is essentially the same as occurs in a spatial domain moment method solution of the same array in free space, except that instead of the Green's function $\exp(-jk_0\rho)/\rho$, in that problem, the asymptotic Green's function $g_q(\vec{\rho})$ is used. Of course, $g_q(\vec{\rho})$, given by Equation (3.3-6), has an exponential decay, rather than the ρ^{-1} decay of the free-space Green's function; hence, the sum of Equation (3.3-30) converges much faster in this case. The similarities, both conceptual and numerical, are fortunate because they allow one to use the wide body of work which has been done on the application of these integrals as occur in the free-space problem.

In keeping with this analogy, the convolution of $g_q(\vec{\rho})$ (one or more terms) with a basis function can be thought of as the asymptotic field of the basis function, asymptotic in the sense that it arises from the asymptotic Green's function. Thus, neglecting the term $e^{j2\pi(m_m + n_n)}$, each term in the spatial sum can be thought of as the convolution of the asymptotic field of the qth basis function in the m, n unit cell, tested at the center of sth testing function in the $0, 0$ unit cell. This is illustrated in Figure 3.10. When testing the field of a basis function in a unit cell sufficiently removed from the $0, 0$ cell (m, n large enough in Equation (3.3-30)), a single-point approximation can be used, evaluating the integrand at the center and multiplying by the appropriate weight. Typically all but the $0, 0$ term are evaluated using this approximation, unless high accuracy is needed or if few unknowns are used.

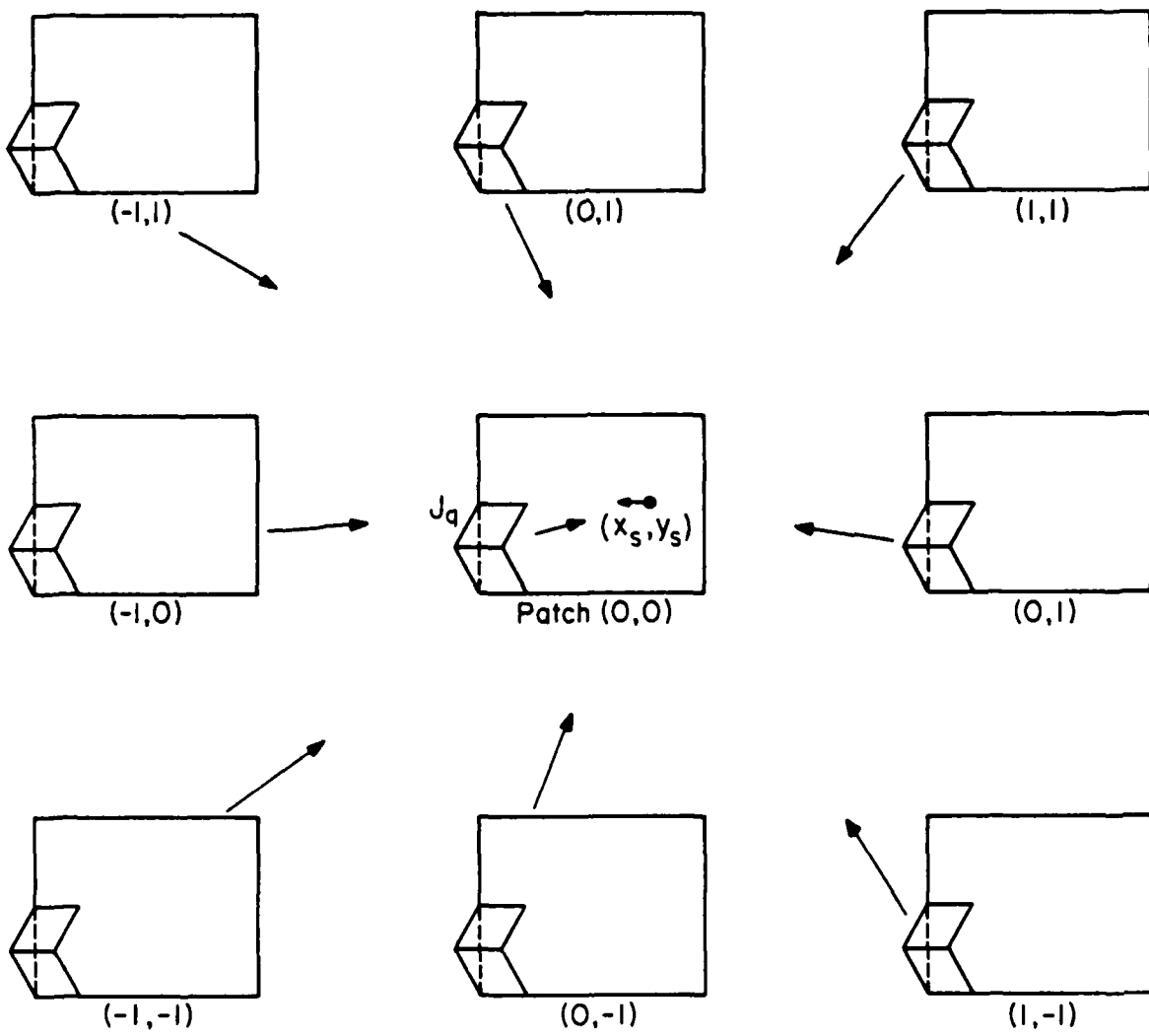


Figure 3.10. Illustration of the spatial domain summation procedure.

The evaluation of the 0,0 term must be handled with more care. The convolution integrals of Equations (3.3-26) and (3.3-29) become singular if $\vec{\rho} = (\vec{\rho}_s - \vec{\rho}_q)$ falls within the range of the integration. The singularity is of order ρ^{-1} , and can be analytically integrated. Using the notation

$$\sum_{\ell=1}^L c_{1,\ell} g_{\ell}(\vec{\rho}) = \sum_{\ell=1}^L c_{1,\ell} g_{\ell}(\vec{\rho}) - \frac{c_{1,\ell}}{2\pi\rho} \quad (3.3-31)$$

and subtracting the singularity, $f_v(\vec{\rho})$ becomes

$$f_v(\vec{\rho}) = \left[L_y \sum_{\ell=1}^L c_{1,\ell} g_{\ell}(\vec{\rho}) \right] * (q(L_y; y) p(w_x; x)) + L_y c_{1,\ell} I_4(w_x; x, L_y; y) \quad (3.3-32)$$

where $I_4(a; i, b; j)$ is the analytically integrated singularity. This integral, along with results for some other singular integrals which arise in this type of problem, are given in Table 3.4 and some associated function definitions are given in Table 3.5. Several integrals from Dwight [62] were used to obtain the results in Table 3.4. If the singularity subtraction method is to be used for evaluating the 0,0 term of all the inner products, care must be taken to avoid numerical difficulty in the evaluation of the terms of the form $\log(a + (a^2 - b^2)^{1/2})$, which can lose precision if a is small and negative. One can avoid this problem either by only subtracting the singularity when necessary, or using an alternative form of the log term [63]. In this report, the high precision of the Cyber 175 allowed the subtraction of the singularity from the 0,0 term of all inner products without loss of precision for all cases except very thin dipoles.

TABLE 3.4

A SHORT TABLE OF SINGULAR INTEGRALS ASSOCIATED WITH THE BASIS
AND TESTING FUNCTIONS USED IN THIS REPORT

$$\vec{\rho} = \hat{i}_o \hat{i} + \hat{j}_o \hat{j} \quad \vec{\rho}' = \hat{i}' \hat{i} + \hat{j}' \hat{j}$$

$$I_1(a; i) = \int_{-\infty}^{\infty} \frac{p(a; i')}{|\vec{\rho} - \vec{i}' i|} di' = \frac{1}{i_o} L_1(j_o, 0, i_o, a, -a)$$

$$I_2(a; i) = \int_{-\infty}^{\infty} \frac{q(a; i')}{|\vec{\rho} - \vec{i}' i|} di' = \frac{1}{a} \{ L_6(i_o, a, j_o) - 2L_6(i_o, 0, j_o) + L_6(i_o, -a, j_o) \}$$

$$I_3(a; i, b; j) = \int_{-\infty}^{\infty} \int_{-\infty}^{\infty} \frac{p(a; i') p(b; j')}{|\vec{\rho} - \vec{\rho}'|} di' dj'$$

$$= L_1(j_o, -b, i_o, -a, a) - L_1(j_o, b, i_o, -a, a)$$

$$+ L_1(i_o, -a, j_o, -b, b) - L_1(i_o, a, j_o, -b, b)$$

$$I_4(a; i, b; j) = \int_{-\infty}^{\infty} \int_{-\infty}^{\infty} \frac{p(a; i') a(b; j')}{|\vec{\rho} - \vec{\rho}'|} di' dj'$$

$$= \frac{1}{b} \{ L_3(j_o, b, i_o, -a, a) - 2L_3(j_o, 0, i_o, -a, a) + L_3(j_o, -b, i_o, -a, a) \}$$

TABLE 3.4 (Cont.)

$$\begin{aligned}
 I_5(a; i, b; j) &= \int_{-\infty}^{\infty} \int_{-\infty}^{\infty} \frac{q(a; i') q(b; j') di' dj'}{|\vec{p} - \vec{p}'|} \\
 &= \frac{1}{b} \{ L_2(j_0, b, i_0, -a, a) - 2L_2(j_0, 0, i_0, -a, a) + L_2(j_0, -b, i_0, -a, a) \\
 &\quad - L_3(i_0, a, j_0, -b, b) + 2L_3(i_0, 0, j_0, -b, b) - L_3(i_0, -a, j_0, -b, b) \} \\
 &\quad + \frac{i_0}{ab} \{ L_3(j_0, b, i_0, -a, 0) - 2L_3(j_0, 0, i_0, -a, 0) + L_3(j_0, -b, i_0, -a, 0) \\
 &\quad - L_3(j_0, b, i_0, 0, a) + 2L_3(j_0, 0, i_0, 0, a) - L_3(j_0, -b, i_0, 0, a) \} \\
 &\quad + \frac{1}{ab} \{ L_4(j_0, b, i_0, 0, a) - 2L_4(j_0, 0, i_0, 0, a) + L_4(j_0, -b, i_0, 0, a) \\
 &\quad - L_4(j_0, b, i_0, -a, 0) + 2L_4(j_0, 0, i_0, -a, 0) - L_4(j_0, -b, i_0, -a, 0) \} \\
 I_6(a_1, a_2; i, b; j) &= \int_{-\infty}^{\infty} \int_{-\infty}^{\infty} \frac{p(a_1; i') * p(a_2; i')}{2a_2} \cdot \frac{q(b; j')}{|\vec{p} - \vec{p}'|} di' dj' \\
 &= \frac{1}{b} [L_2(j_0, b, i_0, -a, a) - 2L_2(j_0, 0, i_0, -a, a) + L_2(j_0, -b, i_0, -a, a)] \\
 &\quad + \frac{(\beta - x_0)}{2a_2 b} [L_2(j_0, b, i_0, -\beta, -a) - 2L_2(j_0, 0, i_0, -\beta, -a) \\
 &\quad + L_2(j_0, -b, i_0, -\beta, -a)] \\
 &\quad - \frac{1}{2a_2 b} [L_4(j_0, b, i_0, -\beta, -a) - 2L_4(j_0, 0, i_0, -\beta, -a) \\
 &\quad + L_4(j_0, -b, i_0, -\beta, -a)] \\
 &\quad + L_4(j_0, b, i_0, \beta, a) - 2L_4(j_0, 0, i_0, \beta, a) + L_4(j_0, -b, i_0, \beta, a)] \\
 &\quad + \frac{1}{2a_2} [L_5(j_0, -b, i_0, -\beta, -a) + L_5(j_0, -b, i_0, \beta, a)]
 \end{aligned}$$

where $a_1 \geq a_2$, $\alpha = a_1 - a_2$, $\beta = a_1 + a_2$

TABLE 3.5
FUNCTIONS USED TO EVALUATE THE SINGULAR INTEGRALS IN TABLE 3.4

$$L_1(e, f, g, h_1, h_2) = (e + f) \log \frac{(g + h_1) + \sqrt{(g + h_1)^2 + (e + f)^2}}{(g + h_2) + \sqrt{(g + h_2)^2 + (e + f)^2}}$$

$$L_2(e, f, g, h_1, h_2) = (e + f) [(g + h_2) \log [e + f + \sqrt{(g + h_2)^2 + (e + f)^2}]$$

$$- (g + h_1) \log [e + f + \sqrt{(g + h_1)^2 + (e + f)^2}]]$$

$$+ \frac{(e + f)^2}{2} \log \frac{g + h_2 + \sqrt{(g + h_2)^2 + (e + f)^2}}{g + h_1 + \sqrt{(g + h_1)^2 + (e + f)^2}}$$

$$+ \frac{(g + h_1)}{2} \sqrt{(g + h_1)^2 + (e + f)^2}$$

$$- \frac{(g + h_2)}{2} \sqrt{(g + h_2)^2 + (e + f)^2}$$

TABLE 3.5 (Cont.)

$$L_3(e, f, g, h_1, h_2) = \frac{(e^2 + f^2)}{2} \log \frac{g + h_1 + \sqrt{(g + h_1)^2 + (e + f)^2}}{g + h_2 + \sqrt{(g + h_2)^2 + (e + f)^2}}$$

$$+ (g + h_1) [e \log (e + f + \sqrt{(e + f)^2 + (g + h_1)^2})]$$

$$- \frac{1}{2} \sqrt{(e + f)^2 + (g + h_1)^2}]$$

$$+ (g + h_2) [e \log (e + f + \sqrt{(e + f)^2 + (g + h_2)^2})]$$

$$- \frac{1}{2} \sqrt{(e + f)^2 + (g + h_2)^2}]$$

$$L_4(e, f, g, h_1, h_2) = \frac{e(g + h_1)^2}{2} \log (e + f + \sqrt{(e + f)^2 + (g + h_1)^2})$$

$$- \frac{e(g + h_2)^2}{2} \log (e + f + \sqrt{(e + f)^2 + (g + h_2)^2})$$

$$+ \frac{e(e + f)}{2} (\sqrt{(e + f)^2 + (g + h_1)^2} - \sqrt{(e + f)^2 + (g + h_2)^2})$$

$$- \frac{1}{3} [((e + f)^2 + (g + h_1)^2)^{3/2} - ((e + f)^2 + (g + h_2)^2)^{3/2}]$$

TABLE 3.5 (Cont.)

$$L_5(e, f, g, h_1, h_2) = \frac{(g + h_1)^2}{2} \log \frac{e - f + \sqrt{(e - f)^2 + (g + h_1)^2}}{e + f + \sqrt{(e + f)^2 + (g + h_1)^2}}$$

$$- \frac{(g + h_2)^2}{2} \log \frac{e - f + \sqrt{(e - f)^2 + (g + h_2)^2}}{e + f + \sqrt{(e + f)^2 + (g + h_2)^2}}$$

$$+ \frac{(e - f)}{2} [\sqrt{(e - f)^2 + (g + h_1)^2} - \sqrt{(e - f)^2 + (g + h_2)^2}]$$

$$- \frac{(e + f)}{2} [\sqrt{(e + f)^2 + (g + h_1)^2} - \sqrt{(e + f)^2 + (g + h_2)^2}]$$

$$L_6(e, f, g) = (e + f) \log(e + f + \sqrt{(e + f)^2 + g^2}) - \sqrt{(e + f)^2 + g^2}$$

Note: log denotes natural logarithm.

3.4. Parameters Affecting the Numerical Evaluation of Inner Products

There are several parameters which affect both the numerical efficiency and accuracy of the evaluation of the inner products. The choices of the constant u and the order of acceleration L have already been discussed, and are primarily determined by their effect on the execution time required to compute the sums to a given tolerance. Ideally, if enough terms of both the spectral and spatial sums are taken, the choice of u and L only affects the execution time and has no effect on accuracy. However, because of the approximation discussed in Section 3.3 to make the evaluation of the convolution integral for the vector potential term more efficient, the choice of u and L can change the contribution of the spectral sum in relation to the spatial sum. This can cause the result to be affected by a change in u or L , regardless of how many terms of the sums are taken. If desired, this can be corrected by using the same approximation on the vector potential term in the spectral sum, i.e., approximating the linear triangle dependence in \vec{y} in the basis and testing functions with constant two-dimensional pulses. However, if the approximation is valid the effect of changing u and L should be slight; in this manner, changing u and L provides a check on the validity of the approximation.

Another parameter which must be chosen is the accuracy to which the convolution integrals are evaluated. Other than the singular term, the convolutions required to evaluate $f_s(\vec{\rho})$ and $f_v(\vec{\rho})$ were not done in closed form except for very simple cases, such as the example in Section 3.3.1.

Several approaches are possible, such as replacing each term of $g_\ell(\vec{\rho})$ by the first few terms of a Taylor series and integrating each term in closed form. This approach was not taken because the number of terms required for sufficient accuracy in the Taylor series depends on the relative locations of the testing and basis functions, and also because a large number of complex analytical integrations are required. Another approach is to approximate the integrals by numerical quadratures. In this report two quadrature methods were used. If the integrations were one dimensional, as when using the thin-wire approximation to analyze dipoles, the IMSL routine DCADRE was used. In the thin-wire approximation the two-dimensional integration required to compute the inner product is approximated by a one-dimensional integration. This approximation is discussed further in Chapter 4. DCADRE is an adaptive quadrature and is very efficient. In fact, no significant improvement in execution time was noted when the single integrals were evaluated with less accuracy using 16 point Gaussian quadratures. To evaluate double integrals, the IMSL routine DBLIN was used, or in some cases, 64 or 128 point Gaussian quadratures [56]. DBLIN is also an adaptive quadrature routine. In general, for the two-dimensional integrals, it was found that if enough basis and testing functions were used the Gaussian quadrature provided sufficient accuracy at a lower cost. In particular, for the self and near-mutual terms where the scalar potential dominates, the singularity accounts for the largest part of the integral, and that part is performed analytically. The remaining nonsingular integration can be evaluated using the Gaussian quadrature. For the other inner products, the integrand varies smoothly enough that the Gaussian quadrature was

sufficient in most cases. Again, if few basis and testing functions were used, the Gaussian quadrature was insufficient, because the range of integration was too large for the singularity to be dominant in the self and near-mutual terms, thereby requiring more accuracy in the nonsingular numerical integration.

Both DCADRE and DBLIN allow the user to select an absolute error bound, and DCADRE allows the user to select a relative error bound. When using DBLIN, the absolute error was chosen by estimating the answer with a simple Gaussian quadrature or one-point approximation, and dividing the absolute value of the estimate by a relative error factor, typically 100 or 1000. The choice of the relative error factor is one of the factors which affects the computational efficiency and accuracy of the inner product evaluation. This choice was selected by numerical experimentation to give satisfactory answers at a low execution time. When using DCADRE, the inverse of the above relative error factor was input for the relative error bound, and no absolute error bound was given (0.0).

As discussed in Section 3.3, the convolution integrals are evaluated using quadratures only for terms with m and n less than some integer, I_{\max} . For all other terms single-point approximations were used. Because of the exponential decay of the asymptotic Green's function, it was found that I_{\max} could be very low, typically 0 or 1. This is another of the user-selectable parameters which affects the evaluation of the inner products.

Another parameter to be chosen is the truncation point of the sums. Choosing the truncation point can be very difficult because of the trade-off between accuracy and efficiency. Rather than use a fixed number

of terms for each problem, or even a formula relating the truncation point to the array spacing and size of the basis function, as done by Rubin and Bertoni [38], two adaptive summation routines were used to compute the spatial and spectral sums. Denoting the sum of all terms with $|m|$ and $|n| < N$ as S_M , the routine compared each partial sum S_M to the previous ones in order to determine a truncation point. Because the spatial sum, S_ρ , converges very rapidly, the routine to compute S_ρ required only that

$$\left| \frac{S_M - S_{M-1}}{S_M} \right| < \text{tol} \quad (3.4-1)$$

where the tolerance tol is chosen to give satisfactory accuracy and efficiency. At the truncation point, S_ρ was set equal to S_M .

Because of the more oscillatory nature of the spectral sum, a more stringent test was used in the routine to compute S_β . Now denoting S_M as the M th partial sum of the spectral sum, the routine required that both

$$\left| \frac{S_M - S_{M-1}}{S_\rho + S_M} \right| < \text{tol} , \quad \left| \frac{S_M - S_{M-2}}{S_\rho + S_M} \right| < \text{tol} \quad (3.4-2)$$

before the sum would be truncated. The routine compared the difference in partial sums to the sum of S_ρ and S_M rather than just to S_M so that if the contribution of the spectral sum to the total was small compared to the contribution of the spatial sum, fewer terms would be taken. This is often the case for the diagonal and near-diagonal (self and near-mutual terms) of the Z matrices.

An alternative definition of a partial sum would be to define the partial sum S_R as the sum of all terms for which the distance from the

origin, β , is less than some distance R . This is known as a spherical sum [64]. However, it was found that for the infinite sums of concern here, the definition of the partial sum S_M used above leads to a significantly better rate of convergence.

One final parameter which can affect convergence rates is the choice of the lattice vectors \vec{S}_1 and \vec{S}_2 . For example, Equation (3.3-14) for the periodic Green's function will fail to converge for a first-order acceleration ($L = 1$ in the asymptotic expansions) if the observation point falls on the array lattice (i.e., the observation point can be expressed as a multiple of one of the lattice vectors alone.) This is caused by the loss of the phase variation in the terms as one index is increased. The higher-order accelerations will converge, but at a somewhat slower rate. This difficulty can be resolved by choosing new lattice vectors such that the observation point is no longer on the array lattice. As an example, if a square array of point sources is defined by $\vec{S}_1 = 1.0\lambda_0 \angle 0^\circ$, $\vec{S}_2 = 1.0\lambda_0 \angle 90^\circ$, and the observation point was at $0.0\vec{S}_1 + 0.5\vec{S}_2$, the above difficulty would occur. However, if the lattice vectors are chosen as $\vec{S}_1 = 1.0\lambda_0 \angle 0^\circ$, $\vec{S}_2 = \sqrt{2}\lambda_0 \angle 45^\circ$, the same observation point would be described in terms of the new lattice vectors as $-0.5\vec{S}_1 + 0.5\vec{S}_2$ --no longer on the array lattice and, therefore, the sum will converge without difficulty.

Obviously, there are many trade-offs to be made in the name of efficiency, such as the choice of the relative error factor mentioned above, the choice of the parameter u , or the level of approximation. In the computer program used to obtain the results of the next two chapters, the various parameters are input at run time. Suitable values have been

chosen after extensive numerical experimentation. However, as different applications will need to stress efficiency and accuracy in different amounts, there probably is no optimum choice of any parameter. Examples of the effects of the parameters on both accuracy and efficiency will be given in the next two chapters.

This chapter has attempted to introduce the acceleration method used to efficiently evaluate the inner products of the Z and b matrices. In addition, the example of Section 3.3.2 has demonstrated the technique for a typical inner product of the type which arises in the examples of the next two chapters. The evaluation of these inner products has been reduced to the evaluation of two rapidly convergent summations. The spectral sum is easily altered for different inner products by choosing the proper component of the Green's functions, from Tables 2.1 and 3.2 and the transforms of the basis and testing functions. The spatial sum is reduced to performing a convolution integral of the type that arises in standard free-space moment method problems, except that the integrals involve the rapidly decaying asymptotic Green's function. To facilitate changing basis and testing functions, a table of the singular integrals which commonly arise has been included. With this background and the formulation in Chapter 2, the acceleration technique can be applied to the analysis of various problems in the next two chapters.

CHAPTER 4

INFINITE ARRAYS OF MICROSTRIP DIPOLES

Microstrip dipole arrays have been receiving increasing attention in recent years. One important advantage that dipole arrays have over patch arrays is the small amount of space on the actual array plane consumed by the antenna element. This conserves room which may be needed for associated circuitry such as matching networks, phase shifters and baluns. In addition, for the purposes of immediate concern here, dipole arrays provide a low-cost starting point for a more general analysis of microstrip patch arrays.

An array of dipoles on a single-layer grounded dielectric slab (GDS) is pictured in Figure 4.1. The dipole will always be oriented along \hat{y} . Because the dipoles are generally very thin in wavelengths, the \hat{x} directed current is generally assumed to be zero. This is the first of the so-called thin-wire approximations that will be used. In addition, the distribution of the current in the transverse (\hat{x}) direction is often assumed, and just one basis function used is in the transverse direction. In this chapter the transverse distribution is chosen to satisfy the edge condition for the current flowing parallel to the edge of a perfectly conducting strip in free space. The result of these two assumptions is that relatively few basis functions are required to approximate the current distribution. In addition, the validity of the assumed transverse current distribution is checked by placing multiple basis functions in the \hat{x} direction and solving for the transverse current distribution.

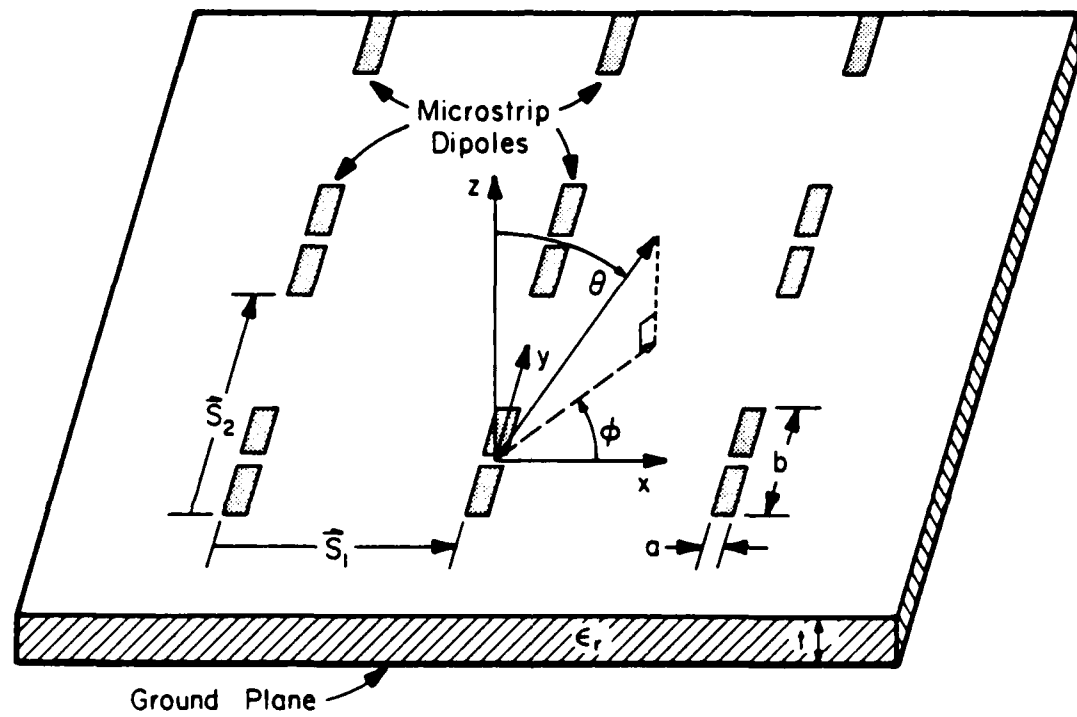


Figure 4.1. Section of an infinite array of microstrip dipoles.

Another computational simplification that can be employed when analyzing dipole arrays is to use the delta-gap feed model [65]. This model assumes an infinitely thin feed gap and thus makes the evaluation of the excitation matrix trivial. While this feed model is commonly used, it is difficult to approximate in practice, particularly with a microstrip array, which generally uses an unbalanced feed. Other feed models are being investigated for future work, but the delta-gap feed frees one from being concerned with the feed problem and allows the properties of the antenna array to be studied without the additional cost of evaluating a complex excitation matrix.

The remainder of this chapter is divided into two parts. Section 4.1 discusses the evaluation of the solution including the choice of suitable basis and testing functions and the evaluation of the elements of the impedance and excitation matrices. Section 4.2 gives experimental and theoretical results for arrays of microstrip dipoles, and discusses the waveguide simulator used to obtain the experimental results.

4.1. Evaluation of the Matrix Elements

4.1.1. Choice of basis and testing functions

A good choice of basis and testing functions is important in achieving a solution which is computationally efficient. As discussed in Chapter 2, a good choice of these functions will have a physical basis and will lead to efficient evaluation of the Z matrix. A brief but excellent discussion of basis functions for surface problems is contained in the reference by Glisson and Wilton [54].

Much of the previous work on microstrip dipoles has employed piecewise sinusoidal basis functions [21,22,37]. In terms of the unshifted function discussed in Section 2.4, this basis function is

$$J_y(x,y) = \frac{\sin(k_{\text{eff}}(L_y - |y|))}{2w_x \sin(k_{\text{eff}}L_y)} p(w_x; x) \quad |y| \leq L_y \quad (4.1-1)$$

The parameter k_{eff} is chosen by numerical experimentation to give rapid convergence. Note that, when referring to the method of moments, rapid convergence implies that a stable solution is achieved with a low number of basis functions compared to a more slowly converging solution. In [21, 22] and [37], the authors assume a constant current distribution in the transverse direction and use only one basis function in the \hat{x} direction. The same piecewise sinusoids are also used as testing functions. This choice of basis and testing functions can lead to rapid convergence, particularly for resonant dipoles, where the current distribution is very nearly sinusoidal. However, this choice has two drawbacks. First, the Fourier transform of Equation (4.1-1) does not have a separate factor of β_y^2 in the denominator, which prevents the simplification of the convolution integrals described in Section 3.4. Second, the edge condition for current flowing parallel to the edge of a conducting strip is not included in the basis functions. In this chapter, results are shown which demonstrate that incorporation of the edge condition is desirable for very thin dipoles, but that satisfactory results can be obtained without it.

Instead of piecewise sinusoids, two different combinations of basis and testing functions were used to obtain the results in this chapter. Because of the computational advantage, linear dependence in \hat{y} was used in both cases. As discussed above, this leads to a simplification of the convolution integrals required to evaluate the elements of the Z matrix. The combination of functions used to obtain most of the results in this chapter consisted of "edge mode" basis functions and linear testing functions,

$$J_{yq}(x, y) = q(L_y; y - y_q) g(w_x; x) \quad (4.1-2)$$

$$T_{ys}(x, y) = q(L_y; y - y_s) \delta(x)$$

An edge mode basis function, which is simply a rooftop function incorporating the edge condition for a strip in free space, is denoted $g(w_x; x)$, where $g(w_x; x)$ is defined as

$$g(w_x; x) = \begin{cases} \frac{1}{\sqrt{1 - (x/w_x)^2}} & |x| \leq w_x \\ 0 & \text{otherwise} \end{cases} \quad (4.1-3)$$

The transform of $g(w_x; x)$ is

$$\tilde{g}(w_x; x) = J_0(w_x \beta_x) \quad (4.1-4)$$

where J_0 is the Bessel function of order zero, and the dependence of $\tilde{g}(w_x; x)$ on β_x is understood in this notation.

Because the dipole is on a GDS, and will vary in width, the accuracy and range of validity of this current distribution are questionable. In addition, to make the evaluation of the inner products more efficient, another "thin-wire" approximation was made when using this method,

referred to as method 1. In particular, the 2-D convolution integral required to evaluate the spatial sum is approximated by a 1-D integration. This will be discussed further in Section 4.1.2.

In order to check the validity of the above two approximations, the second method used in this chapter was a more general technique. This method, referred to as method 2, used the rooftop basis and linear testing functions of Equations (3.3-16) and (3.3-17) and allowed multiple basis functions in the transverse directions. In this manner, no transverse current distribution was assumed, and the actual distribution could be approximated. The layout of the basis functions of this method is pictured in Figure 4.2. The width of the dipole is exaggerated for clarity. As discussed in Chapter 2, all basis functions are identical, differing only by a linear translation. This restriction significantly decreases the cost of filling the impedance, or Z matrix, as will be discussed in Section 4.1.3, but can be easily removed. In addition to allowing the determination of the transverse current distribution, the 2-D convolution integrals were performed numerically, without the approximation made with the previous method, where a 1-D integration was used. These two differences allow the second, more general method to be used as a check for the accuracy of the solution using edge mode basis functions.

4.1.2. Evaluation of the impedance matrix

The elements of the Z matrix with method 2, using rooftop basis functions and linear testing functions, were evaluated in detail in the second example of Section 3.3, and will not be discussed here. Of course, only the Z^{yy} matrix needs to be evaluated, as the \hat{x} directed current is assumed to be zero.

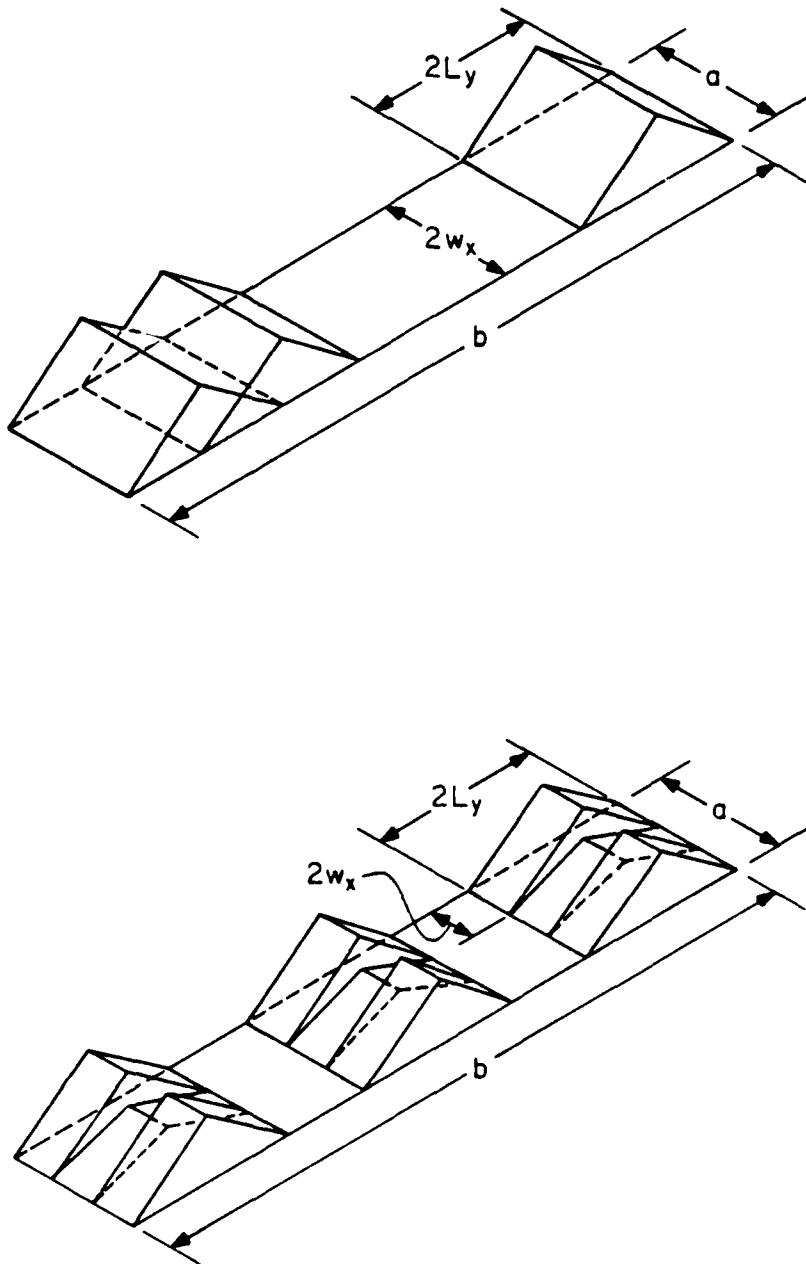


Figure 4.2. Basis function layout on microstrip dipoles.

The application of the acceleration technique to the evaluation of the Z matrix when using the second combination of basis and testing functions also follows the example of Section 3.3, with some differences. As always, the evaluation of the spectral sum is straightforward. One substitutes \tilde{G}_{yy} and \tilde{G}_{yy}^a from Tables 2.1 and 3.2 and the transforms of the basis functions, obtained from Equations (4.1-3) and (3.3-19), into the first infinite sum in Equation (3.2-2). As discussed in the last chapter, \tilde{G}_{yy} and \tilde{G}_{yy}^a are the yy components of the periodic Green's function and its asymptotic form.

The evaluation of the spatial sum, given by Equations (3.3-21) and (3.3-22), also proceeds as in Section 3.3. As in that example, the evaluation of $f_1(\vec{p})$ in Equation (3.3-22) results in two convolution integrals, denoted the scalar potential term, $t_s(\vec{p})$, and the vector potential term, $f_v(\vec{p})$. With the edge mode basis functions of Equation (4.1-1), $f_s(\vec{p})$ and $f_v(\vec{p})$ are obtained from Equations (3.3-26) and (3.3-29) by substituting $g(w_x; x)$ for $p(w_x; x)$. Recall that in obtaining Equation (3.3-29) the y dependency of the basis and testing functions was approximated by pulses. As discussed earlier, these convolution integrals have the same form, and can be numerically evaluated simultaneously. As an example of the evaluation of these integrals, consider the vector potential term, $f_v(\vec{p})$, given by

$$\begin{aligned}
 f_v(\vec{p}) &= L_y \sum_{\ell=1}^L c_{1,\ell} g_\ell(\vec{p}) * (q(L_y; y) g(w_x; x)) \\
 &= L_y \sum_{\ell=1}^L c_{1,\ell} \left[\int_{-L_y}^{L_y} \int_{-w_x}^{w_x} 1 - \frac{|y'|}{L_y} g_\ell(\vec{p} - \vec{p}') \frac{dx' dy'}{\sqrt{1 - (w_x/x')^2}} \right]
 \end{aligned} \tag{4.1-5}$$

where $\vec{\rho}' = \vec{x}'\vec{x} + \vec{y}'\vec{y}$. By a change of variables, this integral can be cast into an integral over the surface of a cylinder, excluding the end-caps, of the form which arises when analyzing cylindrical dipoles [66]. Once in this form, any of the many thin-wire approximations can be used to evaluate the integral.

To proceed, consider the evaluation of $f_v(\vec{\rho})$ for $L = 1$,

$$f_v(\vec{\rho}) = \frac{w_x L y C_{1,1}}{2\pi} \int_{-L_y}^{L_y} \left[1 - \frac{|y'|}{L_y} \right] \int_{-w_x}^{w_x} \frac{e^{-u((y-y')^2+x'^2)^{1/2}}}{((y-y')^2+x'^2)^{1/2}} \cdot \frac{dx'dy'}{(w_x^2 - x'^2)^{1/2}} \quad (4.1-6)$$

recalling that $g_1(\vec{\rho}) = \exp(-u\rho)/2\pi\rho$. Making the change of variable $x' = w_x \sin(\alpha/2)$, Equation (4.1-6) becomes

$$f_v(\vec{\rho}) = \frac{w_x L y C_{1,1}}{2} \int_{-L_y}^{L_y} \left[1 - \frac{|y'|}{L_y} \right] G(y - y', a) dy' \quad (4.1-7)$$

where

$$G(y - y', a) = \frac{1}{2\pi} \int_{-\pi}^{\pi} \frac{e^{-u((y-y')^2+4a^2\sin^2(\alpha/2))^{1/2}}}{((y-y')^2+4a^2\sin^2(\alpha/2))^{1/2}} d\alpha$$

and $a = w_x/2$. $f_v(\vec{\rho})$ can be obtained for arbitrary L by making the substitution $|\vec{\rho} - \vec{\rho}'| = ((y-y')^2 + 4a^2\sin^2(\alpha/2))^{1/2}$ in $g_\ell(\vec{\rho})$ for $\ell = 1, 3, \dots, L$, where $g_\ell(\vec{\rho})$ is given in Equation (3.3-6).

$G(y-y', a)$ is recognized to be the "exact" kernel for a cylinder of current of radius a , equal to one half the strip width. This function is commonly used in cylindrical dipole analysis, and its evaluation is discussed in detail by Poggio [67]. Keeping in mind that the more

rigorous approach using rooftop functions is available as a check, the approximation used here to evaluate $G(y-y', a)$ is

$$G(y - y', a) \approx \frac{e^{-u((y-y')^2 + a^2)^{1/2}}}{((y - y')^2 + a^2)^{1/2}} \quad (4.1-8)$$

This is the simplest reasonable approximation, and is often referred to as the "thin-wire approximation." However, this is only one of several approximations which are valid only for thin wires, and as such is one of many thin-wire techniques. This approximation was chosen in an attempt to obtain reasonably accurate solutions with high efficiency. Poggio discusses the range of the validity of the approximation in Equation (4.1-8). Rather than try to predict the effect of an error in only one of several approximations on the final solution for the current distribution, the accuracy of this approximation will be established by comparison to the results for the more general method employing rooftop basis functions.

Combining Equations (4.1-7) and (4.1-8) and extending to arbitrary L , $f_v(\vec{\rho})$ becomes

$$f_v(\vec{\rho}) = \pi w_x L_y \sum_{\ell=1}^L \left[C_{1,\ell} \int_{-L_y}^{L_y} \left(1 - \frac{|y'|}{L_y} \right) g_\ell((y - y')^2 + 4a^2)^{1/2} dy' \right] \quad (4.1-9)$$

The evaluation of $f_s(\vec{\rho})$, the scalar potential term, is similar. For each inner product, $f_1(\vec{\rho})$, consisting of $f_s(\vec{\rho})$ and $f_v(\vec{\rho})$, must be evaluated for increasing m and n in Equation (3.3-21). As discussed in Section 3.3, each evaluation corresponds to testing the "asymptotic field" of a basis function in the m,n unit cell with a testing function in the $0,0$ unit

cell. Asymptotic field is the term used to describe the convolution of the asymptotic Green's function with a basis function. This concept was illustrated in Figure 3.10. For each inner product, the $m=n=0$ evaluation of $f_1(\vec{\rho})$ was performed by subtracting out the singularity, which can be integrated analytically, and evaluating the remaining integration using an adaptive quadrature, as discussed in Chapter 3. For the contribution from unit cells with m and n less than some integer I_{\max} , but not both zero, the integration was again performed with the adaptive quadrature routine, but the singularity was not subtracted out. Finally, for the remaining terms with either m or n greater than I_{\max} , the integrations were evaluated using a single-point approximation. Because of the rapid decay of the asymptotic field, I_{\max} was typically chosen to be 0 or 1. As discussed in Chapter 3, less expensive Gaussian quadratures could have been used to evaluate the 2-D integrals, but as this technique was meant primarily to provide a check on the more efficient method using edge mode basis functions, these approximations were not used.

4.1.3. Use of symmetry

If all of the basis functions have the same length and width, as in all of the examples in this report, a great deal of symmetry exists in the Z matrix. Recall the unaccelerated form of an element in the Z^{yy} matrix:

$$Z_{sq}^{yy} = \frac{1}{A} \sum_m \sum_n \tilde{G}_{yy} \tilde{J}_y \tilde{T}_y e_{mn}(\vec{\rho}_s - \vec{\rho}_q) \quad (4.1-10)$$

where \tilde{J}_y and \tilde{T}_y are the transforms of the unshifted basis and testing functions, and $e_{mn}(\vec{\rho}_s - \vec{\rho}_q)$ is defined by Equation (2.2-11). Now consider two elements Z_{ij}^{yy} and Z_{kl}^{yy} , where i, j, k and l are integers. As can be

seen from Equation (4.1-10), all elements of the Z^{yy} matrix are identical except for the factor $e_{mn}(\vec{\rho}_s - \vec{\rho}_q)$. For the two general elements Z_{ij}^{yy} and Z_{kl}^{yy} , the vector $(\vec{\rho}_s - \vec{\rho}_q)$ becomes

$$\begin{aligned}\vec{\rho}_i - \vec{\rho}_j &= x_{ij} \hat{x} + y_{ij} \hat{y} = (x_i - x_j) \hat{x} + (y_i - y_j) \hat{y} \\ \vec{\rho}_k - \vec{\rho}_l &= x_{kl} \hat{x} + y_{kl} \hat{y} = (x_k - x_l) \hat{x} + (y_k - y_l) \hat{y}\end{aligned}\quad (4.1-11)$$

Now, with a general phase shift, or beam steering, it is apparent that if $x_{ij} = x_{kl}$ and $y_{ij} = y_{kl}$, then $Z_{ij}^{yy} = Z_{kl}^{yy}$. Furthermore, considering a rectangular lattice with beam steering only in the \hat{y} direction (E-plane), if $|x_{ij}| = |x_{kl}|$ and $y_{ij} = y_{kl}$, the two elements are again equal. Likewise, if the beam is steered only in the \hat{x} direction (H-plane), then whenever $|y_{ij}| = |y_{kl}|$ and $x_{ij} = x_{kl}$ the two elements Z_{ij}^{yy} and Z_{kl}^{yy} are equal. Finally, for the special case of no phase shift, corresponding to no beam steering or a normally incident plane wave in the scattering problem, the requirements for equality of the two elements are $|x_{ij}| = |x_{kl}|$ and $|y_{ij}| = |y_{kl}|$. These conditions can result in substantial savings in filling the matrix, particularly if the beam is scanned only in the principal planes (E and H), or for no beam steering.

For example, consider a dipole with N basis functions in the \hat{y} direction and M basis functions in the \hat{x} direction (all \hat{y} oriented), for a total of $N \cdot M$ unknowns. If there is no beam steering, only $N \cdot M$ elements of the Z matrix are distinct. For H plane scanning, only $(2M-1)N$ elements are distinct, and similarly for E plane scanning, only $(2N-1)M$ elements are unique.

Finally, matrix reduction techniques [65] have been used whenever symmetries exist in the current. In addition, one can take advantage of the Toeplitz or block Toeplitz form of the Z matrix to reduce the storage requirements. If one of these techniques is not used, the number of basis functions that can be used is limited by the time and cost of solving the system of equations, and perhaps by computer storage capacity. While some computer systems overcome the storage capacity problem by using virtual memory or off-core matrix inversion routines, these techniques can be exceedingly slow.

4.1.4. Evaluation of the excitation matrix

The incident field matrix, or V matrix in the system $Zx = V$, is given by $[V_S]$ in Equation (2.3-12). When using the delta-feed [65], this matrix is trivial to evaluate. Assuming an odd number of basis functions in the \hat{y} direction and an antenna fed in the center with a one-volt source, all elements of $[V_S]$ are zero except those for which the testing function is non-zero over the gap. With the normalization chosen for the testing functions, each non-zero element becomes -1, for a one-volt source.

After filling the V and Z matrices, the unknown current coefficients are determined by solving the system of equations. Each current coefficient b_q is the current density at the peak of the qth basis function. The actual current flowing at the peak of the basis function is then the width of that function multiplied by its coefficient, b_q . The normalization of the testing functions could have been chosen so as to yield the current directly. However, when testing for convergence with multiple basis functions in the \hat{x} direction, the current density at a given point will remain constant when the solution has converged, and can

be interpreted more easily than the current, which decreases as the number of unknowns in the \hat{x} direction increases. This is particularly important in the next chapter.

Now, as all of the elements of the matrix $[V_S]$ are zero except those corresponding to an element over the feed gap and all basis functions have the width $2w_x$, the impedance is the excitation voltage divided by the total current flowing across the gap, and can be written as

$$Z_{in} = \frac{1}{[|V_S|]^T [b_Q] 2w_x} \quad (4.1-12)$$

where S , the number of basis functions, is chosen equal to Q , the number of testing functions. The absolute value signs indicate that the absolute value of the elements of $[V_S]$ be taken.

Finally, the solution to the scattering problem is obtained by evaluating $[V_S]$ according to Equation (2.3-12). An example of interest here is scattering due to a normally incident plane wave. If the value of the \hat{y} oriented electric field at the array plane is 1 volt per wavelength, the q th element of $[V_S]$ becomes L_{yq} , where $2L_{yq}$ is the length of the q th testing function. In all examples considered here, all testing functions have the same width, and hence all elements of $[V_S]$ become L_y . Solution of the matrix equation for the current coefficients again gives the value of the current density at the peak of each basis function.

4.2. Numerical Results

Computed results were initially checked by setting ϵ_r of the substrate equal to one and computing results which could be compared to

known free-space cases. Stark has computed the impedance of infinite dipole arrays over a ground plane [68], and results using this method agree very well with his results. In addition, by letting the lattice spacings S_1 and S_2 increase to several wavelengths, the well-known impedance of a half-wave dipole over a ground plane can be approximated, with good agreement. This technique will be discussed further in Section 4.2.3. More recently, independent results for the impedance of a microstrip dipole in an infinite array have been reported [36,37] and the results are in good agreement with results calculated here.

In addition to comparisons to other computed results, several array configurations were tested in a waveguide simulator. These experimental results are the subject of Section 4.2.2. First, the effects of the various parameters that must be chosen are discussed in the next section.

4.2.1 Convergence and the effect of various parameters

All of the results in this section are for an array on a square lattice, with $S_1 = S_2 = 0.6\lambda_0$, $t = 0.15\lambda_0$, $\epsilon_r = 2.55$, and $b = 0.35\lambda_0$. The dipole width varied throughout. In addition, in all of the cases in this section no beam steering was used ($m_0 = n_0 = 0.0$). The other parameters that must be chosen were discussed in Chapter 4, and are

- (1) n = number of basis function
- (2) L = level of acceleration (0,1,3 or 5)
- (3) u = constant used in asymptotic expansion
- (4) I_{\max} = upper limit on partial sums which used adaptive numerical quadratures to evaluate integrals in spatial sum
- (5) relerr = relative error for adaptive numerical quadratures
- (6) tol = tolerance on spectral and spatial sums

The convergence of the impedance of an element in this array as a function of the number of basis functions is shown in Figures 4.3a and 4.3b. Three different dipoles were considered, with widths $a = 0.002\lambda_0$, $0.02\lambda_0$ and $0.05\lambda_0$. The other parameters were $L = 5$, $u = 0.75\beta_{av}$, $I_{max} = 1$, $relerr = 0.1\%$ and $tol = 0.1\%$. Results for all three cases were computed using method 1, which employs edge modes. The results for the case of $a = 0.002\lambda_0$ are very good using this method, but as the width increases the convergence becomes worse, and for $a = 0.05\lambda_0$ the answer does not converge at all. This is due to the breakdown of the thin-wire approximations, and will be further demonstrated later. The case of $a = 0.05\lambda_0$ was also computed using method 2, which used rooftop basis functions and "exactly" computes the two-dimensional convolution integrals using adaptive numerical quadratures. These results are also included in Figures 4.3a and 4.3b, and show reasonable convergence. Figures 4.3a and 4.3b indicate that method 1 should not be used at all for thicknesses greater than approximately $0.02\lambda_0$. All of the cases computed in Sections 4.2.2 and 4.2.3, however, have a thickness less than $0.02\lambda_0$.

Numerical examples for the effect of n , L , u , I_{max} , $relerr$ and tol are given in Tables 4.1 and 4.2. The results in Table 4.1 were all computed using method 1, and the results in Table 4.2 were obtained using method 2. Table 4.1 is broken into seven groups, with one parameter being varied in each of the first six groups, and various combinations of the parameters comprising the seventh group. The large number of digits shown in these tables is included only for purposes of comparison, and do not imply that the answers are accurate to that many significant digits. The inclusion of this table serves two purposes. First, it should serve as a

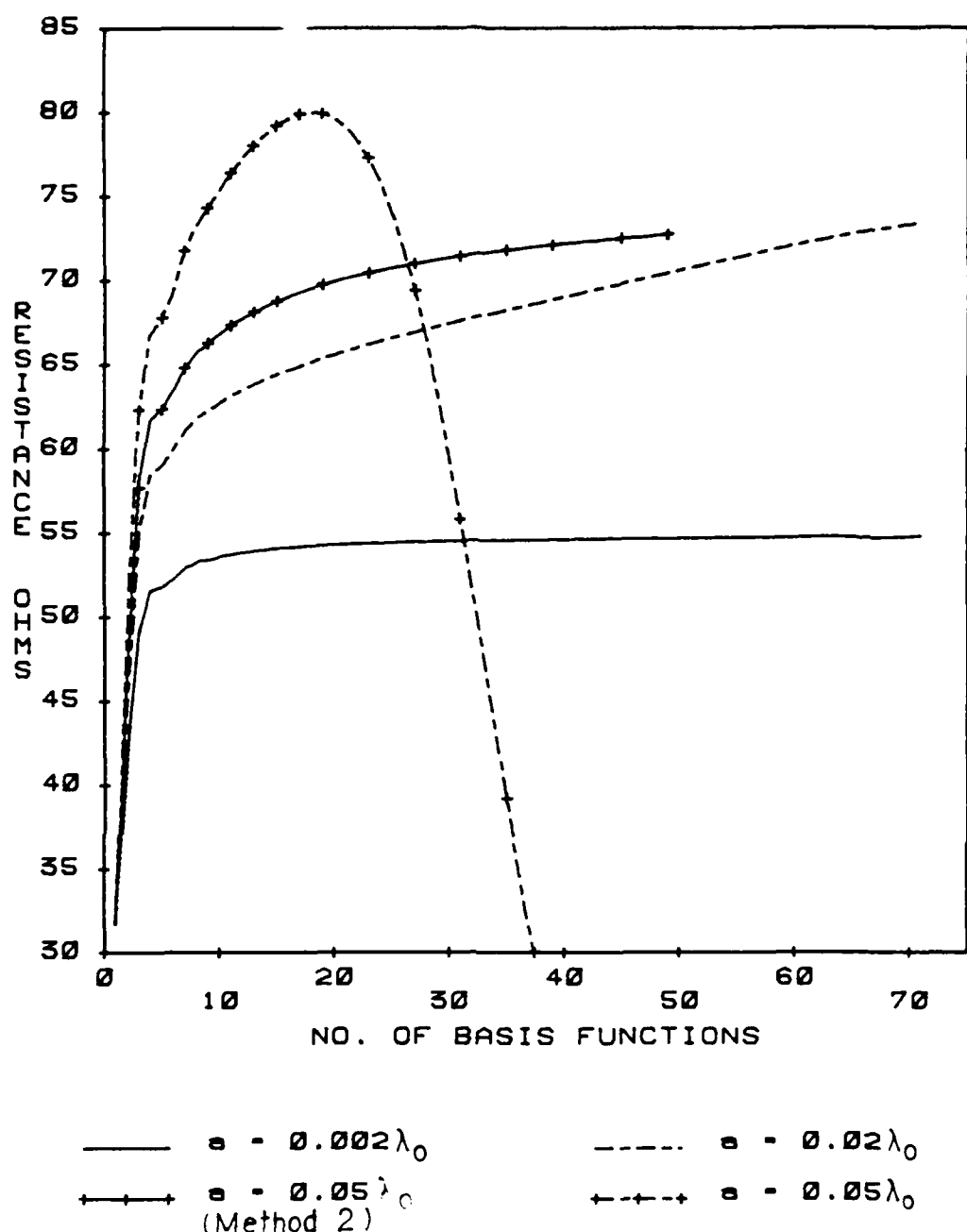


Figure 4.3a. Convergence of the input resistance of a microstrip dipole in an infinite array. Square lattice, $S_1 = S_2 = 0.6 \lambda_0$, $t = 0.15$, λ_0 , $\epsilon_r = 2.55$, $b = 0.35 \lambda_0$.

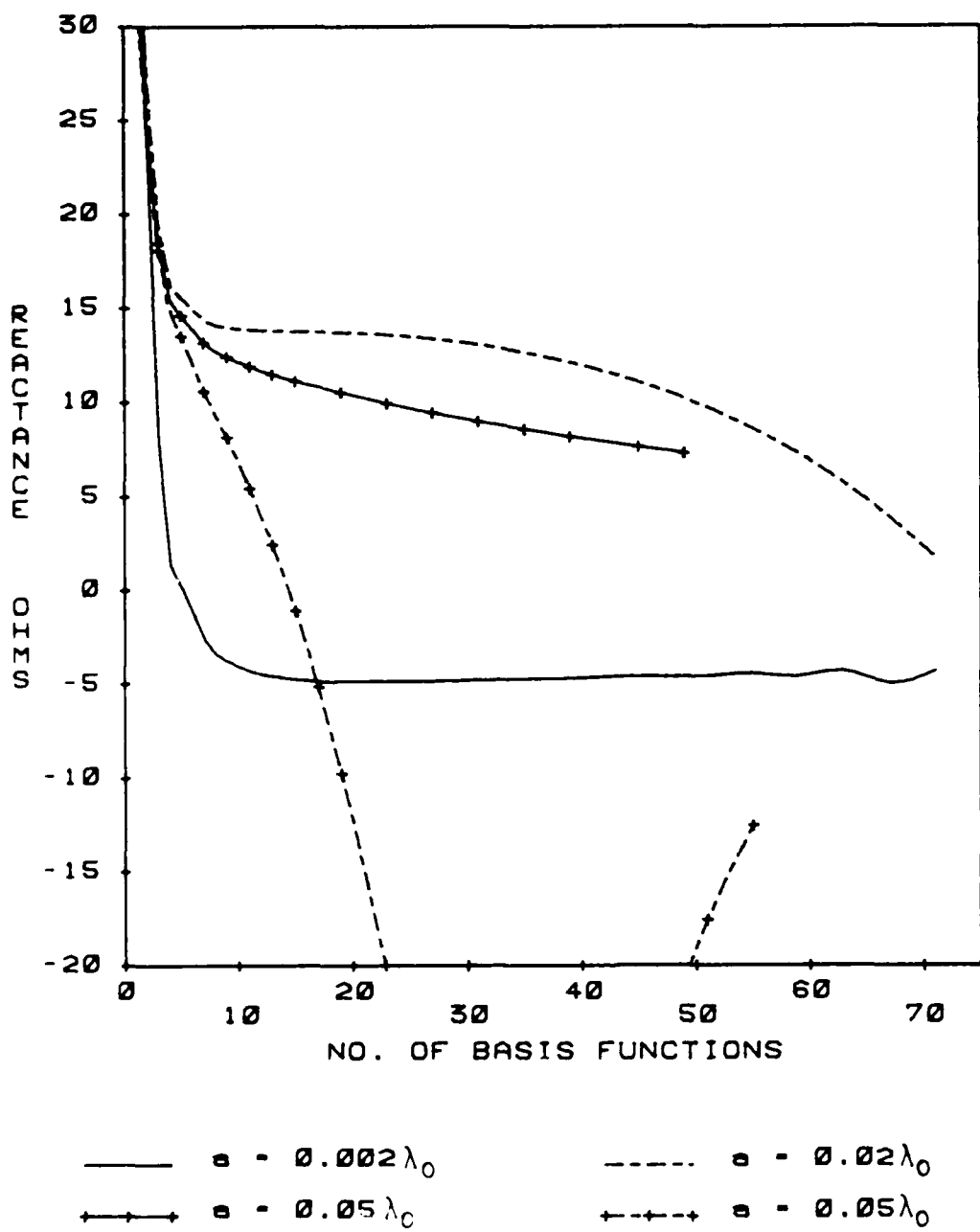


Figure 4.3b. Convergence of the input reactance of a microstrip dipole in an infinite array. Square lattice, $S_1 = S_2 = 0.6 \lambda_0$, $t = 0.15 \lambda_0$, $\epsilon_r = 2.55$, $b = 0.35 \lambda_0$.

TABLE 4.1

THE EFFECT OF VARIOUS PARAMETERS ON THE INPUT IMPEDANCE OF A DIPOLE
IN AN INFINITE ARRAY. (METHOD 1: EDGE MODES)

$\text{LENGTH} = 0.35 \lambda_0$, $\text{WIDTH} = 0.002 \lambda_0$, SQUARE LATTICE , $S_1 = S_2 = 0.6 \lambda_0$, $t = 0.15 \lambda_0$, $\epsilon_r = 2.55$								
n	L	$u(\beta_{av})$	I_{\max}	RELEERR	TOL	R (ohms)	jX (ohms)	TIME (sec.)
11	5	0.75	1	0.001	0.00001	53.709	-4.294	0.62
11	3	0.75	1	0.001	0.00001	53.703	-4.358	1.03
11	1	0.75	1	0.001	0.00001	53.708	-4.306	1.65
11	5	1.25	1	0.001	0.00001	53.709	-4.300	0.69
11	5	1.00	1	0.001	0.00001	53.709	-4.297	0.63
11	5	0.75	1	0.001	0.00001	53.709	-4.294	0.62
11	5	0.50	1	0.001	0.00001	53.706	-4.323	0.77
11	5	0.25	1	0.001	0.00001	53.686	-4.489	1.45
11	5	0.75	2	0.001	0.00001	53.709	-4.294	0.82
11	5	0.75	1	0.001	0.00001	53.709	-4.294	0.62
11	5	0.75	0	0.001	0.00001	53.705	-4.322	0.47
11	5	0.75	1	0.0001	0.00001	53.709	-4.295	0.64
11	5	0.75	1	0.001	0.00001	53.709	-4.294	0.62
11	5	0.75	1	0.01	0.00001	53.709	-4.293	0.59
11	5	0.75	1	0.1	0.00001	53.711	-4.278	0.56
11	5	0.75	1	0.001	0.000001	53.707	-4.309	0.84
11	5	0.75	1	0.001	0.00001	53.709	-4.294	0.62
11	5	0.75	1	0.001	0.0001	53.708	-4.308	0.46
11	5	0.75	1	0.001	0.001	53.692	-4.461	0.38
11	5	0.75	1	0.001	0.01	53.680	-4.568	0.32
17	5	0.75	1	0.001	0.0001	54.158	-4.859	0.71
15	5	0.75	1	0.001	0.0001	54.056	-4.746	0.63
13	5	0.75	1	0.001	0.0001	53.912	-4.595	0.56
11	5	0.75	1	0.001	0.0001	53.708	-4.308	0.46
9	5	0.75	1	0.001	0.0001	53.394	-3.750	0.38
7	5	0.75	1	0.001	0.0001	52.861	-2.573	0.30
5	5	0.75	1	0.001	0.0001	51.784	-0.177	0.21
11	5	0.75	1	0.01	0.001	53.692	-4.459	0.35
11	5	0.75	0	0.01	0.001	53.686	-4.503	0.26
11	5	0.75	1	0.01	0.01	53.680	-4.566	0.30
11	5	0.75	0	0.01	0.01	53.674	-4.610	0.19
9	5	0.75	1	0.01	0.01	53.362	-4.054	0.26
9	5	0.75	0	0.01	0.01	53.354	-4.116	0.16
11	5	0.75	0	0.01	0.01	53.674	-4.610	0.19
7	5	0.75	0	0.01	0.01	52.820	-2.946	0.13
5	5	0.75	0	0.01	0.01	51.737	-0.270	0.09

TABLE 4.2

THE EFFECT OF VARIOUS PARAMETERS ON THE INPUT IMPEDANCE OF A DIPOLE
IN AN INFINITE ARRAY. (METHOD 2: ROOFTOP FUNCTIONS)

$\text{LENGTH} = 0.35 \lambda_0$, $\text{WIDTH} = 0.002 \lambda_0$, SQUARE LATTICE , $s_1 = s_2 = 0.6 \lambda_0$, $t = 0.15 \lambda_0$, $\epsilon_r = 2.55$								
n	L	$u(\beta_{av})$	I_{\max}	RELERR	TOL	R (ohms)	jX (ohms)	TIME (sec.)
11	5	0.75	1	0.001	0.001	53.189	-7.372	3.25
11	5	0.75	0	0.001	0.001	53.184	-7.415	2.67
11	5	0.75	0	0.001	0.01	53.173	-7.521	2.61
11	5	0.75	0	0.01	0.01	53.173	-7.503	1.51
11	5	0.75	0	0.1	0.01	53.173	-7.526	0.62

general guide to the proper choice of the various parameters and indicate that the choice of any of the parameters is not critical. Second, it points out that, while the choice of the parameters is not critical, proper selection can significantly increase execution times without sacrificing significant accuracy. For example, case three in group one used parameters conservatively chosen in order to give high accuracy. For the same array used above, this choice of the parameters gave a result of $Z = 53.708 - j4.306$ ohms, and required 1.65 seconds of execution time using 11 basis functions. (All execution times are for a CDC 6600, approximately 10 times faster than a Vax 11-780.) Conversely, case four in group seven used parameters chosen to given rapid execution time, and gave the result $Z = 53.674 - j4.61$ ohms in only 0.19 second. This is a significant improvement in execution time, and yet the error in magnitude is only 0.016 percent. For a typical array, the data in Table 4.1 indicate that reasonable choices of the parameters would be $L = 5$, $u = 0.75$, β_{av} , $I_{max} = 0$, $relerr = 1\%$ and $tol = 1\%$. In general, more conservative choices were made for the results in this chapter, but for most applications these choices would give a good combination of accuracy and efficiency.

Similar results using method 2 are given in Table 4.2. Because of the similarity of the results, only a few examples are given. Of particular interest are the execution times. Even the fastest case in Table 4.2 required 0.62 second, as compared to 0.19 second for a reasonable choice of the parameters using method 1. While this is approximately a factor of three savings due to the use of the thin-wire approximations, the improvement is not as great as would have been obtained by the same approximations using a spatial domain

element-by-element approach. This is due to the fact that with the approach used here approximately half of the execution time is required to compute the less rapidly convergent spectral sum, which is unaffected by the thin-wire approximations.

It is also interesting to examine the results for the same array as computed without using any acceleration to compute the inner products ($L = 0$). This allows a direct comparison between the method used here and the more standard approach. As discussed in Chapters 3 and 4, when computing the elements of the Z matrix, the upper limit on the infinite sums must be chosen appropriately. Due to the rapid convergence obtained by using the acceleration technique, an adaptive routine discussed in Chapter 4 can be used. However, without any acceleration, most authors simply choose a suitable upper limit which gives satisfactory convergence. For dipole arrays with approximately half-wave spacing, an upper limit of $m = n = 60$ has been used by Pozar and Schaubert [36] with sinusoidal basis functions, which have approximately the same convergence properties as a function of m and n as the rooftop functions of method 2.

Results for the impedance of an element in the array using method 1 with no acceleration are shown in Table 4.3. The accelerated result was obtained with $L = 5$, and is taken from Table 4.1. It is seen that as the upper limits on m and n , denoted M and N , are increased the results approach the accelerated result. Because the unaccelerated results are computed entirely in the spectral domain, this agreement tends to verify the validity of the approximation made in Chapter 3 to improve the efficiency of the evaluation of the vector potential term in the spatial sum. However, even at $M = N = 90$ the unaccelerated result is still changing.

TABLE 4.3

CONVERGENCE FOR UNACCELERATED COMPUTATION
OF INNER PRODUCTS
(METHOD 1: EDGE MODES)

ACCELERATED RESULT: 53.709 - j 4.294 ohms			
Upper limit on M,N	R (ohms)	jX	cpu time (sec.)
10	64.763	14.857	0.41
20	59.007	10.680	1.40
30	57.186	7.450	2.99
40	56.118	4.933	5.13
50	55.497	3.055	8.03
60	55.032	1.510	11.34
70	54.705	0.264	15.71
90	54.246	-1.669	25.23

If one uses $M = N = 60$, the unaccelerated result requires approximately 11 seconds, or approximately 1 second per basis function, as compared to 0.19 second or 0.016 second per basis function for the accelerated method, using parameters chosen for rapid convergence. While the accuracy obtained using $M = N = 60$ for the unaccelerated technique is perhaps not as good as obtained with the accelerated result, it should be pointed out that, because of limitations in the model and the effect of changing the number of basis functions, the accuracy is probably satisfactory. However, the savings in computer time obtained with the acceleration method can become very significant if either large amounts of data are needed, or complex structures are to be analyzed.

Similar results are shown in Table 4.4 for the same array using rooftop basis functions. Again, as M and N are increased, the results approach the accelerated result, taken from Table 4.2. For this case, if $M = N = 60$ is chosen as the upper limit on the summations, the savings in computer time is roughly a factor of 20 by using the acceleration technique. This savings can become very important when analyzing arrays of patches considered in Chapter 5, where hundreds of elements of the Z matrix must be computed.

The final set of results in this section further demonstrates the range of validity of the thin-wire approximation. The same array configuration used in the previous examples was used, with the other parameters chosen as $n = 9$, $L = 5$, $u = 0.75 \beta_{av}$, $I_{max} = 1$, $relerr = 0.1\%$ and $tol = 0.1\%$. First, Figures 4.4-4.7 show the calculated transverse current distribution across the center of the dipole, treating the dipoles as scatterers rather than as an antenna. In this case, the dipole had no

TABLE 4.4

CONVERGENCE FOR UNACCELERATED COMPUTATION
OF INNER PRODUCTS
(METHOD 2: ROOFTOP FUNCTIONS)

ACCELERATED RESULT: 53.184 - j7.415 ohms			
Upper limit on M,N	R (ohms)	jX	cpu time (sec.)
10	64.281	13.737	0.39
20	58.636	9.122	1.31
30	56.829	5.579	2.95
40	55.770	2.856	5.10
50	55.148	0.790	7.85
60	54.682	-0.908	11.27
70	54.350	-2.310	15.27
90	53.876	-4.521	24.98

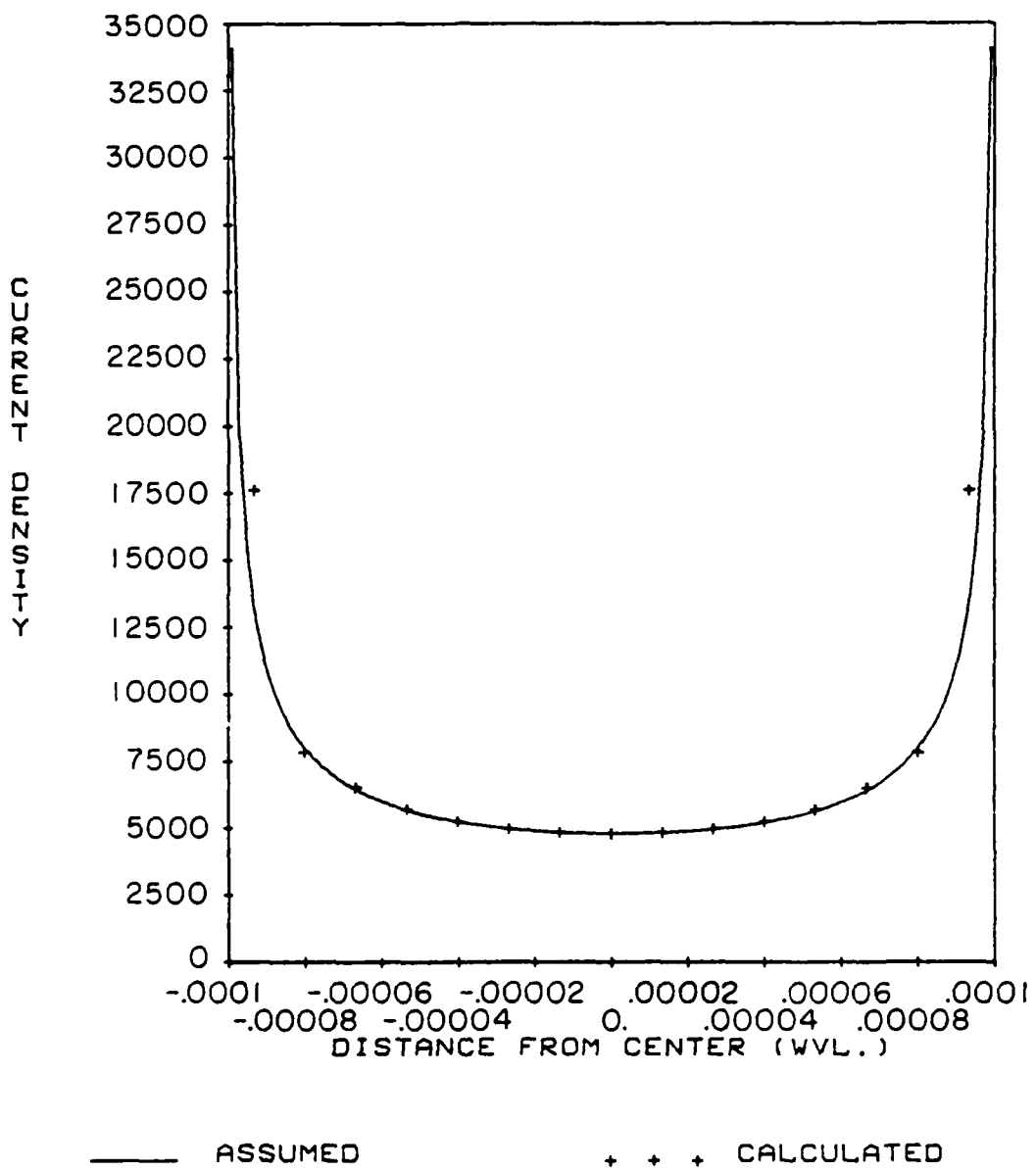


Figure 4.4. Transverse current distribution on a $0.35 \lambda_0$ dipole with $a = 0.0002 \lambda_0$.

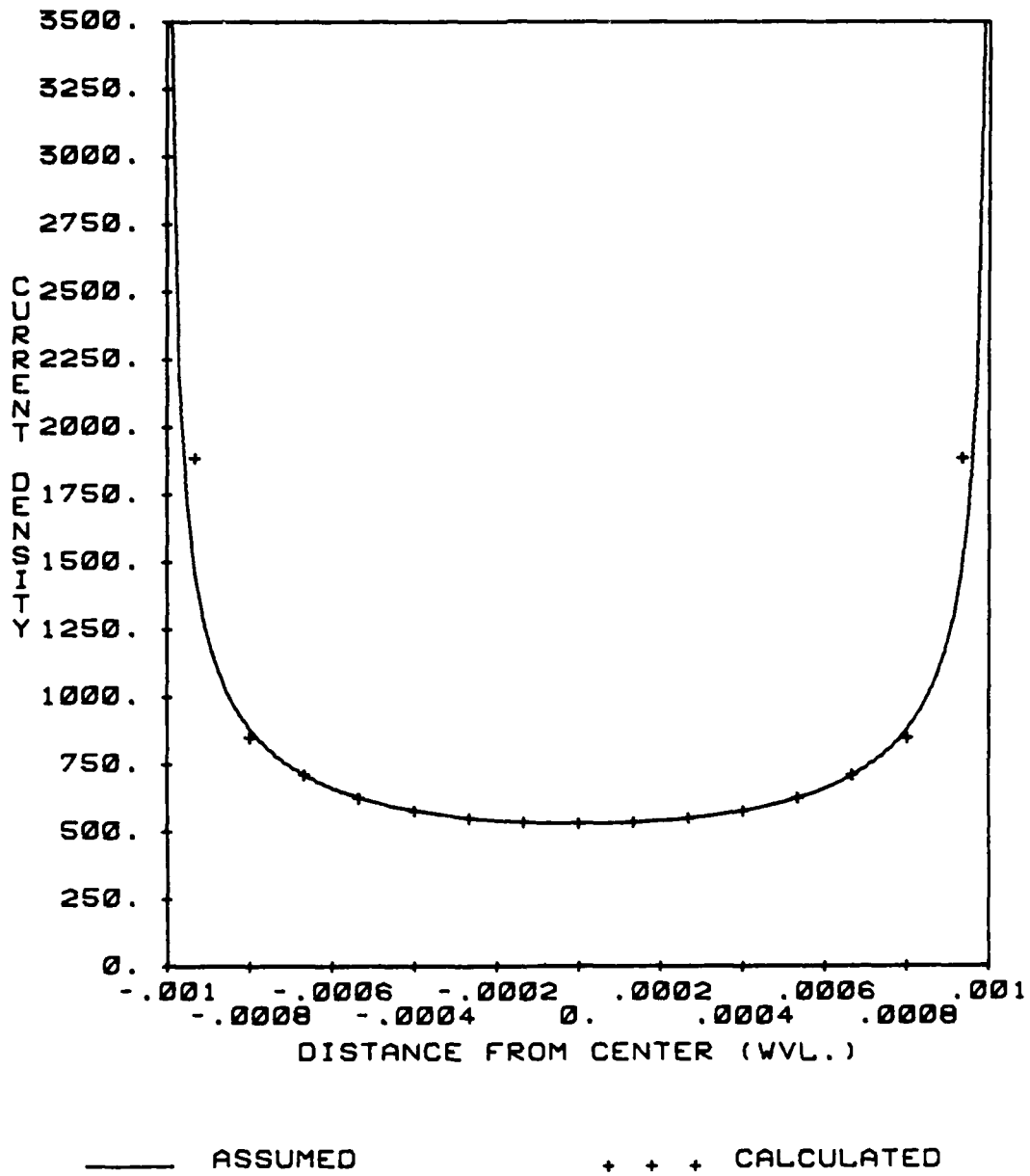


Figure 4.5. Transverse current distribution on a $0.35 \lambda_0$ dipole with $a = 0.002 \lambda_0$.

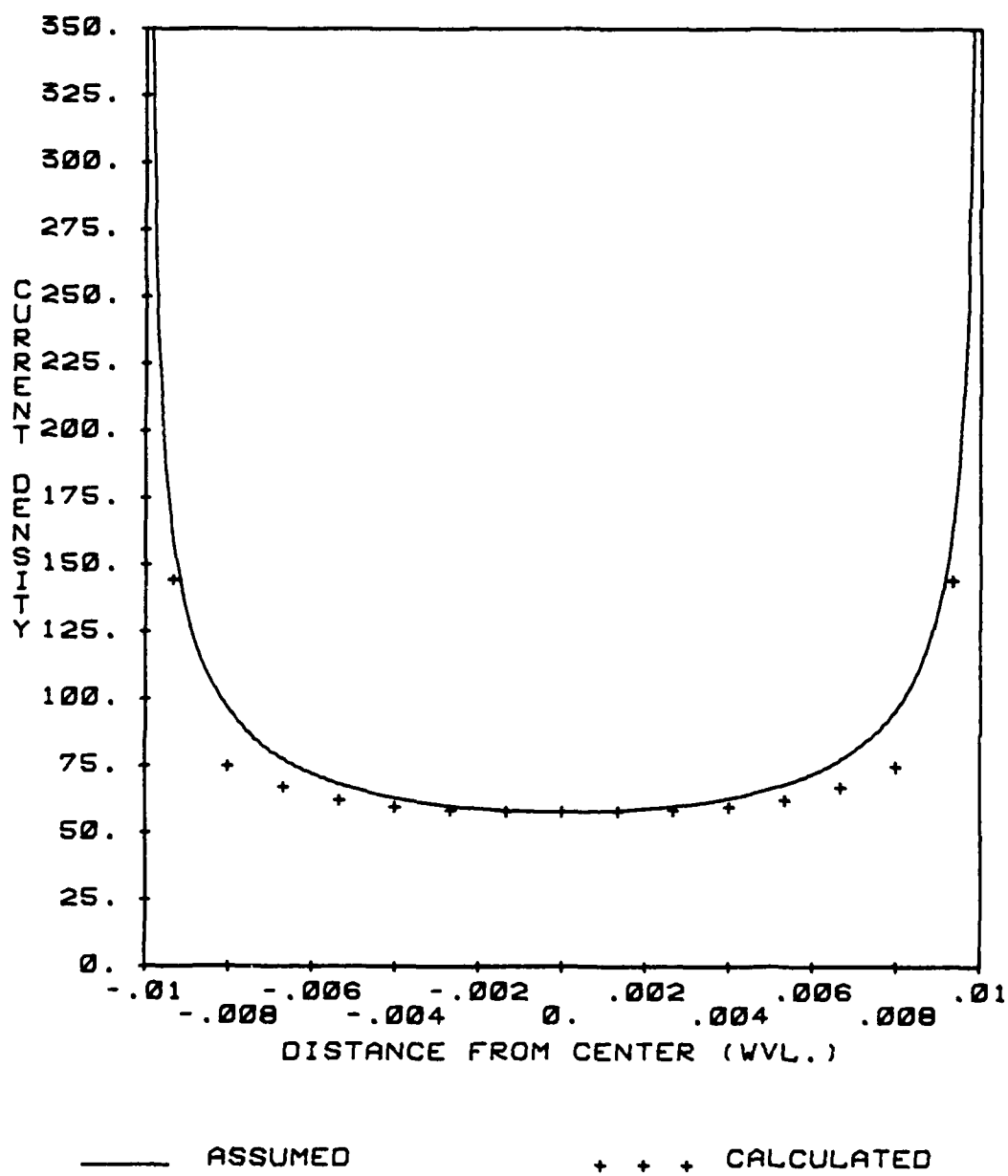


Figure 4.6. Transverse current distribution on a $0.35 \lambda_0$ dipole with $a = 0.02 \lambda_0$.

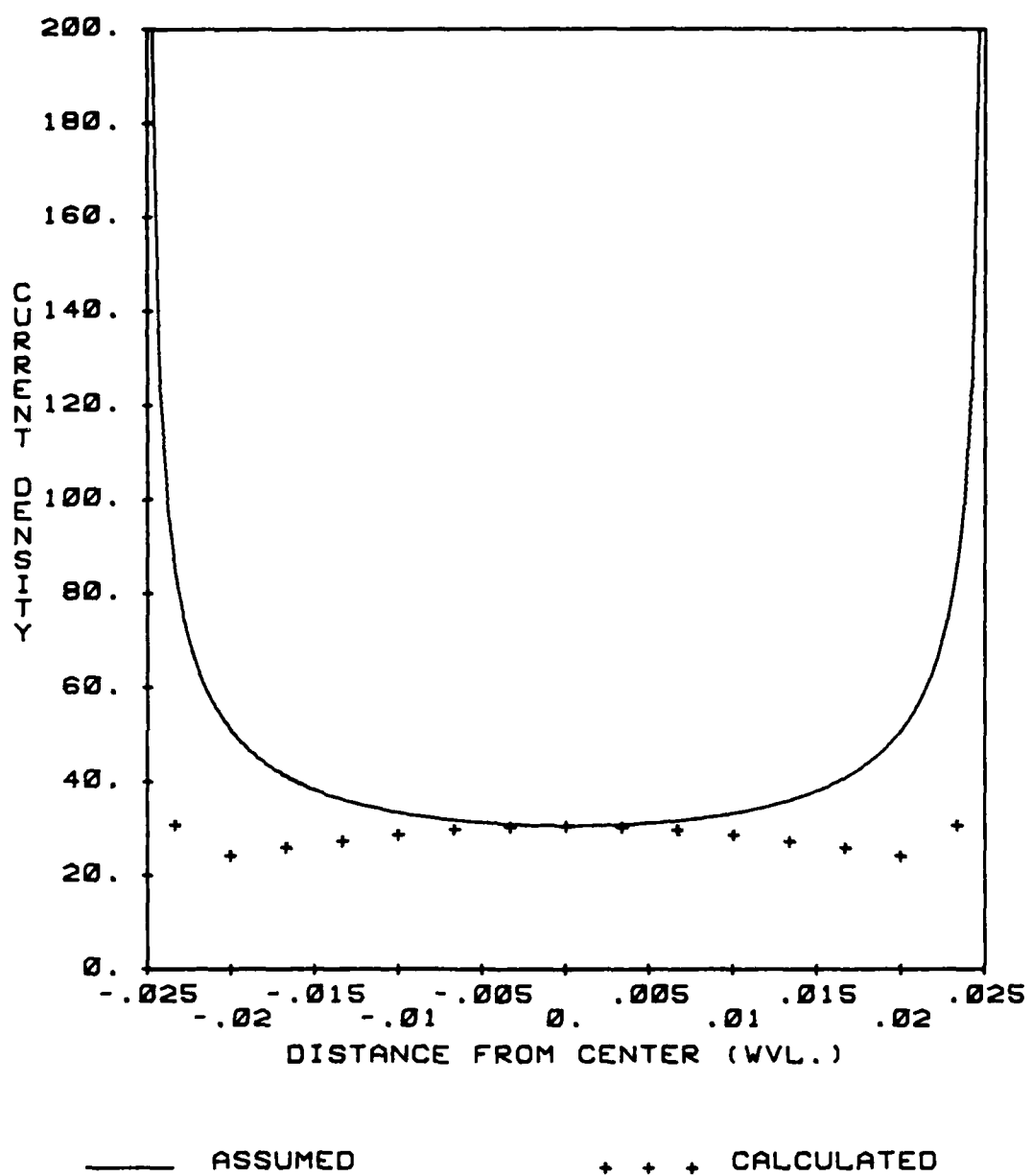


Figure 4.7. Transverse current distribution on a $0.35 \lambda_0$ dipole with $a = 0.05 \lambda_0$.

center gap, and the excitation was a normally incident plane wave, \hat{y} polarized and normalized to give a magnitude of n volts/ λ_0 at the array plane, where n is the intrinsic impedance of free space. Using method 2, the current was computed using 15 basis functions in the transverse direction, for a total of 135 \hat{y} oriented basis functions. As in all cases in this chapter, no \hat{x} oriented basis functions were used. The results are compared to the assumed current distributions for the edge modes, given by Equation (4.1-3). For ease of comparison the assumed value has been normalized to be equal to the computed value in the center of the strip. For $a = 0.0002 \lambda_0$ and $0.002 \lambda_0$, the agreement between the assumed and computed current distributions is very good. For $a = 0.02 \lambda_0$ the agreement worsens, and when $a = 0.05 \lambda_0$, there is a large discrepancy. Of course, this disagreement indicates that the assumed current distribution necessary to use the thin-wire approximations is not valid, and will not lead to correct results, which is consistent with the data in Figures 4.3a and 4.3b.

Finally, methods 1 and 2 are compared in Table 4.5. In this table the impedance of the same array is computed by method 2 for different values of width and for increasing numbers of rooftop functions in the \hat{x} direction. The answers are compared to the results using method 1, with a single edge mode in the \hat{x} direction. As would be expected from the above discussion, as the number of transverse basis functions is increased the results from method 1 approach the result using the edge mode for $a = 0.0002 \lambda_0$ and $a = 0.002 \lambda_0$. However, for the wider strips, where the correct current distribution departs from the assumed edge mode, the agreement is poorer. In addition, it is also evident from these results that unless high accuracy is needed for wide strips, there is no

TABLE 4.5

COMPARISON OF ROOFTOP BASIS FUNCTION SOLUTION TO RESULT
FROM METHOD 1 FOR DIFFERENT WIDTH STRIPS (IMPEDANCE IN OHMS)

(N = 9, L = 5, u = 0.75 β_{av} , $I_{max} = 1$, RELERR = 0.001, TOLERR = 0.001)						
n	a = 0.0002 λ_o	a = 0.002 λ_o	a = 0.02 λ_o	a = 0.05 λ_o		
1	50.826 -j27.617	52.891 -j6.768	59.462 j11.653	66.247 j12.325		
3	50.937 -j25.899	52.164 -j5.055	60.234 j12.057	66.773 j10.466		
5	50.966 -j25.474	53.233 -j4.661	60.450 j12.150	67.035 j10.067		
7	50.978 -j25.291	53.264 -j4.476	60.544 j12.172	67.157 j9.877		
9	50.985 -j25.190	53.281 -j4.385	60.604 j12.205	67.228 j9.766		
11	50.990 -j25.125	53.293 -j4.315	60.643 j12.226	67.274 j9.693		
13	- -	53.300 -j4.276	- -	- -		
one edge mode	51.013 -j24.792	53.375 -j3.930	62.228 j13.943	74.274 j8.074		

point in using more than one basis function in the transverse direction. Even in that case, the limitations of the model make the improved accuracy questionable for such a wide strip. In addition these results point out that, aside from slightly better accuracy for very narrow strips, the advantage of using the edge mode is in the improved efficiency.

4.2.2 Experimental verification

In order to further confirm the results of the moment method solution, several array configurations were tested in a waveguide simulator. The theory of the waveguide simulator has been described by Hannan [69], and will not be discussed in detail here. Briefly, the waveguide simulator concept takes advantage of the null planes that exist in the electric field of an infinite array under certain excitation conditions to allow a section of the array to be enclosed within an infinite waveguide without disturbing the operation of the array. The operation of the simulator is easily understood by considering the superposition of the fields and excitation of the infinite array for two scan angles, $(\theta, \pm\phi)$. By superposition, each element is fed in phase, as are the elements in the waveguide simulator. Two beams are radiated by the array, at $(\theta, \pm\phi)$, simulated by the propagating mode in the waveguide. In these experiments the frequency of operation was chosen such that only the lowest-order TE mode propagated. The scan angle is determined by the effective angle of propagation of this mode in the waveguide.

The basic experimental set-up is shown in Figure 4.8, and a more detailed view of the array fixture is shown in Figure 4.9. The array was scanned in the H-plane by varying the frequency, with the scan angle θ given by

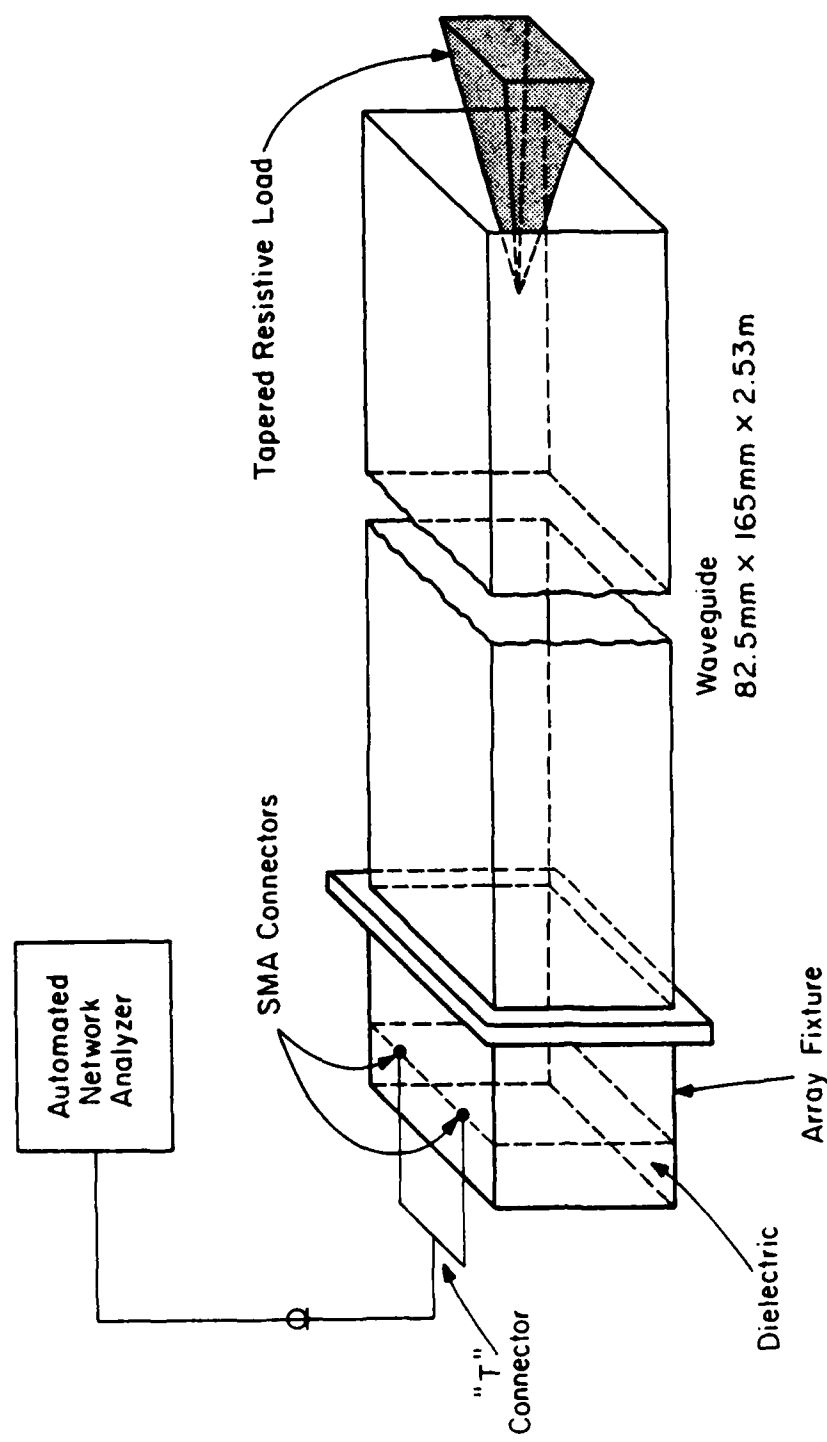


Figure 4.8. Waveguide simulator experimental set-up.

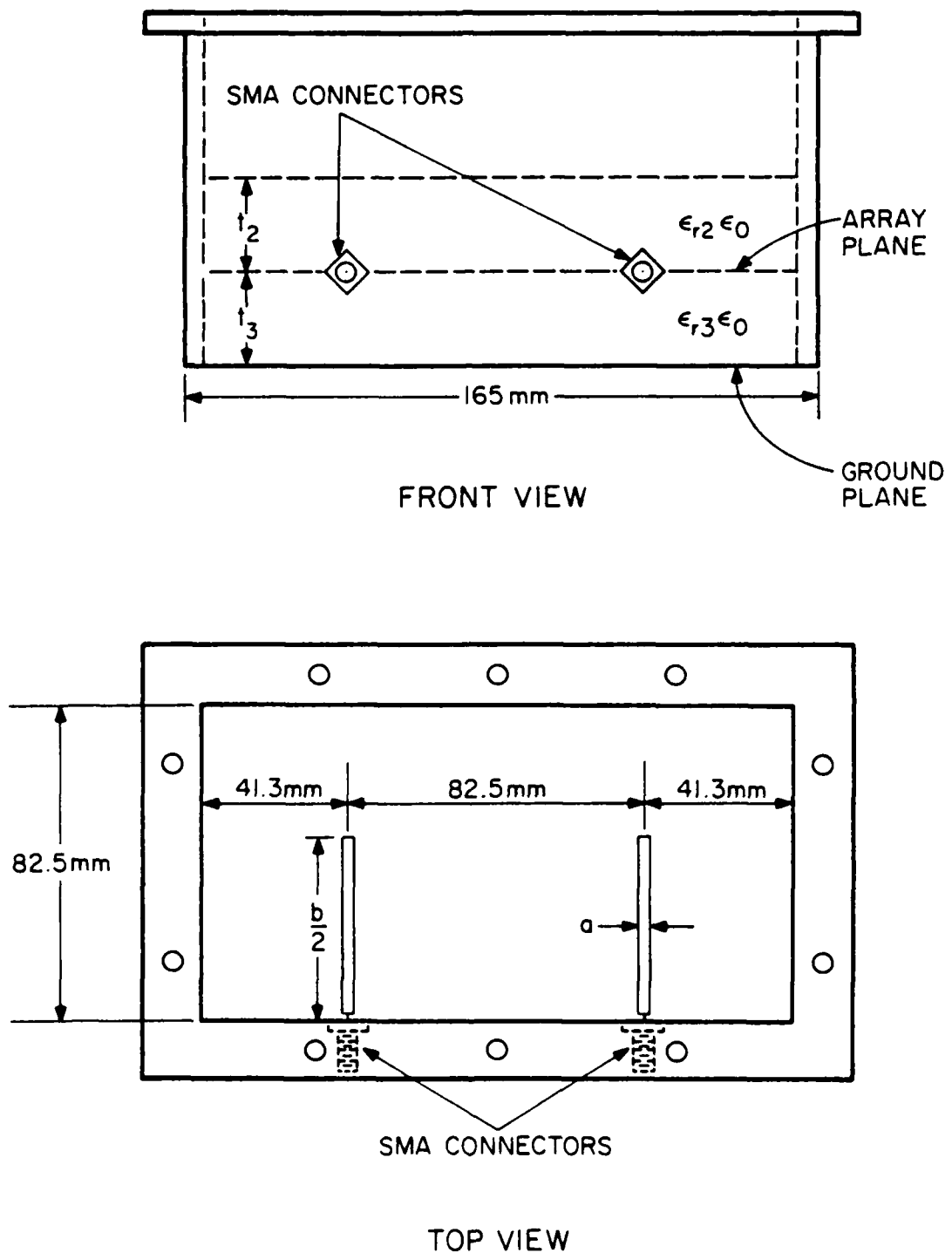


Figure 4.9. Waveguide simulator array fixture.

$$\theta = \sin^{-1} (\lambda_0/2a) \quad (4.2-1)$$

where a is the width of the waveguide in the H-plane, 165 millimeters. In terms of the frequency f , the scan angle is given by

$$\theta = \sin^{-1} (3.0/3.3f) \quad (4.2-2)$$

with f in GHz. The frequency was varied from 0.92 GHz, just above the cutoff frequency, to 1.7 GHz, somewhat below the onset of the next propagating mode. The scan angle ranged from 81.2° at $f = 0.92$ GHz to 32.3° at $f = 1.7$ GHz. Two microstrip monopoles were fed through the waveguide wall using SMA connectors. From image theory, the impedance of each monopole is one half the impedance of the corresponding dipole. The elements were fed in phase and with equal amplitude by using a simple T connector. The balance of the T was tested and was found to be good. In order to simplify the construction of the array section and the array fixture, a very large cross-section waveguide was used. Unfortunately, a matched termination was not available, so a tapered resistive load was used as a termination. The load was placed in the waveguide and adjusted for the best match. However, the remaining mismatch caused fluctuations in the measured data, and was one source of error. Other sources of error included the fitness of the dielectric substrate, losses in the waveguide walls and substrate, and the inability to calibrate the network analyzer over such a wide frequency range. The reflection coefficient measurement was referenced to the single end of the T connector, and the data were later referenced back to the feed point. To compare to the measured data, the impedance of the corresponding dipole was calculated and divided by two to calculate the reflection coefficient

of the monopole into a 50 ohm system. Although an error estimate based on the above factors was not computed, the presence of blind angles gives one indication of the error due to these factors. At blind angles the theory predicts $|\Gamma| = 1$, as will be discussed in the next section. However, due to the various factors, primarily losses, the measured result does not reach 1. Based on the measured results at these points, the error is indicated to be less than $\pm 20\%$. Because losses are not as significant away from the blind angles, this is believed to be an upper bound on the error due to the above factors.

Five array configurations were tested, with the results shown in Figures 4.10 - 4.14. The first case, shown in Figures 4.10a and 4.10b, compares the measured and computed results for an array on a substrate of styrofoam, with a nominal dielectric constant of 1.03 [70]. The agreement is good both for the magnitude and phase of the reflection coefficient, but one set of results appears to be shifted in frequency somewhat. This could be due to the size of the feed region; in particular, the hole in the waveguide that was used to feed the antenna could have given the monopole a longer effective length. This source of error does not affect Γ at a blind angle and, therefore, is not included in the above error estimate.

Figures 4.11a and 4.11b give results for an array on 1 inch of rexolite, $\epsilon_r = 2.53$. The effect of the load mismatch is clearly seen in the magnitude plot, but again agreement between measured and calculated results is good. Results for an array on a high dielectric constant substrate, $\epsilon_r = 6.0$, are shown in Figures 4.12a and 4.12b. The substrate was HI-K Styrene, with a nominal ϵ_r of 6.0. Again, the general agreement is good, and in particular, the predicted blind angle is seen in the experimental results, with a reduced Γ , as discussed above.

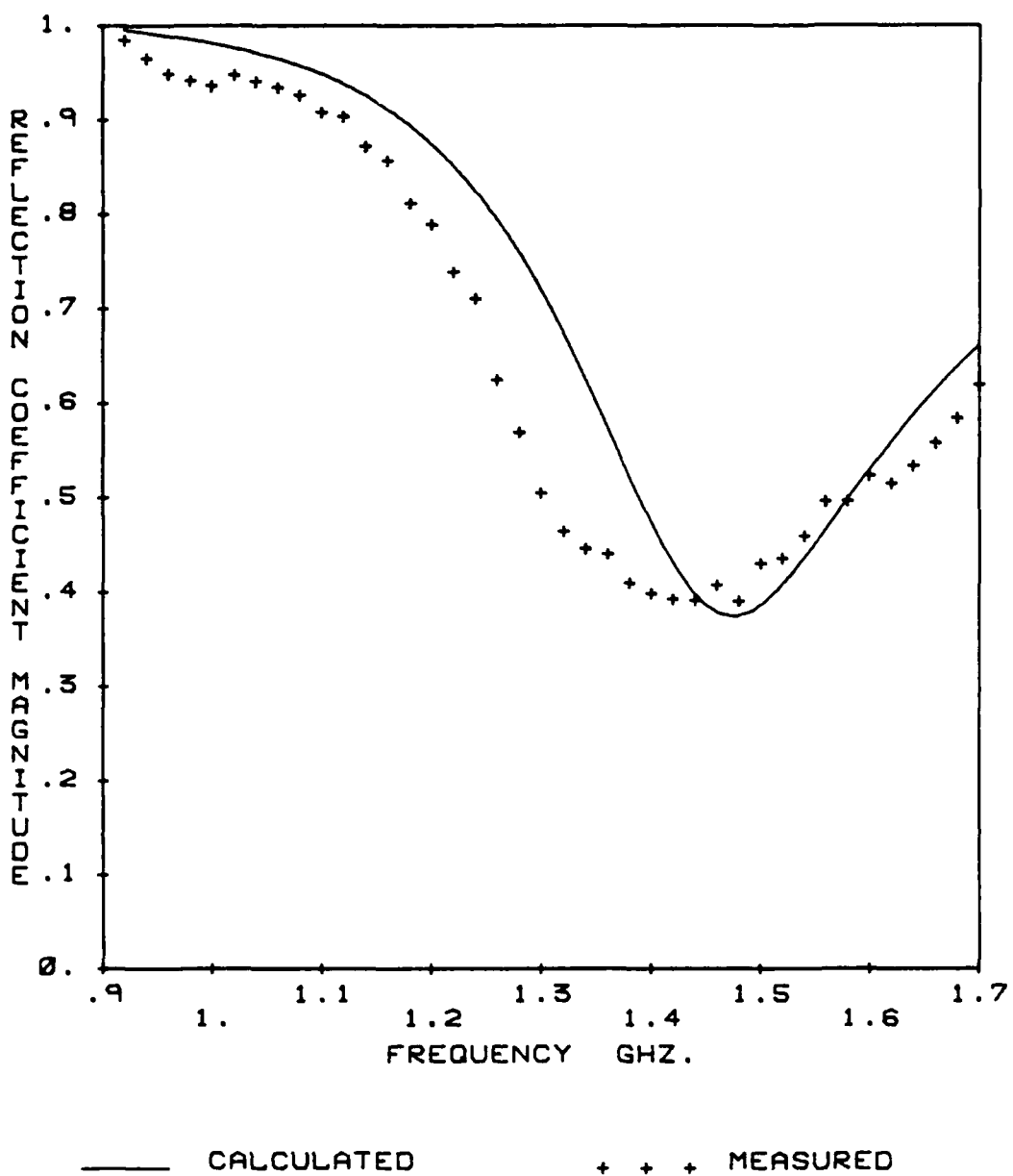


Figure 4.10a. Waveguide simulator results for a dipole array on a single layer substrate $a = 1\text{mm}$, $b = 95\text{mm}$, $t = 25.4\text{mm}$, $\epsilon_r = 1.03$.

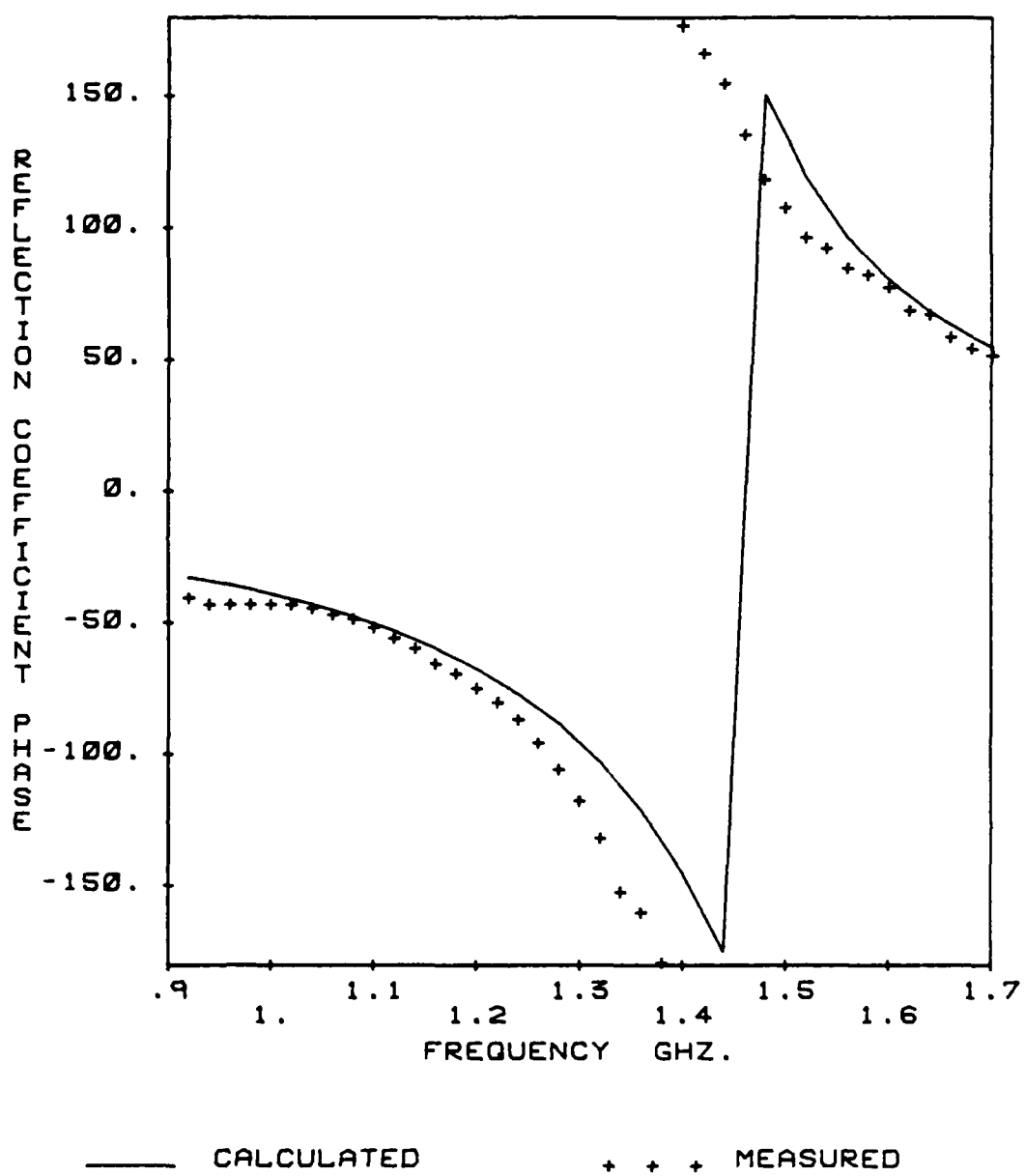


Figure 4.10b. Waveguide simulator results for a dipole array on a single layer substrate $a = 1\text{mm}$, $b = 95\text{mm}$, $t = 25.4\text{mm}$, $\epsilon_r = 1.03$.

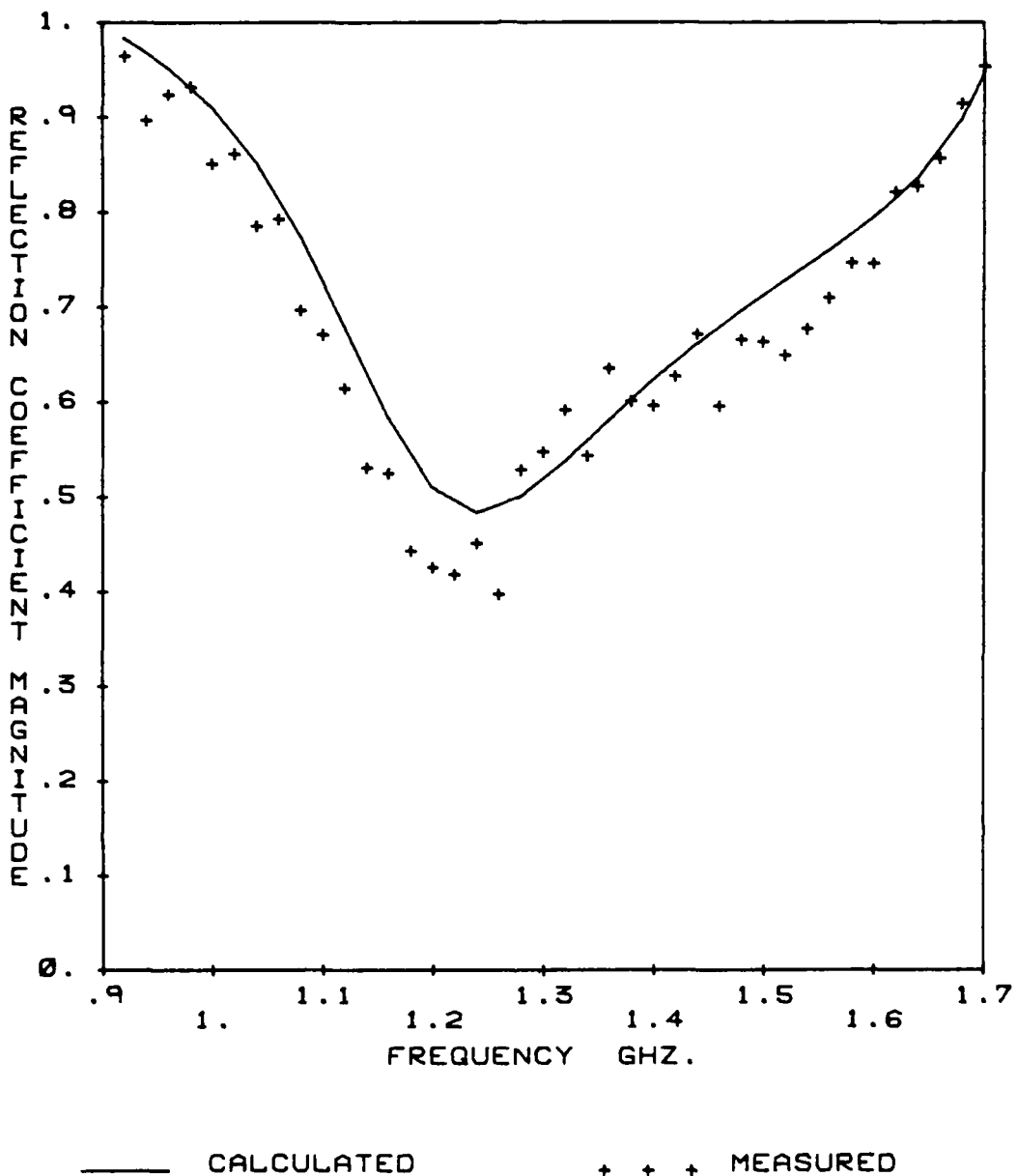


Figure 4.11a. Waveguide simulator results for a dipole array on a single layer substrate $a = 1\text{mm}$, $b = 84\text{mm}$, $t = 25.4\text{mm}$, $\epsilon_r = 2.53$.

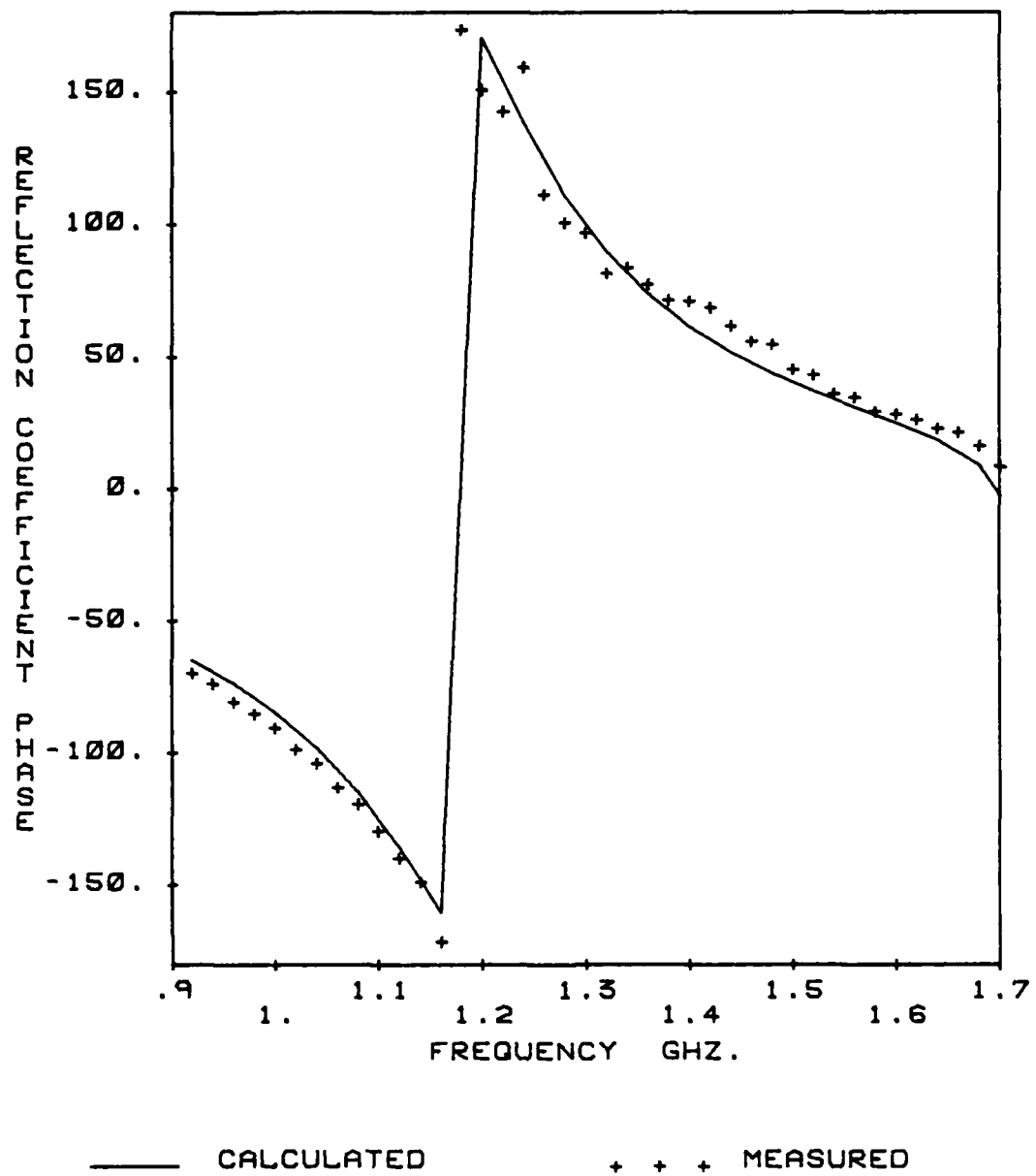


Figure 4.11b. Waveguide simulator results for a dipole array on a single layer substrate $a = 1\text{mm}$, $b = 84\text{mm}$, $t = 25.4\text{mm}$, $\epsilon_r = 2.53$.

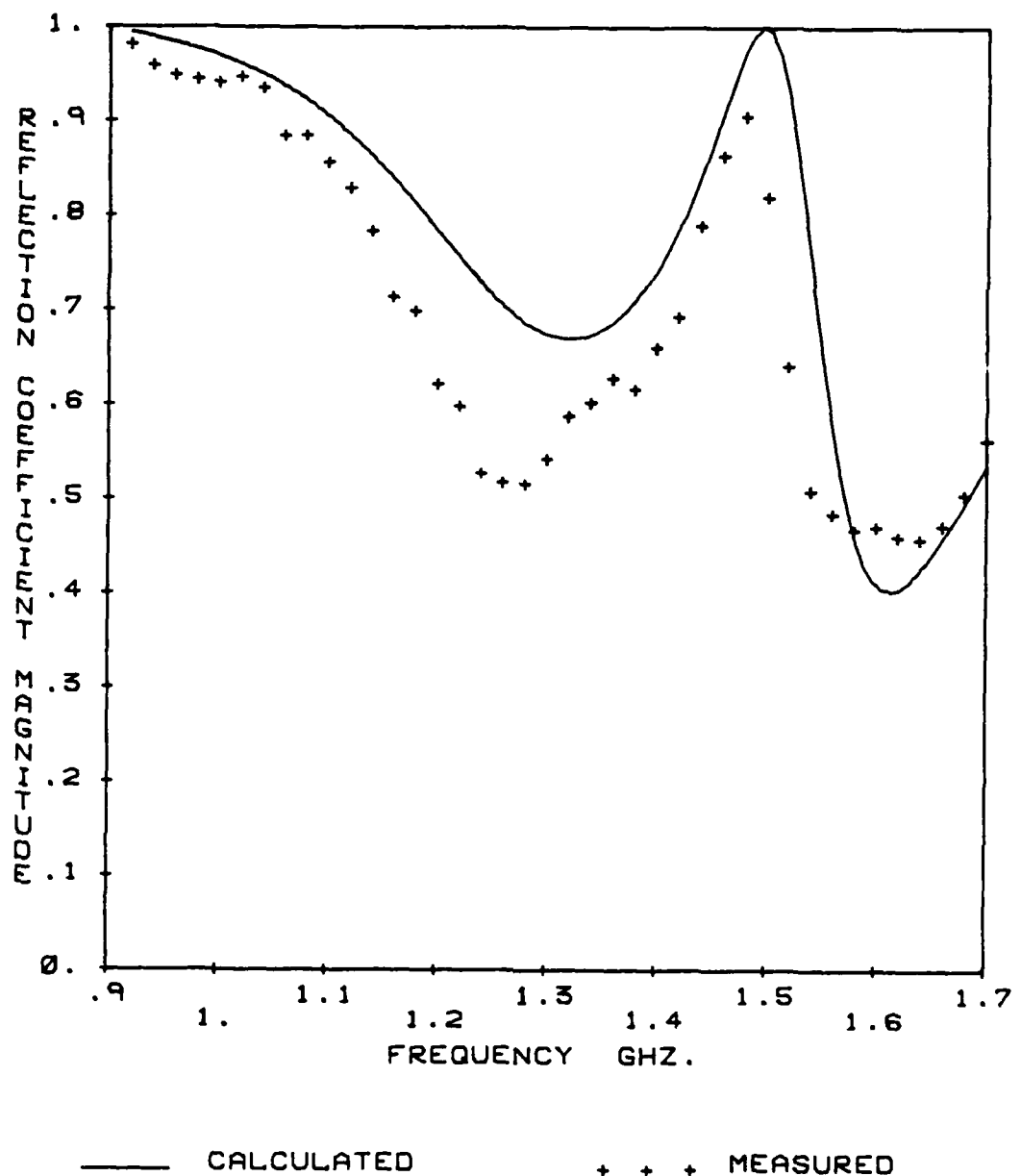


Figure 4.12a. Waveguide simulator results for a dipole array on a single layer substrate $a = 1\text{mm}$, $b = 54\text{mm}$, $t = 19.1\text{mm}$, $\epsilon_r = 6.0$.

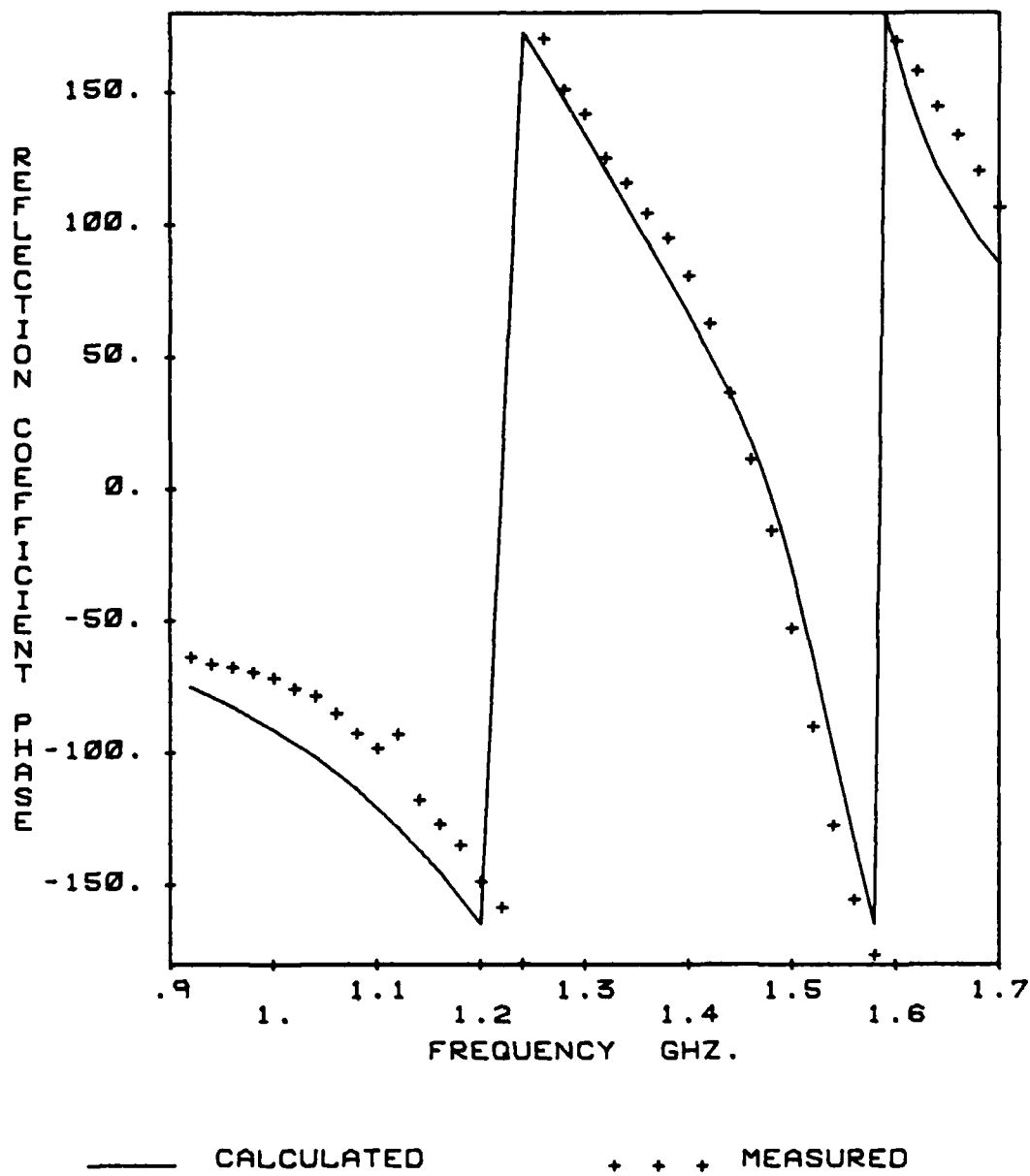


Figure 4.12b. Waveguide simulator results for a dipole array on a single layer substrate $a = 1\text{mm}$, $b = 54\text{mm}$, $t = 19.1\text{mm}$, $\epsilon_r = 6.0$.

Finally, Figures 4.13a through 4.14b present results for two different array configurations - each including a radome. The ability to include a radome is important, not only because of its use in protecting the antenna, but also because it gives the antenna designer an additional degree of freedom in the design of the array. The array considered in Figures 4.13a and 4.13b was built on a 3/4 inch thick substrate with a dielectric constant of 6.0, with a 1 inch thick rexolite radome. Agreement is good, with the predicted blind angle again being seen in the measured data. Again the measured reflection coefficient does not reach 1 at the blind angle. Because the theory predicts a reflection coefficient of one at this point, this is the basis of the $\pm 20\%$ error estimate made earlier. The agreement in the final case in Figures 4.14a and 4.14b is also good.

Overall, the agreement between experimental and theoretical results is quite good, considering the simple construction of the waveguide simulator. These results, along with the agreement with other computed results, indicate that the solution is working as intended, and efficiently predicts the impedance of infinite arrays of microstrip dipoles.

4.2.3. Theoretical results

Having determined the current distribution on the dipole, any of the desired characteristics of the array can be determined to within the accuracy of the model. One of the most important characteristics of a phased array is its impedance or reflection coefficient as a function of scan angle. It has long been known that arrays which can support a slow wave can exhibit nulls at a scan angle closer to broadside than the onset of a grating lobe [13,24]. In infinite arrays, these nulls become blind angles, with a reflection coefficient magnitude of 1. This behavior is

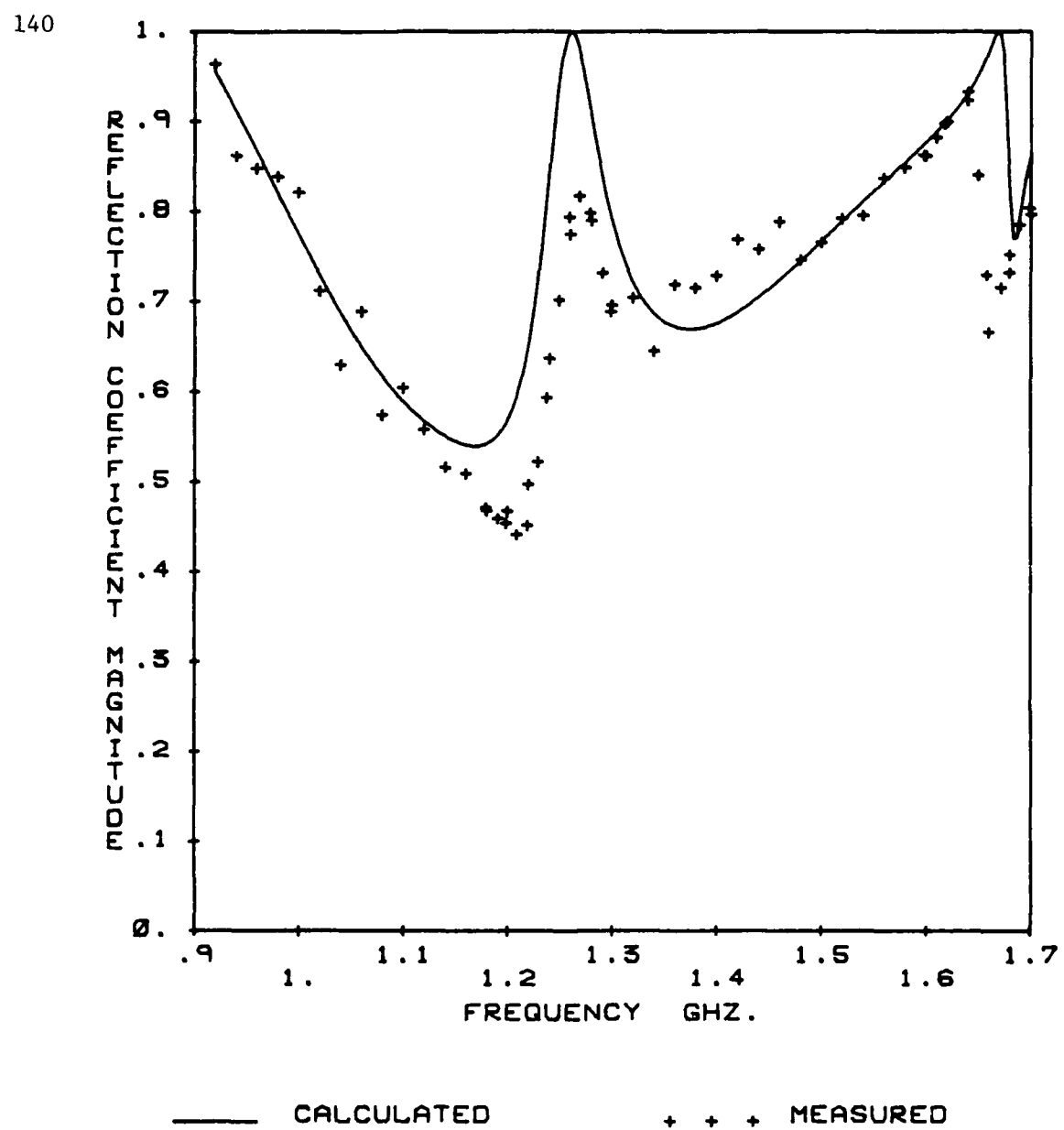


Figure 4.13a. Waveguide simulator results for a dipole array on a multi-layer substrate $a = 1\text{mm}$, $b = 54\text{mm}$, $t_3 = 19.1\text{mm}$, $\epsilon_{r3} = 6.0$, $t_2 = 25.4\text{mm}$, $\epsilon_{r2} = 2.53$.

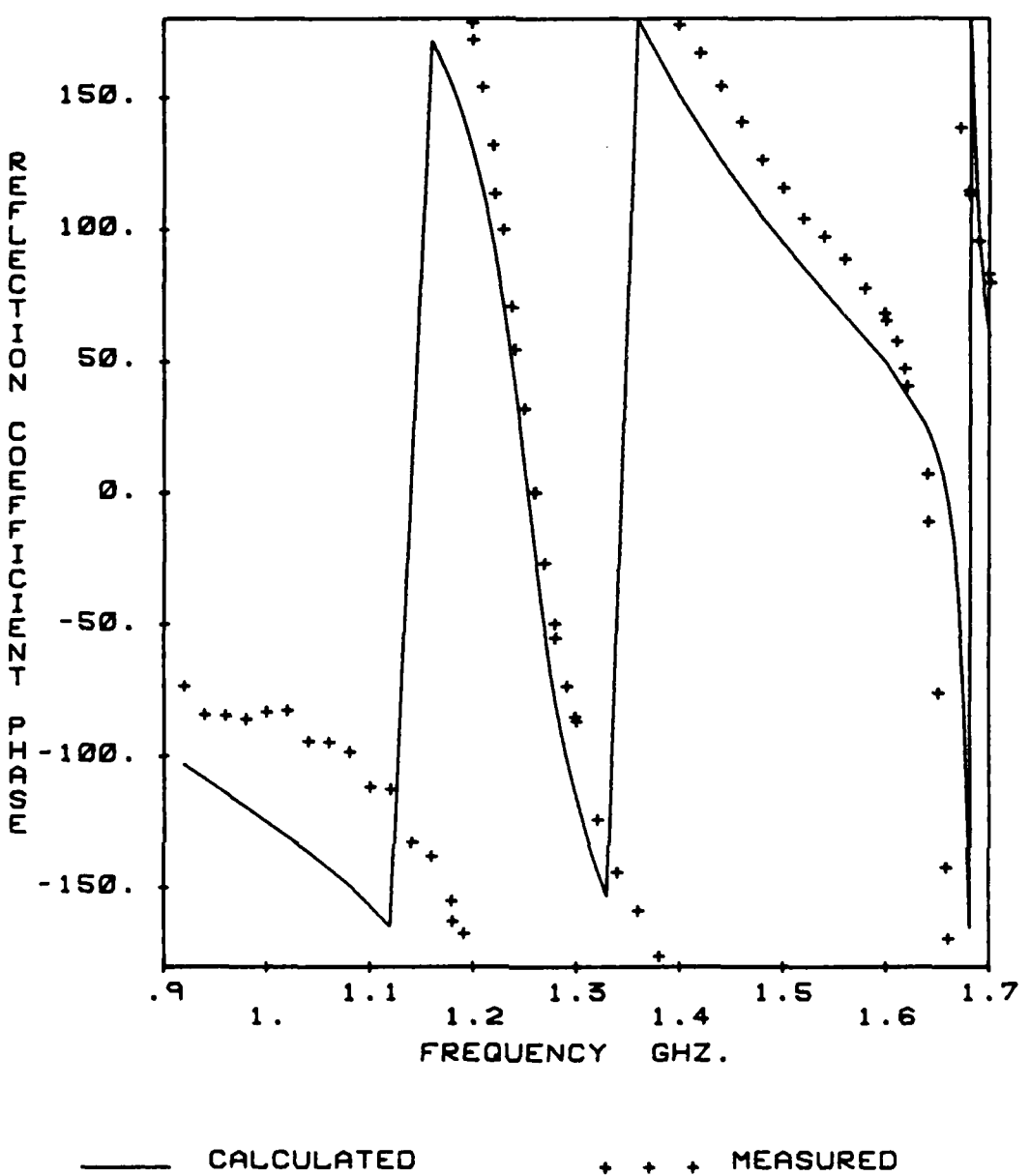


Figure 4.13b. Waveguide simulator results for a dipole array on a multi-layer substrate $a = 1\text{mm}$, $b = 54\text{mm}$, $t_3 = 19.1\text{mm}$, $\epsilon_{r3} = 6.0$, $t_2 = 25.4\text{mm}$, $\epsilon_{r2} = 2.53$.

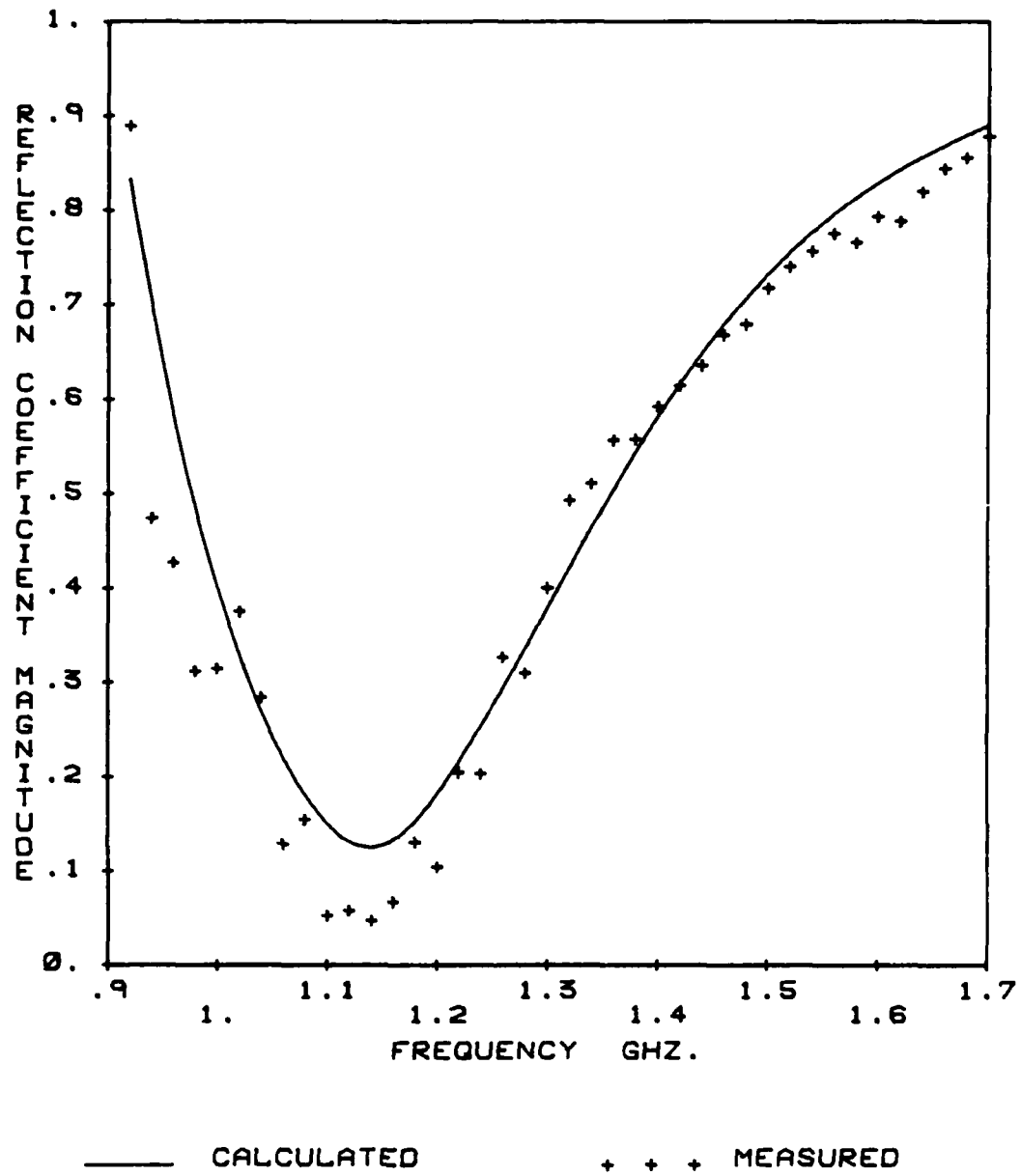


Figure 4.14a. Waveguide simulator results for a dipole array on a multi-layer substrate $a = 1\text{mm}$, $b = 95\text{mm}$, $t_3 = 25.4\text{mm}$, $\epsilon_{r3} = 1.03$, $t_2 = 25.4\text{mm}$, $\epsilon_{r2} = 2.53$.

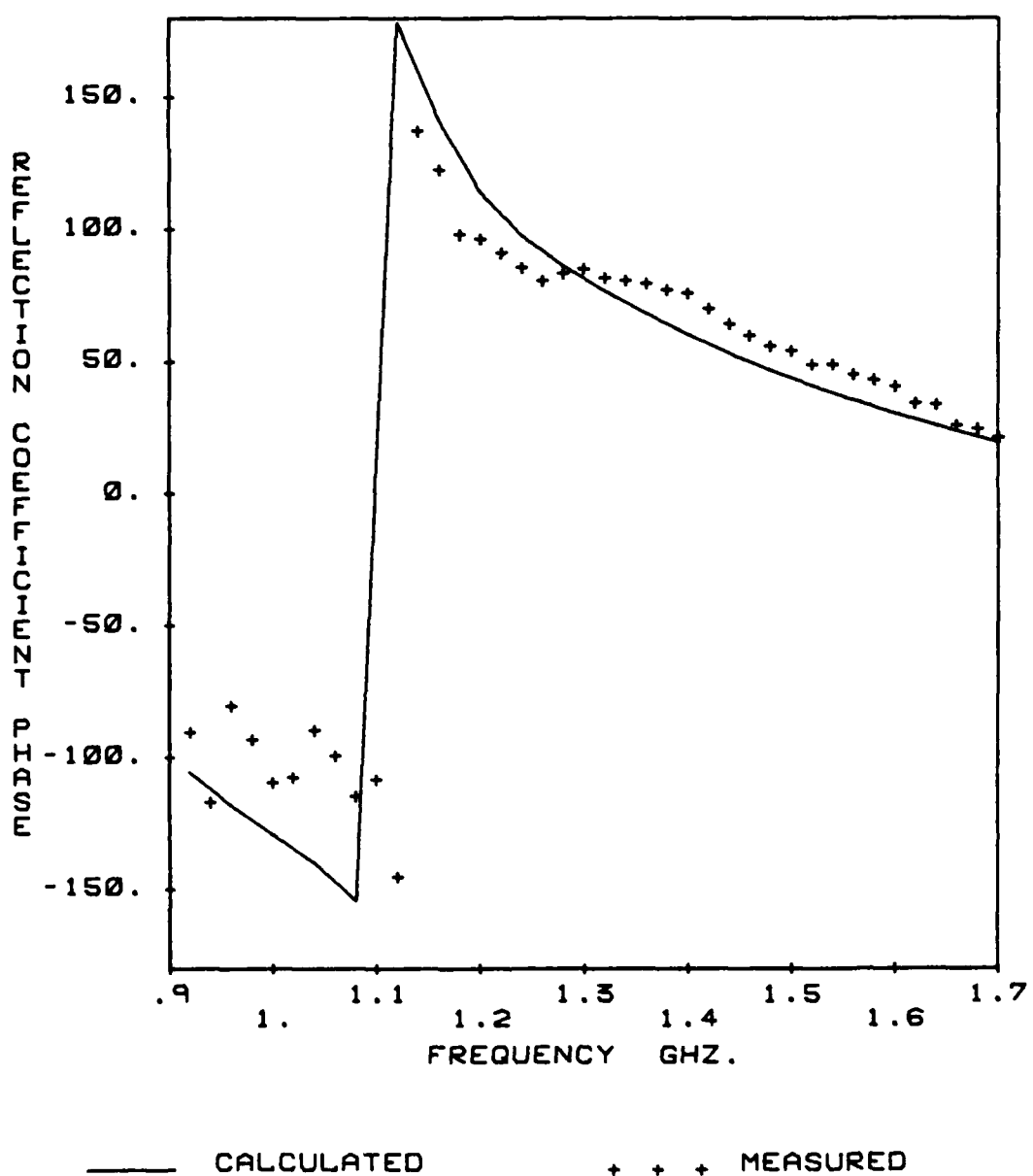


Figure 4.14b. Waveguide simulator results for a dipole array on a multi-layer substrate $a = 1\text{mm}$, $b = 95\text{mm}$, $t_3 = 25.4\text{mm}$, $\epsilon_{r3} = 1.03$, $t_2 = 25.4\text{mm}$, $\epsilon_{r2} = 2.53$.

thought to be due to a "forced" excitation of a surface wave on the array face [13]. For a microstrip array, the location of the blind angles can be predicted by the location of poles in the \hat{yy} component of the periodic Green's function which are not canceled by a zero in the numerator. Physically, these poles are the propagation constants of the surface waves of the grounded dielectric substrate (GDS). The propagation constants of these modes are determined by satisfying the transverse resonance conditions of the GDS without the array, which are

$$s' - js \epsilon_r \cot s't = 0 \quad (\beta_{TM}) \quad (4.2-3)$$

$$s - js' \cot s't = 0 \quad (\beta_{TE})$$

Note that these equations are also stated as $D_1 = 0$ for β_{TM} , and $D_2 = 0$ for β_{TE} , where D_1 and D_2 occur in the denominator of the Green's function, and were defined in Equation (2.2-18). Thus because of the use of the Green's function of the GDS, the effect of the surface waves is built into the solution. However, the occurrence of blind angles is easily predicted by the spectral or grating lobe lattice [71]. The grating lobe lattice, illustrated in Figure 4.15, is the spectral lattice of Figure 2.1b with visible regions of both the half space above the array and the GDS superimposed. Although each lattice point in the spectral lattice represents a Floquet mode, grating lobe lattice is the commonly used term, and will be used here. One or more surface wave modes will always propagate, and a "surface wave circle" [71] can be drawn on the grating lobe lattice for each propagating surface wave mode, with a radius equal to its propagation constant. The main beam of the array

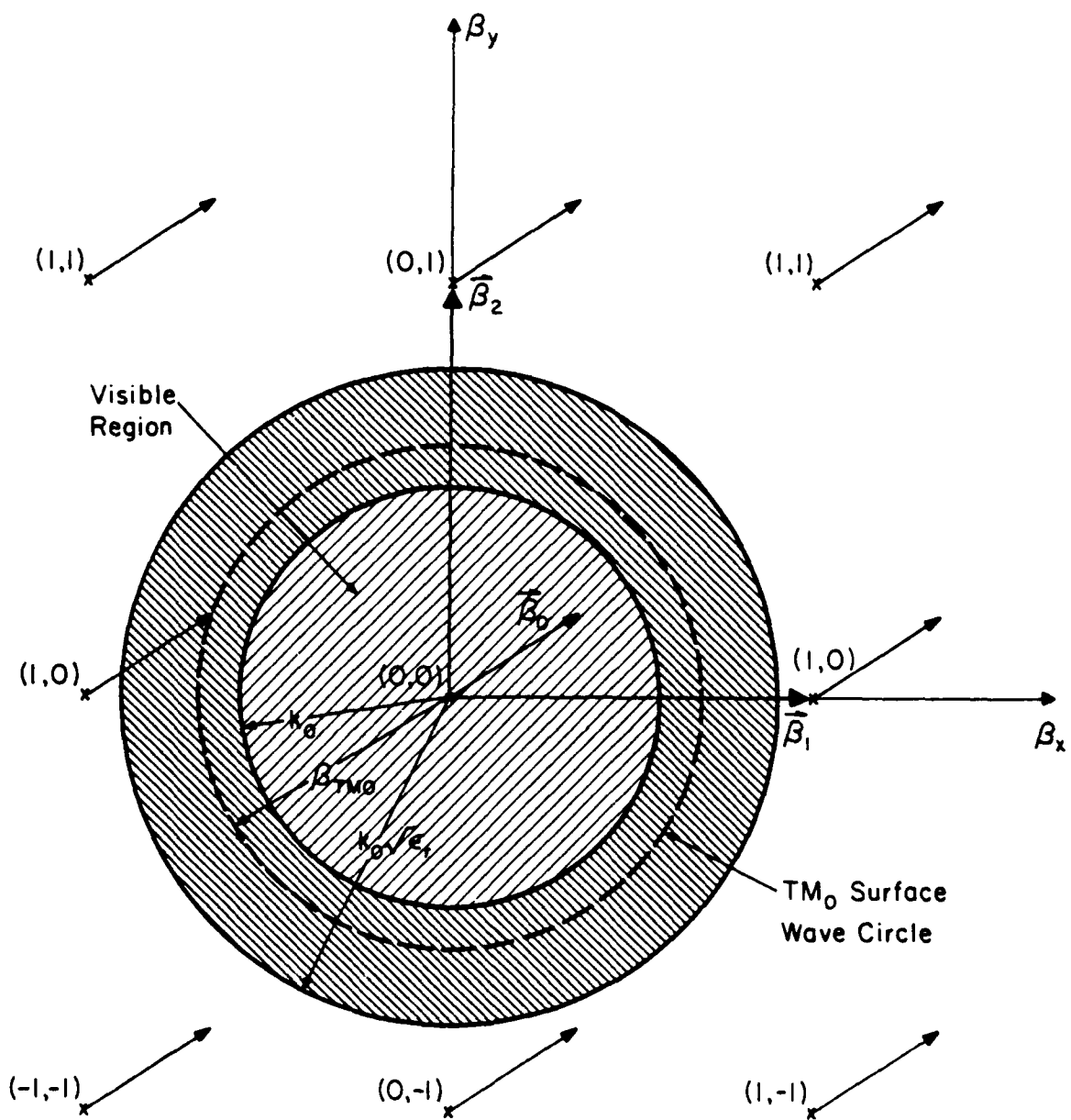


Figure 4.15. Spectral lattice, with visible regions superimposed (grating lobe lattice).

corresponds to the (0,0) Floquet mode, and the scan angle is defined by the vector $\hat{\beta}_o$, defined as

$$\hat{\beta}_o = m_o \hat{\beta}_1 + n_o \hat{\beta}_2 \quad (4.2-4)$$

To scan the main beam in the direction θ, ϕ , as shown in Figure 4.1, m_o and n_o become

$$\begin{aligned} m_o &= -S_1 \sin \theta \sin (\theta_{B2} - \phi) \\ n_o &= -S_2 \sin \theta \sin (\phi - \theta_{B1}) \end{aligned} \quad (4.2-5)$$

where θ_{B1} and θ_{B2} are the angles the vectors $\hat{\beta}_1$ and $\hat{\beta}_2$ make with the \hat{x} or $\hat{\beta}_x$ axis. For a rectangular array, Equation (4.2-5) reduces to

$$\begin{aligned} m_o &= -S_1 \sin \theta \cos \phi \\ n_o &= -S_2 \sin \theta \sin \phi \end{aligned} \quad (4.2-6)$$

The negative sign in these equations is the result of the convention chosen to define a plane wave, as discussed in Section 2.2.2. When the main beam is scanned to θ, ϕ by the vector $\hat{\beta}_o$, all of the Floquet modes are similarly displaced, as shown in Figure 4.15. If any of the Floquet modes are placed on a surface wave circle, the surface wave is excited by that Floquet mode, causing blindness unless the magnitude of that Floquet mode is zero, as defined by the Green's function. Consideration of Figure 4.15 clearly shows the possibility of blind angles at any scan angle, including broadside, for proper array spacings. Furthermore, because at least one surface wave mode can propagate in the GDS, the location of the blind

angles will generally be a limiting factor in determining the scanning range of a phased array.

While the grating lobe lattice provides a clear understanding of the behavior of the array, a more convenient construction for determining blind angles was suggested by Frazita [71], and used more recently by Pozar and Schaubert [37]. This construction, referred to as a surface wave circle diagram [71], is illustrated in Figure 4.16, and is obtained by drawing grating lobe and surface wave circles around the lower-order Floquet modes. When a surface wave circle intersects the visible region, blindness will occur at the corresponding scan angles unless cancellation occurs. This construction gives a very simple technique for determining the blind angles of the array.

As an example, consider a microstrip dipole array in a rectangular lattice, with $s_1 = 0.575\lambda_0$, $s_2 = 0.5\lambda_0$, $t = 0.15\lambda_0$, and $\epsilon_r = 2.55$. No radome was present in this example. For this GDS only the TM_0 surface wave mode is above cutoff, with a normalized propagation constant $\beta_{TM_0}/k_0 = 1.1925$. The elements had dimensions $a = 0.001\lambda_0$ and $b = 0.36\lambda_0$, giving a broadside impedance of $71.8 + j3.9$ ohms using 11 edge mode basis functions. The reflection coefficient versus scan angle in the E, H and D planes is shown in Figure 4.17. An examination of Figure 4.18 easily explains the coarse characteristics of the results in Figure 4.17. In the H-plane scan ($\phi = 0$), the intersection with the TM_0 surface wave pole at $\sin \theta = 0.739$, or $\theta = 33.1$ degrees, does not cause blindness because the (1,0) Floquet mode has zero amplitude for an H-plane scan. In fact for H-plane scans the TM surface wave poles are not excited, and for E-plane scans, the TE surface wave poles are not excited, due to the

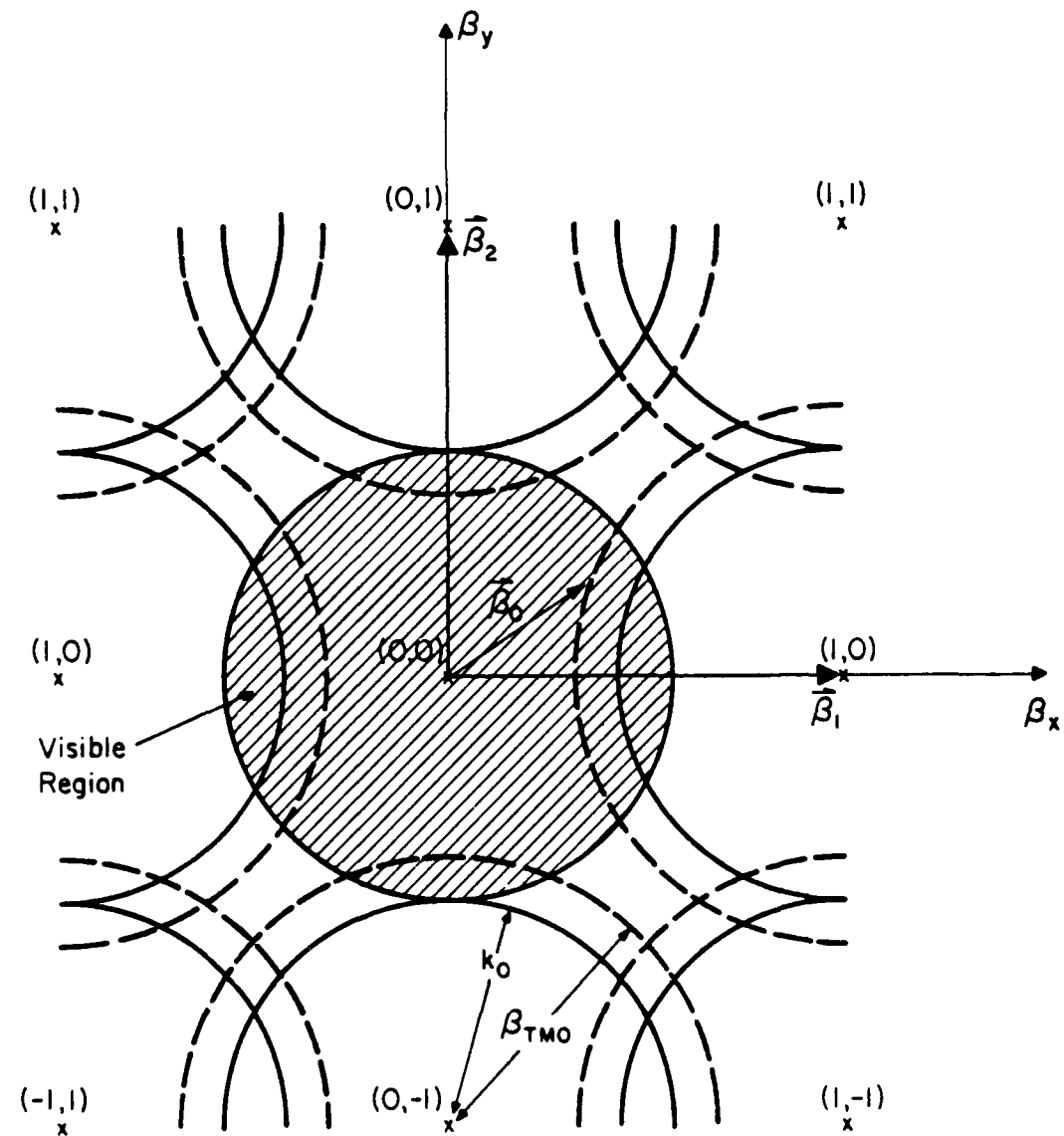


Figure 4.16. Alternate construction of spectral or grating lobe lattice.

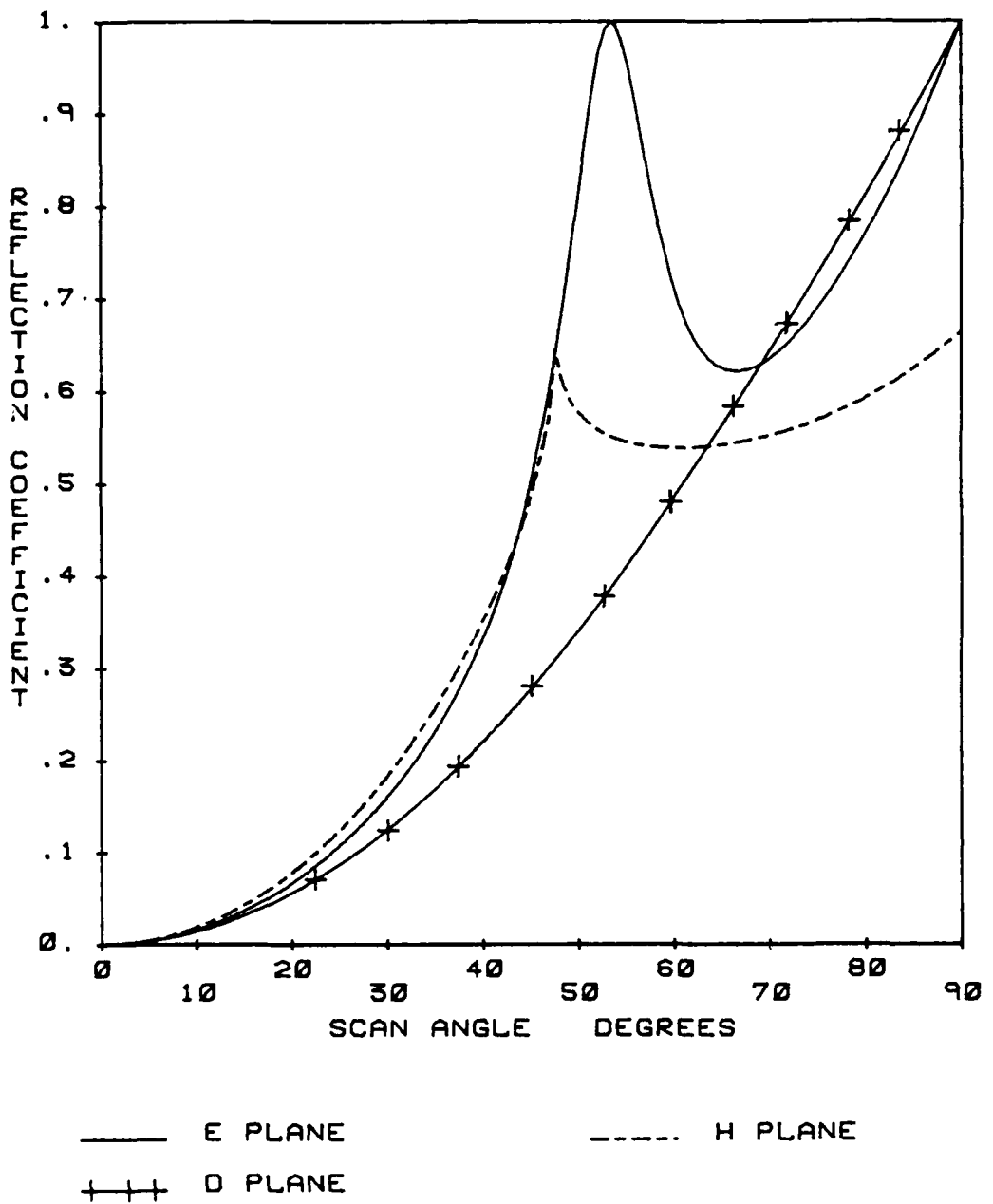


Figure 4.17. Scan performance of an infinite dipole array on a rectangular lattice. $a = 0.001 \lambda_0$, $b = 0.36 \lambda_0$, $t = 0.15 \lambda_0$, $\epsilon_r = 2.55$, $S_1 = 0.575 \lambda_0$, $S_2 = 0.5 \lambda_0$.

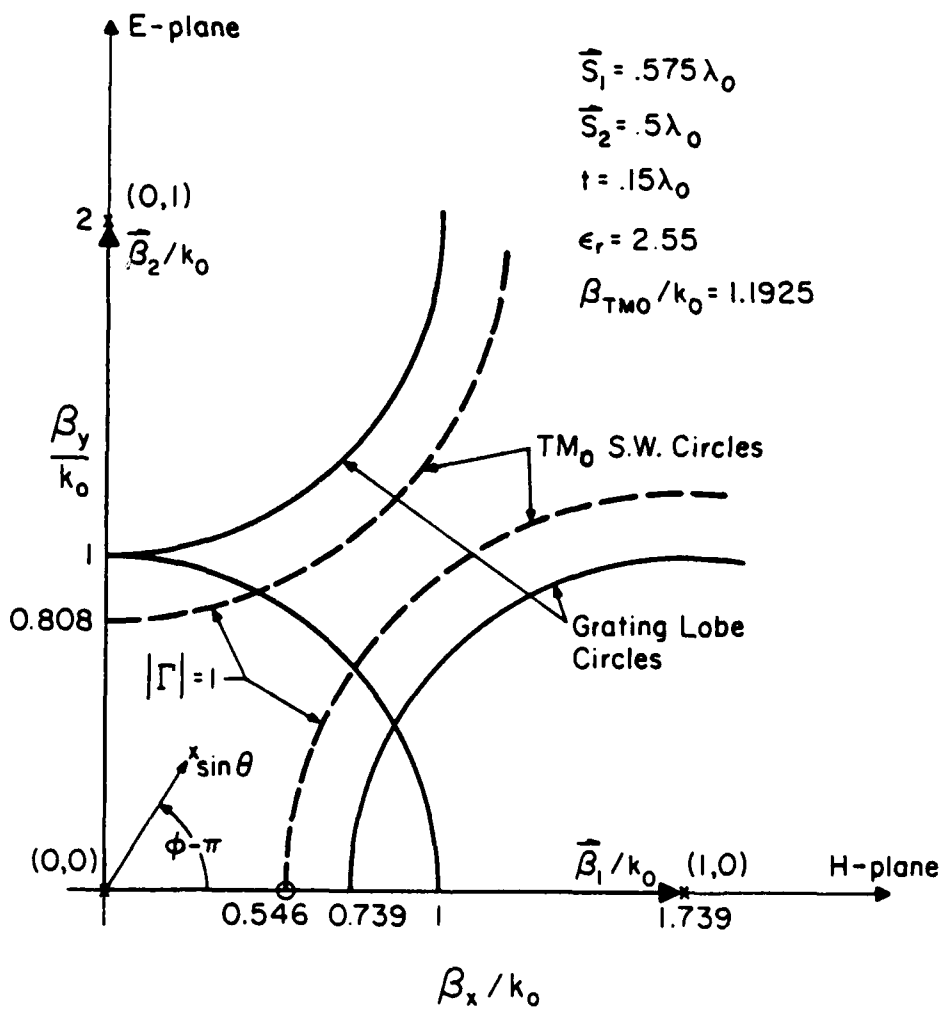


Figure 4.18. Surface wave circle diagram for array in Figure 4.17.

polarization of the electric field in those planes. However, returning to Figure 4.17, a grating lobe (Floquet mode) enters visible space at $\theta = 47.6$ degrees in the H-plane scan, resulting in the observed peak. The excitation of the TM_0 surface wave at $\theta = 53.9$ degrees causes the observed blind angle in the E-plane. The D-plane ($\phi = 45$ degrees) scan is smooth, as no surface wave or grating lobe circles are intersected. At endfire scan ($\theta = 90$ degrees) in the E and D planes $|\Gamma| = 1$, as the array spacing is such that no Floquet modes are propagating (in free space.)

While the basic features of the array are easily predicted by the surface wave circle diagram or the grating lobe diagram, the moment method solution not only accounts for these features but accurately predicts the shapes and magnitudes of the peaks, and the reflection coefficient at all other points. As will be seen in the next example, the shape of the curve can be important.

In the next example, the array of the previous example is covered with a dielectric layer (radome) of thickness $0.1 \lambda_0$ and dielectric constant 2.55. The broadside impedance of this array was $50.1 + j 143.2$ ohms. The results for this array are plotted in Figure 4.19. Because of the additional layer, a second surface wave is permitted, the TE_0 mode, as shown in Figure 4.20. In the H-plane scan, a blind angle occurs at $\theta = 42.0$ degrees due to the excitation of the TE surface wave mode. In addition, a grating lobe (Floquet mode) enters visible space for $\theta = 47.7$ degrees. The result of these two factors is a broadly peaked blind angle. In contrast, the blind angle in the D-plane at $\theta = 36.7$ degrees and the blind angle in the E-plane at 38.1 degrees, both due to excitation of the TM_0 surface wave mode, are very sharply peaked, resulting in a low reflection coefficient over a much broader range than in the H-plane.

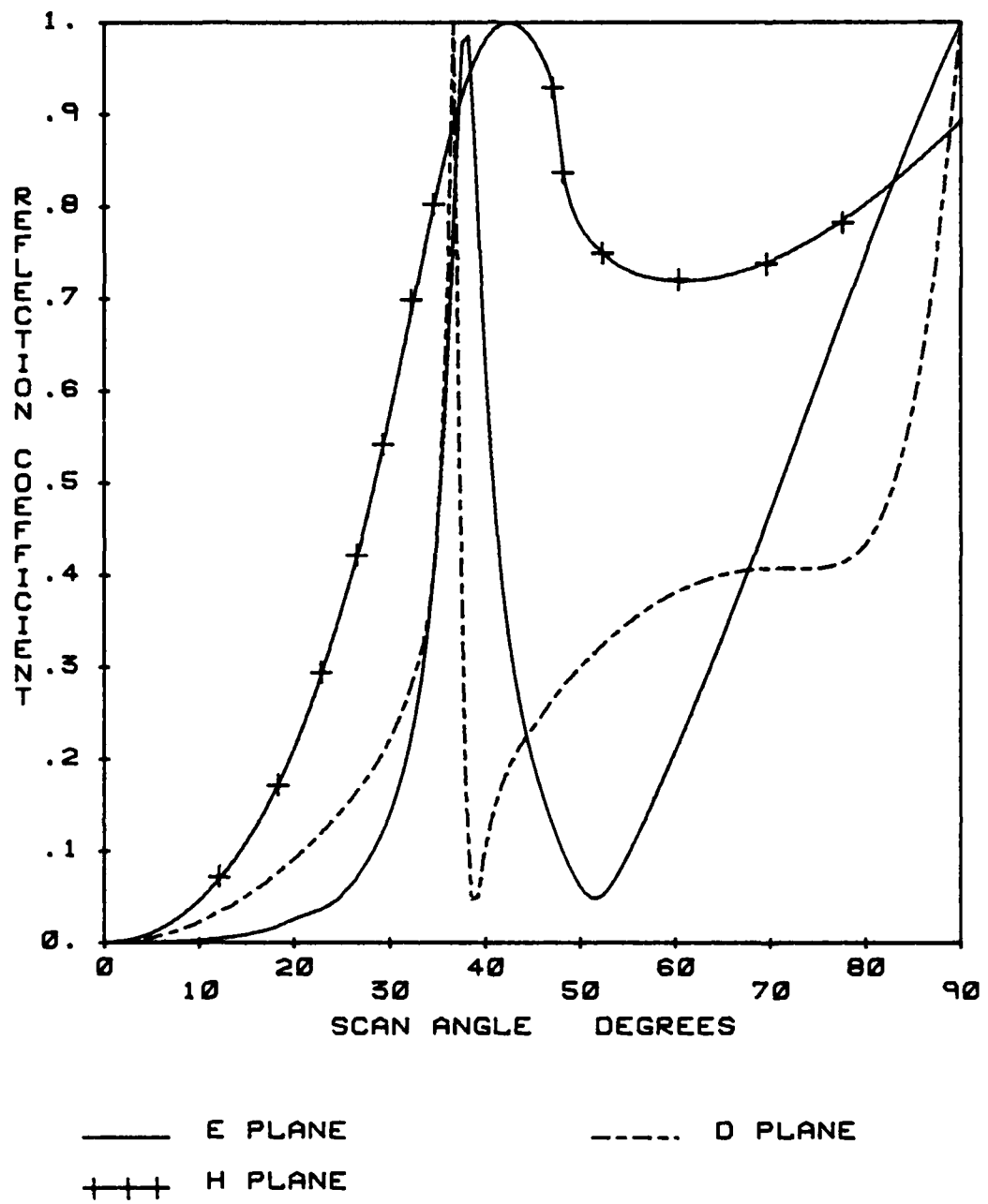


Figure 4.19. Scan performance of an infinite dipole array with a radome on a rectangular lattice. $a = 0.001 \lambda_0$, $b = 0.36 \lambda_0$, $t = 0.15 \lambda_0$, $\epsilon_r = 2.55$, $t = 0.1 \lambda_0$, $\epsilon_r = 2.55$, $S_1 = 0.575 \lambda_0$, $S_2 = 0.5 \lambda_0$.

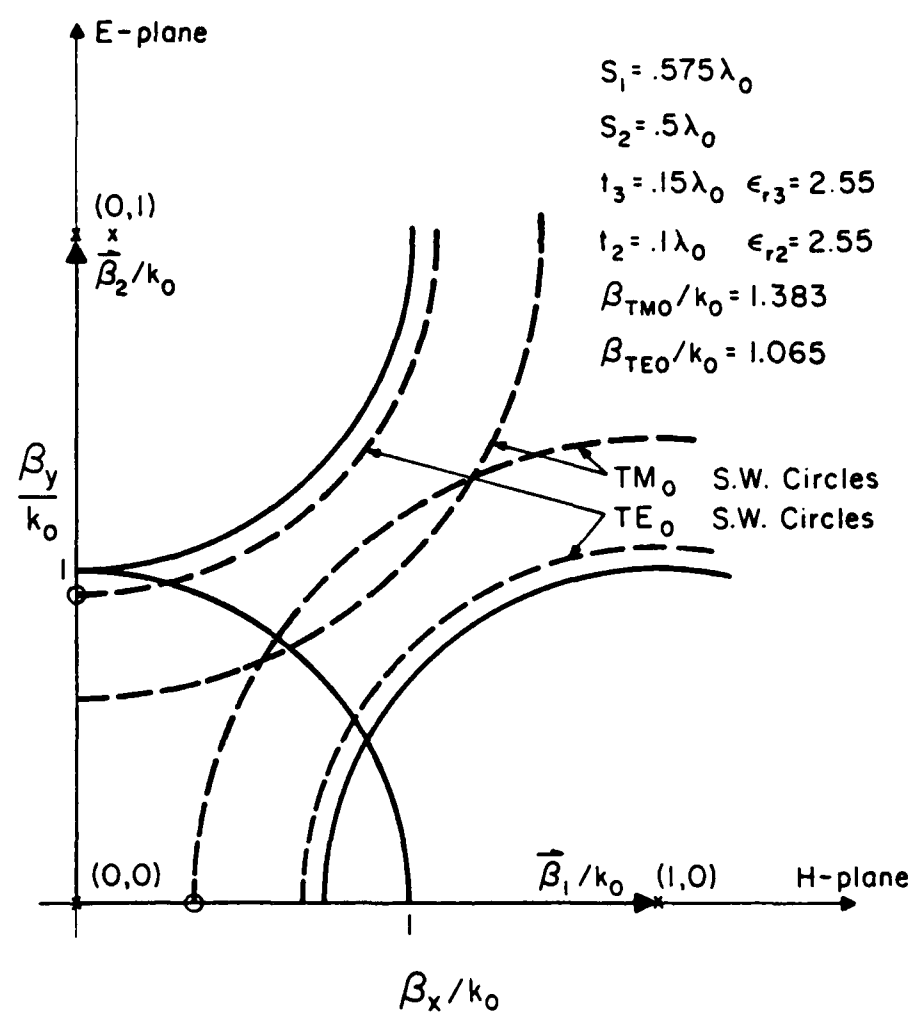


Figure 4.20. Surface wave circle diagram for array in Figure 4.19.

The next example is for a hexagonal array, with $S_1 = S_2 = 0.5774\lambda_0$. The GDS has thickness $0.15\lambda_0$ and a dielectric constant 2.55. As in the previous case, the dipole dimensions were $a = 0.001\lambda_0$ and $b = 0.36\lambda_0$, resulting in a broadside impedance of $70.5 - j3.4$ ohms. The plot of the reflection coefficient in the three principal planes is in Figure 4.21, and the surface wave circle diagram for the array is shown in Figure 4.22. As predicted from Figure 4.22, blind angles occur at 53.9 degrees in the E-plane due to excitation of the TM_0 surface wave mode and at 59.0 degrees in the D-plane due to excitation of the same mode. For this GDS, only the TM_0 mode is above cutoff. The reflection coefficient goes to 1 at $\theta = 90$ degrees in all three principal planes, due to the spacing of the array. The peak in the reflection coefficient in the D-plane is very sharp, permitting operation with a low reflection coefficient over a wide range of scan angles.

As a final example, a case computed by Pozar and Schaubert is included for purposes of comparison. This array is on a rectangular lattice, with $S_1 = 0.5\lambda_0$ and $S_2 = 0.4\lambda_0$, and is on a GDS with $t = 0.08\lambda_0$ and $\epsilon_r = 12.8$. The broadside impedance for this case was $Z = 11.3 - j2.4$ ohms, using seven edge mode basis functions. Two surface wave modes propagate, the TM_0 and TE_0 modes. The reflection coefficient versus scan angle in the E and H planes is plotted in Figure 4.23, and the surface wave circle diagram is shown in Figure 4.24. In this example a blind angle occurs in the E-plane very close to broadside, at $\theta = 22.3$ degrees, due to excitation of the TM_0 surface wave mode. In addition, another blind angle occurs in the E-plane at $\theta = 40.6$ degrees due to excitation of

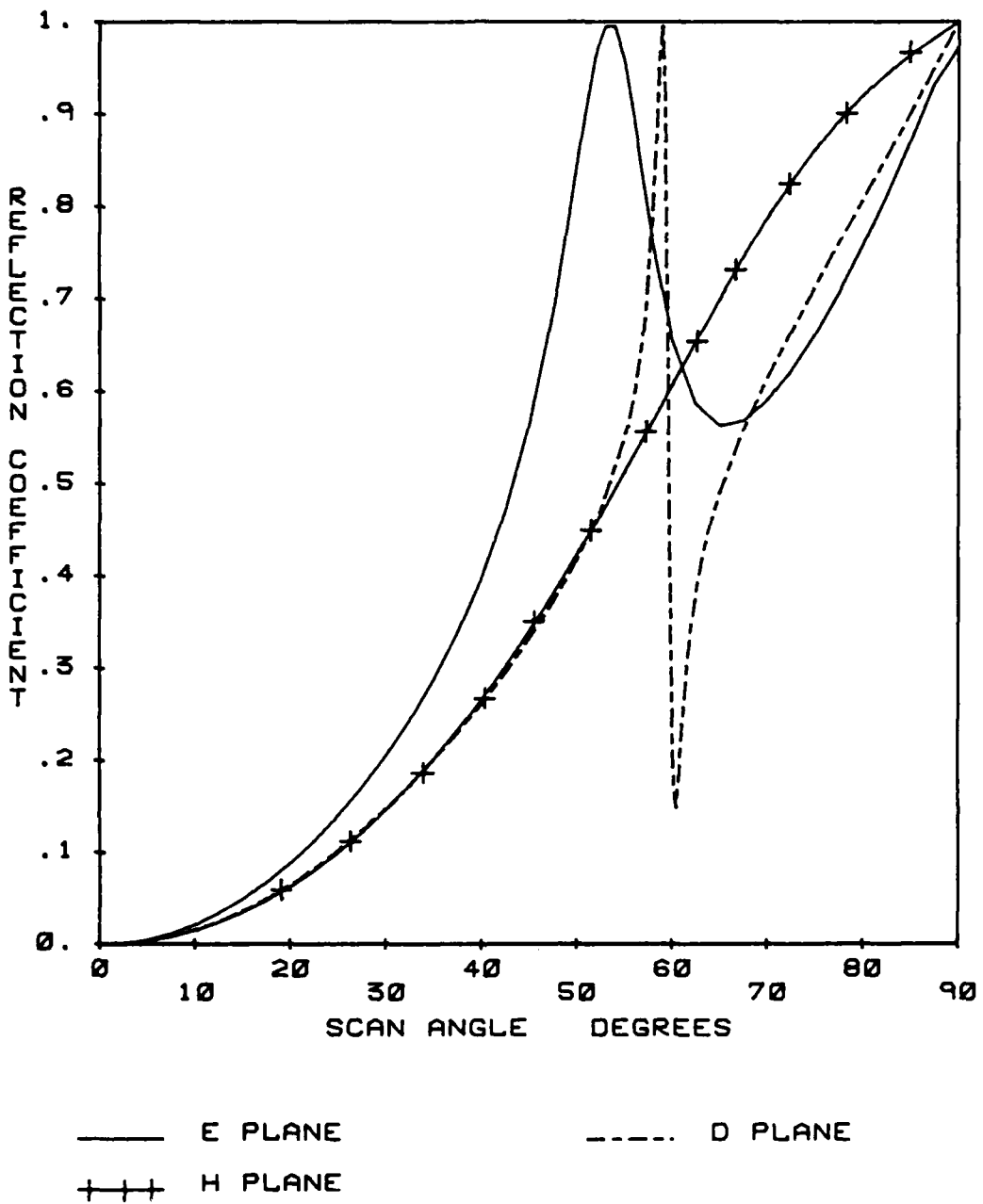


Figure 4.21. Scan performance of an infinite dipole array on a hexagonal lattice. $a = 0.001 \lambda_0$, $b = 0.36 \lambda_0$, $t = 0.15 \lambda_0$, $\epsilon_r = 2.55$, $S_1 = S_2 = 0.5774 \lambda_0$.

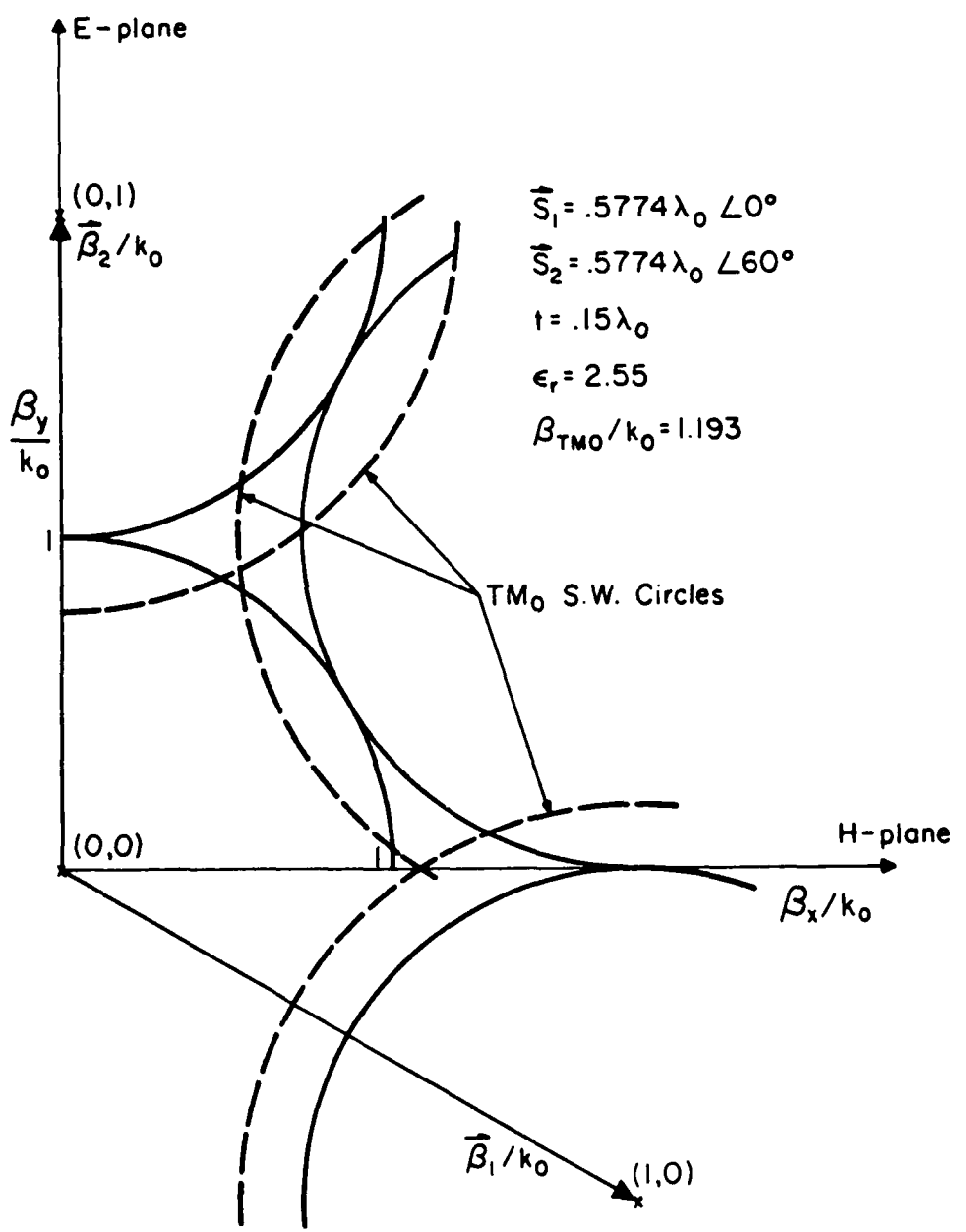


Figure 4.22. Surface wave circle diagram for array in Figure 4.21.

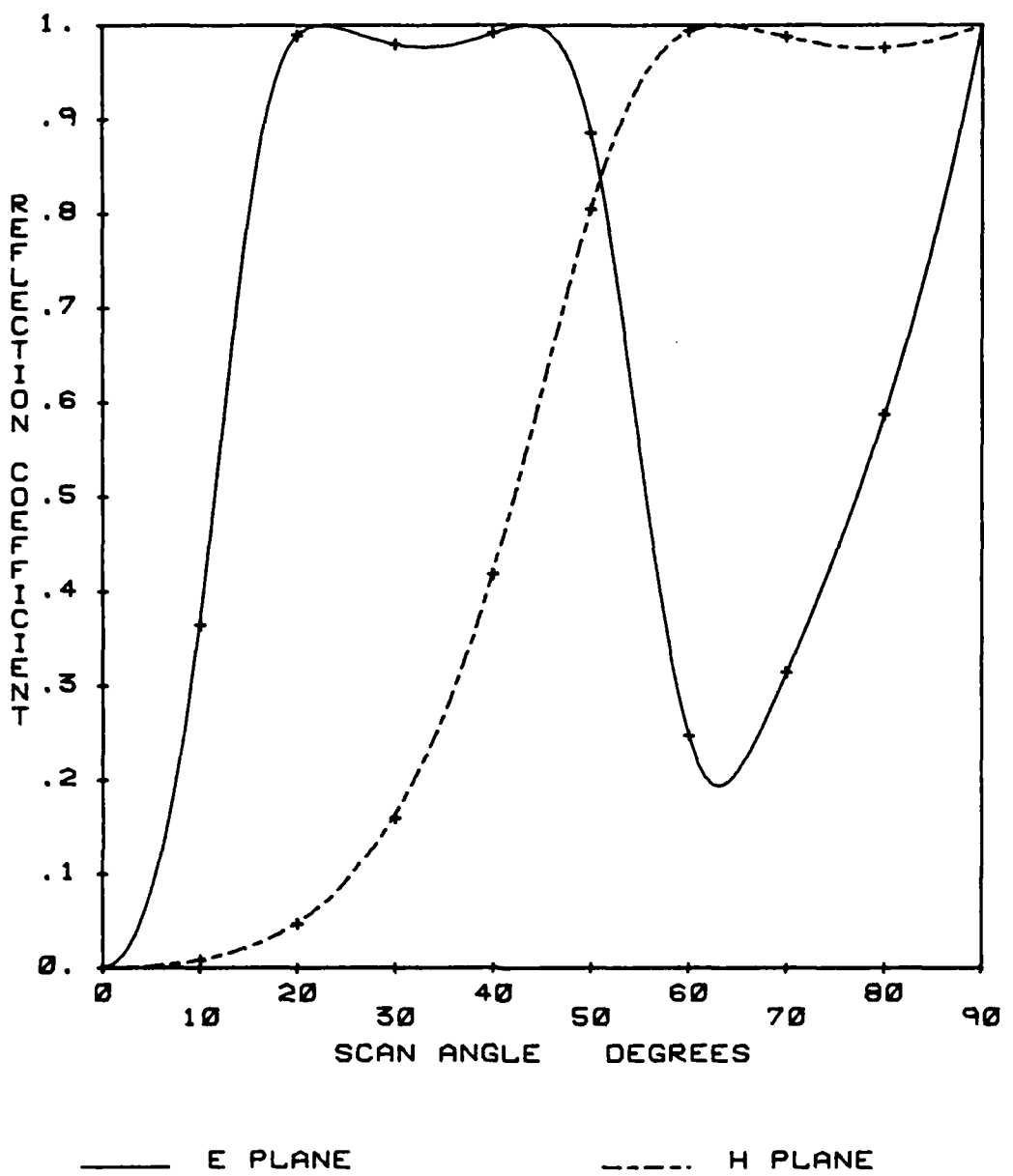


Figure 4.23. Scan performance of an infinite dipole array on a rectangular lattice. $a = 0.002 \lambda_0$, $b = 0.1546 \lambda_0$, $t = 0.08 \lambda_0$, $\epsilon_r = 12.8$, $S_1 = 0.5 \lambda_0$, $S_2 = 0.4 \lambda_0$.

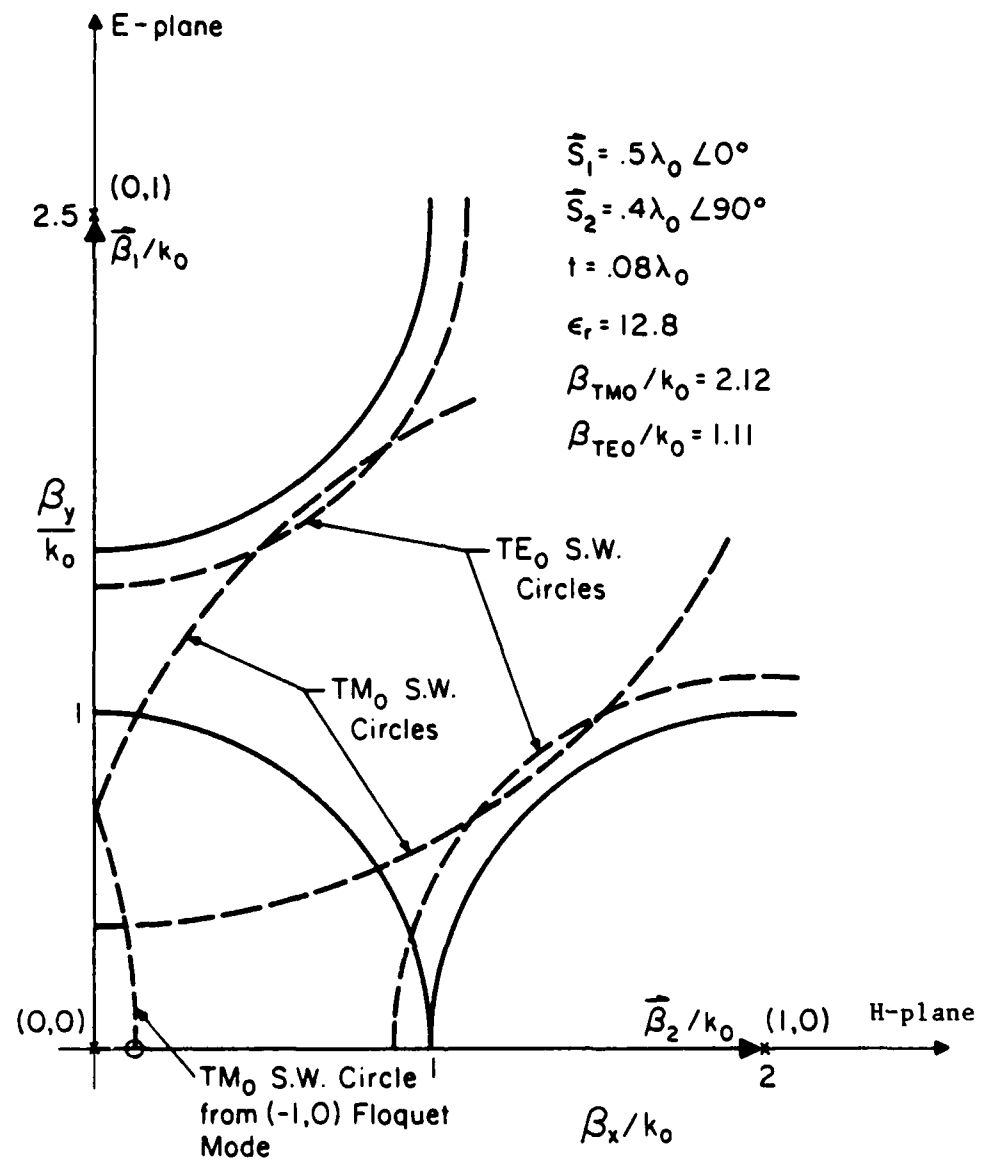


Figure 4.24. Surface wave circle diagram for array in Figure 4.23.

the same surface wave mode by a different Floquet mode. In the H-plane, the TM_0 surface wave pole at $\theta = 6.6$ degrees is not excited, but the TE_0 mode is excited at $\theta = 63.2$ degrees, causing a blind angle. In this case, the resulting reflection coefficient is generally very high and broadly peaked in both planes.

An interesting result concerning the required numerical accuracy is also demonstrated in Figure 4.23. The curves in this figure were obtained using only 7 edge mode basis functions. In addition, several points were computed using 13 edge mode basis functions, and are indicated by crosses on the curves of Figure 4.23. The discrepancy between the results in the two cases is negligible in the plotted reflection coefficient.

Another interesting characteristic of the arrays, which can be determined from the solution for the current distribution, is the bandwidth of the antenna. In the array environment, the bandwidth is additionally dependent on the array spacing, along with the substrate and element parameters. For example, it would be simple to choose an array for which a slight change in frequency places a Floquet mode on a surface wave circle causing blindness. Such an array would have a decreased bandwidth. A detailed discussion of the effect of substrates on the properties of microstrip dipoles has been given by Katehi and Alexopoulos [72], and the effects of a radome on the radiation properties of an infinitesimal microstrip dipole (the Green's function) have been reported by Jackson and Alexopoulos [73].

One example of the effect of substrate thickness on the bandwidth of a rectangular array of microstrip dipoles is shown in Figure 4.25. The array dimensions give $S_1 = S_2 = 0.5 \lambda_0$ at 0.9 GHz, where the three

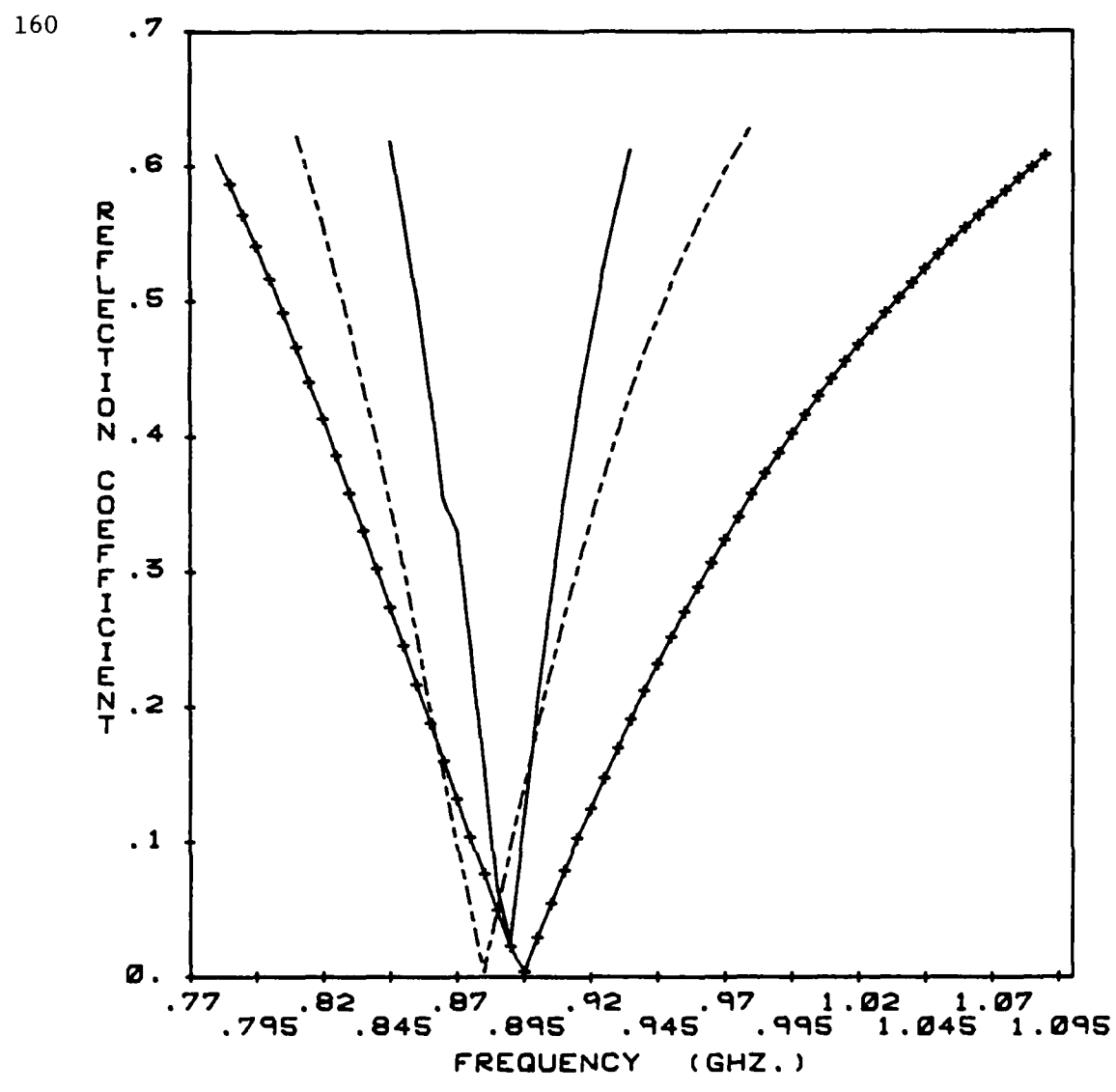


Figure 4.25. Reflection coefficient versus frequency for three microstrip dipole arrays (zero scan.) $a = 2.0\text{mm}$, $b = 115\text{mm}$, $\epsilon_r = 2.53$, $S_1 = S_2 = 166.7\text{mm}$.

substrate thicknesses considered were $0.075\lambda_0$, $0.1\lambda_0$ and $0.125\lambda_0$. ϵ_r of the GDS was 2.53. As expected, the bandwidth of the array increases with substrate thickness, with 2 to 1 VSWR bandwidth results taken from Figure 4.28 of 4.2% for $t = 0.075\lambda_0$, 8.3% for $t = 0.1\lambda_0$ and 15.5% for $t = 0.125\lambda_0$ (thicknesses specified at 0.9 GHz). To obtain the curves of Figure 4.25, the array was considered matched at the resonant frequency for each case, where the three resonant resistances were $R = 19.0$ ohms for $t = 0.075\lambda_0$, 36.3 ohms for $t = 0.1\lambda_0$ and 60.7 ohms for $t = 0.125\lambda_0$.

The final numerical results of this chapter concern the possibility of obtaining data for the single element case from the array solution. Rana and Alexopoulos have computed the impedance of a single microstrip dipole using the method of moments [21]. However, the ability to obtain the same results with an array solution could provide a more efficient technique, as Sommerfeld integrals are not computed in the array solution. As mentioned in the introduction, Munk and Burrell discuss the "array scanning method" [32], where the single element solution is recovered from the array solution by averaging the impedance of an element in an infinite array for all scan angles in real space. This approach is equivalent to the single element problem, as it is essentially a numerical integration of the Sommerfeld integrals which arise in the single element problem.

An alternate approach which seems intuitively plausible is to simply increase the array spacing until the mutual impedance effects are no longer significant. Consider a half-wave dipole in free space but a quarter wavelength above an infinite ground plane. The resistance and reactance for such an element in an infinite array environment as a function of array spacing are shown in Figure 4.26. The impedance of the

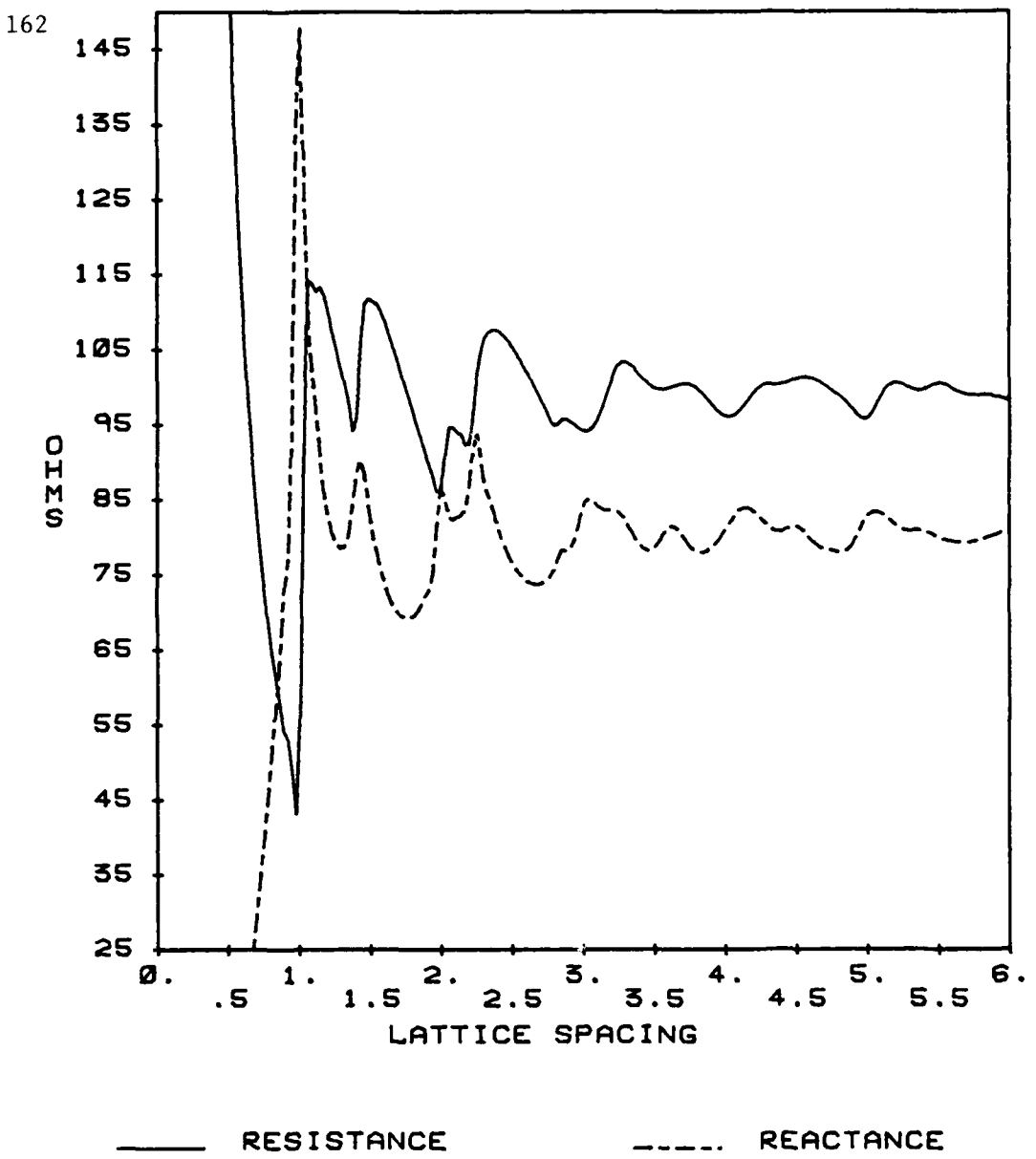


Figure 4.26. Impedance of a dipole in an infinite array in free space as a function of lattice spacing. $a = 0.002 \lambda_0$, $b = 0.5 \lambda_0$, $t = 0.25 \lambda_0$, $\epsilon_r = 1$.

single element was obtained from a standard moment method solution using 7 piecewise sinusoidal basis functions as $100 + j75$ ohms [74]. As the array spacing is increased, the impedance is seen to settle to a value approximately equal to the single element result. While increased spacing increases the number of terms which must be taken in the spectral sum, the solution is still quite efficient at the spacings in Figure 4.26. Thus this method appears to have potential for arrays in free space. The same is not true in general, as is demonstrated by the next example. Rana and Alexopoulos [21] computed the impedance of a single microstrip dipole with a radius of $0.0002 \lambda_0$ and length $0.317 \lambda_0$ on a GDS with $t = 0.1016 \lambda_0$ and $\epsilon_r = 3.25$. The impedance of this element in an array environment is plotted in Figures 4.27 and 4.28. Obviously, the impedance is not approaching a limiting value. The behavior exhibited in these curves is readily explained by considering the effect of the TM_0 surface wave pole. For the GDS, the TM surface wave mode has a normalized propagation constant of $\beta_{TM_0}/k_0 = 1.1349$, and whenever the array spacing is such that a Floquet mode lies on a surface wave circle, the resistance becomes zero and the reactance becomes very large. This will occur whenever the array spacing is a multiple of $1/1.1349$ or at spacings of $n \cdot 0.8813$, for integer values of n . This behavior is clearly seen in Figures 4.27 and 4.28. In addition, in the single element problem the effect of the surface wave is always present, whereas in the array solution its effect is only felt for certain array spacings. Thus without a technique to include the surface wave effect separately, the array solution does not appear to be able to recover the impedance for a single element simply by increasing the lattice spacing, at least for reasonable lattice spacings.

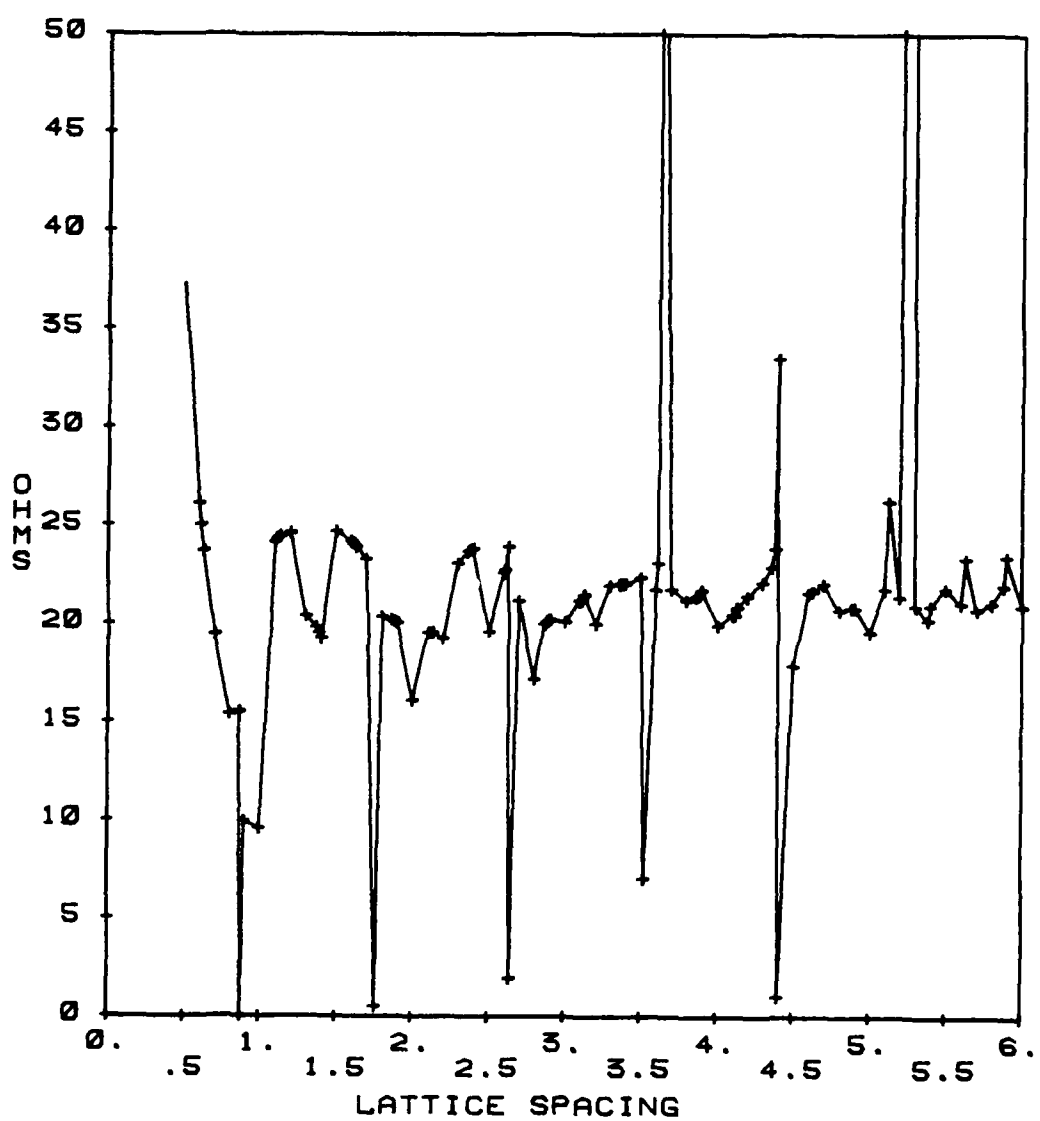


Figure 4.27. Resistance of a microstrip dipole in an infinite array as a function of lattice spacing. $a = 0.0002 \lambda_0$, $b = 0.317 \lambda_0$, $t = 0.1016 \lambda_0$, $\epsilon_r = 3.25$.

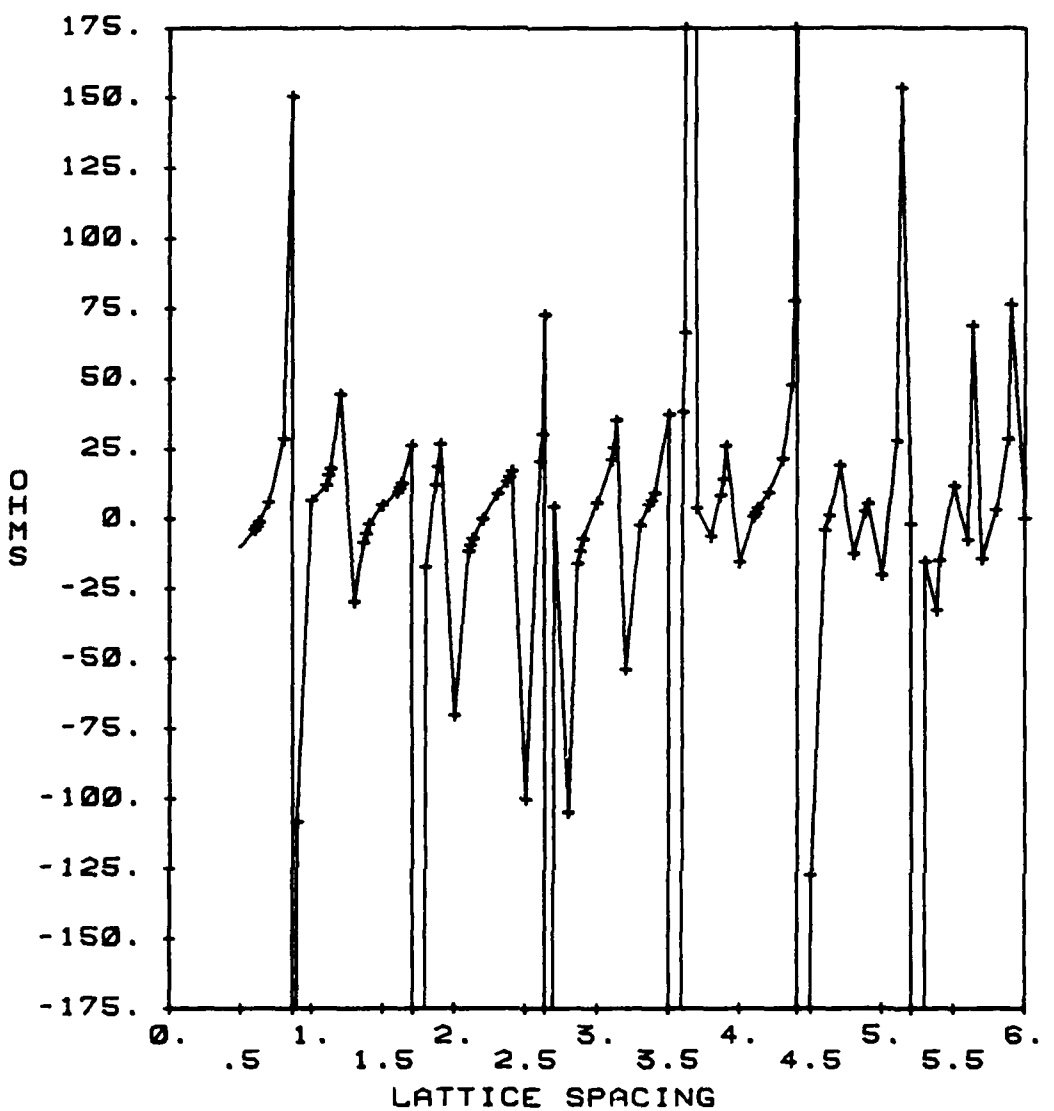


Figure 4.28. Reactance of a microstrip dipole in an infinite array as a function of lattice spacing. $a = .0002 \lambda_0$, $b = 0.317 \lambda_0$, $t = 0.1016 \lambda_0$, $\epsilon_r = 3.25$.

4.2.4. Discussion

Numerical results for the solution of infinite arrays of microstrip dipoles have been presented in this chapter. Through the use of an acceleration technique, a particularly efficient solution was obtained. Agreement with experimental results and other independent results indicates the validity of the technique. While only simple dipole arrays have been solved here, the solution could be easily extended to analyze more complicated thin-wire structures. In addition, the improved efficiency over other solutions is important because it allows the antenna designer the freedom of being able to numerically experiment on the computer without concurrent high costs in computer time.

CHAPTER 5

INFINITE ARRAYS OF MICROSTRIP PATCHES

A moment method solution for infinite arrays of microstrip patches on thick dielectric substrates is considered in this chapter. This problem is considerably more involved than for the dipole arrays of the previous chapter because one must include currents in both the \hat{x} and \hat{y} directions. In addition, unlike solutions for single patch elements on thin substrates [17,18,20], where good results can be obtained by using only one or two entire domain modes to represent the current distribution, a solution for probe fed patches on thick substrates requires the use of enough basis functions to adequately represent the complicated current distribution near the feed region.

One restriction in the present method is that the feed structure is not included in the boundary conditions of the integral equation for the current distribution. While this approach is used with success in the analysis of single patches on thin substrates, a better model is needed to more accurately analyze probe fed patches on thick substrates.

5.1. Evaluation of the matrix elements

5.1.1. The impedance matrix

The general formulation of the solution was considered in detail in Chapter 2, and examples of the application of the acceleration technique to the evaluation of typical inner products were discussed in detail in Chapter 3. Therefore, the evaluation of the impedance matrix elements is only briefly considered here.

As in method 2 in the previous chapter, rooftop basis functions were used to represent the current. While linear testing would have been adequate, employing rooftop testing functions in a Galerkin technique allows significant savings when computing the impedance of the patch, as will be discussed later. These basis and testing functions are defined as

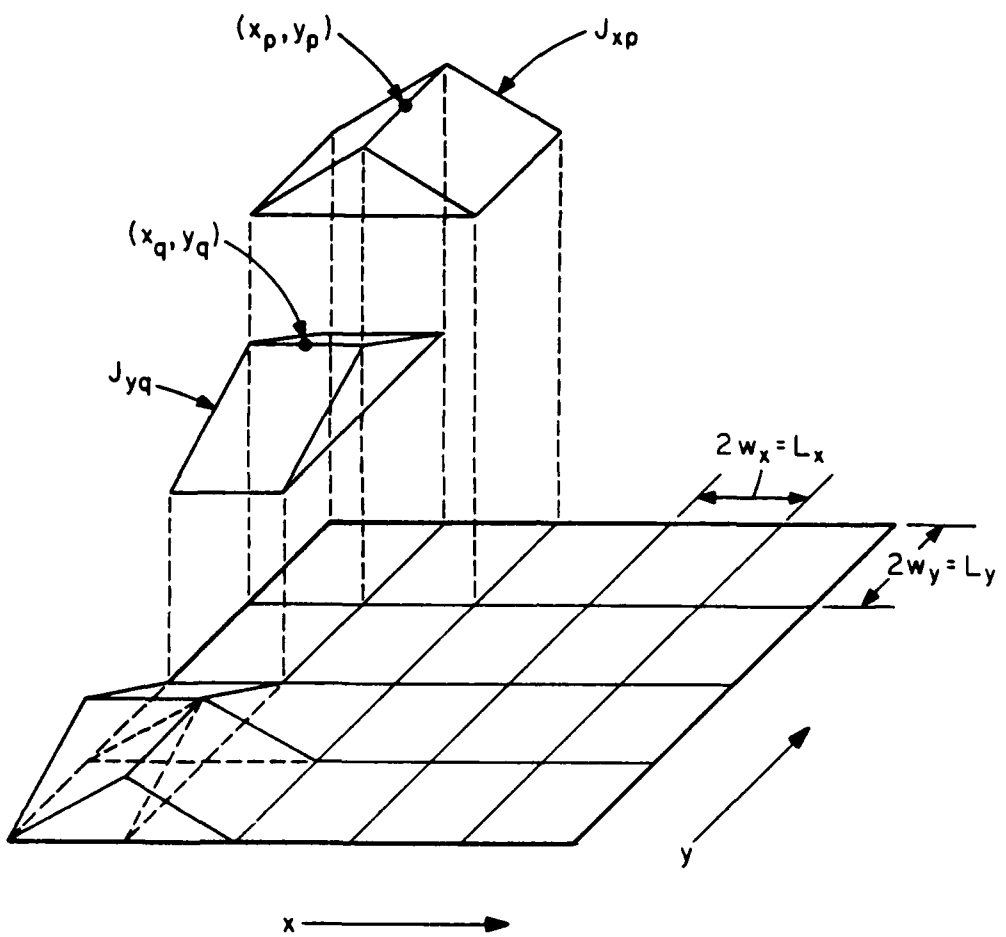
$$J_{xp} = p(w_y; y - y_p) q(L_x; x - x_p) \quad J_{yq} = q(L_y; y - y_q) p(w_x; x - x_q) \quad (5.1-1)$$

$$T_{xr} = p(w_y; y - y_r) q(L_x; x - x_r) \quad T_{ys} = q(L_y; y - y_s) p(w_x; x - x_s)$$

where the functions q and p are defined in Equation (3.3-17). The general layout of the basis functions is illustrated in Figure 5.1. In all cases considered here, the basis functions are chosen such that $w_x = L_x/2$, and $w_y = L_y/2$. The extension to the general case is not difficult, and hence, the more general notation is used. With this layout, the number of basis functions can be described in terms of the number of subpatches of dimension $L_x \cdot L_y$. For example, if 10 subpatches are used in both the \hat{x} and \hat{y} directions, a total of 180 basis functions are defined on the patch, 90 in the \hat{x} direction and 90 in the \hat{y} direction.

The application of the acceleration technique to the evaluation of the impedance matrix elements is straightforward, and follows the example of Section 3.3.2 closely. The spectral sum S_β for an element of the Z^{ij} matrix, where i and j can be either x or y , is given by

$$S_\beta = \frac{1}{A} \sum_{mn} (\tilde{G}_{ij}(\vec{k}_{mn}) - \tilde{G}_{ij}^a(\vec{k}_{mn})) \cdot \tilde{J}_j(\vec{k}_{mn}) \tilde{T}_i(\vec{k}_{mn}) e_{mn}(\vec{\rho}_T - \vec{\rho}_B) \quad (5.1-2)$$



$$J_{xp} = q(L_x; x - x_p) p(w_y; y - y_p)$$

$$J_{yq} = q(L_y; y - y_q) p(w_x; x - x_q)$$

Figure 5.1. Basis function layout on microstrip patches.

where $(\vec{\rho}_T - \vec{\rho}_B)$ is the vector from the basis function to the testing function.

The spatial sum is given by

$$s_\beta = \sum_{mn} f_1(\vec{\rho}_T - \vec{\rho}_B - \vec{s}_{mn}) e^{j2\pi(m\omega_0 + n\omega_0)} \quad (5.1-3)$$

where

$$f_1(\vec{\rho}) = F^{-1} \{ \tilde{G}_{ij}^a(\vec{k}_{mn}) \tilde{J}_j(\vec{k}_{mn}) \tilde{T}_i(\vec{k}_{mn}) \} \quad (5.1-4)$$

$f_1(\vec{\rho})$ is evaluated using the techniques described in Section 3.3.2. The singular term in the convolution integral is evaluated analytically using the integral $I_5(a; i, b; j)$ in Table 3.4, and the remainder is evaluated using a numerical integration routine.

By using a 64 point Gaussian quadrature routine to evaluate the convolution integrals, a typical element of the impedance matrix requires approximately 0.05 second of execution time on a CDC 6600. While this is very rapid, the large number of matrix elements that is required can nevertheless lead to very high fill times (the time required to "fill" the impedance and excitation matrices). However, by choosing square patches in square arrays considerable symmetry exists in the impedance matrix, greatly decreasing the fill time.

5.1.2. The excitation matrix

Unlike the dipole array problem where the use of a delta-gap feed made the computation of the excitation matrix trivial, the cost of filling the excitation matrix can be significant for the patch problem. Conceptually, each element of the excitation matrix can be considered to

be the field of an infinite array of feed probes, one for each patch, tested by a testing function on the reference (0,0) patch. This element-by-element approach is illustrated in Figure 3.10. Through reciprocity considerations, it can be shown that this is equivalent to letting an infinite array of the original testing functions radiate, one on each patch, and evaluating the field with a single feed probe at the reference patch. If a phase shift $\hat{\beta}_0$ is included in the original problem, the opposite phase shift $-\hat{\beta}_0$ must be used in the reciprocal problem. The integration of the field along the probe in the \hat{z} direction becomes a Fourier cosine transform, and is easily evaluated because of the assumption of a constant probe current. In this manner, a typical element of the excitation matrix becomes

$$v_{ri} = -\frac{1}{A} \sum_{mn} [\tilde{G}_{zi}(\hat{K}_{mn}) \tilde{T}_i(\hat{K}_{mn}) \tilde{I}_t(\hat{K}_{mn}) \cdot \frac{\cos s'z \sin s't}{s'} e_{mn}(\hat{\rho}_T - \hat{\rho}')] \quad (5.1-5)$$

where $\hat{\rho}_T$ is the location of the center of the testing function, and $\hat{\rho}'$ is the probe location. \tilde{I}_t is the Fourier transform of the feed current distribution in the \hat{x} and \hat{y} directions. As discussed above, the negative of the impressed phase shift is used in Equation (5.1-5).

Several feed current distributions were tried. An infinitesimally thin probe used by other authors for the single patch problem on thin substrates does not work well here due to convergence problems. In particular, as the the number of basis and testing functions is increased, the solution does not converge due to an inability to model the peaked

feed current. A possible solution to this problem is to extract the behavior of the current distribution in the vicinity of the feed probe, as done by Chew and Kong for the circular patch [15]. Ideally, a cylindrical probe would be used to model the coaxial feed probe, with the current flowing on the exterior of the cylinder. While this model would not be difficult to incorporate into the spectral sum, it makes the convolution integrals of the spatial sum considerably more complicated. As a compromise, a square current distribution was used

$$I_t(\vec{\rho}') = p(E_w; x - x') p(E_w; y - y') \quad (5.1-6)$$

where $\vec{\rho}' = \hat{x}'x + \hat{y}'y$ is the feed location, and E_w is the half-width of the feed.

Having chosen the feed current distribution, the application of the acceleration technique is straightforward and follows the previous examples. The singular integral in the spatial sum is evaluated with the use of I_6 in Table 3.4. For certain scan planes a factor of two savings in fill time is obtained through symmetry by placing the probe in the center of one dimension of the patch. However, filling the excitation matrix still accounts for a significant portion of the fill time.

5.1.3. The voltage matrix

After solving the matrix equation for the current coefficients a_p and b_q , as given in Equation (2.3-10), the impedance of the antenna can be determined. For convenience, the current coefficients will be denoted as I_r . The impedance of the antenna is obtained as

$$Z_{in} = \sum_{r=1}^R I_r \langle E_r, J_s \rangle + jX_L \quad (5.1-7)$$

where E_r is the field of the r th basis function, and J_s is the probe current

$$J_s(\vec{\rho}) = I_t(\vec{\rho}') p(t; z - t/2) \quad (5.1-8)$$

R is of course equal to the total number of basis functions. Other than the sign of the phase shift vector $\vec{\beta}_0$, the inner product $\langle E_r, J_s \rangle$ is given by Equation (5.1-5), with \tilde{J}_r substituted for \tilde{T}_i . Because rooftop functions have been used for both testing and basis functions, the excitation and voltage matrices are equivalent if there is no applied phase shift. Thus the use of Galerkin's method results in a significant savings in execution time for this important case.

Because the feed currents are not included in the integral equation, the self impedance of the feed probe is added as a correction factor in Equation (5.1-7). The self impedance per unit length of an infinite wire is given by [49,17]

$$X_L = \frac{\eta_0 t}{\lambda_0} \log \frac{1}{2\pi E_w \sqrt{\epsilon_r} \cdot 0.5902} \quad (5.1-9)$$

The use of this formula is based on the assumptions that the feed current is constant and that the probe is sufficiently removed from the patch edges that it can be considered to be in an infinite parallel-plate waveguide. If these conditions are met, this correction formula is valid, to the accuracy of the thin-wire approximation used to obtain such a simple expression [49]. This approximation has been tested and found to be very accurate even for probes with diameters as large as $0.05 \lambda_0$. The factor of 0.5902 is the equivalent radius of a square of side length 1,

based on equal static capacitances [75]. This approximate correction, not strictly applicable here, is used in an attempt to compensate for the use of a square current distribution.

5.2. Numerical results

5.2.1. Scattering from square plates

Unfortunately, no computed or measured results for the impedance of large microstrip arrays using individual probe feeds could be found in the literature. Glisson and Wilton have computed current distributions for square plates in free space excited by a normally incident plane wave [54,76]. Based on the successful approximation of the single dipole antenna in free space with the array solution, these results were used as an initial test of the patch array program.

The current distribution on a $0.15 \lambda_0$ square plate in a rectangular array, with $S_1 = S_2 = 3.1 \lambda_0$, was computed first. The array plane was also $3.1 \lambda_0$ above the ground plane, and to agree with Glisson and Wilton's results, a normally incident \hat{y} polarized plane wave was normalized to the value of η_0 volts/ λ_0 at the array plane, where η_0 is the intrinsic impedance of free space. Ten subpatches were used in both the \hat{x} and \hat{y} directions, for a total of 180 basis functions. The resulting current distributions are shown in Figures 5.2a and 5.2b. The results agree well with the free-space case. As expected, as the spacing is changed, the numerical values oscillate somewhat. As an example, the same case with an array spacing of $2.2 \lambda_0$ is shown in Figures 5.3a and 5.3b. Qualitatively, there is little difference, but the values of the current peaks change somewhat.

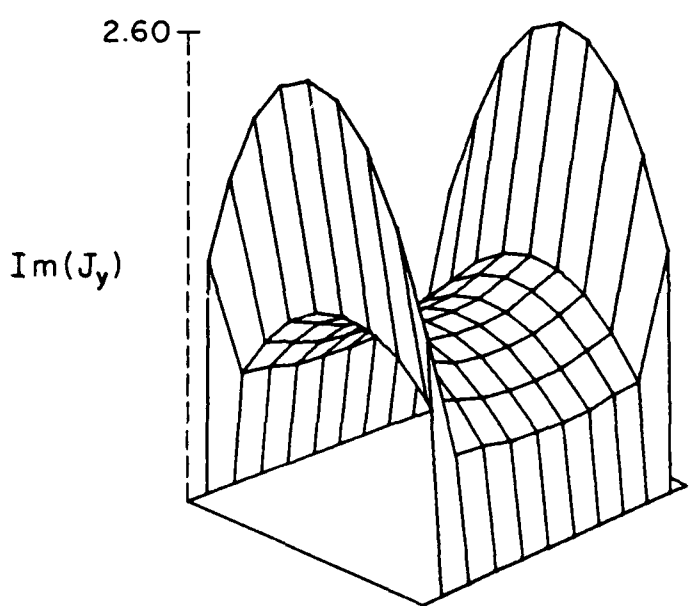
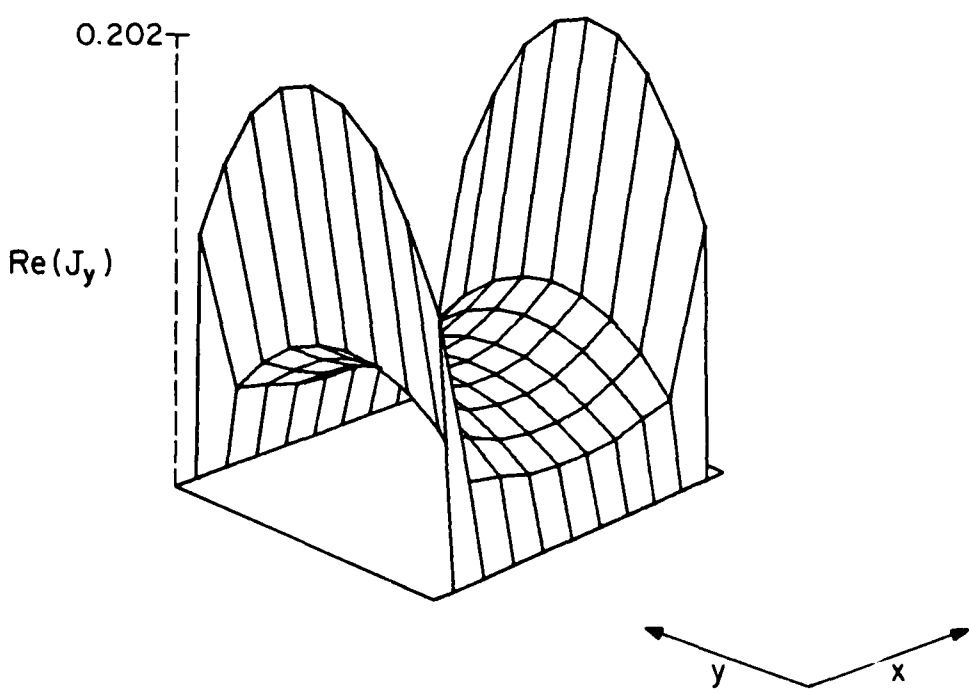


Figure 5.2a. \hat{y} component of current induced on a $0.15 \lambda_0$ square plate in an infinite array by a normally incident plane wave ($S_1 = S_2 = 3.1 \lambda_0$)

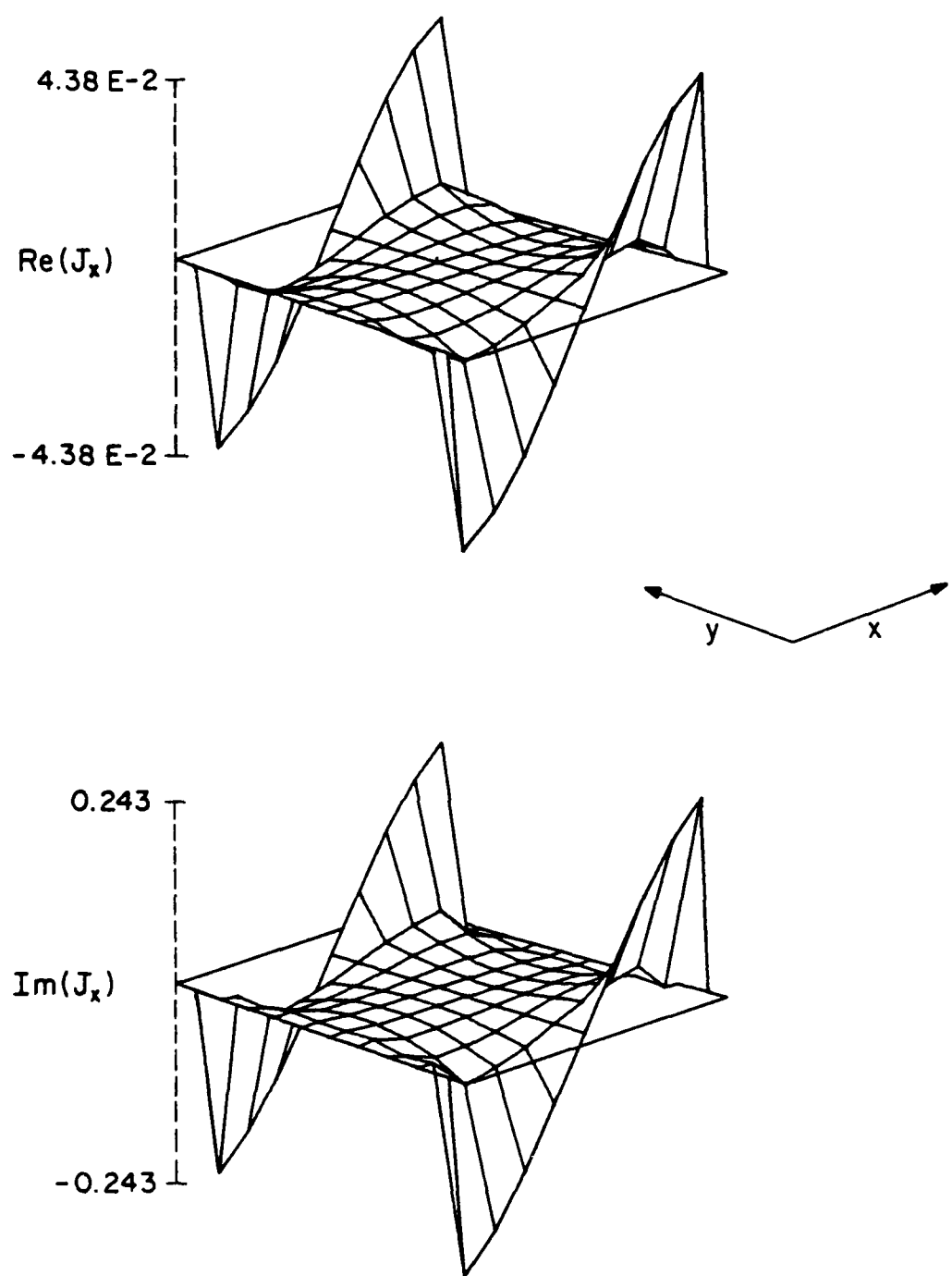


Figure 5.2b. \hat{x} component of current induced on a $0.15 \lambda_0$ square plate in an infinite array by a normally incident plane wave ($S_1 = S_2 = 3.1 \lambda_0$).

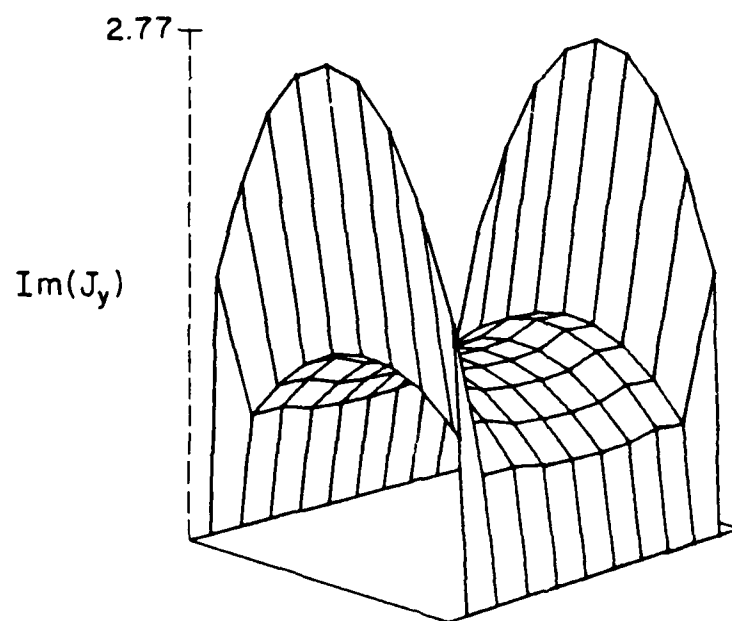
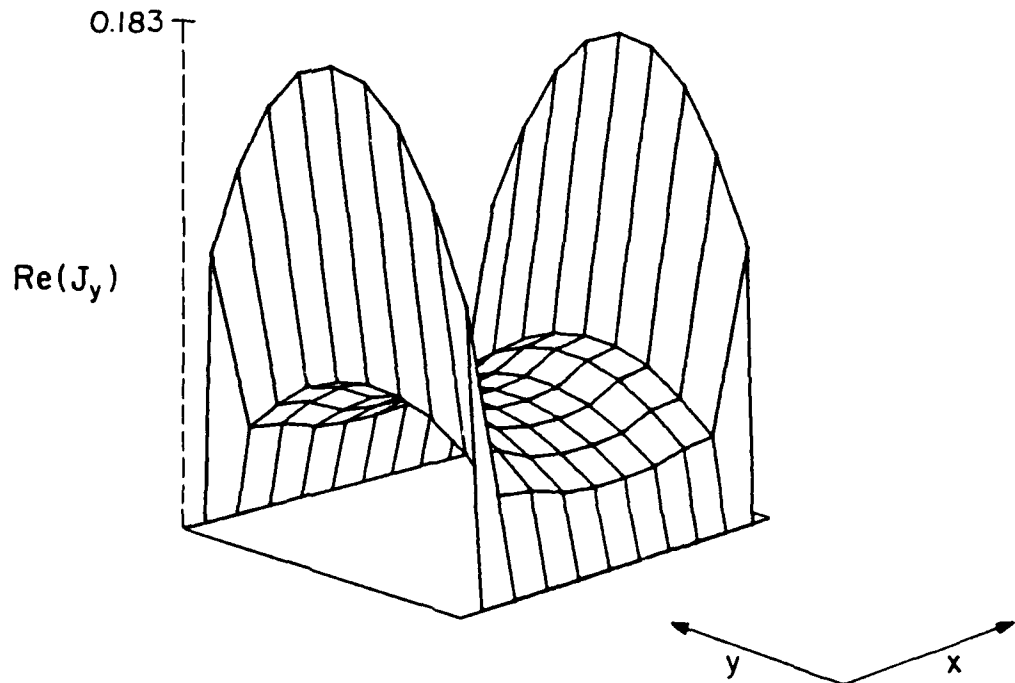


Figure 5.3a. y component of current induced on a $0.15 \lambda_0$ square plate in an infinite array by a normally incident plane wave ($S_1 = S_2 = 2.2 \lambda_0$).

RD-R169 011

A STUDY OF MICROSTRIP ANTENNAS FOR MULTIPLE BAND AND
HIGH FREQUENCY OPERA. (U) ILLINOIS UNIV AT URBANA DEPT
OF ELECTRICAL AND COMPUTER ENGIN. Y T LO ET AL.

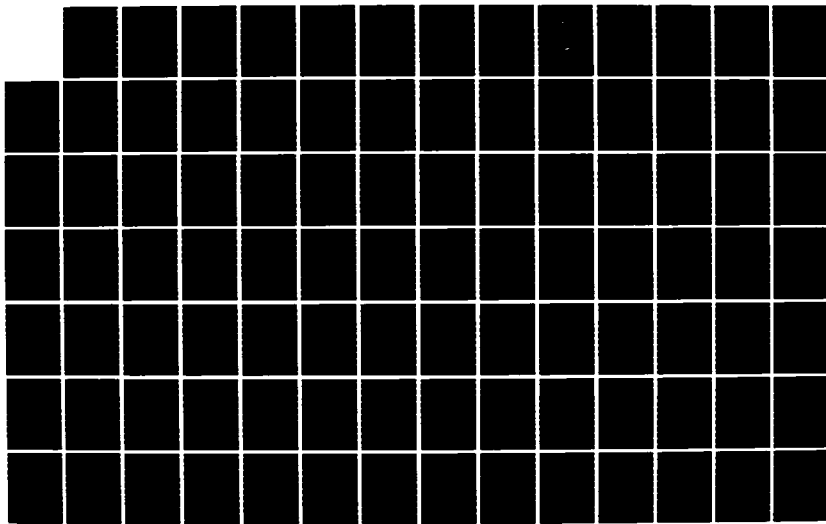
3/4

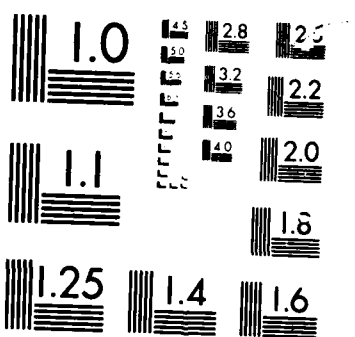
UNCLASSIFIED

MAR 86 UILU-EM-84-15 RADC-TR-86-8

F/G 9/5

NL





MICROCHART

11-101

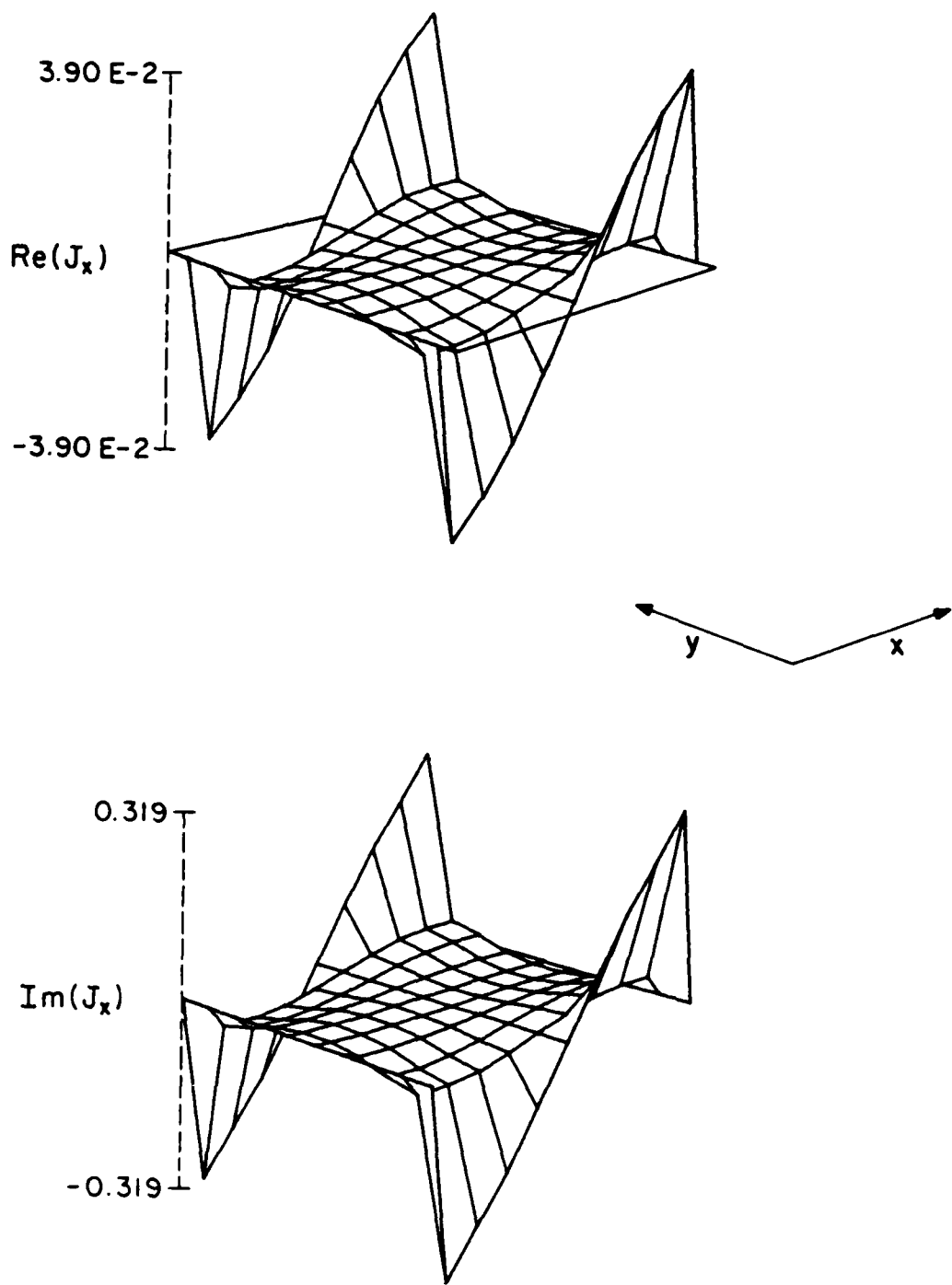


Figure 5.3b \rightarrow x component of current induced on a $0.15 \lambda_0$ square plate in an infinite array by a normally incident plane wave ($S_1 = S_2 = 2.2 \lambda_0$).

As another example, the current distribution on a $1.0 \lambda_0$ square plate with the same excitation is shown in Figures 5.4a and 5.4b. In this case the array spacing was $3.1 \lambda_0$. Again, the current distribution is in good agreement with results published by Glisson and Wilton.

5.2.2. Arrays of microstrip patches

The examples of the previous section are not a complete check on the solution, of course. It is hoped that a series of experiments can be performed in the future on a large array to further verify the solution. Because of the asymmetries in the current distribution due to the probe feed, which will be demonstrated next, a waveguide simulator experiment such as used to verify the results in Chapter 4 is not strictly valid. While the effect of the feed may not significantly affect the experiment, it is felt that an experiment on an actual array would provide a better initial test of the results.

As discussed in Chapter 4, one check of the validity of a moment method solution is to increase the number of basis functions and test for convergence. An example of the convergence of the impedance of an element in an infinite microstrip patch array is given in Table 5.1. In this example, a rectangular lattice with $S_1 = S_2 = 0.5 \lambda_0$ was used, with $t = 0.1 \lambda_0$ and $\epsilon_r = 2.53$. The patch was $0.3 \lambda_0$ square, and was fed at the center of one side, $0.045 \lambda_0$ from the edge. The feed had a half-width of $0.025 \lambda_0$. Such a large feed was used to get convergence in a reasonable number of basis functions. Thin feeds are handled just as easily, except that more basis functions are required to represent the resulting current distribution. Table 5.1 shows the answer is relatively well converged with 9 subpatches in the \hat{x} and \hat{y} directions, for a total of 220 matrix elements, including the excitation matrix.

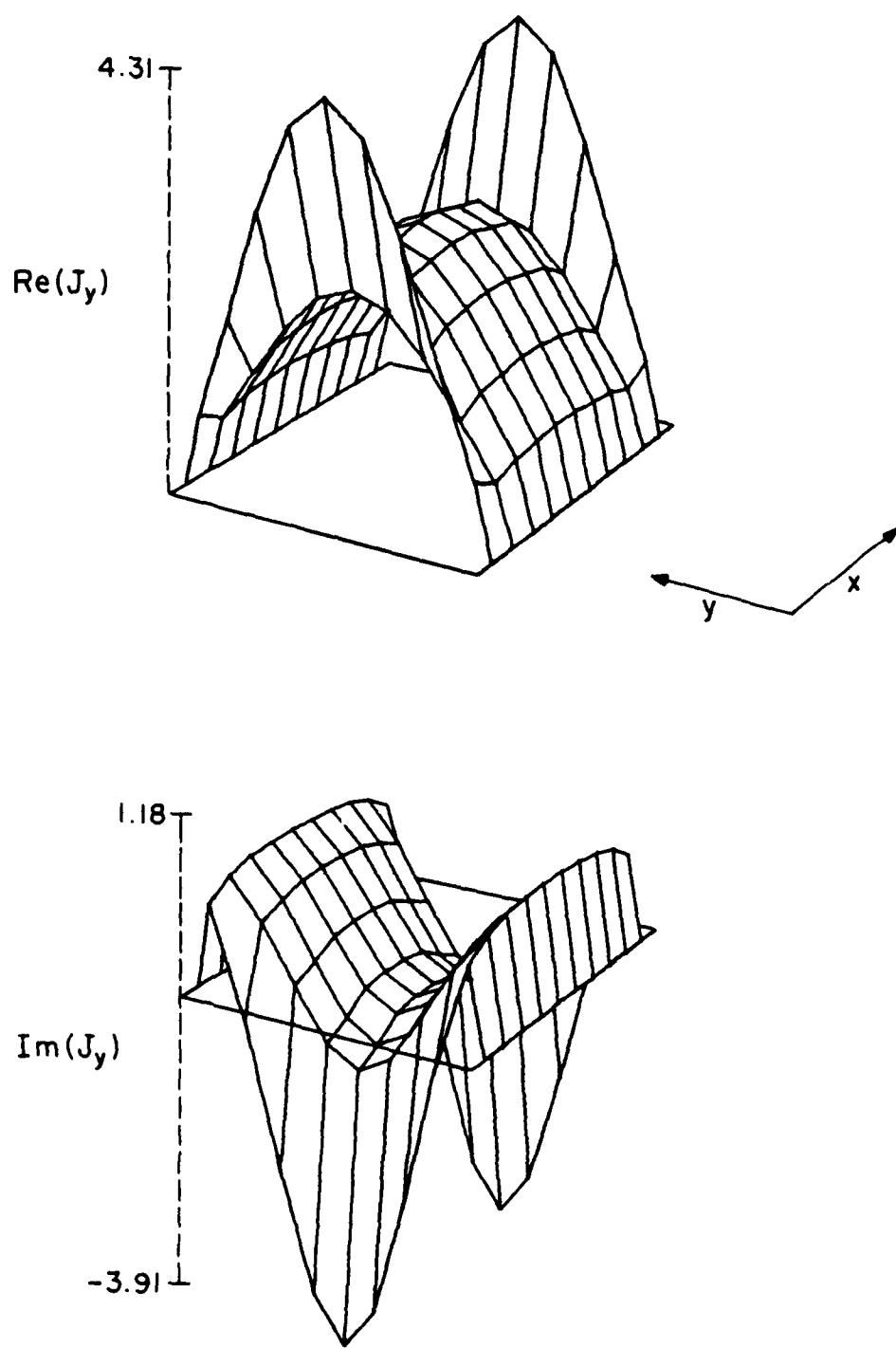


Figure 5.4a y component of current induced on a $1.0 \lambda_0$ square plate in an infinite array by a normally incident plane wave ($S_1 = S_2 = 3.1 \lambda_0$).

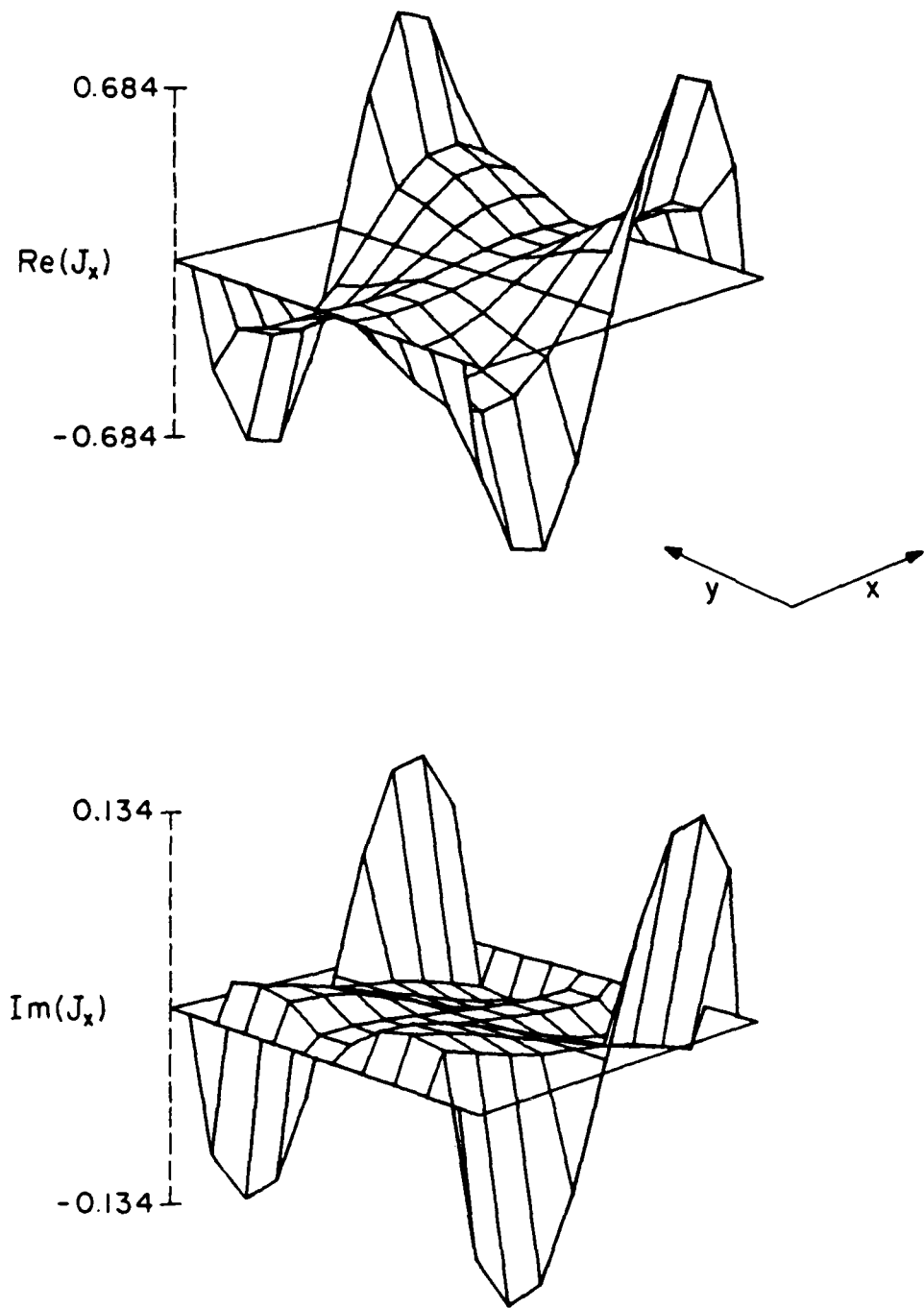


Figure 5.4b. \hat{x} component of current induced on a $1.0 \lambda_0$ square plate in an infinite array by a normally incident plane wave ($S_1 = S_2 = 3.1 \lambda_0$).

TABLE 5.1

CONVERGENCE AND EXECUTION TIMES FOR MOMENT METHOD SOLUTION OF MICROSTRIP PATCH ARRAY, USING THREE DIFFERENT INTEGRATION TECHNIQUES

No. of Subsections	"Exact"	144 point Gaussian Quadrature	64 point Gaussian Quadrature
3	$44.3 + j124.4$ (4.1 sec)	$44.1 + j124.2$ (1.03)	$43.6 + j124.0$ (0.69)
5	$41.3 + j145.7$ (13.2 sec)	$41.1 + j145.6$ (3.52)	$40.8 + j145.3$ (2.37)
7	$36.5 + j154.7$ (18.1 sec)	$36.4 + j154.6$ (7.66)	$36.1 + j154.4$ (5.27)
9	$34.0 + j167.1$ (37.2 sec)	$33.8 + j166.9$ (13.22)	$34.0 + j167.0$ (9.31)
11	$32.5 + j167.8$ (53.5 sec)	$32.3 + j167.6$ (20.41)	$32.1 + j167.4$ (14.26)

Also included in Table 5.1 are results for the same problem using three different methods of evaluating the convolution integrals of the spatial sum. The first columns show the results using the adaptive numerical integration routine DBLIN, described in Chapter 3. The remaining columns give the corresponding results and execution times obtained using 144 and 64 point Gaussian quadratures. Although the savings in execution time varied with the number of subpatches, approximately a factor of four improvement is obtained using the 64 point Gaussian quadrature, with little loss in accuracy. Using 11 subpatches, and including the excitation matrix, a total of 335 distinct matrix elements need to be evaluated for the zero phase shift case. Using the 64 point Gaussian quadrature, the average time to evaluate the matrix elements was 0.043 second. Recall from Chapter 4 that without any acceleration, approximately one second per matrix element was required, using rooftop basis functions and linear testing, only slightly less smooth than this case. The same problem would then require approximately 6.5 minutes of execution time on the CDC 6600.

The current distribution for the patch of the previous example is shown in Figures 5.5a and 5.5b. The imaginary component of the \hat{y} directed current is very smooth, and probably can be adequately represented with one sinusoidal mode, assuming the effect of the edge condition can be neglected, as concluded by Deshpande and Bailey [17]. The real component, on the other hand, is dominated by the peaked behavior in the feed region. Similarly, the real component of the \hat{x} directed current is essentially zero everywhere but at the edges and near the feed point. These results clearly illustrate the major difficulty in analyzing probe fed patch

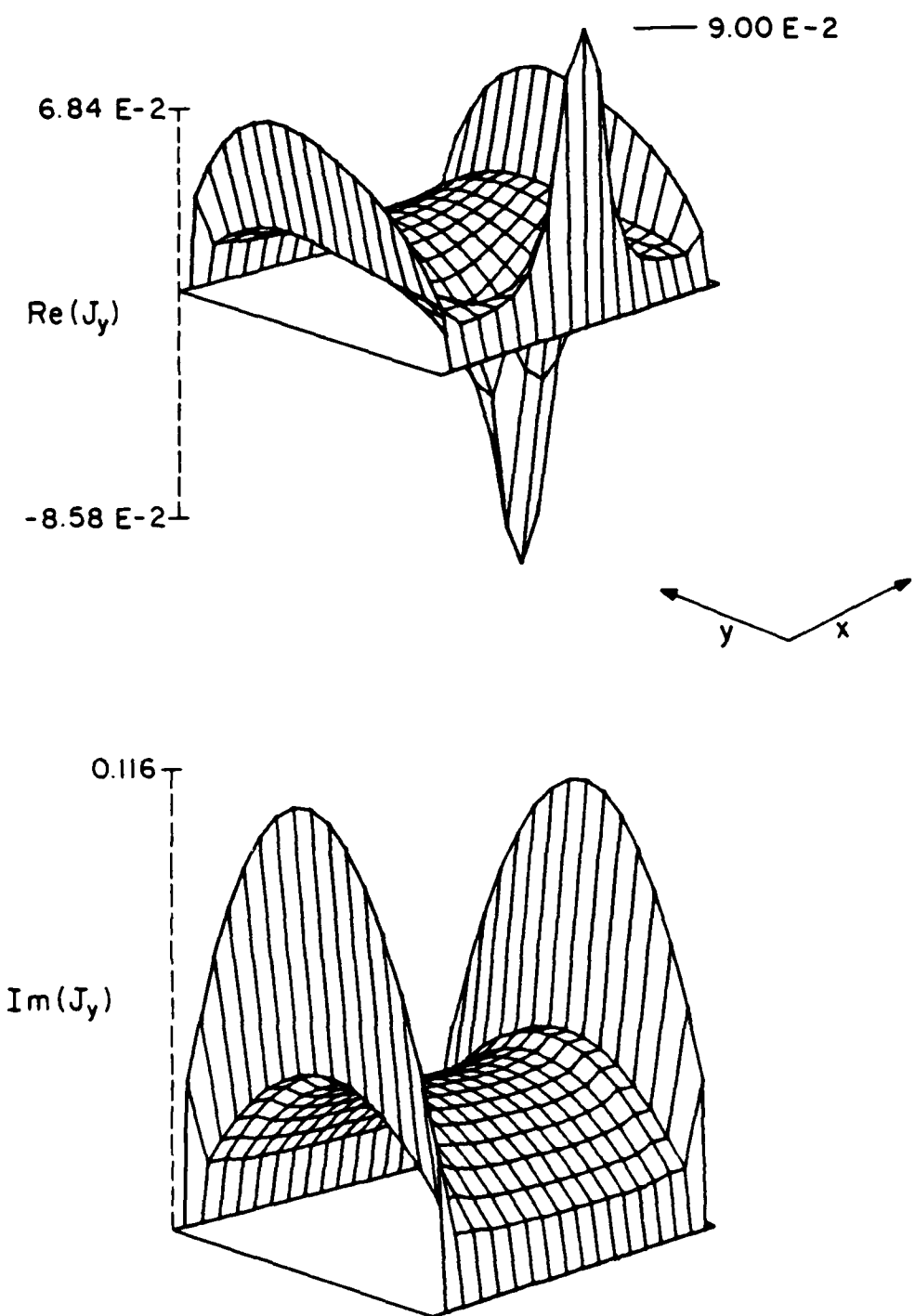


Figure 5.5a. \hat{y} component of current distribution on a probe fed microstrip patch.

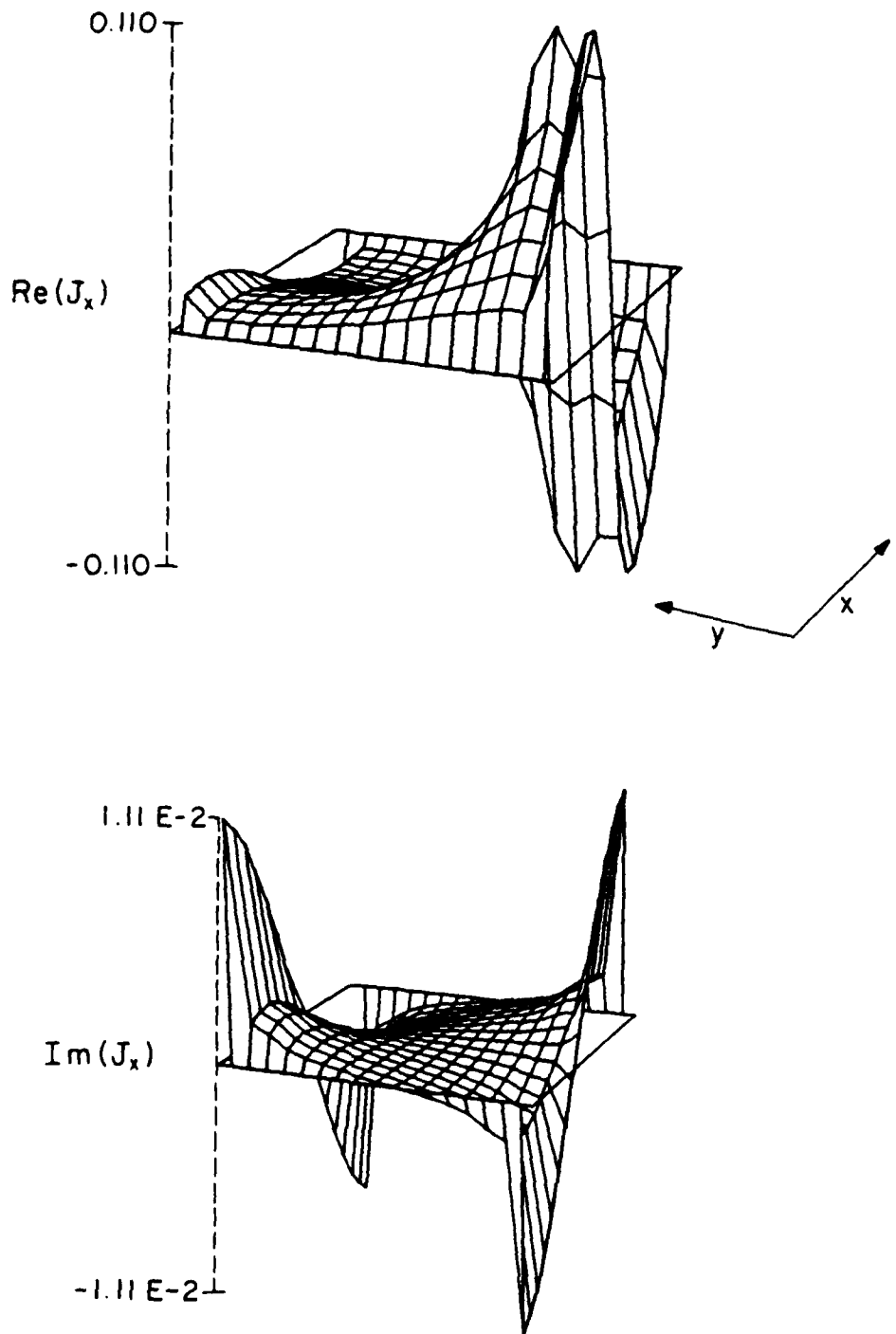


Figure 5.5b. \hat{x} component of current distribution on a probe fed microstrip patch.

arrays on thick substrates; in order to adequately model the current distribution a large number of basis functions is required.

Results for the impedance as a function of frequency for two probe-fed microstrip patch arrays are shown in Figures 5.6 and 5.7. The array dimensions are chosen such that at 0.9 GHz the dimensions are the same as in the previous examples. Two substrate thicknesses were used, $t = 0.08 \lambda_0$ and $t = 0.1 \lambda_0$, at 0.9 GHz. In both Figures 5.6 and 5.7 the 10 plotted points are, proceeding clockwise, 0.7 to 1.0 GHz by 0.05 GHz, and 1.1, 1.2 and 1.25 GHz. As expected from results for single patches [17,18,20], the curves for these patches on thick substrates are on the inductive side of the Smith chart. Consistent with this, the array on the thicker substrate is more inductive. The curves could be moved towards the center of the Smith chart if desired by either using a matching network or by moving the feed location to improve the match to a 50 ohm line. However, due to the cost and storage requirements of an off-center feed this was not attempted.

Obviously, the feed presents a difficult problem. Other feed models giving smoother excitation fields are one possibility. Alternatively, including a basis function which models the feed behavior, as done by Chew and Kong [15], appears to be a reasonable approach. It is evident from the current distributions in Figures 5.5a and 5.5b that extracting the feed region current would leave a relatively smooth current which could be represented with relatively few basis functions. This would help alleviate the matrix storage problem which arises with the present technique.

While the feed problem is important, useful information about the array can be obtained by considering the scattering problem. All of the

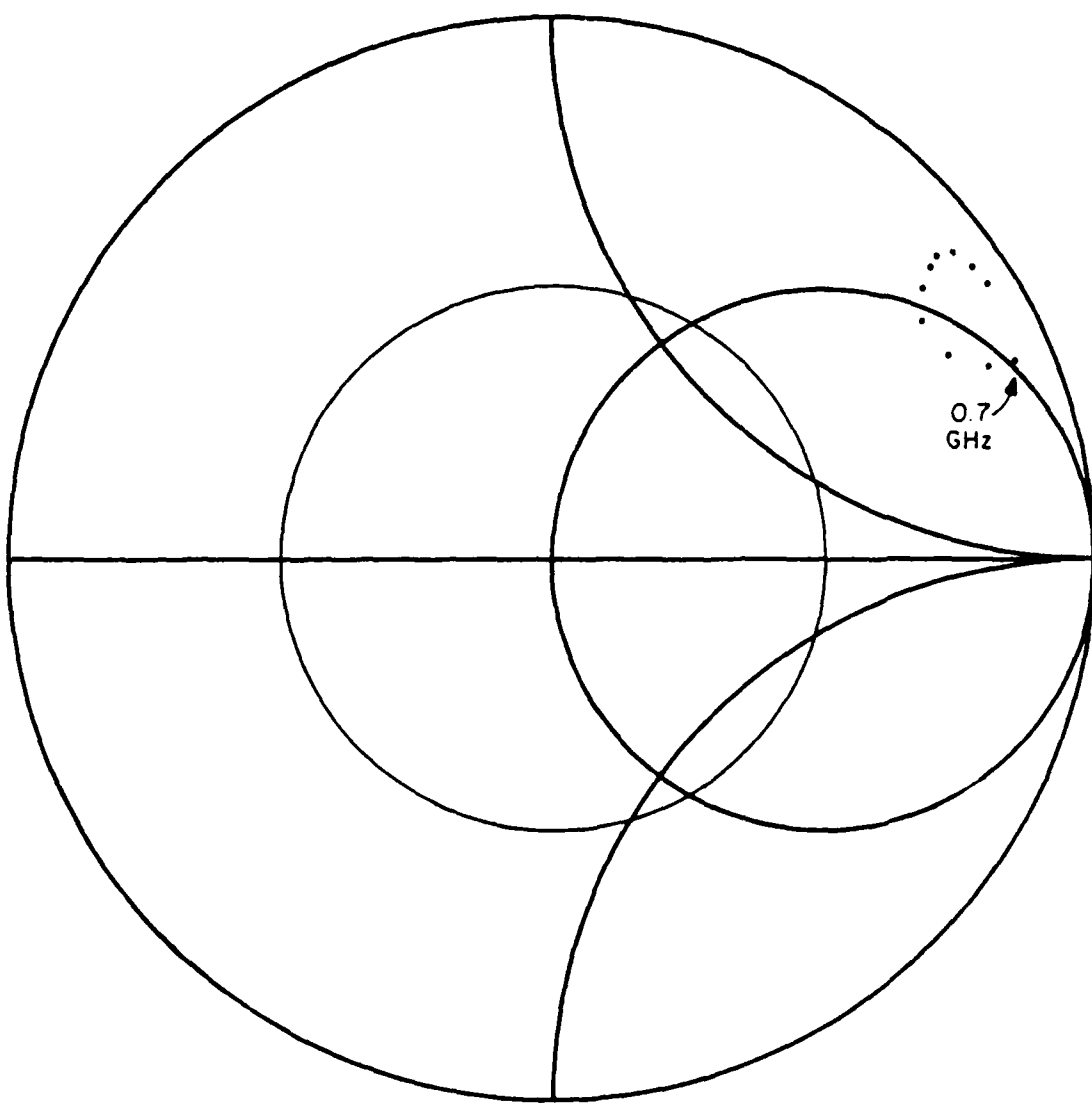


Figure 5.6. Impedance of an element in an infinite rectangular array of microstrip patches on a thick substrate ($Z_0 = 50\Omega$) $t = 26.7\text{mm}$, $\epsilon_r = 2.53$, $S_1 = S_2 = 167\text{mm}$, $a = b = 100\text{mm}$.

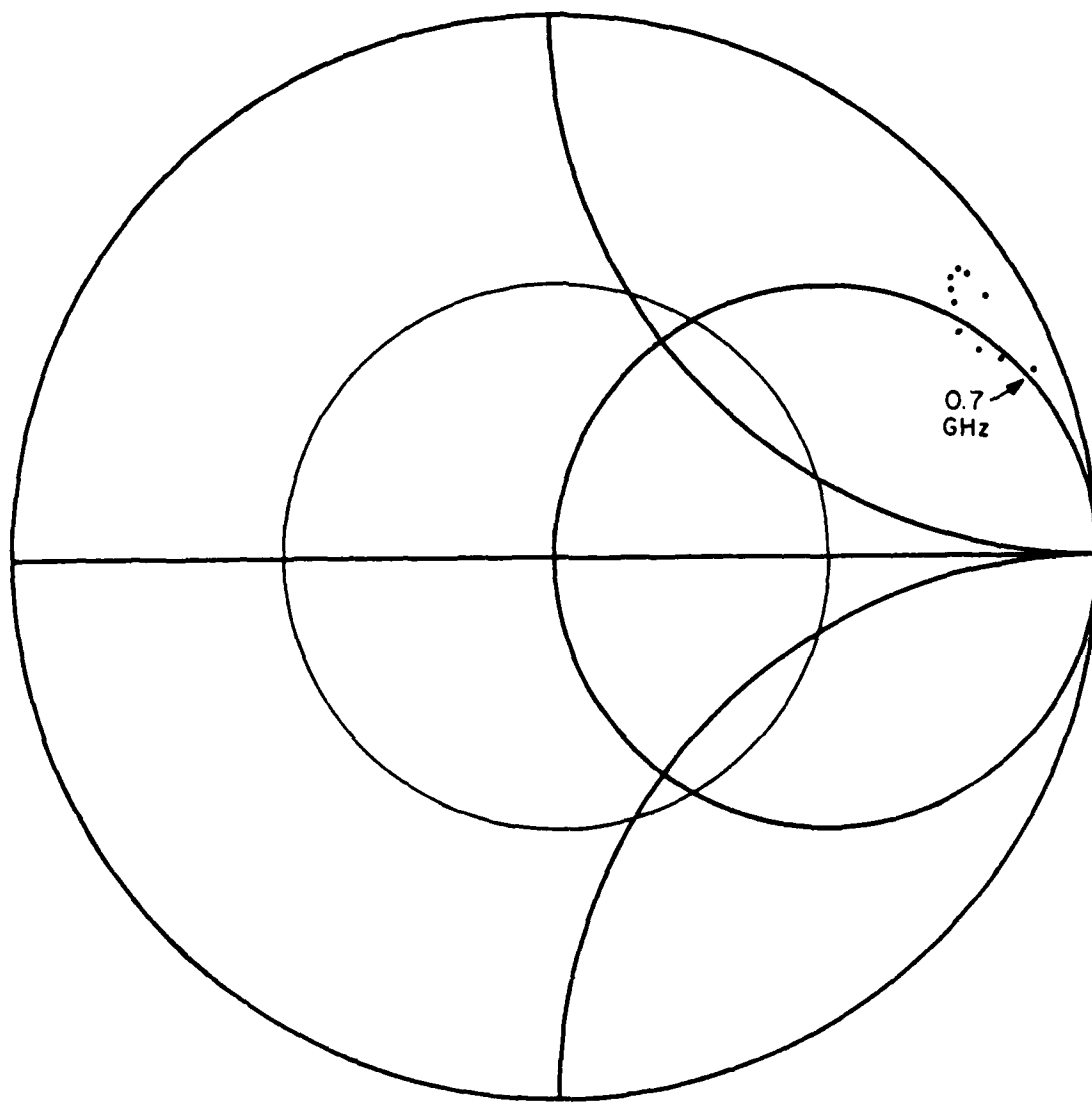


Figure 5.7. Impedance of an element in an infinite rectangular array of microstrip patches on a thick substrate ($Z_0 = 50\Omega$) $t = 33.3\text{mm}$, $\epsilon_r = 2.53$, $S_1 = S_2 = 167\text{mm}$, $a = b = 100\text{mm}$.

information about the basic array is still included in the Z matrix, including bandwidth and scan performance information. Thus the scattering problem essentially provides a source free solution, somewhat similar to analyzing a dipole using a delta gap feed. While the delta gap feed is accurate for monopoles and dipoles with small feed regions, a more complete analysis including the feed structure is needed for the more general case [74]. Nevertheless, the feed-independent models can provide very useful information about the array.

As an example, Bailey and Deshpande, using a single mode approximation to the current distribution, plot the real and imaginary values of the current coefficient as a function of frequency and use the result to predict the resonant frequency and bandwidth of the patch [19]. Because of the difficulty in defining a resonant frequency for a patch on a thick substrate, where the imaginary component of the current may never change sign, a slightly different approach will be used in this example. Using the same array as in the previous examples, the real and imaginary parts of the current at the center of the patch were calculated as a function of frequency for five different substrate thicknesses. The results for the cases of $t = 0.04 \lambda_0$ and $t = 0.08 \lambda_0$ at 0.9 GHz are shown in Figures 5.8 and 5.9. By plotting the current on a Smith chart and rotating the resulting curve until it was symmetric about the zero reactance axis, the Q factor of the antenna can be determined using the half-power method [77]. This approach is used due to the asymmetry of the current as plotted in Figures 5.8 and 5.9. In this manner, the Q factor for each of the five cases was determined, and the results plotted in Figure 5.10. As expected, the Q factor decreases as the substrate

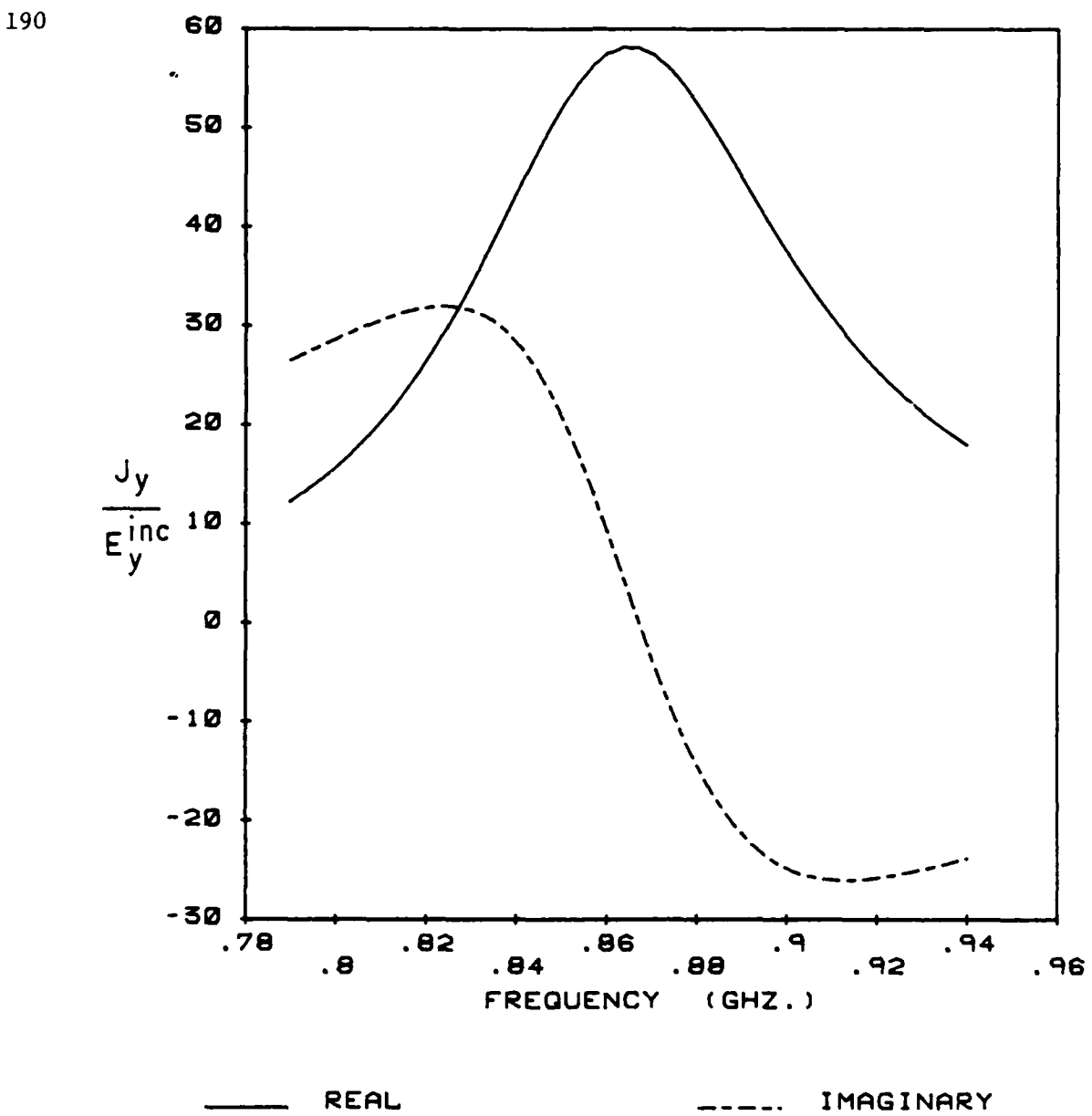


Figure 5.8. Current density induced on a microstrip patch in an infinite array by a normally incident plane wave. $S_1 = S_2 = 167\text{mm}$, $\epsilon_r = 2.53$, $a = b = 100\text{mm}$, $t = 13.3\text{mm}$.

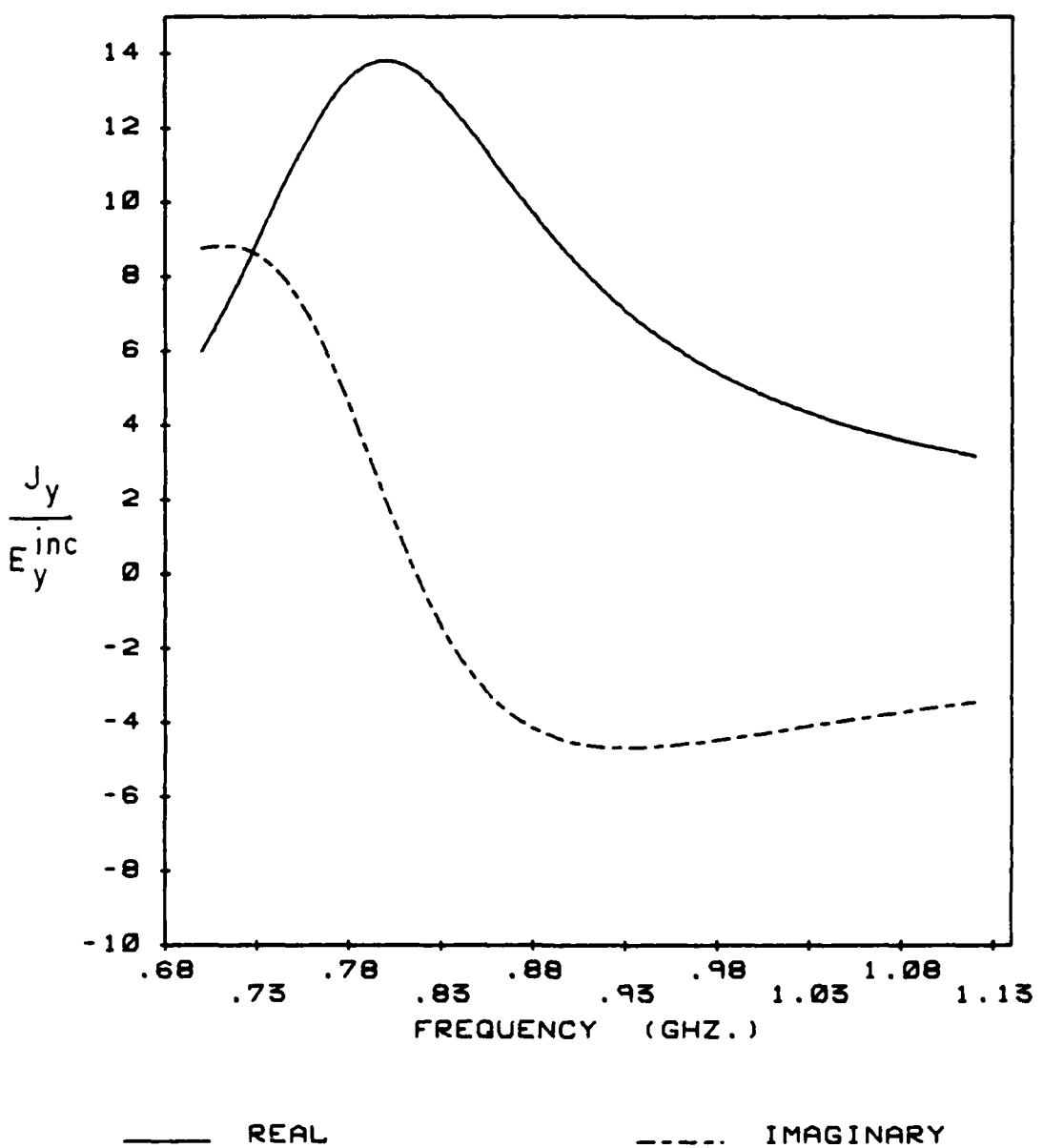


Figure 5.9. Current density induced on a microstrip patch in an infinite array by a normally incident plane wave. $S_1 = S_2 = 167\text{mm}$, $\epsilon_r = 2.53$, $a = b = 100\text{mm}$, $t = 26.6\text{mm}$.

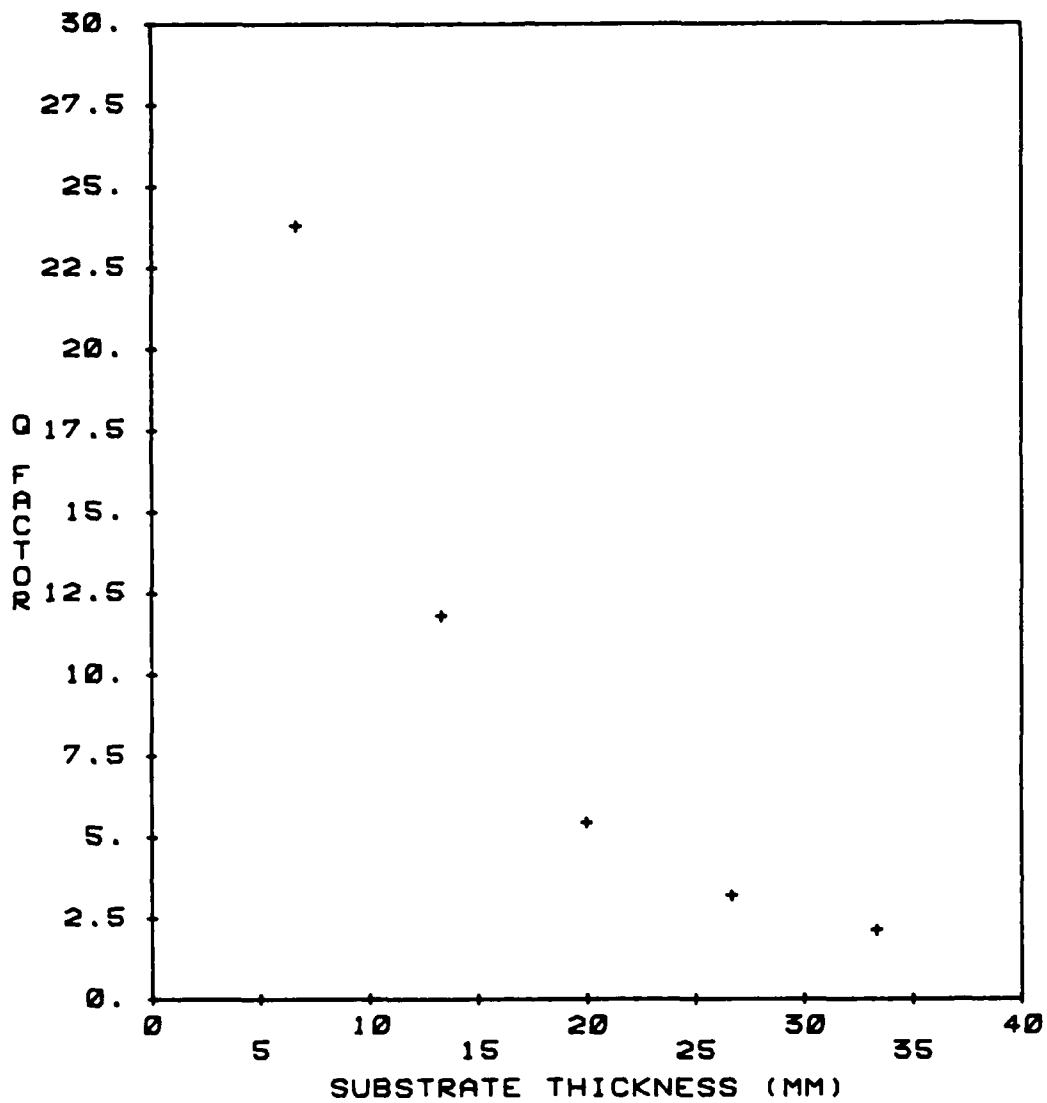


Figure 5.10. Q factor for an infinite microstrip patch array obtained from scattering current distribution. $S_1 = S_2 = 167\text{mm}$, $\epsilon_r = 2.53$, $a = b = 100\text{mm}$.

thickness increases. For the thicker substrates, a very small Q is obtained, indicating a correspondingly wide bandwidth.

The examples in this chapter demonstrate an efficient solution for complex current distributions on a probe fed microstrip patch, allowing a variety of problems to be solved. At the same time, they point out several remaining difficulties. First, computer storage is a major problem. An alternate technique to solve the matrix equation, such as an iterative technique, should be investigated. Second, the feed region becomes a significant problem for patches on thick substrates, and the need for a more rigorous analysis is indicated.

CHAPTER 6

CONCLUSION

Infinite arrays of microstrip antennas on electrically thick substrates have been analyzed using an efficient solution technique. In Chapter 2, a standard infinite array formulation was used to obtain an integral equation for the periodic current distribution, which was then cast into matrix form using the method of moments. The computation of the matrix elements, ordinarily very time-consuming, was performed efficiently using series acceleration techniques. Because the Green's function for the dielectric slab was used, the solution is not restricted to thin substrates, as are many other techniques. In addition, the efficient computation of the matrix elements allows large numbers of basis functions to be used with reasonable execution times, providing a more general solution than previously available.

The solution retained the simplicity of the infinite array formulation, while significantly improving the efficiency. In particular, the geometry of the problem manifested itself primarily in the spectral domain, where it was easily handled, allowing easy alteration of the Green's function to that of a different medium. The singularity in the Green's function, which ordinarily leads to slow convergence in a spectral domain sum, was extracted and handled easily in the spatial domain as a singular integral. Because only the asymptotic form of the Green's function singularity was extracted, the singular integral was essentially independent of the media. Two examples of the application of the acceleration technique were considered in detail in Chapter 3.

In Chapter 4, the method was applied to the analysis of infinite arrays of microstrip dipoles. In an attempt to further improve the efficiency of the solution, several thin-wire approximations were made, and their range of validity studied. It was found that the approximations significantly improved the efficiency of the solution, but were only valid for dipoles with widths less than approximately $0.02\lambda_0$. A series of waveguide simulator experiments were conducted which demonstrated the validity of the theory. Several arrays were modeled, both with and without radomes. Because the effect of surface waves was included through the use of the Green's function for the grounded dielectric substrate and the infinite array formulation, blind angles in the array scan performance were accurately predicted.

An initial analysis of arrays of microstrip patches on thick substrates was discussed in Chapter 5. Because of the lack of published results and the complexity of a suitable experiment, the theory was initially tested by treating the array of patches as a scatterer. Good agreement with independently computed current distributions on single plate scatterers was observed if the array spacing was several times the plate size, and for similar separations from the ground plane. Based on this agreement and the success of the dipole results, several examples were computed for probe-fed microstrip patches, using a simplified feed model commonly used in the analysis of patches on very thin substrates. In one example, the current distribution on a patch was computed, which clearly demonstrated that a major difficulty in analyzing probe-fed microstrip patches is in adequately representing the currents in the feed region.

Several areas remain in need of further investigation. First, it is felt that a series of experiments are needed to provide confirmation for theoretical results. Lacking such data, it is unclear to what extent the feed region model needs to be improved, but clearly a more detailed analysis would be beneficial. In addition, the possibility of extracting the feed region currents, leaving a smooth current distribution on the patch should be investigated. For example, a single function closely modeling the feed region behavior could be included in the set of basis functions. Finally, in order to analyze general antenna elements many basis functions will be required. Although the improved efficiency of this technique keeps the matrix fill-time reasonable, a practical limitation on the number of basis functions that can be used exists due to either memory requirements or matrix inversion times. Thus, alternative methods of solving the matrix equation should be investigated.

REFERENCES

- [1] R. F. Harrington, Field Computation by Moment Methods. New York: Macmillan, 1968.
- [2] W. F. Richards, J. R. Zinecker, D. R. Wilton, S. Singh, Y. T. Lo and S. M. Wright, "Acceleration of periodic Green's functions in free space," URSI Symposium Proceedings, Houston TX, p. 81, May 23-26, 1983.
- [3] S. M. Wright, Y. T. Lo, W. F. Richards and J. R. Zinecker, "Efficient evaluation of the periodic Green's function for a grounded dielectric substrate," URSI Symposium Proceedings, Houston TX, p. 83, May 23-26, 1983.
- [4] D. R. Wilton, S. Singh and W. F. Richards, "Application of series acceleration techniques to problems involving periodic media," URSI Symposium Proceedings, Houston TX, p. 82, May 23-26, 1983.
- [5] K. R. Carver and J. W. Mink, "Microstrip antenna technology", IEEE Trans. Antennas Propagat., vol. AP-29, no. 1, pp. 1-24, Jan. 1981.
- [6] R. J. Mailloux, J. McIlvenna, and N. Kernweis, "Microstrip array technology", IEEE Trans. Antennas Propagat., vol. AP-29, no. 1, pp. 25-38, 1981.
- [7] G. A. Deschamps, "Microstrip microwave antennas," presented at the 3rd USAF Symp. on Antennas, 1953.
- [8] R. E. Munson, "Conformal microstrip antennas and microstrip phased arrays," IEEE Trans. Antennas Propagat., vol. AP-22, no. 1, pp. 74-77, Jan. 1974.
- [9] R. F. Harrington, Time Harmonic Electromagnetic Fields. New York: McGraw-Hill, 1961.
- [10] Y. T. Lo, D. Solomon, and W. F. Richards, "Theory and experiment on microstrip antennas," IEEE Trans. Antennas Propagat., vol. AP-27, no. 2, pp. 137-145, Mar. 1979.
- [11] W. F. Richards and Y. T. Lo, "An improved theory for microstrip antennas and applications", IEEE Trans. Antennas Propagat., vol. AP-29, no. 1, pp. 38-46, Jan. 1981.
- [12] E. H. Newman and P. Tulyathan, "Analysis of microstrip antennas using moment methods," IEEE Trans. Antennas Propagat., vol. AP-29, no. 1, pp. 47-53, Jan. 1981.
- [13] G. H. Knittel, A. Hessel and A. A. Oliner, "Element pattern nulls in phased arrays and their relation to guided waves," Proc. IEEE, vol. 56, no. 11, pp. 1822-1836, Nov. 1968.

- [14] T. Itoh and W. Menzel, "A full wave analysis method for open microstrip structures," IEEE Trans. Antennas Propagat., vol. AP-29, no. 1, pp. 63-68, Jan. 1981.
- [15] W. C. Chew and J. A. Kong, "Analysis of a circular microstrip disk antenna with a thick dielectric substrate," IEEE Trans. Antennas Propagat., vol. AP-29, no. 1, pp. 68-76, Jan. 1981.
- [16] K. Araki and T. Itoh, "Hankel transform domain analysis of open circular microstrip radiating structures", IEEE Trans. Antennas Propagat., vol. AP-29, no. 1, pp. 84-89, Jan. 1981.
- [17] M. D. Deshpande and M. C. Bailey, "Input impedance of microstrip antennas," IEEE Trans. Antennas Propagat., vol. AP-30, no. 4, pp. 645-650, Nov. 1982.
- [18] D. M. Pozar, "Input impedance and mutual coupling of rectangular microstrip antennas," IEEE Trans. Antennas Propagat., vol. AP-30, no. 6, pp. 1191-1196, Nov. 1982.
- [19] M. C. Bailey and M. D. Deshpande, "Integral equation formulation of microstrip antennas," IEEE Trans. Antennas Propagat., vol. AP-30, no. 4, pp. 651-656, July 1982.
- [20] E. H. Newman, J. H. Richmond, and B. W. Kwan, "Mutual impedance computation between microstrip antennas," IEEE Trans. Microwave Theory Tech., vol. MTT-31, no. 11, pp. 941-945, Nov. 1983.
- [21] I. E. Rana and N. G. Alexopoulos, "Current distribution and input impedance of printed dipoles," IEEE Trans. Antennas Propagat., vol. AP-29, no. 1, pp. 99-105, Jan. 1981.
- [22] N. G. Alexopoulos and I. E. Rana, "Mutual impedance computation between printed dipoles," IEEE Trans. Antennas Propagat., vol. AP-29, no. 1, pp. 106-111, Jan. 1981.
- [23] R. Mittra and T. S. Li, "A spectral domain approach to the numerical solution of electromagnetic scattering problems," AEU, vol. 29, pp. 217-222, 1975.
- [24] R. C. Hansen (Ed.), Microwave Scanning Antennas, vol. II: Array Theory and Practice. New York: Academic Press, 1966.
- [25] J. S. Herd and D. M. Pozar, "Design of a microstrip antenna array fed by a Rotman lens," IEEE/AP-S Symposium Proceedings, Boston MA, pp. 729-732, June, 1984.
- [26] E. H. Newman and J. E. Tahan, "Analysis of a linear microstrip array coupled by microstrip transmission lines," URSI Symposium Proceedings, Boston, MA, p. 126, June 1984.

- [27] H. A. Wheeler, "The radiation resistance of an antenna in an infinite array or waveguide," Proc. IRE, pp. 478-487, April 1948.
- [28] N. Amitay, V. Galindo and C. P. Wu, Theory and Analysis of Phased Array Antennas. New York: Wiley-Interscience, 1972.
- [29] E. A. Blasi, "Effects of mutual interactions on the design of various dipole arrays," TM 336, Hughes Aircraft Co., December 1953.
- [30] P. S. Carter Jr., "Mutual impedance effects in large beam scanning arrays," IRE Trans. Antennas Propagat., vol. AP-8, no. 3, pp. 276-285, May 1960.
- [31] L. Stark, "Microwave theory of phased-array antennas - a review," Proc. IEEE, vol. 62, no. 12, pp. 1661-1701, Dec. 1974.
- [32] B. A. Munk and G. A. Burrell, "Plane-wave expansion for arrays of arbitrarily oriented piecewise linear elements and its application in determining the impedance of a single linear antenna in a lossy half space," IEEE Trans Antennas Propagat., vol. AP-27, no. 3, pp. 331-343, May 1979.
- [33] D. R. Pflug and H. K. Schuman, "Radiation from infinite arrays of microstrip antennas," IEEE/AP-S Symposium Proceedings, Boston, MA, pp. 733-736, June 1984.
- [34] S. M. Wright and Y. T. Lo, "Efficient analysis for infinite microstrip dipole arrays," Electron. Lett., vol. 19, no. 24, pp. 1043-1045, November 24, 1983.
- [35] S. M. Wright and Y. T. Lo, "An efficient moment method analysis of infinite microstrip arrays," URSI Symposium Proceedings, Boston, MA, p. 125, June 1984.
- [36] D. M. Pozar and D. H. Schaubert, "Scan blindness in infinite phased arrays of printed dipoles," personal communication, September 21, 1983.
- [37] D. M. Pozar and D. H. Schaubert, "Analysis of infinite phased arrays of printed dipoles," IEEE/AP-S Symposium Proceedings, Boston, MA, pp. 737-740, June 1984.
- [38] B. J. Rubin and H. L. Bertoni, "Reflection from a periodically perforated plane using a subsectional current approximation," IEEE Trans. Antennas Propagat., vol. AP-31, pp. 829-836, Nov. 1983.
- [39] B. J. Rubin and H. L. Bertoni, "Waves guided by conductive strips above a periodically perforated ground plane," IEEE Trans. Microwave Theory Tech., vol. MTT-31, pp. 541-549, July 1983.

- [40] B. J. Rubin, "The propagation characteristics of signal lines in a mesh-plane environment", IEEE Trans. Microwave Theory Tech., vol. MTT-32, pp. 522-531, May 1984.
- [41] A. Papoulis, The Fourier Integral and Its Applications. New York: McGraw-Hill, 1962.
- [42] A. J. Poggio and E. K. Miller, Computer Techniques for Electromagnetics and Antennas, Chapter 4, R. Mittra, Ed. London: Pergamon Press, 1973.
- [43] P. C. Clemmow, The Plane Wave Spectrum Representation of Electromagnetic Fields. Oxford: Pergamon Press, 1966.
- [44] E. C. Dufort, "Finite scattering matrix for an infinite antenna array," Radio Sci., vol. 2, pp. 19-27, January 1967.
- [45] A. Sommerfeld, Partial Differential Equations in Physics. New York: Academic Press Inc., 1949.
- [46] J. N. Brittingham, E. K. Miller and J. T. Okada, "Somint: an improved model for studying conducting objects near lossy half-spaces," Rept. no. UCRL-52423, Lawrence Livermore Lab., Univ. of California, Livermore, California, 1978.
- [47] Y. Rahmat-Samii, R. Mittra and P. Parhami, "Evaluation of Sommerfeld integrals for lossy half-space problems," Electromagnetics, vol. 1, pp. 1-28, 1981.
- [48] P. E. Mayes, Electromagnetics for Engineers. Ann Arbor, Michigan: Edwards Brothers, Inc., 1965.
- [49] E. C. Jordan and K. G. Balmain, Electromagnetic Waves and Radiating Systems. New Jersey: Prentice Hall, 1968.
- [50] S. W. Lee, J. Boersma, C. L. Law and G. A. Deschamps, "Singularity in Green's function and its numerical evaluation," IEEE Trans. Antennas Propagat., vol. AP-28, no. 3, pp. 311-317, May 1980.
- [51] J. J. H. Wang, "A unified and consistent view on the singularities of the electric dyadic Green's function in the source region," IEEE Trans. Antennas Propagat., vol. AP-30, no. 3, pp. 463-468, May 1982.
- [52] D. B. Miron, "The singular integral problem in surfaces," IEEE Trans. Antennas Propagat., vol. AP-31, no. 3, pp. 507-509, May 1983.
- [53] D. R. Wilton and C. M. Butler "Effective methods for solving integral integro-differential equations," Electromagnetics, vol. 1, no. 3, pp. 289-308, July-Sept. 1981.

- [54] A. W. Glisson and D. R. Wilton "Simple and efficient numerical methods for problems of electromagnetic radiation and scattering from surfaces," IEEE Trans. Antennas Propagat., vol. AP-28, no. 5, pp. 593-603, Sept. 1980.
- [55] R. E. Collin, Field Theory of Guided Waves. New York: McGraw-Hill, 1960.
- [56] Handbook of Mathematical Functions. Ed. by M. Abramowitz and I. A. Stegun. Wash. D.C.: National Bureau of Standards, 1972.
- [57] A. Erdelyi, Asymptotic Expansions. New York: Dover, 1956.
- [58] A. Erdelyi, Ed., Tables of Integral Transforms, vol. 1, Bateman Manuscript Project. New York: McGraw-Hill, 1954.
- [59] V. W. H. Chang, "Infinite phased dipole array," Proc. IEEE, vol. 56, no. 11, pp. 1892-1900, November 1968.
- [60] C. M. Butler and T. L. Keshavamurthy, "Investigation of a radial, parallel-plate waveguide with an annular slot," Radio Sci., vol. 16, no. 2, pp. 159-169, March-April 1981.
- [61] C. M. Butler, "Analysis of a coax-fed circular microstrip antenna," Proc. Workshop Printed Ckt. Antenna Tech., pp. 13/1-13/17, New Mexico State University, Las Cruces, New Mexico, 1979.
- [62] H. B. Dwight, Tables of Integrals and other Mathematical Data. New York: Macmillan, 1961.
- [63] C. W. Harrison, Jr., "On the evaluation of potential integrals occurring in antenna theory using digital computers," IEEE Trans. Antennas Propagat., (Commun.), vol. AP-11, page 576, Nov. 1963.
- [64] Salomon Bochner, "Summation of multiple Fourier series by spherical means," Trans. Amer. Math. Soc., vol. 40, Sept. 1936.
- [65] W. L. Stutzman and G. A. Thiele, Antenna Theory and Design. New York: Wiley and Sons, 1981.
- [66] C. M. Butler, "A formulation of the finite-length narrow slot or strip equation," IEEE Trans. Antennas Propagat., (Commun.), vol. AP-30, pp. 1254-1257, Nov. 1982.
- [67] A. J. Poggio, "Numerical solution of integral equations of dipole and slot antennas including active and passive loading," Ph.D. Dissertation, University of Illinois, 1969.
- [68] L. Stark, "Radiation impedance of a dipole in an infinite planar phased array," Radio Sci., vol. 1, No. 3, pp. 361-377, March 1966.
- [69] P. W. Hannan and M. A. Balfour, "Simulation of a phased-array antenna in a waveguide," IEEE Trans. Antennas Propagat., vol. AP-13, pp. 342-353, May 1965.

- [70] W. F. Richards, "Anisotropy, birefringence and dispersions in artificial dielectrics," Ph.D. Dissertation, University of Illinois, 1979.
- [71] R. F. Frazita, "Surface-wave behavior of a phased array analyzed by a grating-lobe series," IEEE Trans. Antennas Propagat., (Commun.), vol. AP-15, pp. 823-824, Nov. 1967.
- [72] P. B. Katehi and N. G. Alexopoulos, "On the effect of substrate thickness and permittivity on printed circuit dipole properties," IEEE Trans. Antennas Propagat., vol. AP-31, pp. 34-39, Jan. 1983.
- [73] D. R. Jackson and N. G. Alexopoulos, "Superstrate (cover) effects on printed circuit antennas," IEEE/AP-S Symposium Proceedings, Boston, MA, pp. 563-565, June 1984.
- [74] S. M. Wright, "Comparison of measured and theoretical impedance of the AM broadcast tower," M. S. Thesis, University of Illinois, 1981.
- [75] Y. T. Lo, "A note on the cylindrical antenna of noncircular cross section," J. Appl. Phys., vol. 24, pp. 1338-1339, October 1957.
- [76] A. Glisson, "On the development of numerical techniques for treating arbitrarily shaped surfaces," Ph.D. Dissertation, University of Mississippi, 1978.
- [77] Reference Data for Radio Engineers. Indianapolis: Howard W. Sams, 1977.

PART II

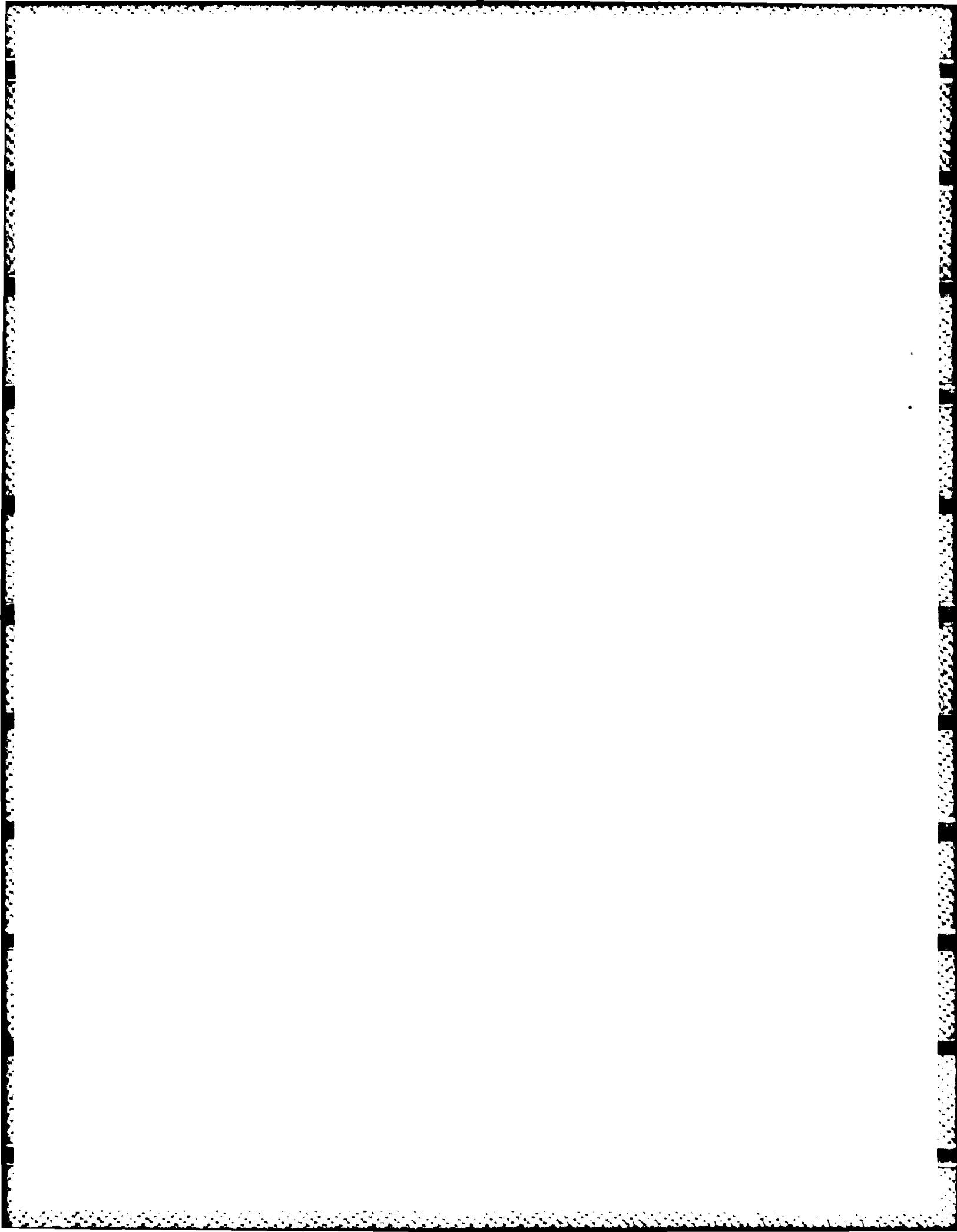
THEORETICAL AND EXPERIMENTAL
INVESTIGATION OF A MICROSTRIP
RADIATOR WITH MULTIPLE LUMPED
LINEAR LOADS

BY

W. F. RICHARDS

AND

Y. T. LO



ABSTRACT.

A simple theory is developed for the analysis of microstrip patch elements which are loaded at one or more points with lumped linear load impedances. The analysis is based on a "cavity model" in which the shape of the field distribution between the patch and ground plane is assumed to be well approximated by that of the resonant modes of a corresponding magnetic and electric walled cavity. The resonant mode of the loaded cavity is represented as an appropriate superposition of the modes of the corresponding unloaded cavity. The characteristic equation for the resonant frequencies of the loaded cavity is obtained in terms of the load impedances and the unloaded cavity multiport open circuit parameters. An analysis of the input impedance of a rectangular microstrip element shorted at an arbitrary point is implemented and the results show good agreement with experiment. Two ancillary results are also obtained. First, the modeling of the radiative power loss in terms of an artificially lossy dielectric in an otherwise ideal cavity is justified for thin elements. Second, an equivalence is derived between a thin strip and a circular cylinder model of the feed current distribution.

1. Introduction.

Loading a microstrip element by one or more lumped impedances can alter the radiative and impedance properties of the element [1]. Such loads can also be used to change the resonant frequency of the element over a wide range without substantially changing the match and pattern [2]. If the loads are varactor diodes whose capacity can be altered by changing an applied bias or PIN diodes which can play the role of open or short circuits in the element according to the bias applied, the element can be made adaptable. Indeed, it is possible by introducing appropriately placed diodes to change an element pattern from one with a null in

the zenith direction to one with a beam maximum there [3] for a given fixed band of operation.

It is useful in the design of such elements, of course, to be able to predict with some accuracy the element pattern, impedance, and resonant frequency. Shaubert, Farrar, Sindoris, and Hayes [2] developed an analysis for such loaded elements. Their analysis, is based on a "transmission line model" of a rectangular element. This model is quite efficient because of its simplicity and their predictions of resonant frequency versus shorting pin location agree fairly well with experimental measurements. However, because the transmission line model has no facility for predicting the variations in the inductive component of a load as its position is varied within the element, it fails to predict certain trends in the resonant frequency of a short-loaded element as the shorting pin approaches the patch edge. This model also cannot predict the impedance of the element very accurately. This is because the field distribution between the ground plane and the patch of a loaded element is much too complicated to be adequately represented by a single-mode, transmission line model.

The goal of this research was to improve the accuracy of the analysis of loaded elements by considering a full modal analysis. Using such an analysis, all of the qualitative trends in the resonant frequencies of loaded elements with respect to load position are fully explained. Moreover, for thin elements, the quantitative agreement between predicted and measured resonant frequencies is also quite good. Furthermore, the impedance variation with frequency is predicted rather accurately for any location of the load as the results in the last section of this report demonstrate. It is noted that while the analysis presented in this report is more complicated than a transmission line model, it has still been efficiently implemented as evidenced by the fact that the program used to compute the results of the last section was written for a microcomputer running under a BASIC interpreter.

This part is organized in the following sections:

Section 2: An approximate equivalence between a radiating element and an artificially lossy cavity is established. While such an equivalence was proposed and used by the authors in previous work [1], a more rigorous justification is given in this section.

Section 3: Having established that one can deal with a cavity rather than the actual patch radiator to estimate the resonant mode field distribution, the orthogonality of resonant modes in a loaded cavity is addressed.

Section 4: The characteristic equation for the resonant frequency of a cavity loaded by a single short is derived and the expression of the loaded cavity resonant mode in terms of the corresponding unloaded cavity modes obtained.

Section 5: The results of Section 4 are generalized to the case of an arbitrary number of arbitrary lumped loads.

Section 6: The loaded cavity mode distribution derived in the previous section is used to estimate quality factor of the associated patch radiator. Also, determination of the "feed reactance" associated with the loaded cavity is discussed. From these results and the results of Section 2, the expression for the input impedance of the loaded patch element is given.

Section 7: The details of how the series required by this multimode theory were efficiently summed is presented in this section. This section also shows that a thin strip of electric current of a certain "effective feed width" can be used to model a uniform circular cylindrical electric surface source current.

Section 8: This section contains the results of the application of this theory to a rectangular patch element with a single shorting pin. Experimental and theoretical results are compared and evaluated.

2. Rigorous basis of cavity model and "effective loss tangent."

The exact fields under the patch illustrated in Fig. 1a can be attributed, through the use of Huygen's principle, to the primary source distribution, $J_{\text{source}}(\vec{r})$, and a secondary source distribution, $-J_{\text{eq}}(\vec{r})$, acting within an ideal cavity formed by joining the patch edge to the ground plane with magnetic conductor as illustrated in Fig. 1b. This secondary current, of course, is given by

$$J_{\text{eq}}(\vec{r}) = \hat{n} \times \vec{H},$$

where \hat{n} is an outwardly pointing unit normal to the patch edge and \vec{H} is the exact total magnetic field.

Before proceeding any further, the context of the discussion is simplified by the following approximation. While the actual fields within the cavity vary in general with the z coordinate and thus any cavity mode expansion that represents these fields should be summed over z -dependent modes as well, the fields can, to a very good approximation be considered z -independent. This is because most practical microstrip antennas are still rather thin compared to a wavelength. Thus, any z -dependent cavity mode will evanesce quickly away from the point at which it is generated. Furthermore, if one attributes the radiated field and surface waves as being due to a ribbon of magnetic current encircling an electrically conducting "mesa" formed by shorting the patch edge to the ground plane, it can be seen that the z -dependent magnetic currents will produce negligible radiated fields because of their multiple phase reversals. This approximation is not necessary, but it does simplify the discussion that follows and is completely adequate in that context.

If $\{\psi_{mn}(\vec{r})\}$ is the set of orthonormal cavity modes which represent the source free electric fields of the cavity with k_{mn} being their corresponding resonant wave numbers, then the exact total electric field $E_r(\vec{r})$ due to the source current $J_{\text{source}}(\vec{r})$ and the secondary current $J_{\text{eq}}(\vec{r})$ is given by

$$E_r(\vec{r}) = j\omega\mu \sum \frac{\psi_{mn}(\vec{r})}{k^2 - k_{mn}^2} I_{mn}, \quad (1)$$

where

$$I_{mn} = I_{mn}^0 - \int_{\partial S} \psi_{mn}(\vec{r}) J_{eq}(\vec{r}) ds, \\ I_{mn}^0 = \int_{\text{source}} \psi_{mn}(\vec{r}) J_{\text{source}}(\vec{r}) ds, \quad (2)$$

S is the surface of the patch ∂S being its boundary, and $k = k_r(1-j\delta)$, is the complex intrinsic wave number of the dielectric substrate. The dielectric loss tangent is δ which can be written as $1/Q_d$, where Q_d is the dielectric quality factor. The " k_r " is the real part of the intrinsic wave number. The " \sum " without limits indicates a summation over all of the z -independent modes. The " ds " in (2) is the element of arc length along the cross section of the primary and secondary surface current distributions. The sum in (1) converges uniformly as the observation point nears the edge of the patch although its gradient which is proportional to the internal electric patch surface current has a non-uniform convergence.

Multiplying equation (1) by the negative of the complex conjugate of the secondary source current and integrating over the magnetic wall yields the total "complex power" leaving the element,

$$P_r + j2\omega\Delta W_{\text{ext}} = -j\omega\mu t \sum \frac{(I_{mn}^0 - \bar{I}_{mn}) I_{mn}}{k^2 - k_{mn}^2}, \quad (3)$$

where P_r is the power radiated in the space and surface waves and ΔW_{ext} is the difference between the averages of the electric and magnetic stored energies *external to the cavity*. The parameter t is the thickness of the substrate and μ is its permeability. The "bar" over the I_{mn} denotes complex conjugation. The primary source distribution can be assumed to be real so that \bar{I}_{mn}^0 in (2) is also real. The time average *internal* electric stored energy is

$$W_E = \frac{1}{2} \mu k_r^2 t \sum \frac{|I_{mn}|^2}{|k^2 - k_{mn}^2|^2}.$$

The ratio of the complex power in (3) to twice ω times this energy is

$$1/Q + j\chi = \frac{-j \sum \frac{(I_{mn}^0 - \bar{I}_{mn}) I_{mn}}{k^2 - k_{mn}^2}}{k_r^2 \sum \frac{|I_{mn}|^2}{|k^2 - k_{mn}^2|^2}} \quad (4)$$

If this ratio is computed for frequencies such that $k \approx k_{MN}$, then $Q = Q_{MN}$ is (or can be defined as) the radiative "quality factor" of the MN^{th} mode of the antenna. Solving for I_{MN} , one obtains

$$I_{MN} = \frac{k^2 - k_{MN}^2}{k_{\text{eff}}^2 - k_{MN}^2} I_{MN}^0 + \frac{|k^2 - k_{MN}^2|^2}{k_{\text{eff}}^2 - k_{MN}^2} \frac{1}{I_{MN}} R , \quad (5)$$

where k_{eff} is the effective dielectric wave number around the MN^{th} mode and is given by

$$k_{\text{eff}}^2 = k_r^2(1 - \chi_{MN}) - jk_r^2(1/Q_d + 1/Q_{MN}) , \quad (6)$$

and R is a "remainder" term which is given by

$$R = \sum' \left\{ \frac{(I_{ms}^0 - I_{ms})\bar{I}_{ms}}{k^2 - k_{ms}^2} + (\chi_{MN} + j/Q_{MN})k_r^2 \frac{|I_{ms}|^2}{|k^2 - k_{ms}^2|^2} \right\} .$$

The prime on the summation indicates that the sum is over all cavity modes *except* the MN^{th} mode. Rather than solving the quadratic equation for I_{MN} in (5), it is convenient to think of this equation as a contraction mapping which can be solved by iteration. Stopping at the first iteration, I_{MN} is given by

$$I_{MN} \approx \frac{k^2 - k_{MN}^2}{k_{\text{eff}}^2 - k_{MN}^2} I_{MN}^0 + (k^2 - k_{MN}^2) \frac{\bar{k}_{\text{eff}}^2 - k_{MN}^2}{k_{\text{eff}}^2 - k_{MN}^2} \frac{1}{I_{MN}^0} R . \quad (7)$$

Upon substitution of this into (1),

$$\begin{aligned} E_z(\vec{r}) = & j\omega\mu \frac{\psi_{MN}(\vec{r})}{k_{\text{eff}}^2 - k_{MN}^2} I_{MN}^0 \\ & + j\omega\mu \sum' \frac{\psi_{ms}(\vec{r})}{k^2 - k_{ms}^2} I_{ms} \\ & + j\omega\mu \frac{\bar{k}_{\text{eff}}^2 - k_{MN}^2}{k_{\text{eff}}^2 - k_{MN}^2} \frac{1}{I_{MN}^0} R \psi_{MN}(\vec{r}) . \end{aligned} \quad (8)$$

When the frequency is in the band of the MN^{th} resonant mode, especially for thin elements for which the Q_{MN} is large, the first term of (8) strongly dominates the last term which can be neglected. The physical interpretation of the first term of (8) is that the field due to the primary source and the secondary source associated with the resonant mode of the element can be attributed to the field due to the primary source *acting alone* if the actual dielectric substrate is replaced by an artificially lossy dielectric with effective wave number of k_{eff} given by (6). The radiative loss is accounted for in the dominant mode through the introduction of the effective loss tangent, $\delta_{\text{eff}} = 1/Q_{MN} + 1/Q_d$. The real part of the wave number is also modified by the χ_{MN} . The excess capacity in the vicinity of the edge of the patch results in a larger average *external* electric stored energy than magnetic stored energy so that χ_{MN} is a positive parameter. One can

introduce an estimate for this parameter into the k_{eff} or, what amounts to the same thing, one can simply add an "edge extension" to the overall size of the cavity. Whether or not the same replacement of k with k_{eff} is done for the non-resonant modes is of very little importance since the real parts of their denominators never cancel as it does for the resonant mode. This simple prescription of replacing the actual dielectric by an effective dielectric to account for the radiative loss was first postulated and used by the authors in earlier published work [1]. The simple but rigorous analysis considered above vindicates this particular aspect of the cavity model analysis. To more completely evaluate the implications of the results obtained above some bounds on the remainder term in (8) should be estimated. This is not within the scope of the present report but will be the subject of another report.

In order to use this principle, one must obtain an estimate for the quality factor and (often less importantly) an estimate for χ_{MN} . There is a plethora of methods for estimating both of these parameters. From the edge extension formula of Hammerstad [4], one can estimate χ_{MN} . A simple "impedance boundary" condition such as used in [5,6] will provide an estimate for Q_{MN} . A more refined approach by Chang [7] also provides an estimate for this parameter. One can use a patch current moment method formulation such as those used by Deshpande and Bailey [8] and by Pozar [9] to obtain an estimate for Q_{MN} that should be valid for a larger range of dielectric thicknesses than for these other more approximate methods. One of the simplest ways of estimating Q_{MN} (though, like the impedance boundary condition methods, limited to thin dielectrics) is the method used by the authors' in [1]. Since the main objective of this report is to analyze loaded elements for which more rigorous analyses have not yet been implemented, the latter will be used to obtain the resonant quality factors of the loaded structure and the edge extension formula of Hammerstad will be used to improve the resonant frequency estimates.

For the case of microstrip elements which have been loaded at one or more points, the unloaded cavity modes $\psi_{mn}(\vec{r})$ are no longer applicable to equation (8). Instead, the actual resonant mode of the loaded cavity must be found. This is the subject of the next three sections.

3. Cavity modes of loaded elements.

A microstrip patch that has been modified by placing lumped loads between the patch and the ground plane at one or more points has an altered internal modal field distribution. Let the orthonormal modes of the unloaded cavity be $\{\psi_{mn}\}$ and the normalized modes of the loaded cavity be $\{\phi_{mn}\}$. In general, the latter is not an orthogonal set. An application of Green's theorem will show that the modes of a cavity with lumped impedances of $Z_L(k)$ attached at \vec{r}_L on the patch have inner products given by

$$\int_S \phi_{ij} \phi_{mn} dS = -\frac{j\eta}{k_{mn}^2 - k_{ij}^2} \sum_L \left\{ \frac{k_{mn} t}{Z_L(k_{mn})} - \frac{k_{ij} t}{Z_L(k_{ij})} \right\} \phi_{ij}(\vec{r}_L) \phi_{mn}(\vec{r}_L)$$

The set $\{\phi_{mn}\}$ is only orthogonal when the load impedances are shorts or inductors. The simple modal field expansion of equation (1) depends, however, on the orthogonality of the cavity modes. Since the central result of section 2 will be used to analyze the loaded antenna, it would appear that the analysis must be narrowed to these two types of loads so that the expansion of (1) remains valid. However, it will be shown in section 5 that the Green's function of the loaded cavity containing any type of lumped linear load is of the form

$$E_z(\vec{r}) = j\omega\mu a \frac{\phi_{MN}(\vec{r})\phi_{MN}(\vec{r}')}{k^2 - k_{LMN}^2} + f(\vec{r}, \vec{r}', k) \quad (9)$$

in the vicinity of the resonant frequency of the ϕ_{MN} mode. The resonant wave number of this mode is k_{LMN} . The function f is a slowly varying function of k in the vicinity of the resonant frequency and a is a constant. The same conclusions concerning the distribution of radiation loss in an effective loss tangent for the dominant mode can be obtained using this representation of internal fields as were obtained using equation (1). Thus the scope of the analysis developed in this report extends to a general class of lumped loads, the most important members of which are shorts, capacitors, resonators, and other microstrip radiators in a series fed array.

Since the loaded cavity in general does not correspond to a separable geometry regardless of the separability of the unloaded cavity, it is inconvenient to directly determine the ϕ_{mn} 's. Instead, one can represent the resonant loaded cavity mode in terms of a superposition of unloaded cavity modes,

$$\phi_{mn} = \sum a_{ij} \psi_{ij} . \quad (10)$$

The coefficients in this expansion can be found through a simple circuit analysis which is justified through an application of Lorentz reciprocity. The simplest case of a single short circuit load is considered first.

4. Resonant mode of cavity loaded by a single short.

The method for finding the resonant mode of the loaded cavity is developed, initially, for a patch with a single shorting pin as illustrated in the cross sectional view of Fig. 2a. To find the coefficients in (10), one can assume a unit total current flowing on the short and enforce the electric boundary condition at its surface. A reasonable assumption for the distribution of this load current is that it flows uniformly over the surface of the short. If one removes the short, through Huygen's principle, impressing in its place the assumed unit current acting in a now *unloaded cavity*, then, in general, a voltage V is induced at the load point between the patch and the ground plane. This voltage is defined by

$$V = \frac{-1}{\text{shorting pin perimeter}} \int_{\text{perimeter}} (E_z(\vec{r}) d\sigma) . \quad (11)$$

The voltage V can be thought of as the driving point impedance of an *unloaded cavity*. This impedance will be denoted by Z_{11} for reasons that will become apparent in the next section. The modes that are sought are z -independent fields so that enforcement of the electric boundary condition on the surface of the shorting pin is well approximated by enforcing the condition that Z_{11} vanish. Thus, one obtains the obvious result that the resonant frequencies of the *loaded cavity* are the zeros of the driving point impedance Z_{11} of the *unloaded cavity*.

In the vicinity of an isolated mode, ψ_{MN} , of the *ideal lossless unloaded cavity*, the driving point impedance behaves as if it were that of a resonant L-C tank circuit in series with an inductor [1]. That is,

$$Z_{11}(\omega) = j\omega L_1 + \frac{j\omega L}{1 - \omega^2 LC} . \quad (12)$$

Figure 3a represents a plot of the second term of this expression and the negative of the first term versus frequency. The intersection between these two curves, of course, marks the resonant fre-

quency of the *loaded* cavity. The parameters L and C are

$$L = \mu \frac{t}{k_{MN}^2} \psi_{MN}^2(\vec{r}')$$

$$C = 1/(c^2 \eta^2 \psi_{MN}^2(\vec{r}') t),$$

where c is the speed of light in a vacuum and \vec{r}' is the center coordinate of the feed point (that is, where the shorting pin will be placed). The feed inductance is

$$L_f = -j \mu t \sum' \frac{(I_{mn}^0)^2}{k^2 - k_{mn}^2}.$$

The I_{mn}^0 coefficients are given by (2) where the source current density $J_{\text{source}}(\vec{r})$ is a unit current flowing uniformly over the surface of the shorting pin. (Of course, L_f is not *exactly* an inductance since it clearly is not independent of frequency as this equation shows. However, in the vicinity of the *isolated* resonant mode ψ_{MN} , it is very slowly varying). These expressions are obtained by comparing equation (12) to the integration of equation (1) in (11) to obtain Z_{11} (where $J_{\text{eq}}(\vec{r})$ is set to zero, of course). The approximation, $I_{MN}^0 \approx \psi_{MN}(\vec{r}')$ for low order modes was used in the expression for C and L .

Since the cavity currently in question is *not* loaded, it supports a DC mode. That is, a constant source-free electric field can exist within the unloaded cavity. Since, all modes are orthogonal, any resonant mode other than the DC mode *must have* a nodal curve. That is, there must be a curve on the patch on which the mode $\psi_{MN}(\vec{r}) = 0$. If the short is to be placed near a nodal point on this curve, then its corresponding resonant inductance L in (12) becomes very small and the reactance curve in Fig. 3a becomes very sharp as illustrated in Fig. 3b. In this case, the zero of Z_{11} occurs essentially at the same frequency as that of the resonant mode of the unloaded cavity. This is consistent with the physical observation that near a nodal point, the field is so small anyway that the short has little loading effect. However, as the load point is moved away from the nodal line to an antinode such as an appropriately chosen point on the patch edge, then the L increases and the reactance curve "fills out" as in Fig. 3a. This increase is slow at first since $|\psi_{MN}(\vec{r}')|^2$ is stationary at a node. If the feed inductance remains constant independent of load location, then the resonant frequency of the loaded element clearly increases as the load is moved from a nodal to an antinodal point. The increase, however, would be less and less as the load

point approached the antinode since $\psi_{MN}(\vec{r}')$ is stationary at such a point. Thus, one would expect an initially accelerating rise in resonant frequency as the load point moves away from the node and then a slowing and eventual saturation when the load approaches the antinode.

The conclusions obtained in the previous paragraph were predicated upon the assumption that the feed inductance *does not vary* with the location of the shorting pin. This, in fact, is not at all the case as the theoretical and experimental evidence presented by Richards, Zinecker, Clark, and Long [10] demonstrates. They found that the feed reactance increases rapidly as the load point approaches the edge of the patch. Thus, in the determination of the zero of Z_{11} , there are two opposing tendencies. The first is the *increased* loading effect of the short as it moves toward an edge (which is or at least contains an antinode) due to the increase in the resonant inductance L as just discussed. The opposing tendency is the *decreased* loading effect of the short as it moves toward the edge due to the associated *increase* in feed inductance. Thus, what one actually calculates in finding the zero of Z_{11} is that the resonant frequency at first increases as the load is moved from a nodal point toward the patch edge. However, as it nears the edge, the resonant frequency begins to drop although typically never back to as low a frequency as that of the unloaded patch.

The discussion above centers on finding the resonant frequency of the loaded cavity. The considerations of section 2 indicate that in order to determine the resonant component of the loaded patch antenna internal field, the real and imaginary parts of the dielectric wave number must be modified to account for an *external* energy imbalance and the radiation loss, respectively. The respective measures for these two parameters are χ_{MN} and $1/Q_{MN}$. For the *unloaded* patch antenna, χ_{MN} is typically positive indicating a net excess of external electric energy over magnetic energy. For the loaded element, of course, this energy balance is affected by *both* the primary impressed current and its corresponding reaction current induced on the short. The net result is that χ_{MN} is no longer necessarily positive and in fact becomes negative as the short position nears the edge. Ignoring the χ_{MN} correction factor results in an *underestimate* of the resonant frequency as the load approaches the patch edge.

An alternative to the discussion in the last paragraph which is more physically appealing is to observe that the feed inductance of the cavity and that of the antenna are different. In fact, it has been shown in [10] that the feed inductance of the cavity will be somewhat larger than that of the antenna, and considerably so near the patch edge. Use of the correct antenna feed inductance to determine the resonant frequency of the loaded element will yield a more accurate result and will obviate the need for determining X_{MN} .

The predictions of the resonant frequency of an antenna element with a shorting pin including the predicted effects of neglecting the X_{MN} correction factor are corroborated by the computed and measured results presented in section 8.

Once the resonant frequency or, the resonant wave number k_{LMN} is obtained, the distribution of the resonant mode, ϕ_{MN} , can be found. For a cavity with a single shorting pin, the loaded cavity resonant mode must be

$$\phi_{MN}(\vec{r}) = j\omega\mu \sum \frac{I_{ms}^0}{k_{LMN}^2 - k_{ms}^2} \psi_{ms}(\vec{r}).$$

This, of course, is the electric field due to the assumed unit load current. A normalized expression for the resonant mode is

$$\phi_{MN}(\vec{r}) = \frac{\sum \frac{I_{ms}^0}{k_{LMN}^2 - k_{ms}^2} \psi_{ms}(\vec{r})}{\left\{ \sum \frac{(I_{ms}^0)^2}{(k_{LMN}^2 - k_{ms}^2)^2} \right\}^{1/2}}. \quad (13)$$

The results obtained in this section for a single short can be easily generalized to the case of a cavity with several shorts or other types of lumped loads. This is considered in the next section.

5. Resonant mode of the general loaded cavity.

For a cavity loaded with two or more shorts such as the one illustrated in Fig. 2b, one can use Lorentz reciprocity to establish the corresponding circuital equations from which the resonant frequency is obtained. One can assume that a unit current flows on short number one. An application of the Lorentz reciprocity integral between the fields in Fig. 2c and 2d, and between those

of Fig. 2c and 2e, respectively lead to the circuit equations,

$$\begin{aligned} Z_{in} &= Z_{11} + Z_{12}I_L \\ 0 &= Z_{12} + Z_{22}I_L \end{aligned} \quad (14)$$

where Z_{in} is the voltage (calculated through the definition in equation (11)) due to the unit impressed current in Fig. 2c, and I_L is the corresponding total current induced on the shorting pin. The Z_{11} , $Z_{12} = Z_{21}$, and Z_{22} are the open circuit parameters of the two port *unloaded* cavity. The parameters Z_{11} and Z_{22} are obtained from (12). The Z_{12} is given by

$$Z_{12} = -j\omega\mu t \sum \frac{I_{ms}^{01} I_{ms}^{02}}{k^2 - k_{ms}^2},$$

where I_{ms}^{01} and I_{ms}^{02} are given by equation (2) with $J_{source}(\vec{r})$ taken respectively to be the unit current distributions over the first and second shorting pins.

It is useful to note at this point that the definition used in (11) for the voltage is not as arbitrary as one might first suspect. Some flexibility is afforded in the definition of the voltage in the consideration of a cavity with a single short. For example, one could define the voltage as the $-iE_z(\vec{r})$ where \vec{r} is the coordinate of the center line of the source current distribution. However, the assumption of uniformly distributed currents on the loads and the application of Lorentz reciprocity to reduce field quantities to circuit quantities lead one naturally to define the voltage by equation (11). Since the source currents are assumed to be uniform, the computation of I_{ms}^0 for a unit current can be thought of as averaging the mn^{th} mode ψ_{ms} over the source distribution. Computation of the corresponding voltage through (11) requires one more such average so that all of the impedance parameters can be thought of as arising from a "double averaging" of the cavity Green's function.

The resonance condition for the two-short cavity is that the impedance, Z_{in} , in equation (14) be zero. This requires, of course, that the determinant of the open circuit parameter matrix vanish since in general, the load current I_L is not zero.

More generally, for the case of a cavity with N lumped impedances, Z_1 , Z_2 , ..., Z_N , the resonance condition is

$$\det \mathbf{Z} = 0,$$

where the matrix \mathbf{Z} is

$$\mathbf{Z} = \begin{bmatrix} Z_{11} + Z_1 & Z_{12} & \cdots & Z_{1N} \\ Z_{12} & Z_{22} + Z_2 & \cdots & Z_{2N} \\ \vdots & \vdots & \ddots & \vdots \\ \vdots & \vdots & \ddots & \vdots \\ Z_{1N} & Z_{2N} & \cdots & Z_{NN} + Z_N \end{bmatrix}.$$

With the current in load one assumed to be unity, the currents in loads two through N , I_{L2}, \dots, I_{LN} , are

$$\mathbf{I}_L = -\mathbf{Z}_{11}^{-1} \mathbf{Z}_{12}$$

where

$$\mathbf{I}_L = \begin{bmatrix} I_{L2} \\ I_{L3} \\ \vdots \\ I_{LN} \end{bmatrix}, \quad \mathbf{Z}_{12} = \begin{bmatrix} Z_{12} \\ Z_{13} \\ \vdots \\ Z_{1N} \end{bmatrix}, \quad \text{and}$$

\mathbf{Z}_{11} is the matrix obtained from \mathbf{Z} by removing its first row and column. Letting

$$i_{ms} = I_{ms}^0 + \sum_{l=2}^N I_{Ll} I_{ms}^{0l},$$

the normalized resonant mode is given by equation (13) with I_{ms}^0 replaced by i_{ms} where I_{ms}^{0l} is defined analogously to I_{ms}^{01} for a unit current distribution over the l^{th} load.

The results obtained here pertain to a general lumped linear load although as noted in section 3, the associated set of resonant loaded cavity modes are not necessarily orthogonal. However, a representation of the field due to a unit filamentary source acting in the loaded cavity which is similar to that in (1) can be derived. Consider for simplicity the case of a cavity with a single lumped load of impedance, Z_1 . Then the load current induced by a unit filamentary source located at \vec{r}' is

$$I_L = -\frac{Z_{12}}{Z_{11} + Z_1}, \quad (15)$$

where here port 2 is taken to be the driven port. Since the exciting current is a unit filament,

$$Z_{12} = -j\omega\mu t \sum \frac{I_{ms}^{01}}{k^2 - k_{ms}^2} \psi_{ms}(\vec{r}') .$$

The denominator of (15) has a zero at $k = k_{LMN}$. (Assume that this is a simple zero. For the case of a purely reactive load, it is easy to see through Fig. 3a that this must be a simple zero since the slope of the reactance function must be positive for lossless passive networks). Expanding about this zero,

$$\begin{aligned} Z_{11}(k) + Z_1(k) &= [Z_{11}'(k_{MN}) + Z_1'(k_{MN})](k - k_{MN}) \\ &+ \frac{1}{2}[Z_{11}''(k_{MN}) + Z_1''(k_{MN})](k - k_{MN})^2 + \dots, \end{aligned} \quad (16)$$

where the "''" represents differentiation with respect to k . Similarly,

$$\begin{aligned} Z_{12} &= -j\omega\mu t \sum \frac{I_{ms}^{01}}{k_{LMN}^2 - k_{ms}^2 + (k^2 - k_{LMN}^2)} \psi_{ms}(\vec{r}') \\ &= -j\omega\mu t \phi_{MN}(\vec{r}') \left\{ \sum \frac{(I_{ms}^{01})^2}{(k_{LMN}^2 - k_{ms}^2)^2} \right\}^{1/2} \\ &+ (k^2 - k_{LMN}^2) [-j\omega\mu t \sum \frac{I_{ms}^{01}}{(k_{LMN}^2 - k_{ms}^2)^2} \psi_{ms}(\vec{r}')] + \dots \end{aligned} \quad (17)$$

Substituting (16) and (17) into (15), one arrives at the conclusion that

$$I_L = a \frac{\phi_{MN}(\vec{r}')}{k^2 - k_{LMN}^2} + g(\vec{r}', k),$$

where a is a constant independent of \vec{r}' and k , and $g(\vec{r}', k) = O(1)$ as $k \rightarrow k_{LMN}$. Furthermore, the electric field at observation point \vec{r} is

$$j\omega\mu \sum \frac{\psi_{ms}(\vec{r})\psi_{ms}(\vec{r}')}{k^2 - k_{ms}^2} + j\omega\mu I_L \sum \frac{I_{ms}^{01}}{k^2 - k_{ms}^2} \psi_{ms}(\vec{r}); \quad (18)$$

where the first term of (18) is the field due to the primary source filament and the second term is the field due to the load current. The first term is a slowly varying function of k in the vicinity of the loaded cavity resonance, k_{LMN} . The second term can be written in the same form as (17) so that the Green's function for the loaded cavity takes the form of equation (9).

Now that the loaded cavity resonant frequency and mode has been obtained, the next step is to estimate the quality factor Q for the associated antenna so that the result of section 2 can be applied. This is considered next.

6. Quality factor and feed reactance of loaded antenna.

The quality factor of the loaded element is obtained using the approximate method described in [1]. Briefly, the approach is based on (1) the fact that the quality factor depends on the *shape* of the internal field distribution and not its *amplitude*; and (2) that the quality factor is primarily influenced by the *resonant* modal field distribution, ϕ_{MN} , since it dominates all other terms. Thus, to compute Q , one need not know the exact coefficient of ϕ_{MN} in a modal expansion, but only the shape of ϕ_{MN} .

A magnetic current distributed as ϕ_{MN} on the patch edge is impressed on an infinite ground plane and the power radiated by it is computed. Several approximations are made in this process such as neglecting the presence of the dielectric substrate and the redistribution of the radiating magnetic current on a flat ground plane rather than on the sides of a conducting "mesa" called for by Huygen's principle. These approximations are sound for thin elements, but they can be removed at the price of slight to major additional computational efforts depending on the desired rigor.

Since it is quite possible that no one of the cavity modes ψ_{mn} will dominate in the series (13) for ϕ_{MN} , the latter is computed along the edge of the patch at discrete sample points only. The magnetic current between samples is obtained through linear interpolation and the result is used to compute the far field and radiated power.

The time average internal stored electric energy required to compute Q is simply obtained from the formula,

$$2\omega W_E = \frac{k_{LMN} l}{\eta}.$$

This expression is very simple because the resonant mode ϕ_{MN} in (13) is normalized.

Once the antenna quality factor has been estimated and the effective wave number k_{eff} computed, the internal fields of the loaded cavity can be written as

$$j\omega\mu \frac{\phi_{MN}(\vec{r})\phi_{MN}(\vec{r}')}{{k_{\text{eff}}^2 - k_{MN}^2}} + jX_f,$$

where X_f is the feed reactance of the loaded cavity. Since this parameter has little to do with radiative properties of the element, it can be computed as the driving point impedance of the

ideal lossless cavity at the resonant frequency of ϕ_{MN} .

All of the expressions discussed above require the summation of series over all the modes of the unloaded cavity. These series are typically very slowly converging. Thus, an efficient method of summing them is important in order to implement the analysis discussed above. Techniques of efficient summation of these series is the topic of the next section.

7. Efficient summation of series.

Consider first the case of a rectangular microstrip antenna of dimensions a by b . The Green's function for the corresponding unloaded cavity is

$$G(\vec{r} | \vec{r}') = jk\eta \sum \frac{\psi_{mn}(\vec{r})\psi_{mn}(\vec{r}')}{k^2 - k_{mn}^2} \quad (19)$$

The Green's function is first accelerated and then the "double averaging" of the result discussed in section 6 is applied to find the necessary fields. The authors have used several different methods of efficiently accelerating the series. Only the latest method used which is the simplest to follow is discussed below.

The expression in (19) is a *spectral* representation of the Green's function. Its corresponding *spatial* representation is obtained by accumulating the fields due to the primary source and all of its multiple images acting in a uniform parallel plate waveguide. This representation is

$$\begin{aligned} G(\vec{r} | \vec{r}') = & -\frac{k\eta}{4} \sum \{ H_0^{(2)}[k((x-x'-2ma)^2 + (y-y'-2nb)^2)^{1/2}] \\ & + H_0^{(2)}[k((x+x'-2ma)^2 + (y-y'-2nb)^2)^{1/2}] \\ & + H_0^{(2)}[k((x-x'-2ma)^2 + (y+y'-2nb)^2)^{1/2}] \\ & + H_0^{(2)}[k((x+x'-2ma)^2 + (y+y'-2nb)^2)^{1/2}] \} \end{aligned} \quad (20)$$

The summation indices in (20) range over all pairs of integers, m, n , both positive and negative while only positive pairs are used in the spectral sum (and expressions to be derived from it later) in (19). The $H_0^{(2)}$'s in (20) are the Hankel functions of the second kind. The series in (20) converges even more slowly than its counterpart in (19). However, if one replaces "k" in both of these expressions by " $-ju$ " where u is some real positive parameter, then the following identity is obtained:

$$\begin{aligned} & \sum \frac{\psi_{ms}(\vec{r})\psi_{ms}(\vec{r}')} {u^2 + k_{ms}^2} \\ &= \frac{1}{2\pi} \sum \{ K_0[u((x-x'-2ms)^2 + (y-y'-2nb)^2)^{1/2}] + \dots \}, \end{aligned} \quad (21a)$$

where the K's are the modified Bessel functions of the second kind. While (20) converges very slowly, the right-hand side of (21a) converges very rapidly if u is chosen sufficiently large. Differentiation of both sides of (20) with respect to u yields a second identity,

$$\begin{aligned} & \sum \frac{\psi_{ms}(\vec{r})\psi_{ms}(\vec{r}')} {(u^2 + k_{ms}^2)^2} \\ &= \frac{1}{4\pi u} \sum \{ ((x-x'-2ms)^2 + (y-y'-2nb)^2)^{1/2} K_1[u((x-x'-2ms)^2 + (y-y'-2nb)^2)^{1/2}] \} \\ & \quad + \dots \}. \end{aligned} \quad (21b)$$

These identities suggest the following acceleration scheme.

The sum in (19) can be thought of as a sum over a "reciprocal lattice." The vectors drawn from the origin to the points in the lattice illustrated in Fig. 4 represent the resonant wave vectors of the cavity. Their magnitudes are the resonant wave numbers of the cavity. Typically, one is only interested in operating an element somewhere in the frequency range of the lowest few resonant modes. Suppose f_{\max} is the maximum frequency of interest in the analysis of a given element. Let k_{\max} be its corresponding dielectric substrate wave number. Then the coefficients in the spectral series above,

$$\frac{1}{k^2 - k_{\max}^2} = \frac{1}{\kappa^2 - \kappa_{\max}^2} \quad (22)$$

can be expanded in a series of Tchebyshev polynomials [11] in the normalized parameter, $z = \xi(\kappa/\kappa_{\max})$ for $\kappa_{\max} > \xi\kappa$, where ξ is a real number larger than one, $\kappa^2 = k^2 + u^2$, and $\kappa_{\max}^2 = k_{\max}^2 + u^2$. This expansion is given by

$$\frac{1}{k^2 - k_{\max}^2} = -\frac{1}{\kappa_{\max}^2} \frac{\xi}{(\xi^2 - 1)^{1/2}} \sum_{i=0}^{\infty} \epsilon_i [\xi + (\xi^2 - 1)^{1/2}]^{-2i} T_{2i}(z), \quad (23)$$

where $\epsilon_i = 2$ for $i \neq 0$ and $\epsilon_0 = 1$, and $T_{2i}(z)$ is the $2i$ -degree Tchebyshev polynomial. The parameter ξ establishes a boundary between two regions within the reciprocal lattice illustrated in Fig. 4. For the inner region, I, the factor in (22) is computed directly, while over region II an appropriate truncation of the series in (23) is used. The radius of this boundary is

$k_b = \xi \{ k_{\max}^2 + [(\xi^2 - 1)/\xi^2] u^2 \}^{1/2}$. If the parameter ξ is chosen to be "2" and the series in (23) is truncated to two terms, one obtains the approximation

$$\frac{1}{k^2 - k_{\max}^2} \approx -\frac{1}{\kappa_{\max}^2} [0.989 + 1.331(\kappa/\kappa_{\max})^2]$$

with a maximum error of about one percent. Thus, the Green's function for an unloaded cavity can be approximated by the spectral series,

$$G(\vec{r} | \vec{r}') \approx jk\eta \sum_I \frac{\psi_{\max}(\vec{r})\psi_{\max}(\vec{r}')}{k^2 - k_{\max}^2} - jk\eta [0.989 U_0(\vec{r} | \vec{r}') + 1.331 U_1(\vec{r} | \vec{r}') \kappa^2], \quad (24)$$

where

$$U_l(\vec{r} | \vec{r}') = \sum_{\text{II}} \frac{\psi_{\max}(\vec{r})\psi_{\max}(\vec{r}')}{\kappa_{\max}^{2l+2}}, \quad l = 0, 1. \quad (25)$$

The "I" and the "II" under the summation symbols in these expressions indicate the respective regions in the reciprocal lattice over which the sums are to be performed.

The approximation of $G(\vec{r} | \vec{r}')$ in (24) represents a considerable improvement over a "brute force" summation of the Green's function since it amounts to a "wide band approximation." However, the series for $U_0(\vec{r} | \vec{r}')$ and $U_1(\vec{r} | \vec{r}')$ in (25) are still very slowly converging series and acceleration is also sought for them. It is not particularly simple to accelerate these series when summed over region II. However, the U 's can be written as

$$U_l = \sum_I \frac{\psi_{\max}(\vec{r})\psi_{\max}(\vec{r}')}{\kappa_{\max}^{2l+2}} - \sum_I \frac{\psi_{\max}(\vec{r})\psi_{\max}(\vec{r}')}{\kappa_{\max}^{2l+2}}. \quad (26)$$

The last term of (26) is a finite sum which can be summed once for all frequencies. The first term can be transformed to a rapidly converging spatial sum through the identities in (21). The choice of

$$u = \frac{\pi}{2\min\{a, b\}}$$

yields a compromise which allows both the spectral and spatial sums to converge rapidly.

In order to find the normalization factor for the resonant mode, the series

$$W(\vec{r} | \vec{r}') = \sum \frac{\psi_{mn}(\vec{r})\psi_{mn}(\vec{r}')}{(k^2 - k_{mn}^2)^2}$$

is first accelerated. Using a similar procedure to that applied for $G(\vec{r} | \vec{r}')$ above, W is found to be

$$W(\vec{r} | \vec{r}') = \sum_i \frac{\psi_{mn}(\vec{r})\psi_{mn}(\vec{r}')}{(k^2 - k_{mn}^2)^2} + [0.962U_1(\vec{r} | \vec{r}') + 3.08U_2(\vec{r} | \vec{r}')\kappa^2],$$

where U_2 is also given by (25). This function can be accelerated as U_0 and U_1 or can simply be summed directly since it already has rapid convergence.

Having computed the required Green's functions, all that remains to find the impedance parameters is to apply the "double-averaging" over the source distributions. Let $\langle\langle f(\vec{r} | \vec{r}') \rangle\rangle_{12}$ denote

$$\frac{1}{P_1 P_2} \int_{P_1} \int_{P_2} f(\vec{r} | \vec{r}') ds_2 ds_1,$$

where P_i is the perimeter of the i^{th} load. Since the loads are typically small, $\langle\langle f(\vec{r} | \vec{r}') \rangle\rangle_{12} \approx f(\vec{r}_1 | \vec{r}_2)$. On the other hand, the approximation $\langle\langle G(\vec{r} | \vec{r}') \rangle\rangle_{11} \approx G(\vec{r}_1 | \vec{r}_1)$ is clearly nonsense since $G(\vec{r} | \vec{r}')$ is singular at the source point. However, G can be written as

$$G(\vec{r} | \vec{r}') = G_0(\vec{r} | \vec{r}') + jk\eta 0.159 \ln |\vec{r} - \vec{r}'|, \quad (27)$$

where G_0 has no singularities. The last term of (27) arises from the singular part of the field due to primary source in the spatial sum in (21). Thus,

$$\begin{aligned} Z_{11} &= -i \langle\langle G(\vec{r} | \vec{r}') \rangle\rangle_{11} \\ &= -i G_0(\vec{r}_1 | \vec{r}_1) - jk\eta 0.159 \langle\langle \ln |\vec{r} - \vec{r}'| \rangle\rangle_{11}. \end{aligned}$$

For the case of a circularly cylindrical load (or feed current distribution) with diameter, d , the average of the logarithm term is $\ln(d/2)$.

If the feed distribution were assumed to be a uniformly distributed current on a thin strip, then the corresponding average of the logarithm is $\ln w - 3/2$, where w is the width of the strip. If one wished to model a circular distribution by a strip distribution as has been done at times in

other papers [1,12] then the appropriate equivalent or "effective feed width" is obtained by equating these two averages. This leads to the result that w should be chosen as $2.24d$. The fact that the authors of these papers have noted that a somewhat larger feed width yields better agreement with measurements is a reflection of the fact that the cavity model overestimates the feed inductance because it neglects the equivalent electric currents on the magnetic walls. Choosing an artificially wide feed gives a compensatory reduction in the feed inductance, but has no real rigorous basis.

To find the normalization constant, one notes that the denominator in equation (13) can be written as the square root of $\langle\langle W(\vec{r}|\vec{r}')\rangle\rangle_{11} \approx W(\vec{r}_1|\vec{r}_1)$ since W is non-singular. The approximations used in computing these averages have been very carefully tested against more rigorous numerical averages and have been found to be quite accurate.

The case of other elements with a separable geometry can be handled in other ways. The authors have, in fact, used similar methods to accelerate the series associated with circular, circular sector, annular, and annular sector elements.

8. Experimental and Theoretical Results and Conclusions.

The driving point impedances of a rectangular patch element shorted at a variety of points was measured and computed using the method described above. The element had dimensions of 7.62 X 11.43 X 0.152 cm and was etched from a sample of 3M CuClad 250 printed circuit board (glass reinforced PTFE with a manufacturer quoted relative dielectric constant of 2.43). In all the measurements (except the one noted later), the element was fed with a coaxial SMA connector placed at (2.54, 1.27)cm. (The reference axes have an x-axis at a long edge of the patch and the y-axis along a short edge). The measurements were made at the University of Houston using an automated Hewlett-Packard, HP 8410B network analyzer controlled with an HP 9816S microcomputer. The analysis method used to produce the theoretical results was also implemented on the HP 9816S using the HP BASIC 2.0 language.

A short was placed, in turn, at $(x',y') = (5.72, 0.76n)$ cm for $n = 0, 1, 2, 3, 4, 6, 7, 8, 9$, and 10. The Smith chart plots of the measured impedances corresponding to each of these short locations are shown in Fig's. 5(a-e) for $n = 0$ through 4 and Fig's. 6(a-e) for $n = 6$ through 7. Superimposed on these plots are the corresponding computed impedances at discrete frequencies. For both the computed and measured results, the frequency interval between each marker on the plots is 5 MHz.

Figure 7 represents a plot of both the theoretically computed and actually measured resonant frequencies for the patch corresponding to each of the ten short locations above. The horizontal axis is the normalized shorting pin location given by $(3.81 \text{ cm} - y')/(3.81 \text{ cm})$. (Note that $y = 3.81 \text{ cm}$ is a center line of the patch which is also a nodal line of the unloaded cavity mode that resonates in the frequency range in which the measurements were made).

It is quite clear that the theory used to predict these results is well corroborated by the measurements. The worst discrepancy between theory and experiment occurs (not surprisingly) for shorts near the patch edge. The agreement between predicted and measured resonant frequencies was also quite good. (It is noted again that the "Hammerstad edge correction" was used to help account for the fringing at the patch edge. Furthermore, the manufacturer's quoted dielectric constant was used in the theoretical computations.) One notes that the theoretical resonant frequency is consistently above the observed frequency (though not by much) for all short locations except on the edge of the patch. There, the theory actually underestimates the resonant frequency. This is because the cavity model overestimates the "feed inductance" at points close to the edge as explained in Section 4.

Figure 8 shows the computed magnetic current distributions for a patch shorted on the edge and for one shorted somewhat away from the edge. The magnetic current distribution of the loaded cavity mode being considered shows the expected dip for observation points closest to the short. One can see from these distributions why the patterns remain relatively stable, as the location of the short is moved from the edge toward the center of the patch. Figure 9(a) shows the magnetic current distribution associated with the resonant mode of a patch shorted near a corner. Note that the magnetic current on one entire edge is strongly suppressed by a single short. To check the accuracy of this current distribution, the input impedance was measured at (2.54,1.27) cm and is shown in Fig. 9(b) along with the theoretical impedance. The feed was moved to the symmetrical location in the opposite corner, (8.89,6.35) cm, and the impedance was again measured and computed. These results are shown in Fig. 9(b). Again, the predicted and measured results agree rather closely thus lending support to the validity of the predicted modal field variation.

9. References.

1. W. F. Richards, Y. T. Lo, and D. D. Harrison, "An Improved Theory for Microstrip Antennas and Applications," IEEE Transactions on Antennas and Propagation, Vol. AP-29, No. 1, January 1981, pp. 38-46
2. D. H. Schaubert, F. G. Farrar, A. Sindoris, and S. T. Hayes, "Microstrip Antennas with Frequency Agility and Polarization Diversity," IEEE Transactions on Antennas and Propagation, Vol. AP-29, No. 1, January 1981, pp. 118-123
3. W. F. Richards and S. A. Long, "A Mode-switched Adaptive Microstrip Element," (submitted to IEEE Transactions on Antennas and Propagation)
4. E. O. Hammerstad, "Equations for Microstrip Circuit Design," Proceedings of the 5-th European Microwave Conference, Hamburg, FRG, September 1975, pp. 268-272
5. K. R. Carver, "Practical Analytical Techniques for the Microstrip Antenna," Proceedings of the Workshop on Printed Circuit Antenna Technology, New Mexico State University, Las Cruces, NM, October 1979, pp. 7/1-20
6. L. C. Shen, "Analysis of a Circular-Disc Printed-Circuit Antenna," Proceedings of IEE, Vol. 126, No. 12, December 1979, pp. 1220-1222
7. D. C. Chang, "Analytical Theory of an Unloaded Rectangular Microstrip Patch," IEEE Transactions on Antennas and Propagation, Vol. AP-29, No. 1, pp. 54-62
8. M. D. Deshpande and M. C. Bailey, "Input Impedance of Microstrip Antennas," IEEE Transactions on Antennas and Propagation, Vol. AP-30, No. 4, July 1982, pp. 645-650
9. D. M. Pozar, "Input Impedance and Mutual Coupling of Rectangular Microstrip Antennas," IEEE Transactions on Antennas and Propagation, Vol. AP-30, No. 6, November 1982, pp. 1191-1196
10. W. F. Richards, J. R. Zinecker, R. D. Clark, S. A. Long, "Experimental and Theoretical Investigation of the Inductance Associated with a Microstrip Antenna Feed," (accepted for publication in Electromagnetics)
11. Y. L. Luke, The Special Functions and Their Approximations, Vol II, Academic Press, 1969, p. 33
12. K. R. Carver, "Input Impedance to Probe-fed Microstrip Antennas," in the Digest of the 1980 IEEE Antennas and Propagation Society Symposium, Quebec City, Canada, June 1980, pp. 617-620

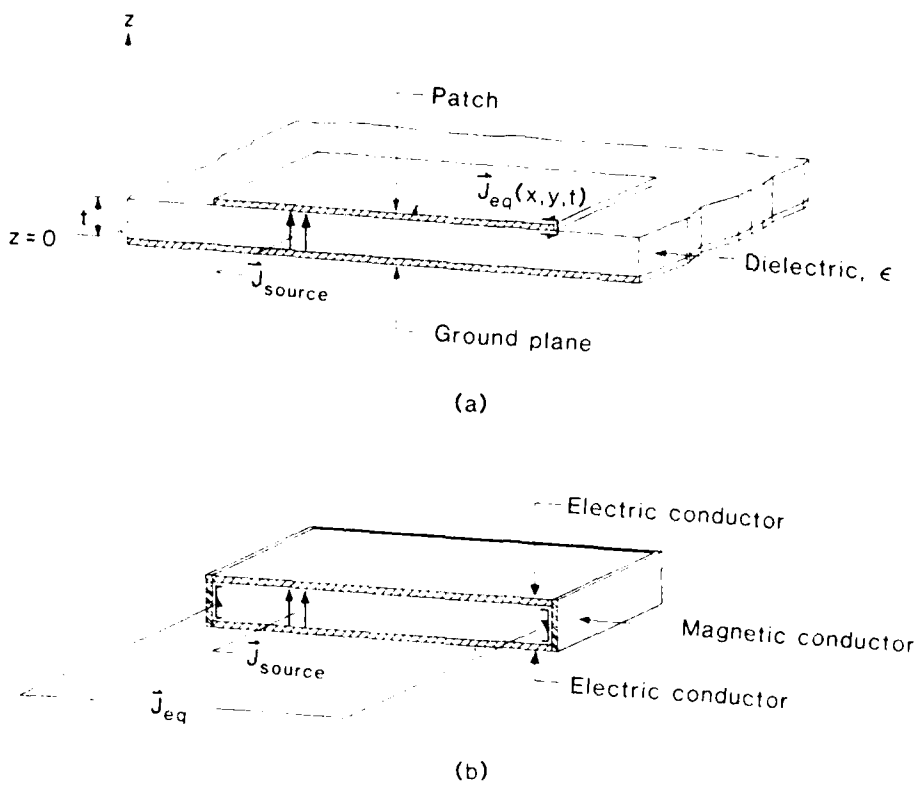


Fig. 1. (a) A cut-away view through the primary source of patch element.
 (b) The associated equivalent magnetic and electric walled cavity with equivalent secondary electric current sources impressed.

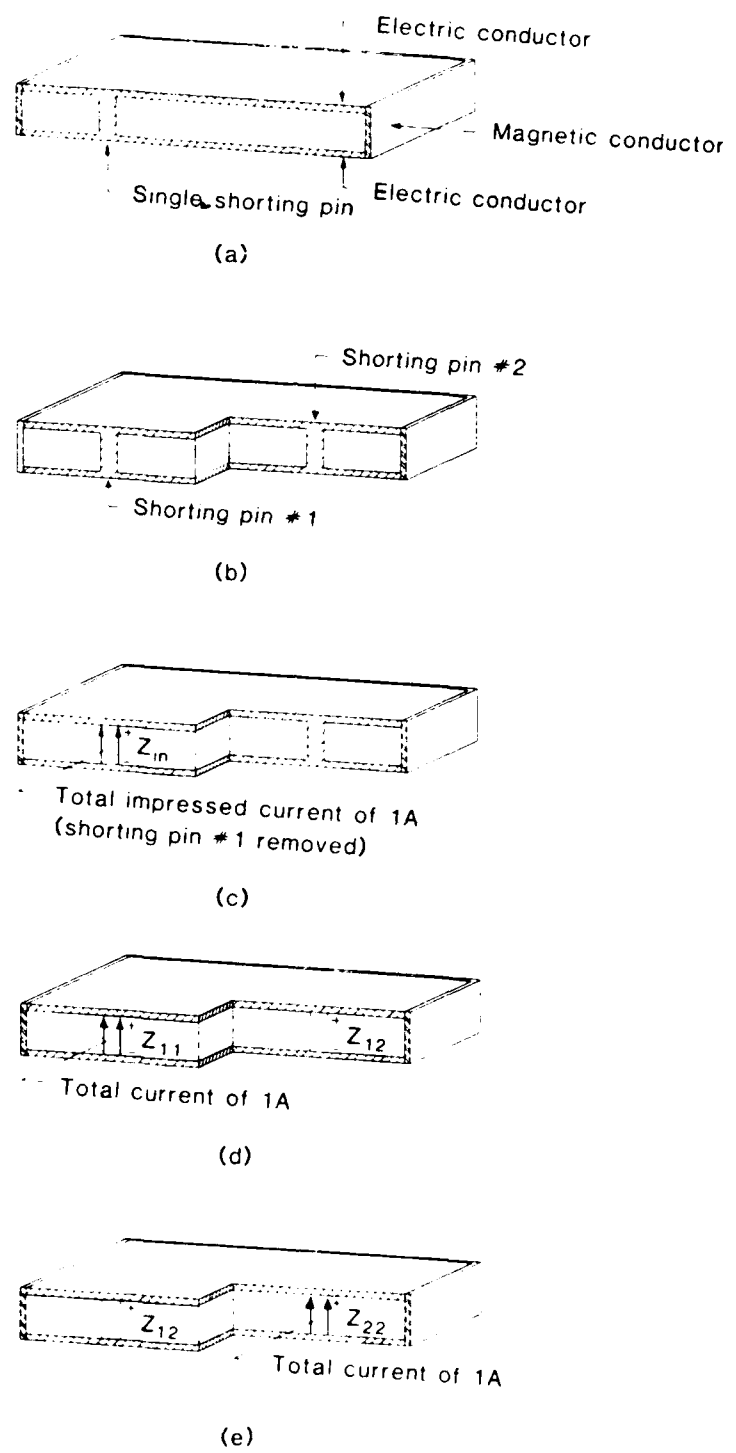


Fig. 2. (a) A cut-away view of a cavity with a single shorting pin.
 (b) A cut-away view of a cavity with two shorting pins.
 (c) The cavity in (b) with pin 1 removed and a unit, uniform electric surface current impressed in its place.
 (d and e) The associated unloaded cavity with unit currents impressed at the locations of the removed pins.

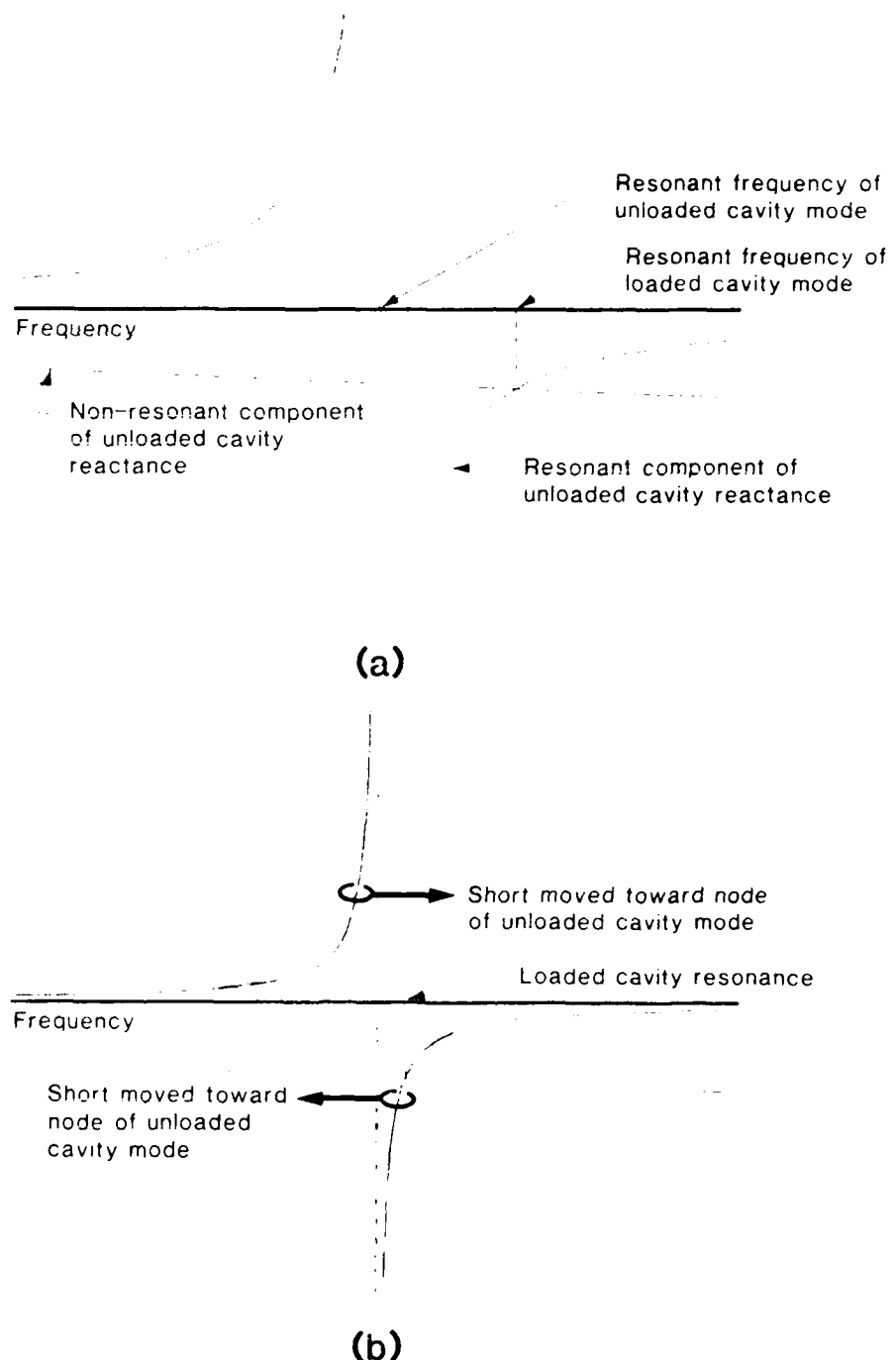


Fig. 3. A plot of the "resonant mode" reactance of an unloaded element and the negative of the corresponding "feed reactance". (a) Corresponds to short location far from a nodal point of the unloaded cavity resonant mode. (b) Corresponds to a short location near a nodal point.

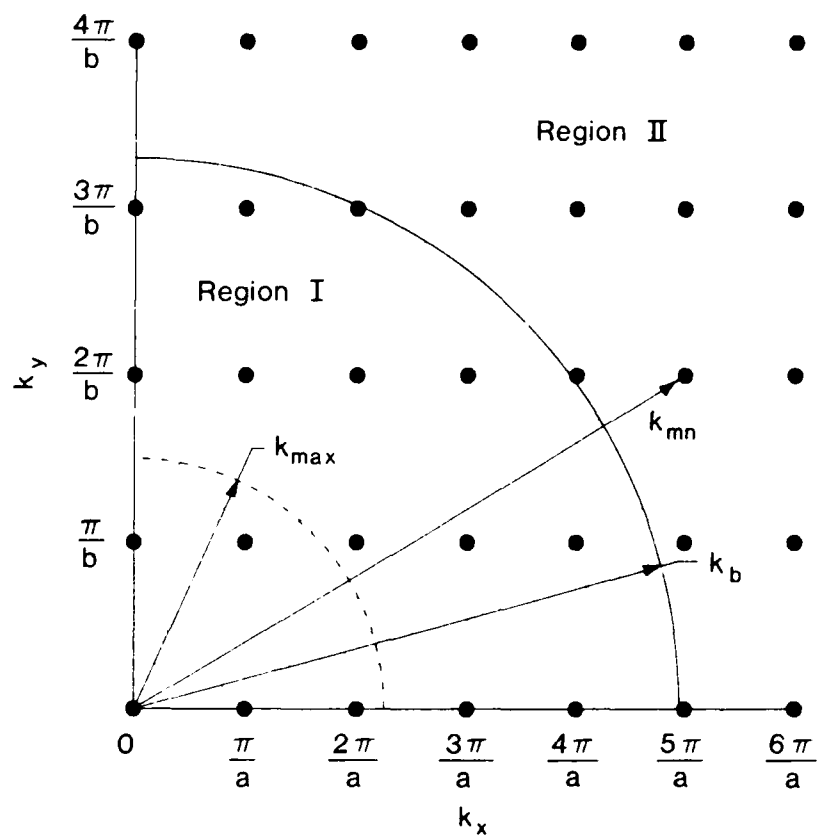


Fig. 4. A portion of the "reciprocal lattice" associated with a rectangular cavity showing the boundary (solid curve) between Regions I and II.

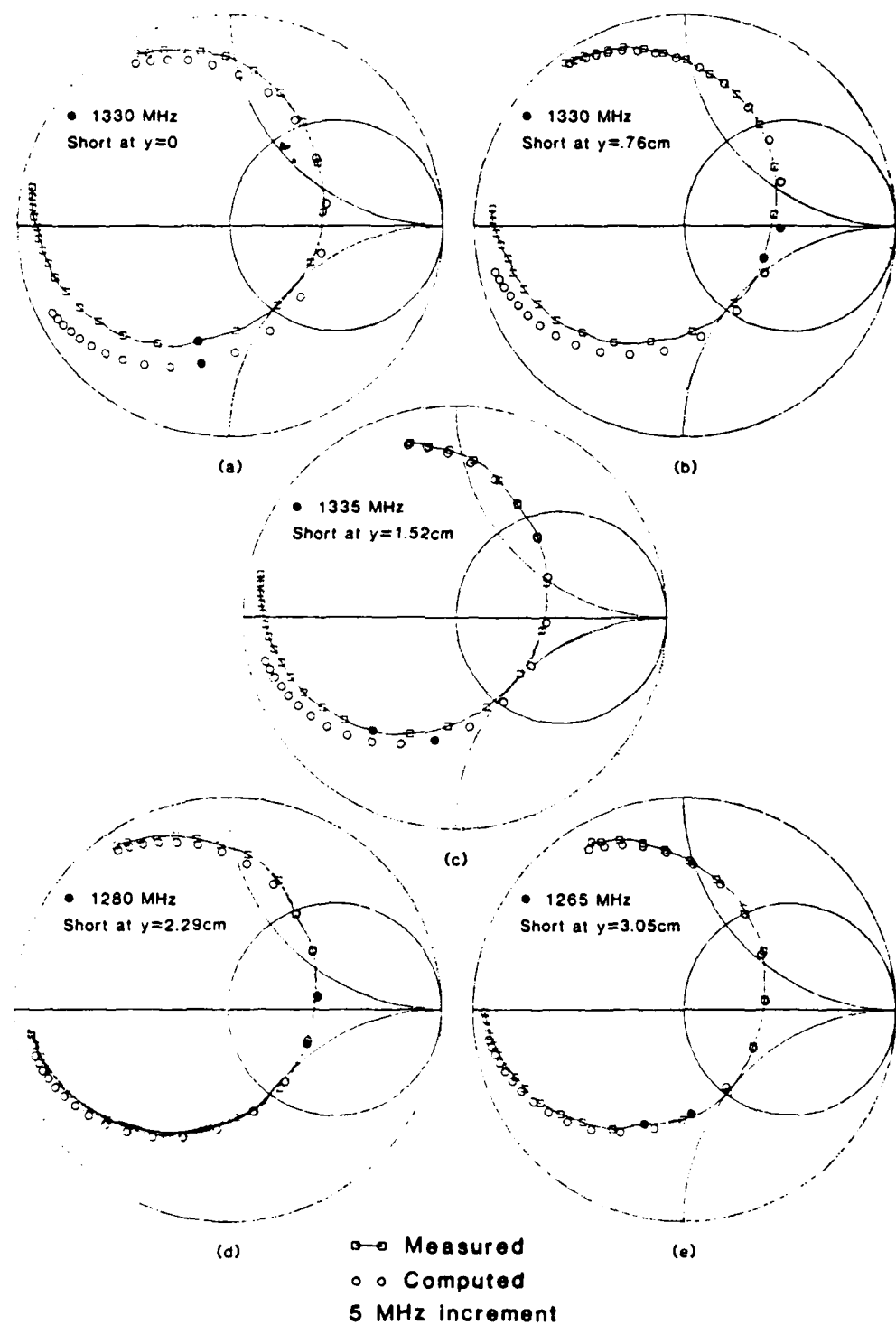


Fig. 5. Measured and computed input impedance of a rectangular element with a single shorting pin located at $x = 5.72\text{ cm}$ and y as indicated on the figure.

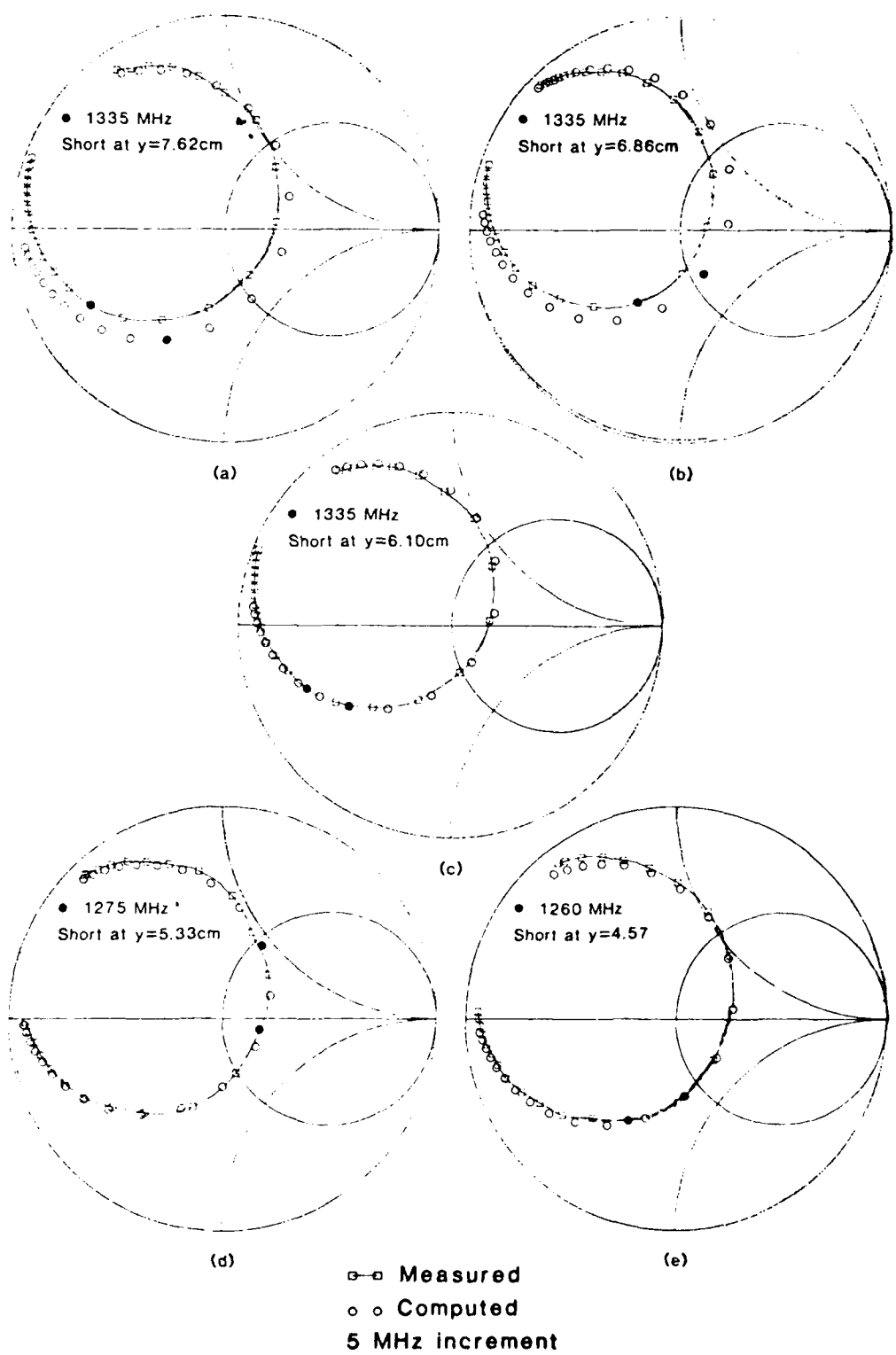


Fig. 6. Measured and computed input impedance of a rectangular element with a single shorting pin located at $x = 5.72\text{ cm}$ and y as indicated on the figure

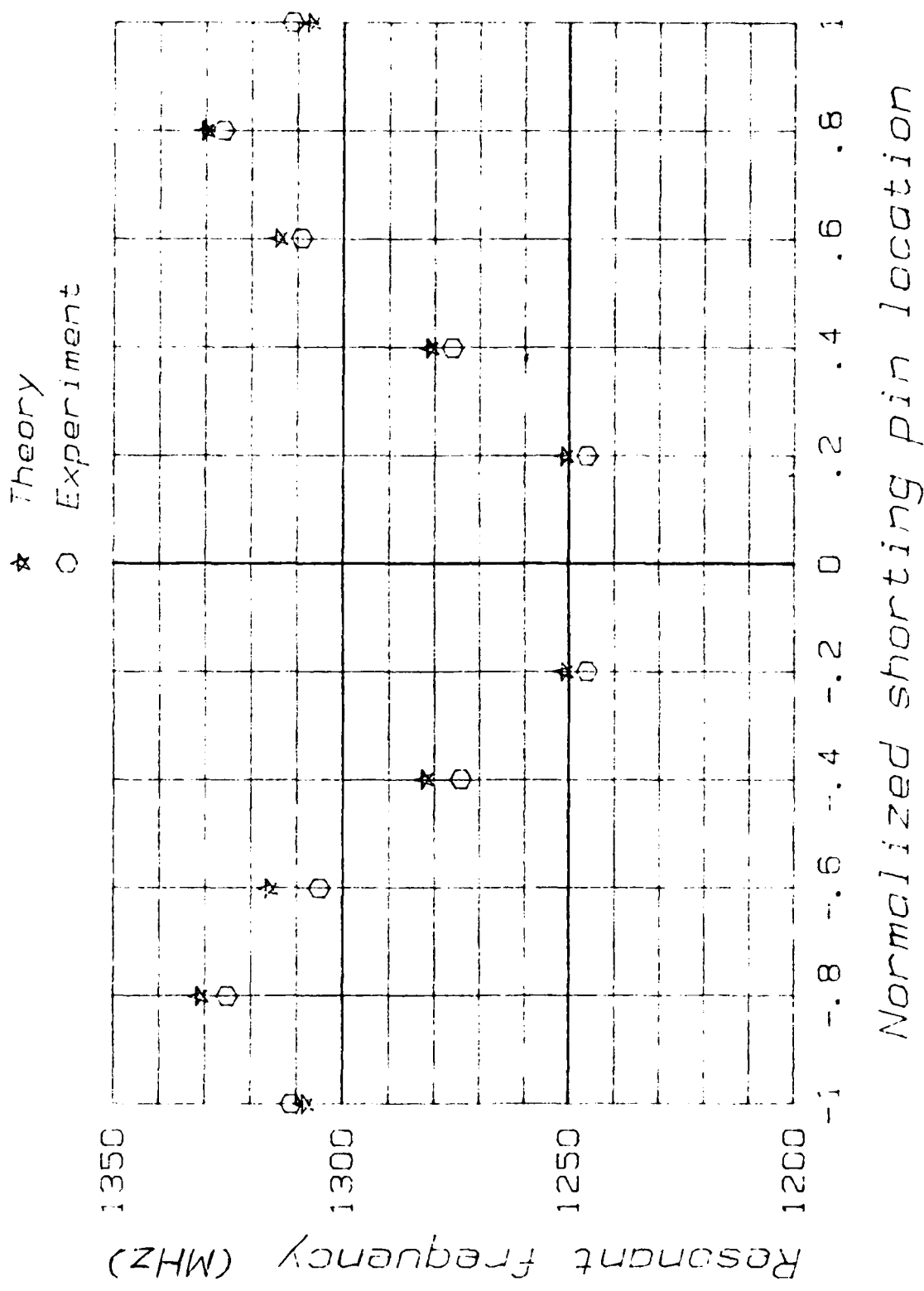
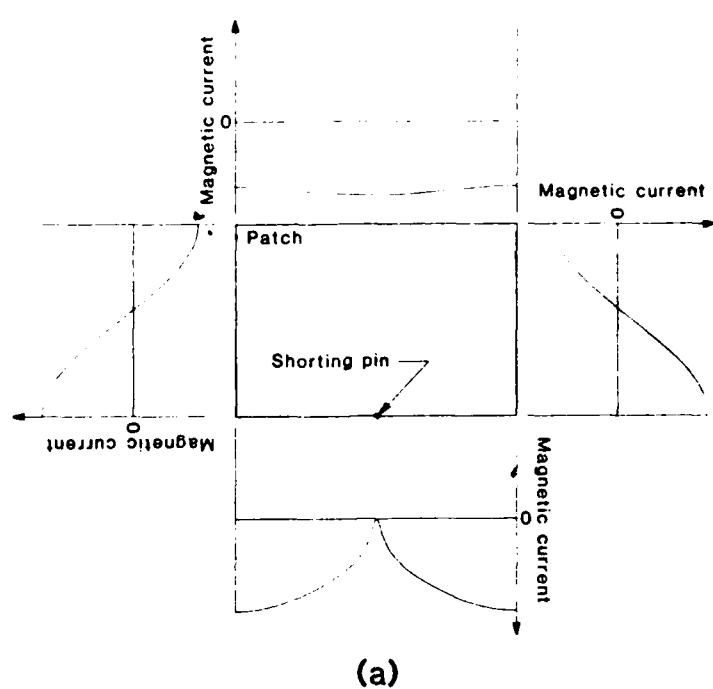
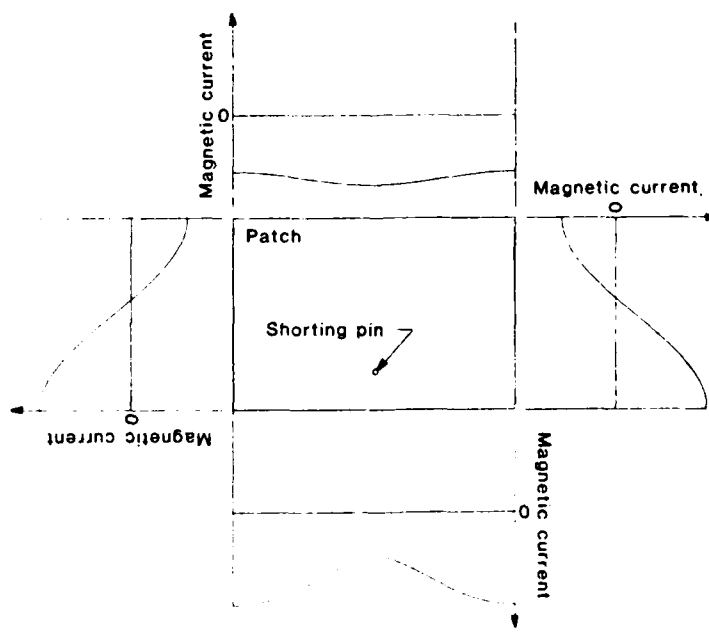


Fig. 7. Measured and computed resonant frequencies of a rectangular element with a single shorting pin versus pin location.



(a)



(b)

Fig. 8. Plots of the computed magnetic current distribution around the edge of a rectangular patch element with a single short located (a) on the patch edge and (b) away from the patch edge.

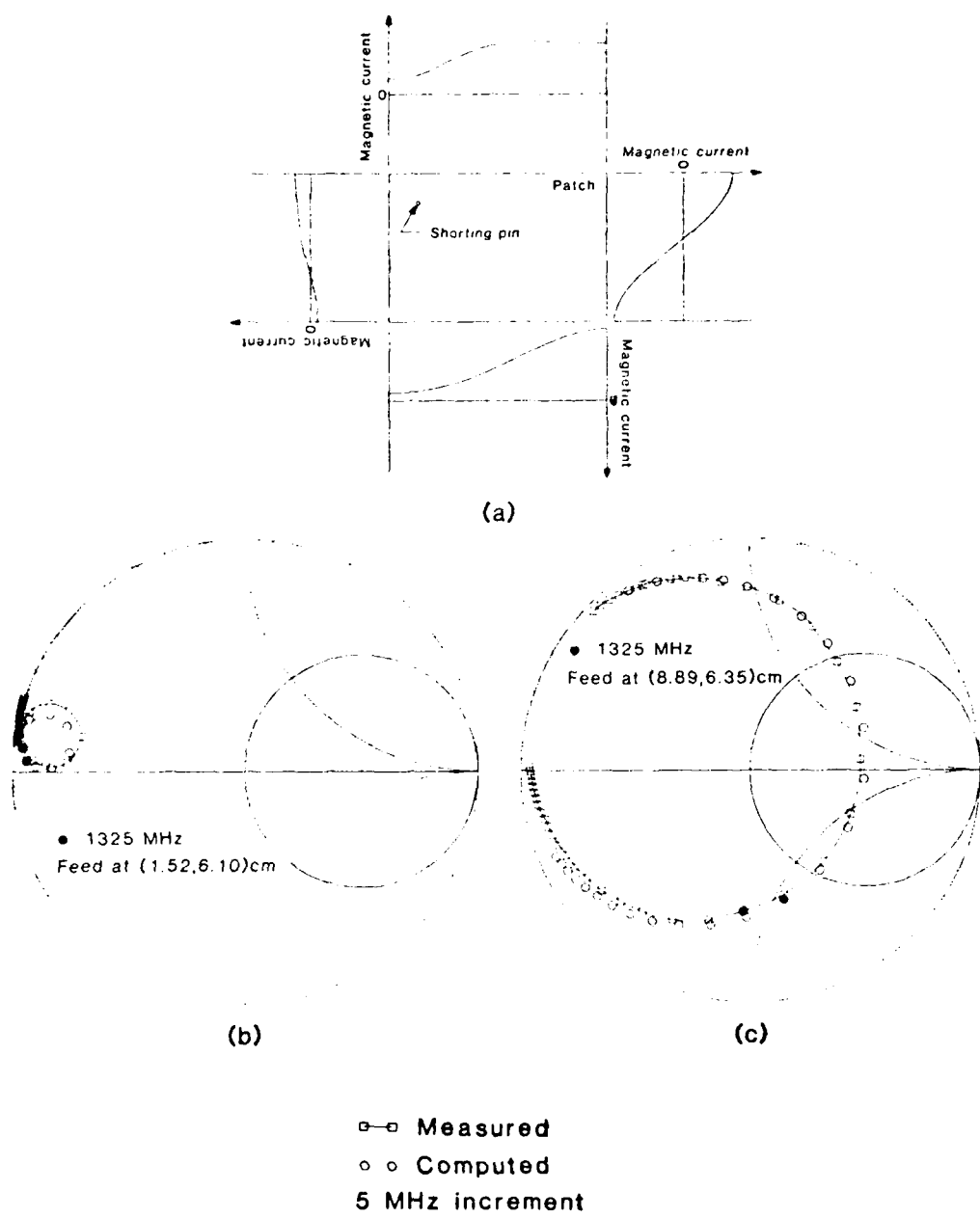


Fig. 9. (a) The computed magnetic current distribution around the edge of a rectangular patch element with a single short placed near a corner of the patch. (b) The corresponding input impedance when the patch is fed at (2.54, 1.27) cm (near lower left corner). (c) The impedance when fed at (8.89, 6.35) cm (near upper right corner).

PART III

MICROSTRIP ANTENNAS
FOR
DUAL-FREQUENCY OPERATION

BY

Y. T. LO

AND

B. F. WANG

ABSTRACT--Single element microstrip antennas for dual frequency operation have been investigated. By placing shorting pins at appropriate locations in the patch, the ratio of two band frequencies can be varied from 3 to 1.8. In many applications a smaller ratio is desired, and this can be achieved by introducing slots in the patch. In so doing, the ratio can be reduced to less than 1.3. For this type of antenna, a hybrid multiport theory is developed and theoretical results are found to be in excellent agreement with the measured.

I. INTRODUCTION

One of the outstanding features of a thin microstrip antenna is its compactness in structure. Unfortunately it is notoriously narrow-banded unless some degree of compactness can be sacrificed by using a thick substrate. In many applications, it is not operation in a continuous wide-band, but, operation in two or more discrete bands that is required. In this case, a thin patch capable of operating in multiple bands is highly desirable, particularly for large array application where considerable saving in space, weight, material and cost can be achieved. For that goal, a few attempts have been made [1,2], by using two or more patch antennas stacked on top of each other, or placed side by side, or using a complex matching network which takes as much space and weight, if not more, as the element itself. Obviously in all those designs, the advantage of compact structure is sacrificed.

*On leave from Beijing Aeronautics and Astronautics Institute, China

This work is supported in part by RADC/EEAA, Hanscom AFB, MA and NASA Lewis Research Center, Cleveland, OH.

From the cavity-model theory, a single patch antenna can easily be made to resonate at many frequencies associated with various modes. But for most applications, all bands are required to have the same polarization, radiation pattern and input impedance characteristics. It is also desirable to have a single input port and an arbitrary separation of the frequency bands. All of these impose severe constraints on the use of the modes. In this paper we shall describe some methods which can practically achieve all these goals.

An annular patch can have predominantly broadside radiation when excited for the (1,1), (1,2) and even the (1,3) mode. Unlike a circular disc, the frequencies for those modes can be adjusted by choosing the inner and outer radius dimensions. All the aforesaid properties can be obtained except that the variation of the two frequency band ratio is somewhat limited [3].

By making use of the difference in the field distributions for various modes, it is possible to practically tune the operating frequencies associated with those modes independent of each other. One method is to place a series of shorting pins at the nodal lines of, for example, the (0,3) modal electrical field of a rectangular patch [3]. These pins will have practically no effect on the (0,3) modal field structure but can have a strong effect on the (0,1) field and thus raise the (0,1) modal frequency. Therefore the low band frequency can be tuned independently. However, the ratio of the two operating frequencies, F_H/F_L , can be varied only from 3 to 2 approximately. On the other hand, if slots are cut in the patch where the magnetic field of the (0,3) mode is maximum, they can have a strong effect on the (0,3) modal field but little on the (0,1) modal field. Thus the operating frequency for the (0,3) mode can be lowered. By using both slots and pins, the two operating bands can be varied over a wide range. In this paper an analytic theory is developed for this type of antenna and then verified by experiment.

II. A MICROSTRIP ANTENNA EXCITED BY A MAGNETIC CURRENT \tilde{K}

First consider a microstrip antenna excited by a magnetic current K in the slot centered at (x_2, y_2) as shown in Figure 1. Following the cavity model theory [4], the antenna can be considered as a cavity bounded by magnetic walls along its perimeter and electric walls at $z = 0$ and t . Since the substrate thickness t is typically a few hundredths of a wavelength, we can assume that the field excited by the magnetic current

$$\tilde{K} = x[U(x - x' + d_{\text{eff}}/2) - U(x - x' - d_{\text{eff}}/2)] \delta(y - y') \delta(z - t)$$

in the slot is approximately the same as that excited by

$$\tilde{K} = x[U(x - x' + d_{\text{eff}}/2) - U(x - x' - d_{\text{eff}}/2)] \delta(y - y') [U(z) - U(z - t)]/t$$

where d_{eff} is the effective width of the magnetic current strip of one V/M, and $U(\cdot)$ is the unit step function. The field in the cavity due to \tilde{K} can then be found by modal-matching as given below:

In region I ($y' \leq y \leq b$)

$$\begin{aligned} E_{z1} &= \frac{d_{\text{eff}}}{at} \sum_{m=0}^{\infty} \frac{\sin(\beta_m y') \cos(m\pi x'/a)}{\sin(\beta_m b)} j_0\left(\frac{m\pi d_{\text{eff}}}{2a}\right) \cos(m\pi x/a) \cos[\beta_m(b - y)] , \\ H_{x1} &= \frac{j d_{\text{eff}}}{at \omega_0 \mu_0} \sum_{m=0}^{\infty} \frac{\beta_m \sin(\beta_m y') \cos(m\pi x'/a)}{\sin(\beta_m b)} j_0\left(\frac{m\pi d_{\text{eff}}}{2a}\right) \cos(m\pi x/a) \sin[\beta_m(b - y)] , \\ H_{y1} &= \frac{j \pi d_{\text{eff}}}{a^2 t \omega_0 \mu_0} \sum_{m=0}^{\infty} \frac{m \sin(\beta_m y') \cos(m\pi x'/a)}{\sin(\beta_m b)} j_0\left(\frac{m\pi d_{\text{eff}}}{2a}\right) \sin(m\pi x/a) \cos[\beta_m(b - y)] . \end{aligned} \quad (1)$$

In region II ($0 \leq y \leq y'$)

$$E_{z2} = \frac{-d_{\text{eff}}}{at} \sum_{m=0}^{\infty} \frac{\sin[\beta_m(b - y')] \cos(m\pi x'/a)}{\sin(\beta_m b)} j_0\left(\frac{m\pi d_{\text{eff}}}{2a}\right) \cos(m\pi x/a) \cos(\beta_m y) ,$$

$$H_{x2} = \frac{j d_{\text{eff}}}{a t \omega \mu_0} \sum_{m=0}^{\infty} \frac{m \sin[\beta_m(b - y')] \cos(m\pi x'/a)}{\sin(\beta_m b)} j_o \left(\frac{m\pi d_{\text{eff}}}{2a} \right) \cos(m\pi x/a) \sin(\beta_m y) ,$$

$$H_{y2} = \frac{-j\pi d_{\text{eff}}}{a^2 t \omega \mu_0} \sum_{m=0}^{\infty} \frac{m \sin[\beta_m(b - y')] \cos(m\pi x'/a)}{\sin(\beta_m b)} j_o \left(\frac{m\pi d_{\text{eff}}}{2a} \right) \sin(m\pi x/a) \cos(\beta_m y) , \quad (2)$$

where a and b are the dimensions of the patch along the x and y axes, respectively; $\beta_m^2 = k^2 - (m\pi/a)^2$, $k^2 = k_o^2 \epsilon_r (1 - j\delta_{\text{eff}})$, k_o = free space wave number, ϵ_r = relative dielectric constant of the substrate, δ_{eff} = effective loss tangent [5], μ_0 = permeability of free space, $j_o(x) = \sin(x)/x$, and d_{eff} = "effective width" of the magnetic current strip of one V/M. The concept of effective feed width and its implication are discussed in [5].

Examination of Equations (1) and (2) indicates that the resonance occurs when $\text{Re}(\beta_m b) \approx n\pi$, $n = 1, 2, \dots$, or $\text{Re}(k) \approx [(m\pi/a)^2 + (n\pi/b)^2]^{1/2}$ since $\delta_{\text{eff}} \ll 1$. We shall denote the value β_m for the particular value of n as β_{mn} , and its associated field is called the mn th mode. Clearly in the neighborhood of this resonance the field will be dominated by the term associated with β_{mn} , the value of which depends on the feed location (x_1, y_1) in Fig. 1. Following the cavity model theory, once the field distribution is found, the Huygen source, $\hat{K}(x, y) = \hat{n} \times \hat{z} \hat{E}(x, y)$, along the perimeter can be determined. From \hat{K} , the far field can then be computed as given below:

$$E_\theta = jk_o (F_x \sin \phi + F_y \cos \phi) ,$$

$$E_\phi = -jk_o (F_x \cos \phi + F_y \sin \phi) \cos \theta , \quad (3)$$

where

$$F_x = \frac{d_{\text{eff}} e^{-jk_o r}}{2\pi r} \sum_{m=0}^{\infty} A_m \{ \sin(\beta_m y') e^{jk_o b \sin \theta \sin \phi} + \sin[\beta_m(b - y')] \}$$

$$. \frac{jk_o a \sin \theta \cos \phi}{(m\pi)^2 - (k_o a \sin \theta \cos \phi)^2} , \quad (4)$$

$$F_y = \frac{b d_{\text{eff}} e^{-jk_0 r}}{2\pi r a} \sum_{m=0}^{\infty} A_m \left\{ \sin(\beta_m b) e^{jk_0 y' \sin \theta \sin \phi} + \sin(\beta_m y') e^{jk_0 b \sin \theta \sin \phi} \right. \\ \left. + \sin[\beta_m(b - y')] \right\} \frac{jk_0 b \sin \theta \sin \phi}{(\beta_m b)^2 - (k_0 b \sin \theta \sin \phi)^2} , \quad (5)$$

$$A_m = \frac{\cos(m\pi x'/a) j_0(m\pi d_{\text{eff}}/2a)}{\sin(\beta_m b)} [(-1)^m e^{jk_0 a \sin \theta \cos \phi} - 1] . \quad (6)$$

Also, from the field in the cavity, the ohmic and dielectric losses as well as the stored energy can be computed and finally the effective loss tangent can be determined.

III. MULTI-PORT ANALYSIS

Let us consider a rectangular microstrip antenna with two ports: port 1 at (x_1, y_1) is fed with an electric current J_1 , and port 2 at (x_2, y_2) is fed with a magnetic current K_2 as shown in Fig. 1. The following hybrid matrix [6] can then be used to describe the relationship between the voltage and current at these ports:

$$\begin{bmatrix} V_1 \\ I_2 \end{bmatrix} = \begin{bmatrix} h_{11} & h_{12} \\ h_{21} & h_{22} \end{bmatrix} \begin{bmatrix} I_1 \\ V_2 \end{bmatrix} \quad (7)$$

where $I_1 = d_{\text{eff}} J_1$, d_{eff} = effective width of source J_1 , $V_2 = t K_2$ and the h parameters are given below:

$$h_{11} = -j\omega \mu_0 \sum_{m=0}^{\infty} \frac{\cos^2(m\pi x_1/a) \cos(\beta_m y_1) \cos[\beta_m(b - y_1)]}{a \beta_m \sin(\beta_m b)} j_0^2(m\pi d_{\text{eff}}/2a) \quad (8)$$

$$h_{12} = -\frac{d_{\text{eff}}}{a} \sum_{m=0}^{\infty} \frac{\sin[\beta_m(b - y_2)] \cos(\beta_m y_1)}{\sin(\beta_m b)} \cos(m\pi x_1/a) \cos(m\pi x_2/a) \\ \cdot j_0(m\pi d_{\text{eff}}/2a) j_0(m\pi d_{\text{eff}}/2a) \quad (9)$$

$$h_{21} = -h_{12} \quad (10)$$

$$h_{22} = \frac{j d_{2\text{eff}}^2}{\tau \omega \mu_0} \sum_{m=0}^{\infty} \frac{\beta_m \sin(\beta_m y_2) \sin[\beta_m(b - y_2)]}{\sin(\beta_m b)} \cos^2(m\pi x_2/a) j_o^2\left(\frac{m\pi d_{2\text{eff}}}{2a}\right) \quad (11)$$

From Equations (8) - (11) all the Z-parameters can thus be determined by the relationship between h and Z parameters. Then, the input impedance at port 1, Z_{in} , can be computed:

$$Z_{in} = Z_{11} - Z_{12}^2 / (Z_{22} + Z_L) \quad (12)$$

where Z_L is the load impedance across the slot terminals at (x_2, y_2) . The far field electric vector potential, \mathbf{E} , for the two sources can be obtained by superposition as given below:

$$\mathbf{E} = \mathbf{E}_1 + P \mathbf{E}_2 \quad (13)$$

where

$$\begin{aligned} \mathbf{E}_1 = & \frac{j k_o \eta t b e^{-jk_o r}}{2\pi r} \sum_{m=0}^{\infty} \frac{\epsilon_{om} \cos(m\pi x_1/a) j_o(m\pi d_{1\text{eff}}/2a)}{\beta_m b \sin(\beta_m b)} \left[(-1)^m e^{jk_o a \sin \theta \cos \phi} - 1 \right] \\ & \cdot \left[x \left[\cos(\beta_m y_1) e^{jk_o b \sin \theta \sin \phi} - \cos[\beta_m(b - y_1)] \right] \frac{j k_o a \sin \theta \cos \phi}{(m\pi)^2 - (k_o a \sin \theta \cos \phi)^2} \right. \\ & \left. - y \frac{b}{a} \left[\beta_m b \sin(\beta_m b) e^{jk_o y_1 \sin \theta \sin \phi} + j k_o b \sin \theta \sin \phi \left[\cos(\beta_m y_1) e^{jk_o b \sin \theta \sin \phi} \right. \right. \right. \\ & \left. \left. \left. - \cos[\beta_m(b - y_1)] \right] \right] \cdot \left[(\beta_m b)^2 - (k_o b \sin \theta \sin \phi)^2 \right] - 1 \right] \end{aligned} \quad (14)$$

$$\begin{aligned}
 F_2 = & \frac{d_{2\text{eff}} e^{-jk_0 r}}{2\pi r} \sum_{m=0}^{\infty} \frac{\cos(m\pi x_2/a) j_0(m\pi d_{2\text{eff}}/2a)}{\sin(\beta_m b)} [(-1)^m e^{jk_0 a \sin \theta \cos \phi} - 1] \\
 & \cdot \left\{ \hat{x} [\sin(\beta_m y_2) e^{jk_0 b \sin \theta \sin \phi} + \sin(\beta_m (b - y_2))] \frac{jk_0 a \sin \theta \cos \phi}{(m\pi)^2 - (k_0 a \sin \theta \cos \phi)^2} \right. \\
 & + \hat{y} \frac{b}{a} [\sin(\beta_m b) e^{jk_0 y_2 \sin \theta \sin \phi} + \sin(\beta_m y_2) e^{jk_0 b \sin \theta \sin \phi} + \sin(\beta_m (b - y_2))] \right. \\
 & \left. \frac{j k_0 b \sin \theta \sin \phi}{(\beta_m b)^2 - (k_0 b \sin \theta \sin \phi)^2} \right\} . \quad (15)
 \end{aligned}$$

$$P = j\omega\mu_0 \frac{\cos(m\pi x_1/a) j_0(m\pi d_{1\text{eff}}/2a)}{\beta_m \sin(\beta_m b)} \cos(\beta_m y_1) \cos(m\pi x_2/a) \cos(\beta_m (b - y_2)) \quad (16)$$

From these and equation (3), the far field is readily computed. The analysis can be generalized for N slots in a straightforward manner.

A similar theory has been developed for a microstrip antenna with shorting pins [3]. For N pins at N ports, the impedance parameters Z_{ii} and Z_{ij} are given by

$$Z_{ii} = -jk_0 \epsilon \eta_0 \sum_{m=0}^{\infty} \frac{\epsilon_{om}}{a} \cos^2(m\pi x_i/a) j_0^2\left(\frac{m\pi d_{i\text{eff}}}{2a}\right) \frac{\cos(\beta_m y_i) \cos(\beta_m (b - y_i))}{\beta_m \sin(\beta_m b)} \quad (17)$$

$$\begin{aligned}
 Z_{ij} = & -jk_0 \epsilon \eta_0 \sum_{m=0}^{\infty} \frac{\epsilon_{om}}{a} \cos(m\pi x_i/a) \cos(m\pi x_j/a) j_0^2\left(\frac{m\pi d_{i\text{eff}}}{2a}\right) \\
 & \cdot \frac{\cos(\beta_m (b - y_j)) \cos(\beta_m y_i)}{\beta_m \sin(\beta_m b)} \quad (18)
 \end{aligned}$$

where $\eta_0 = 377$ ohms, $\epsilon_{om} = 1$ for $m = 0$, and 2 otherwise, (x_i, y_i) and (x_j, y_j) are the coordinates of the source J and shorting pin, respectively. For a general

case, when the N ports consist of both slots and pins as shown in Fig. 4, the currents and voltages at the N ports can also be written as follow

$$\sum_j I_j Z_{ij} = V_i, \quad i, j = 1, \dots, N. \quad (19)$$

since the solutions to E and H everywhere in the patch for any J and K have been obtained, one can therefore compute the input impedance Z_{in} at any port, using the same method as discussed above.

IV. THEORETICAL AND EXPERIMENTAL RESULTS

Our approach to the dual-frequency microstrip antenna, as stated earlier, is based on the theoretical argument that shorting pins and slots if placed at appropriate locations in the patch can raise the (0,1) and lower the (0,3) operating frequencies, respectively. In general, with pins and slots, the modal field is no longer pure. The existence of a substantial amount of higher order modes will modify the antenna overall resonant frequency which, as defined in [3], occurs when the reflection coefficient $|\Gamma|$ reaches a minimum.

Several antennas have been constructed and tested to determine the validity of the theory. All of them were made of double copper-clad laminate Rexolite 2200, 1/16" thick. The relative permittivity $\epsilon_r \approx 2.62$, the loss tangent $\delta \approx 0.001$, and the copper cladding conductivity $\approx 270 \text{ K} \text{Mho/m}$. These values were used for theoretical computations.

One of the rectangular microstrip antennas, having the dimensions $a = 19.4 \text{ cm}$ and $b = 14.6 \text{ cm}$, is fed with a miniature cable at $x_1 = 9.7 \text{ cm}$ and $y_1 = 0$ as shown in Figure 1. A slot of length $l = 3.0 \text{ cm}$ and width $w = 0.15 \text{ cm}$ is cut at $x_2 = 9.7 \text{ cm}$ and $y_2 = 7.3 \text{ cm}$ on the patch. The feed location was chosen for a good match to the 50Ω line for both F_H and F_L bands. The calculated

and measured input impedance loci for both bands are shown in Figure 2a and 2b, where for comparison the corresponding loci without slot are also shown by the dashed curves. The calculated and measured radiation patterns are shown in Figure 2c. Similar results for slot length $\ell = 4.5$ cm are shown in Figure 3a and 3b. It is seen that the agreement between theoretical and measured results is excellent for both bands and that the slot has only a minor effect on the low band impedance locus, but a significant effect on the high band impedance locus as expected.

To further reduce the ratio of the operating frequencies of the high and low band, F_H/F_L , in addition to the slots, shorting pins can be inserted along the nodal lines of the (0,3) mode electric field as illustrated in Figure 4. Due to limited space here, only a few typical measured impedance loci and radiation patterns for both bands are shown in Figures 3, 5 and 6. From Figures 3, 5 and 6, it is seen that while the "resonant" frequencies are changed for both bands with pins and slots, in general, the radiation patterns for both bands remain primarily the same. It may also be noted that the input impedance can vary widely with the feed position and one is therefore free to choose the feed position for a desired impedance without undue concern about its effect on the pattern. The measured gains of these microstrip antennas as compared with those of a $\lambda/2$ -tuned dipole, 0.2λ over a ground plane, are -0.5 to -1db for the low band and $-1.5 \sim 2\text{db}$ for the high band.

Table 1 summarizes the values of F_H/F_L for six cases. From these results, it is seen that in general the slots can lower F_H and shorting pins raise F_L , resulting in a variation of F_H/F_L from 3.02 to 1.31. In fact, this ratio can be reduced even further by adding more pins and slots. However the effectiveness of adding more pins and slots will eventually diminish. Instead, we find that the ratio F_H/F_L can be reduced to about 1.07 by using a C-shaped slot (or a wrap-around microstrip line). This will be reported in Part IV.

TABLE 1
THE OPERATING FREQUENCIES FOR BOTH F_L AND F_H

CASE	F_L (MHz)	F_H (MHz)	F_H/F_L
A. One slot $\ell_1 = 1.0$ cm at (9.7,7.3)	628	1900	3.02
B. One slot $\ell_1 = 3.0$ cm at (9.7,7.3)	596	1700	2.85
C. Three slots $\ell_1 = 7.0$ cm $\ell_2 = \ell_3 = 3.0$ cm at (9.7,2.4), (9.7,7.3) and (9.7,12.2)	555	1420	2.55
D. Three slots $\ell_1 = \ell_2 = \ell_3 = 7.0$ cm at the same location as in case C.	553	1310	2.36
E. Same as case D but with four pins as shown in Figure 4.	698	1087	1.56
F. Same as case E with six additional pins at (3.7,2.4), (9.7,2.4), (15.7,2.4), (3.7,12.2), (9.7,12.2) and (15.7,12.2)	890	1181	1.31

V. CONCLUSION

This investigation shows that a single rectangular microstrip antenna element can be designed to perform for dual frequency bands corresponding approximately to the (0,1) and (0,3) modes. The frequencies of both bands can be tuned over a wide range, with their ratio from 3 to less than 1.3, by adding shorting pins and slots in the patch. A method for analyzing these antennas has been developed and treats the antenna as a multi-port cavity. The validity of this theory is verified by comparing the computed impedance loci and radiation patterns with the measured for a few simple cases.

As a design guide, in general, the effect of slot on the high-band frequency is stronger if it is placed where the high-order modal magnetic field is stronger, and the effect of short pin on the low-band frequency is stronger if it is placed where the low-order modal electric field is stronger.

LIST OF REFERENCES

- [1] Sanford, G. G. and R. E. Munson, "Conformal VHF Antenna for the Apollo-Soyuz Test Project," IEEE AP-S Int. Symp. Digest, October 1976.
- [2] Derneryd, A. G., "Microstrip Disc Antenna Covers Multiple Frequencies," Microwave Journal, pp. 77-99, May 1978.
- [3] Lo, Y. T., C. E. Skupien and S. S. Zhong, "A Study of Microstrip Antennas for Multiple Band Operation," Report No. RADC-TR-82-236, September 1982. Also Lo, Y. T., C. E. Skupien, S. S. Zhong, and W. F. Richards, "Dual-Frequency Microstrip Antennas," 1983 National Radio Science Meeting Digest, URSI, p. 98, Houston, TX, and Schaubert, D. H., F. G. Garrar, A. Sindoris and S. T. Hayes, "Microstrip Antennas with Frequency Agility and Polarization Diversity," IEEE Trans. on Antennas and Propagation, vol. 29, pp. 118-123, Jan. 1981 for using shorting post for tuning.
- [4] Richards, W. F., Y. T. Lo and D. D. Harrison, "An Improved Theory for Microstrip Antennas and Applications," Report No. RADC-TR-79-111, May 1979 and also appear in IEEE Trans. Antenna Propagat., Vol. AP-29, No. 1, January 1981.
- [5] Lo, Y. T., W. F. Richards, P. S. Simon, J. E. Brewer and C. P. Yuan, "Study of Microstrip Antenna Elements, Arrays, Feeds, Losses and Applications," Report No. RADC-TR-81-98.
- [6] Desoer, Charles A. and Ernest S. Kuh, "Basic Circuit Theory," 1969 by McGraw-Hill, Inc.

LIST OF FIGURES

- Figure 1. Geometry of a rectangular microstrip antenna with idealized feeds.
- Figure 2a. Measured and computed impedance loci of a rectangular microstrip antenna with one slot ($l = 3.0$ cm) for low band. $a = 19.4$ cm, $b = 14.6$ cm and $t = 0.158$ cm.
- Figure 2b. Measured and computed impedance loci for high band. $a = 19.4$ cm, $b = 14.6$ cm and $t = 0.158$ cm.
- Figure 2c. Measured and computed radiation patterns for both bands. $a = 19.4$ cm, $b = 14.6$ cm and $t = 0.158$ cm.
- Figure 3a. Measured and computed impedance loci for a rectangular microstrip antenna with one slot ($l = 4.5$ cm). $a = 19.4$ cm, $b = 14.6$ cm, and $t = 0.158$ cm.
- Figure 3b. Measured and computed radiation pattern for a rectangular microstrip antenna with one slot ($l = 4.5$ cm). $a = 19.4$ cm, $b = 14.6$ cm and $t = 0.158$ cm.
- Figure 4. The microstrip antenna with shorting pins and slots. All dimensions are in mm.
- Figure 5a. Measured impedance loci for a rectangular microstrip antenna with 3 slots and 4 pins. $a = 19.4$ cm, $b = 14.6$ cm and $t = 0.158$ cm.
- Figure 5b. Measured radiation patterns for a rectangular microstrip antenna with 3 slots and 4 pins. $a = 19.4$ cm, $b = 14.6$ cm and $t = 0.158$ cm.
- Figure 6a. Measured impedance loci for a rectangular microstrip antenna with 3 slots and 10 pins. $a = 19.4$ cm, $b = 14.6$ cm and $t = 0.158$ cm.
- Figure 6b. Measured radiation pattern for a rectangular microstrip antenna with 3 slots and 10 pins. $a = 19.4$ cm, $b = 14.6$ cm and $t = 0.158$ cm.

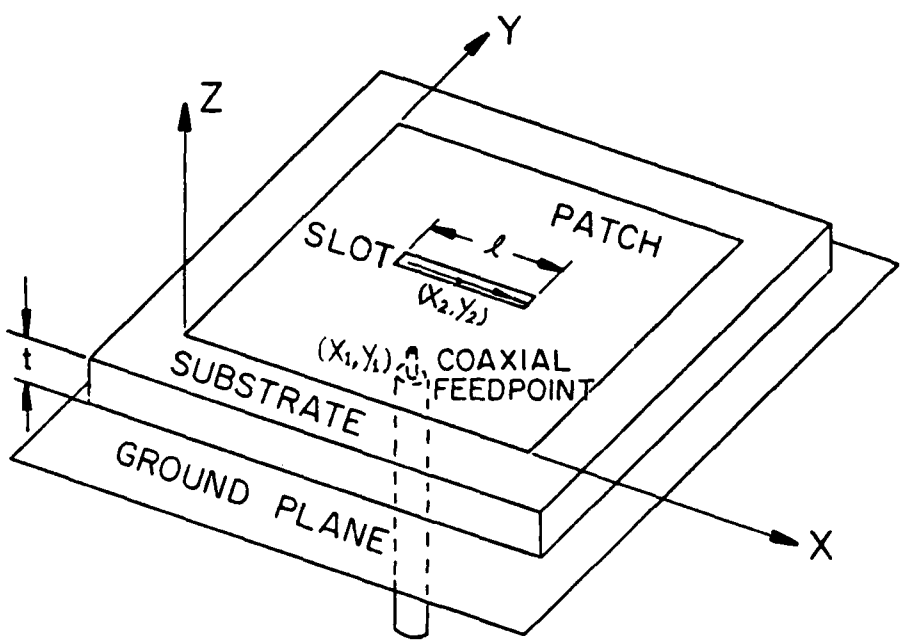


Figure 1. Geometry of a rectangular microstrip antenna with idealized feeds.

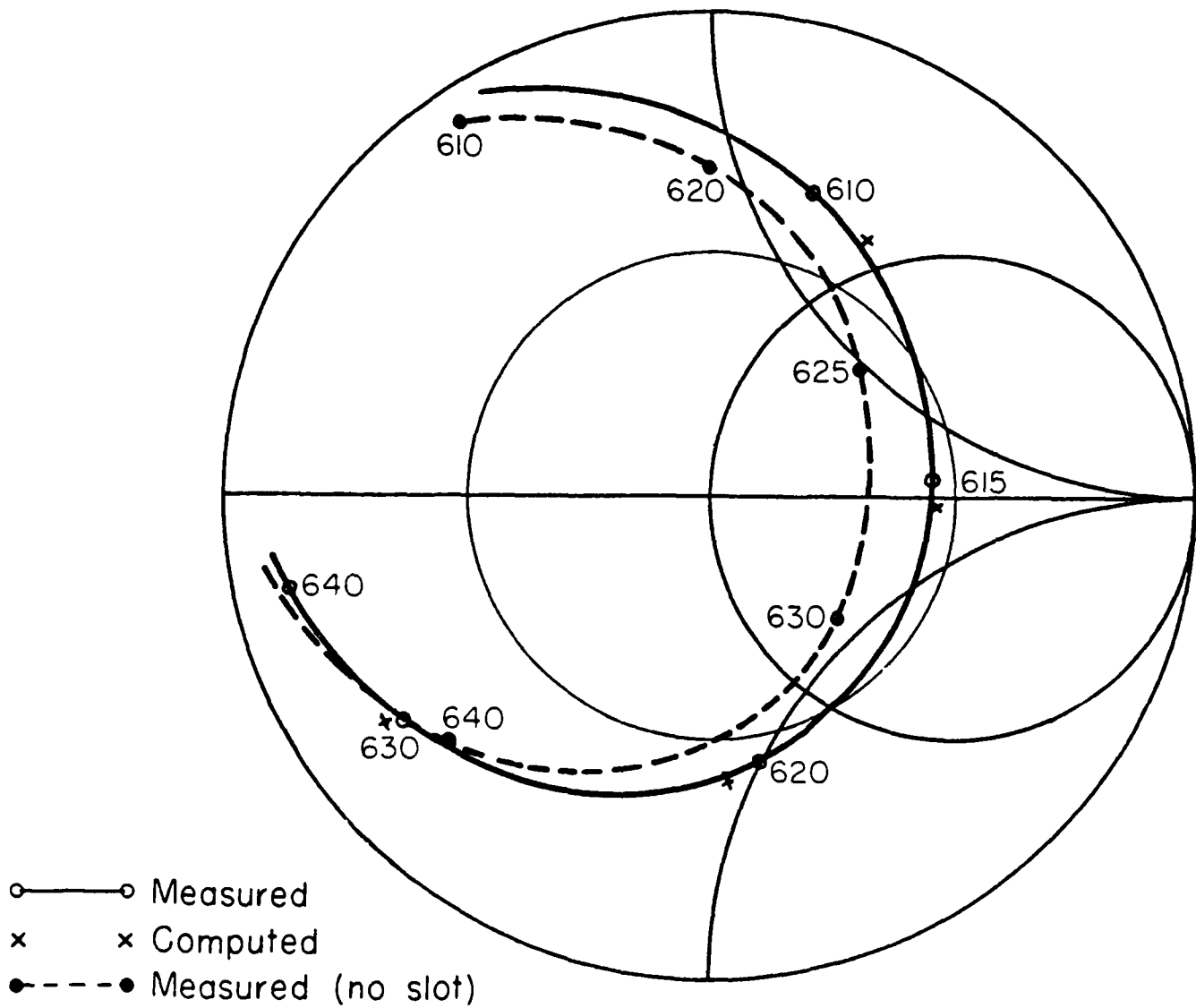


Figure 2a. Measured and computed impedance loci of a rectangular microstrip antenna with one slot ($l = 3.0$ cm) for low band. $a = 19.4$ cm, $b = 14.6$ cm and $t = 0.158$ cm.

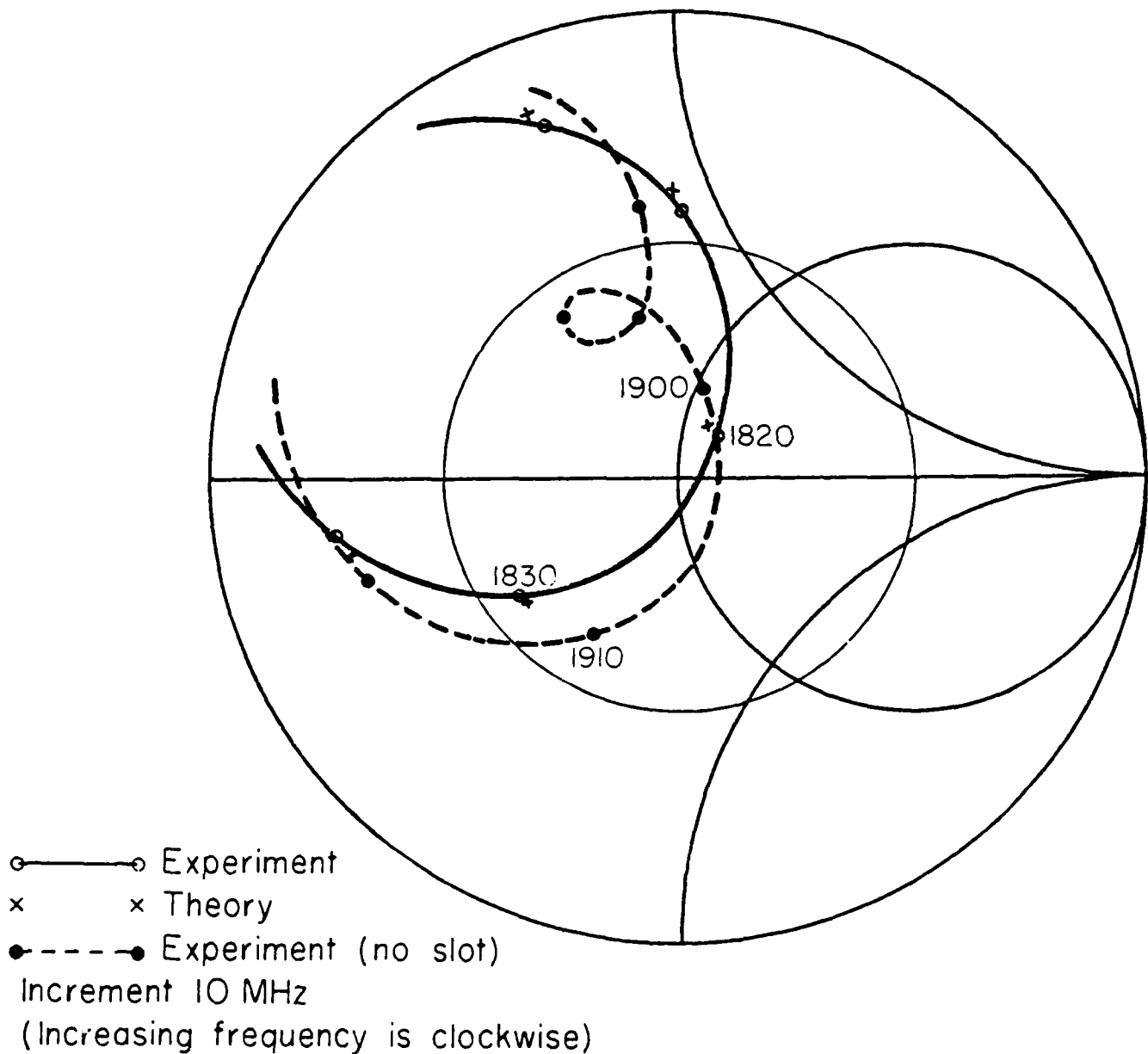


Figure 2b. Measured and computed impedance loci for high band. $a = 19.4$ cm,
 $b = 14.6$ cm and $t = 0.158$ cm.

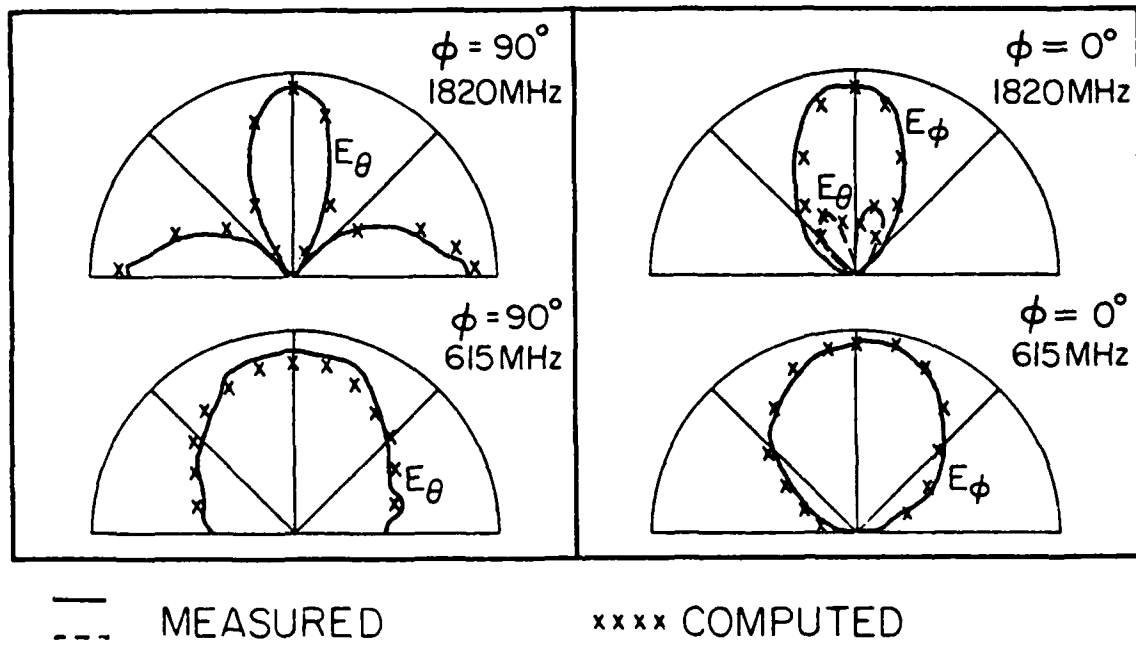


Figure 2c. Measured and computed radiation patterns for both bands.
 $a = 19.4$ cm, $b = 14.6$ cm and $t = 0.158$ cm.

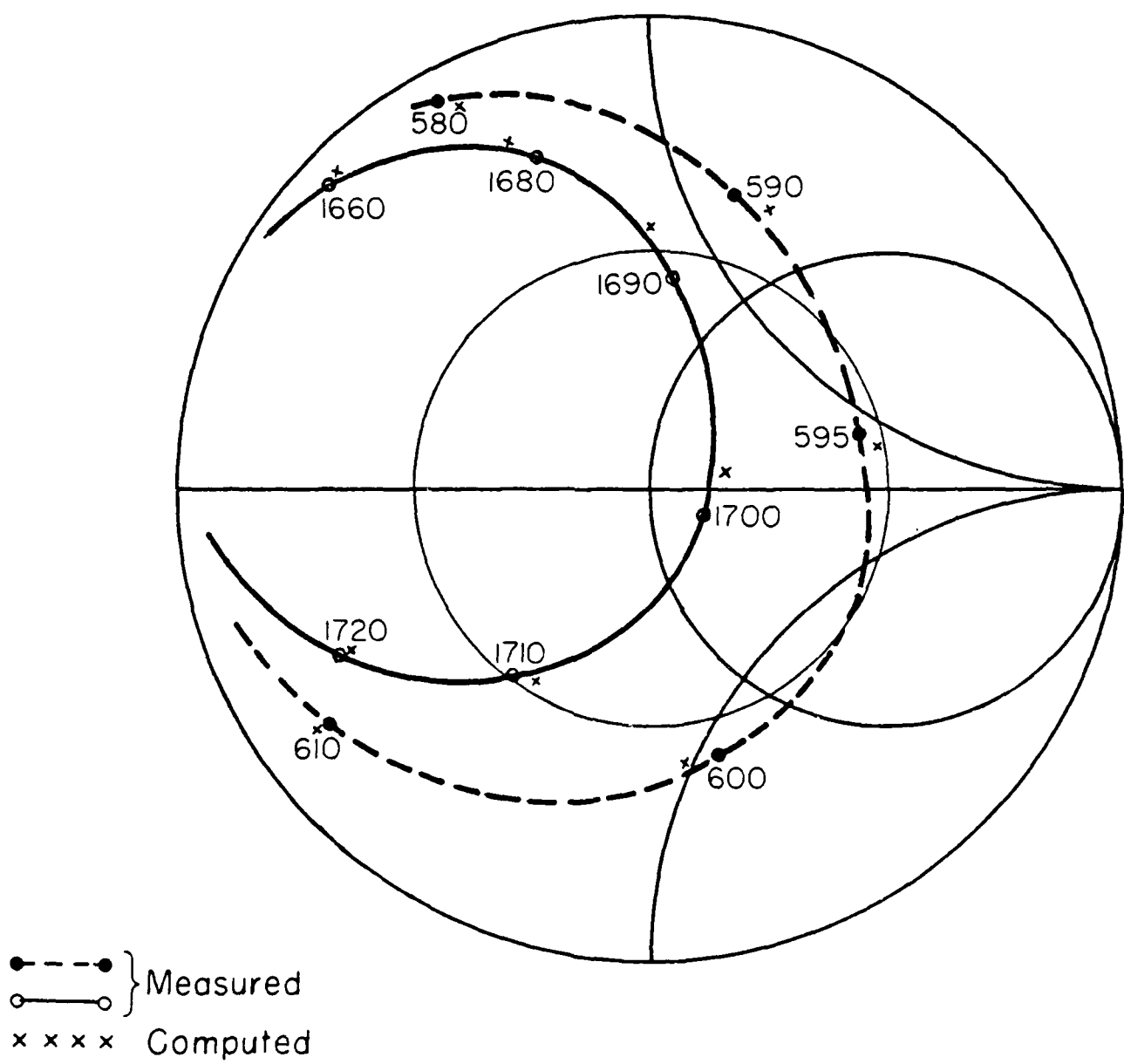


Figure 3a. Measured and computed impedance loci for a rectangular microstrip antenna with one slot ($l = 4.5$ cm). $a = 19.4$ cm, $b = 14.6$ cm, and $t = 0.158$ cm.

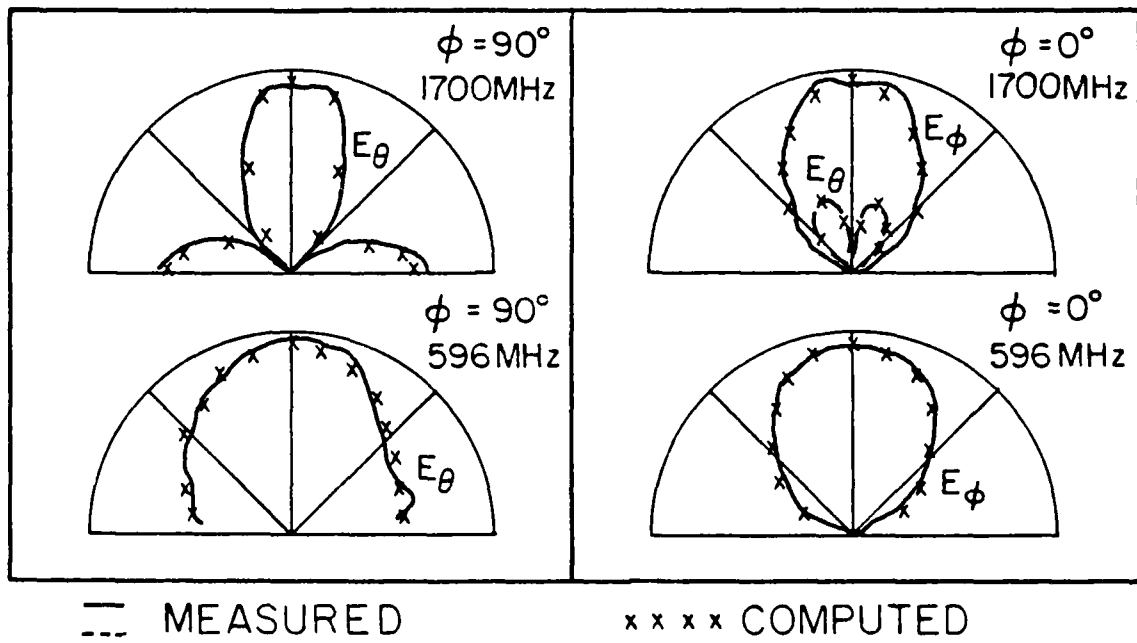


Figure 3b. Measured and computed radiation pattern for a rectangular microstrip antenna with one slot ($\ell = 4.5$ cm). $a = 19.4$ cm, $b = 14.6$ cm and $t = 0.158$ cm.

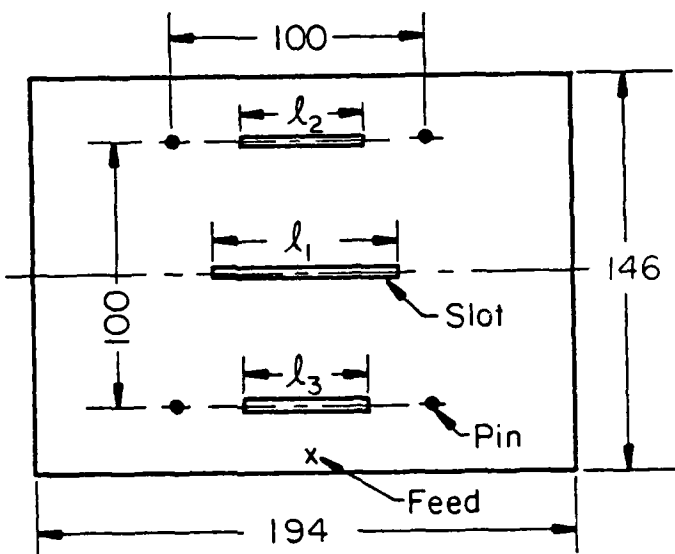


Figure 4. The microstrip antenna with shorting pins and slots. All dimensions are in mm.

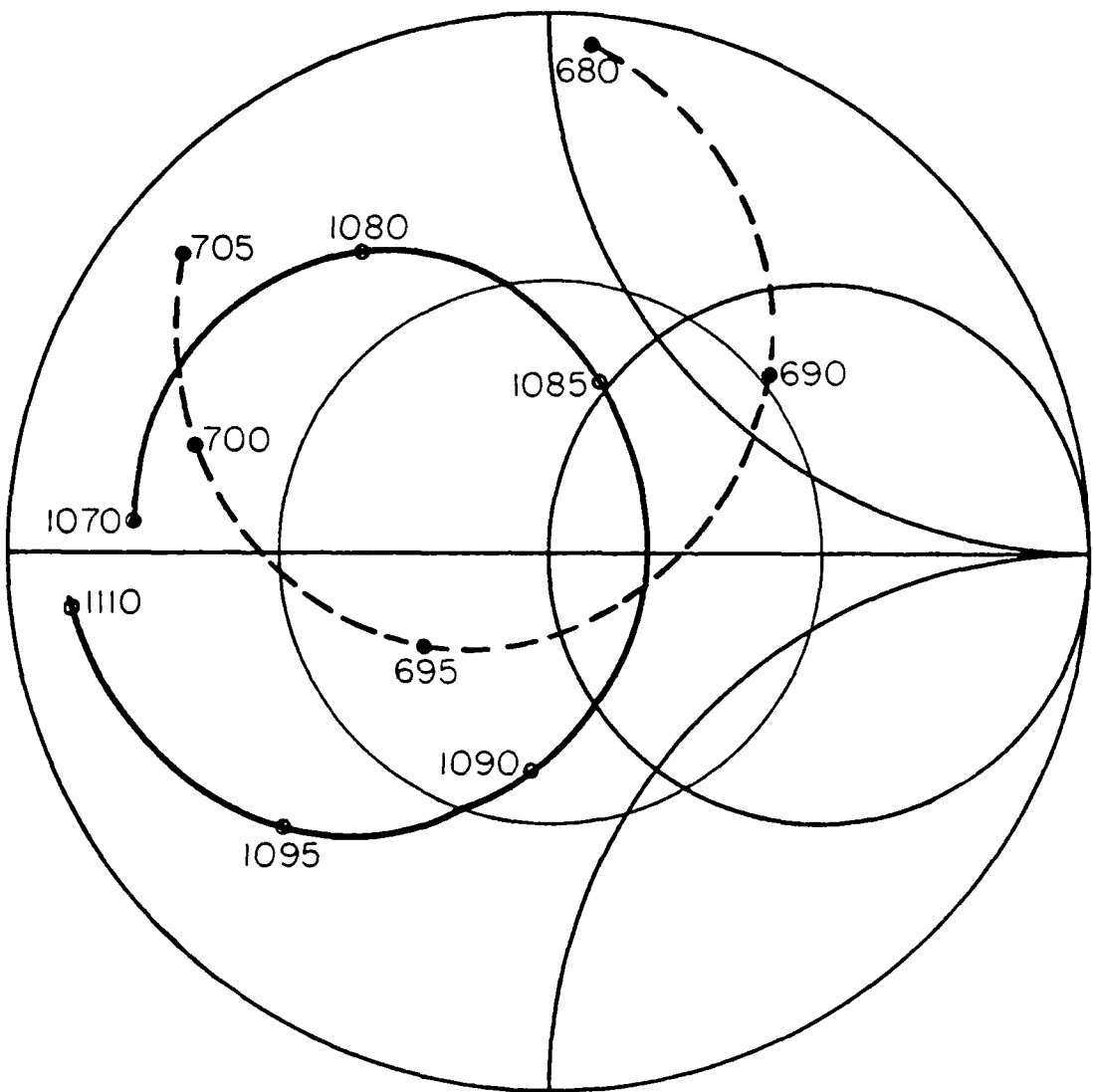


Figure 5a. Measured impedance loci for a rectangular microstrip antenna with 3 slots and 4 pins. $a = 19.4$ cm, $b = 14.6$ cm and $t = 0.158$ cm.

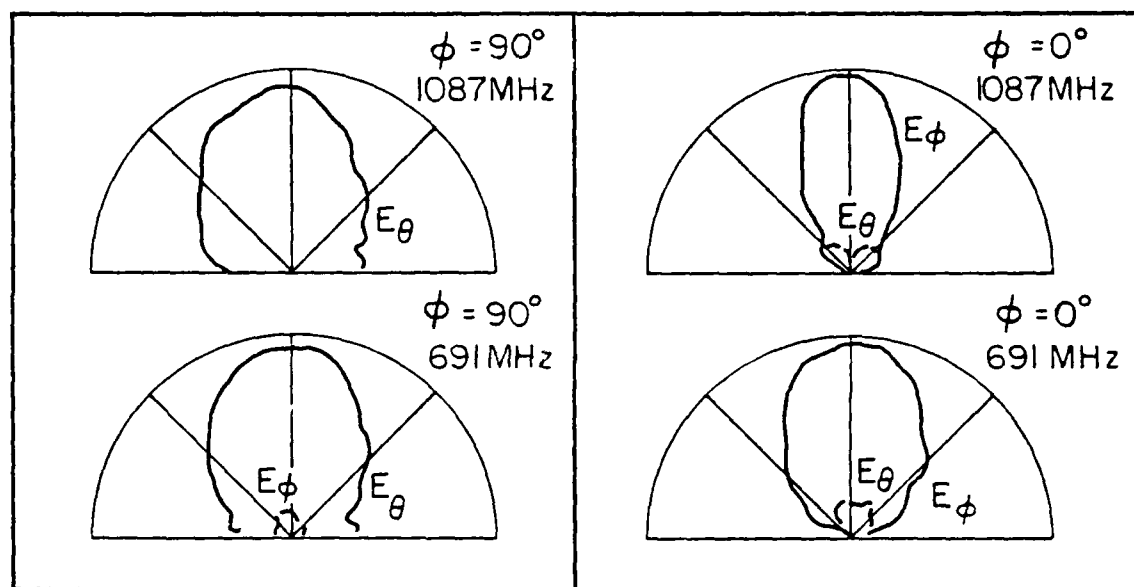


Figure 5b. Measured radiation patterns for a rectangular microstrip antenna with 3 slots and 4 pins. $a = 19.4$ cm, $b = 14.6$ cm and $t = 0.158$ cm.

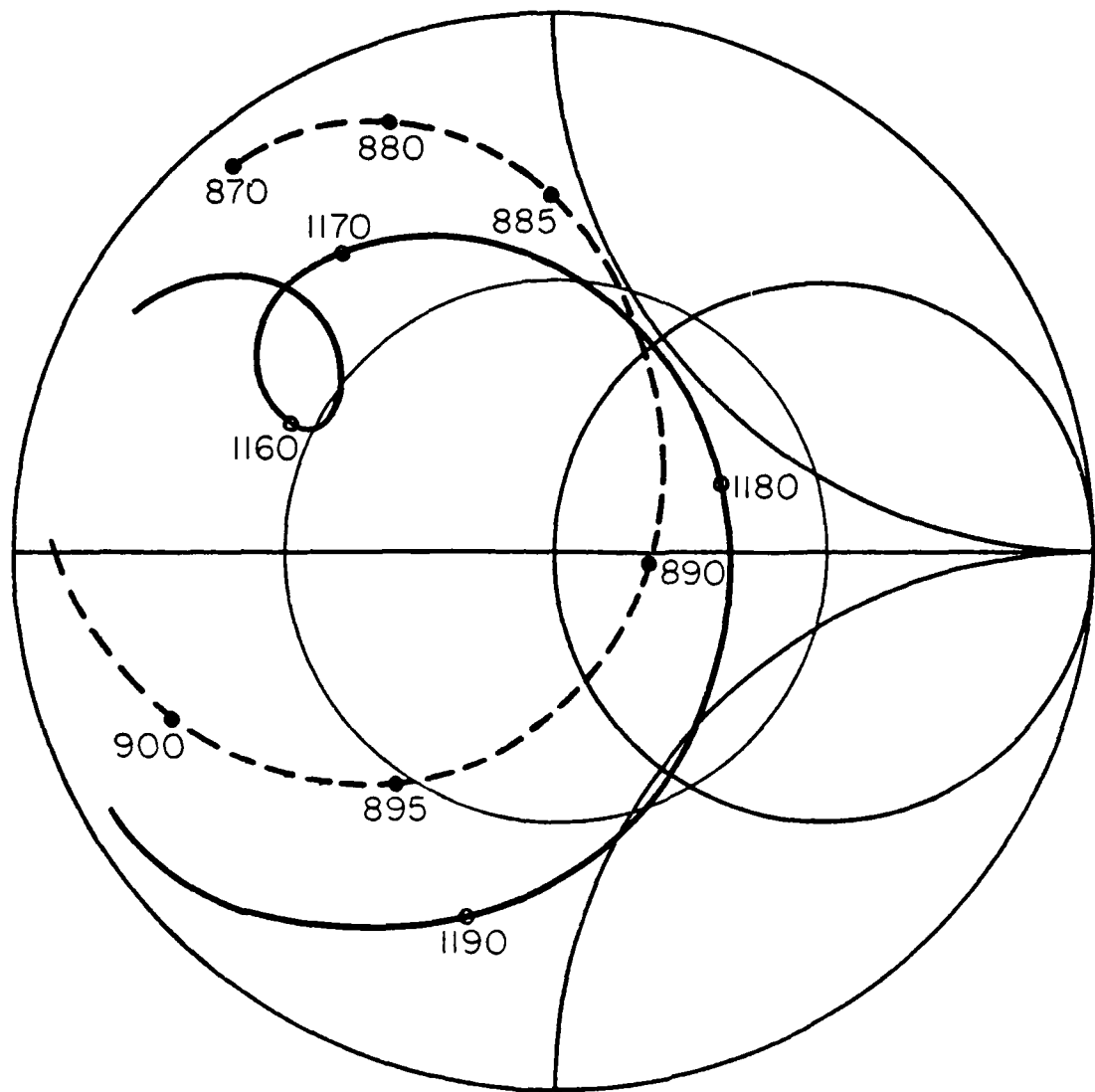


Figure 6a. Measured impedance loci for a rectangular microstrip antenna with 3 slots and 10 pins. $a = 19.4$ cm, $b = 14.6$ cm and $t = 0.158$ cm.

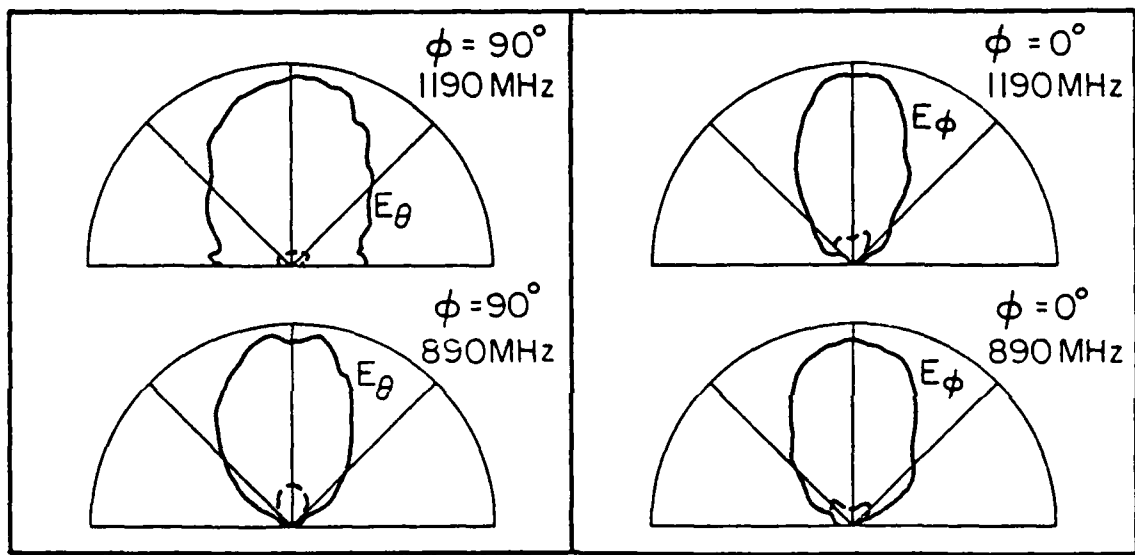


Figure 6b. Measured radiation pattern for a rectangular microstrip antenna with 3 slots and 10 pins. $a = 19.4$ cm, $b = 14.6$ cm and $t = 0.158$ cm.

PART IV

FURTHER STUDY OF
DUAL-FREQUENCY MICROSTRIP
ANTENNAS

BY
Y. T. LO
AND
B. F. WANG

Introduction

In many applications it is desirable to have a single element microstrip antenna capable of simultaneous operation at two different bands. For two orthogonal linear polarizations, the solution is obvious and simple. For a single linear polarization, there are a few possible solutions. In particular, it was shown [1] that by cutting slots and/or inserting shorting pins in the patch the ratio of the two frequency bands could be varied from 3 to 1.3. However, for some applications, such as GPS, a smaller ratio is required. To that end, a patch with a c-shaped slot is found successful.

A. Simple Theory and Some Results

A rectangular microstrip antenna with a c-shaped slot as shown in Fig. 1 can be analyzed numerically by the moment method [2]. In this communication a simple approximate theory is attempted, because it could provide much physical insight into the system and lead to a better design. This is based on two speculations. First, for thin microstrip antennas a strong field should be built up under the patch. Second, the structure might be considered as a parallel connection between a conventional rectangular microstrip patch antenna (PA) and a wrap-around microstrip transmission line (TL). From the first observation, one perhaps could neglect the difficult problem of evaluating the coupling effect between PA and TL and obtain a useful first-order solution. To gain some credence to this approach, the impedance characteristics of the PA and the TL in the absence as well as in the presence of each other is measured as shown in Figs. 2 and 3. Although there are some differences, the coupling effect appears to be not serious.

From Reference [3] one could compute the input impedance of the PA. The computed susceptance, B_{PA} , for the patch made of Rexolite 2200, 1/16" thick is shown in Fig. 4 with its dimensions. Also shown is the susceptance of the

wrapped TL, using the following approximate formula [4], [5],

$$B_{TL} = 2 Y_0 \tan(k_0 \sqrt{\epsilon_e} l_e) \quad (1)$$

where ϵ_e = effective permittivity for the line

$$\approx \frac{1}{2} [(\epsilon_r + 1) + (\epsilon_r - 1) (1 + \frac{10t}{d})^{-1/2}] ,$$

$$Y_0 \approx \frac{2\sqrt{\epsilon_r}}{377} \left\{ \frac{d}{2t} + 0.441 + 0.082 \left(\frac{\epsilon_r - 1}{\epsilon_r^2} \right) \right.$$

$$\left. + \left(\frac{\epsilon_r + 1}{2\pi\epsilon_r} \right) [1.451 + \ln(\frac{d}{2t} + 0.94)] \right\} ,$$

ϵ_r = relative permittivity of the substrate,

d = width of the TL,

t = thickness of the substrate,

k_0 = free-space wave number,

l_e = effective TL length \approx average of one half of the rectangular ring length.

Because of the symmetry in this case, the rectangular ring TL can be considered as two open lines, each being one half the ring, in parallel, which lead to the simple Eq. (1). In this simple computation, the discontinuities at the bends and T-junction are neglected. The two adjacent resonant frequencies of the TL are indicated by F_1 and F_2 and that of the PA by F_o . As seen from the figure, with the two connected in parallel, the resonant frequencies should occur at $F_L \approx 1.17 - 1.19$ GHz and $F_H \approx 1.336 - 1.344$ GHz. These predicted values, despite the simple rough theory, agree very well with the experimentally measured values of 1.174 and 1.335 GHz, respectively, as shown in Fig. 5.

The values of the input impedances at the junction point between the PA and TL shown in Fig. 5 are not desirable. Much improved values, for example, for matching to a 50Ω line for both bands, can be obtained by moving the feed inside the patch as shown in Fig. 6. A more rigorous approach for this case can be made by using the multiple port theory [6]. This will be reported elsewhere later. The radiation patterns are essentially those of the PA alone as shown in Figs. 7 and 8.

For this method, the PA resonant frequency F_0 must be between the two adjacent resonant frequencies F_1 and F_2 of the TL. The separation between F_1 and F_2 is inversely proportional to λ_e of the TL:

$$F_1 - F_2 = v/4\lambda_e$$

where $v = 3 \times 10^8/\sqrt{\epsilon_r}$ if λ_e is in meters. Thus to reduce the ratio (F_H/F_L) , in general λ_e shall be increased. This is shown in Tables 1 and 2 for $a = 99$ mm, $b = 77$ mm, $w = a_1 = a_2 = b_1 = b_2 = 6$ mm. First it is seen that the ratio for this example can be reduced to as small as 1.05. Second, the ratio does not necessarily decrease as λ_e increases as in Table 2. This could be caused by the unknown coupling effect since the gap Δ between the PA and the TL is much smaller in this case. Furthermore, the input susceptance of the PA is not that of a simple parallel resonant circuit or TL [3].

There are many possible ways to tune or to change the ratio of F_H and F_L . For example, if $a = 99$ mm, $b = 77$ mm, $a_1 = a_2 = 28$ mm, $w = 5$ mm, and $\Delta = 2$ mm, the ratio F_H/F_L can be varied with b_1 and b_2 as shown in Table 3. Shorting pins, a short tab, or a varactor if placed on the TL, for example, at $x = a_1 + \Delta + \frac{a}{2}$, $y = b + 2(\Delta + b_1)$, can obviously be used for tuning F_H and F_L . These results are deleted for brevity.

TABLE 1
VARIATION OF OPERATING FREQUENCIES F_L AND F_H WITH TL LENGTH ℓ_e

Δ (mm)	81	86	88.5
ℓ_e (mm)	350	360	365
F_H (MHz)	1280	1244	1235
F_L (MHz)	1190	1174	1180
F_H/F_L	1.075	1.06	1.05

TABLE 2
VARIATION OF OPERATING FREQUENCIES F_L AND F_H WITH TL LENGTH ℓ_e

Δ (mm)	38.5	36	31	23.5	16	9
ℓ_e (mm)	265	260	250	235	220	206
F_H (MHz)	1199	1204	1216	1236	1225	1312
F_L (MHz)	955	980	996	1071	1103	1164
F_H/F_L	1.255	1.228	1.22	1.154	1.137	1.126

TABLE 3
VARIATION OF OPERATING FREQUENCIES F_L AND F_H WITH TL WIDTH b_1 AND b_2

b_1 (mm)	23	15.5	8
b_2 (mm)	23	15.5	8
F_H (MHz)	1228	1210	1215
F_L (MHz)	976	990	1055
F_H/F_L	1.258	1.22	1.15

Conclusion

Several means are found for tuning a single element dual-frequency microstrip antenna. Its structure is only slightly larger than a conventional single frequency band patch antenna. A simple theory is found capable of predicting the two frequency bands quite accurately and also provides much physical insight into the operation mechanism. From this theory it is obvious that this technique can be applied to patch antennas of other geometries as well.

REFERENCES

- [1] B. F. Wang and Y. T. Lo, "Microstrip antennas for dual-frequency operation," IEEE Trans. Antennas Propagat., vol. AP-32, pp. 938-943, Sept. 1984.
- [2] S. M. Wright and Y. T. Lo, "Efficient analysis of infinite microstrip antenna arrays of electrically thick substrates," Part I of this report.
- [3] Y. T. Lo, W. F. Richards and D. D. Harrison, "An improved theory for microstrip antennas and applications - Part I," Technical Report RADC-TR-79-111, May 1979.
- [4] H. A. Wheeler, "Transmission-line properties of parallel strips separated by dielectric sheet," IEEE Trans., vol. MTT-13, pp. 172-185, 1965.
- [5] M. V. Schneider, "Microstrip lines for microwave integrated circuits," Bell Syst. Tech. J., vol. 48, pp. 1421-1444, 1969.
- [6] W. F. Richards and Y. T. Lo, "Theoretical and experimental investigation of a microstrip radiator with multiple lumped linear loads," Electromagn., vol. 3, no. 3-4, pp. 371-385, July-Dec. 1983.

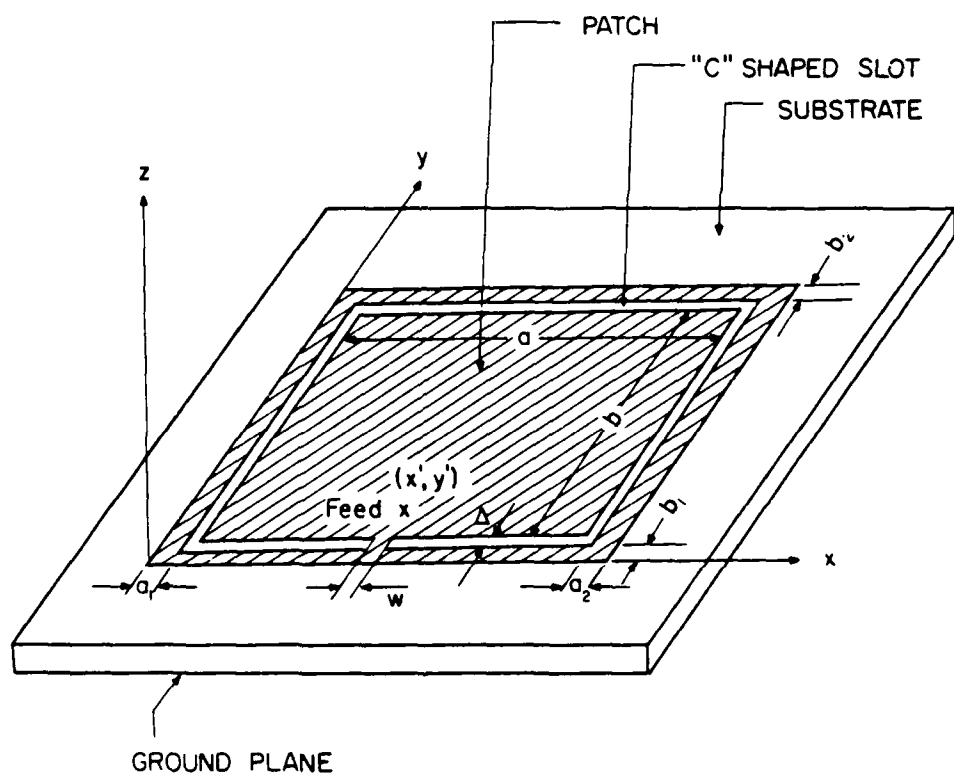


Figure 1. A rectangular microstrip antenna with a c-shaped slot.

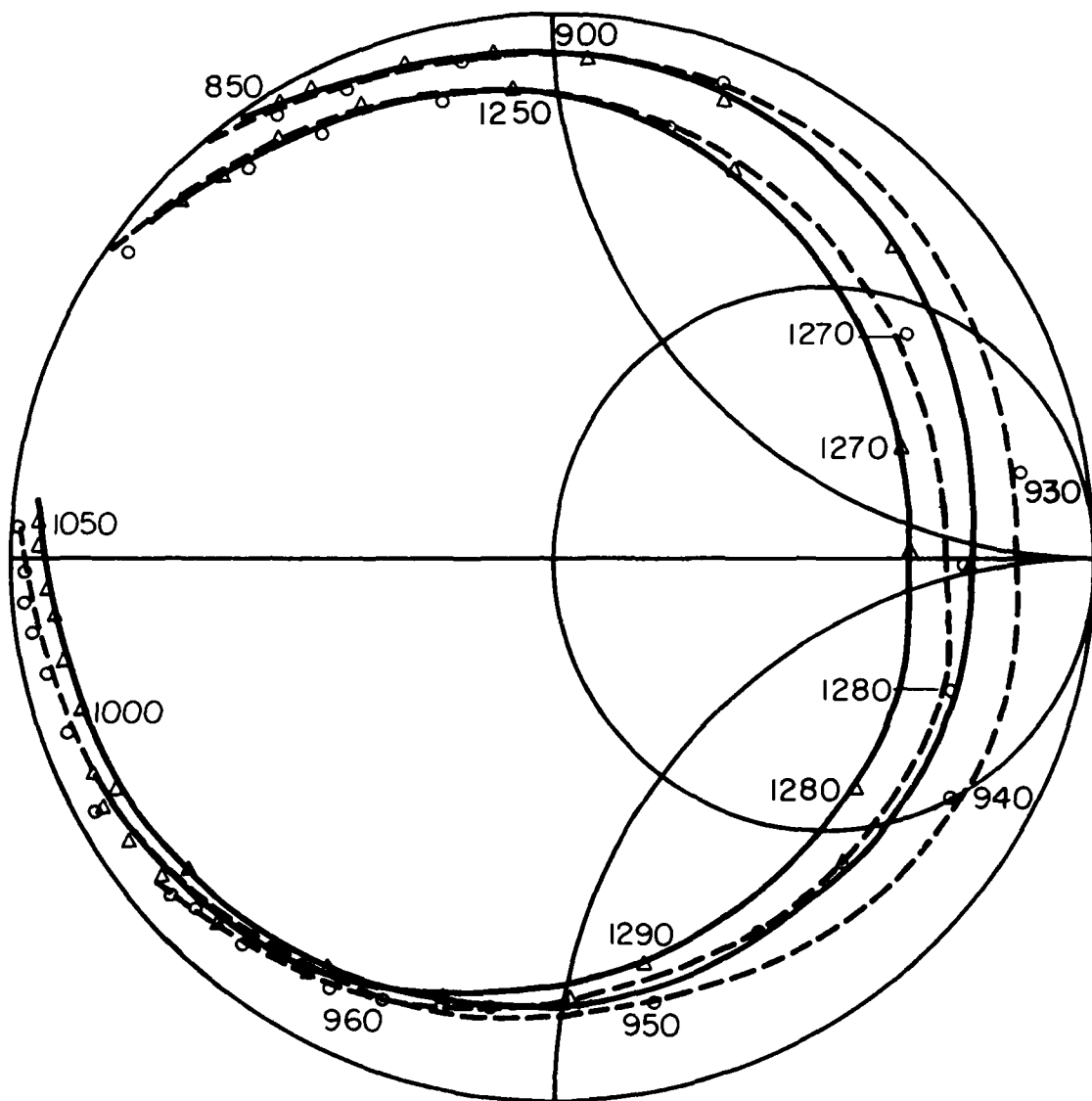


Figure 2. Impedance loci of the rectangular ring-shaped transmission line in the absence (—) of the patch antenna and in the presence (---) of the patch antenna. $a = 99$ mm, $b = 77$ mm, $a_1 = a_2 = 10$ mm, $b_1 = b_2 = 8$ mm, $t = 1.58$ mm, $\Delta = 2$ mm, $w = 5$ mm.

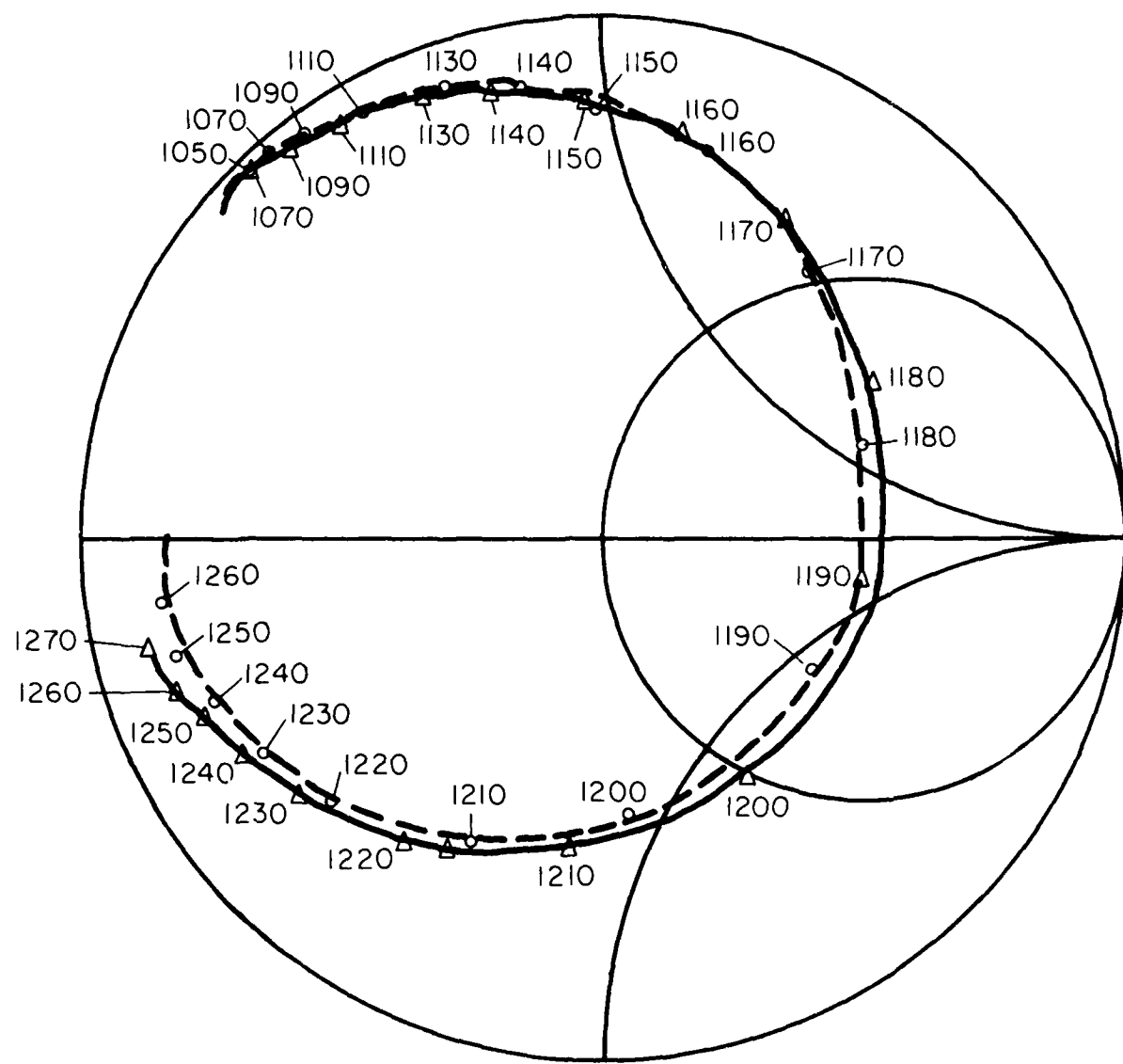


Figure 3. Impedance loci of the patch antenna in (a) the absence (—) and (b) in the presence (---) of the rectangular ring-shaped transmission line. $a = 99$ mm, $b = 77$ mm, $a_1 = a_2 = 10$ mm, $b_1 = b_2 = 8$ mm, $\Delta = 2$ mm, $t = 1.58$ mm, $w = 5$ mm.

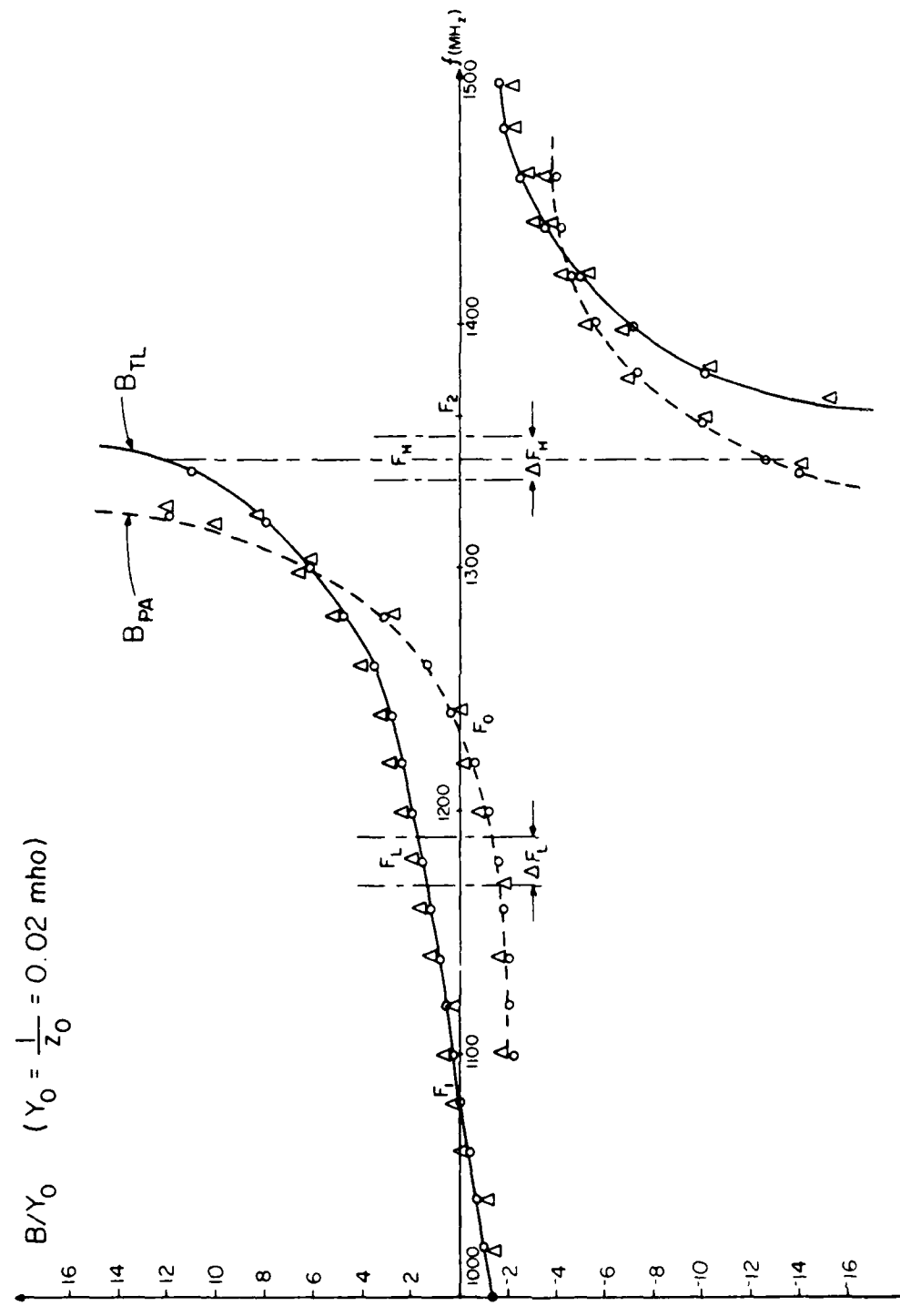


Figure 4. Computed and measured susceptance of the patch antenna and that of the ring-shaped microstrip line patch dimensions: $a = 99$ mm, $b = 77$ mm, and line dimensions: $a_1 = a_2 = b_1 = b_2 = 8$ mm, $\ell_e = 200$ mm.

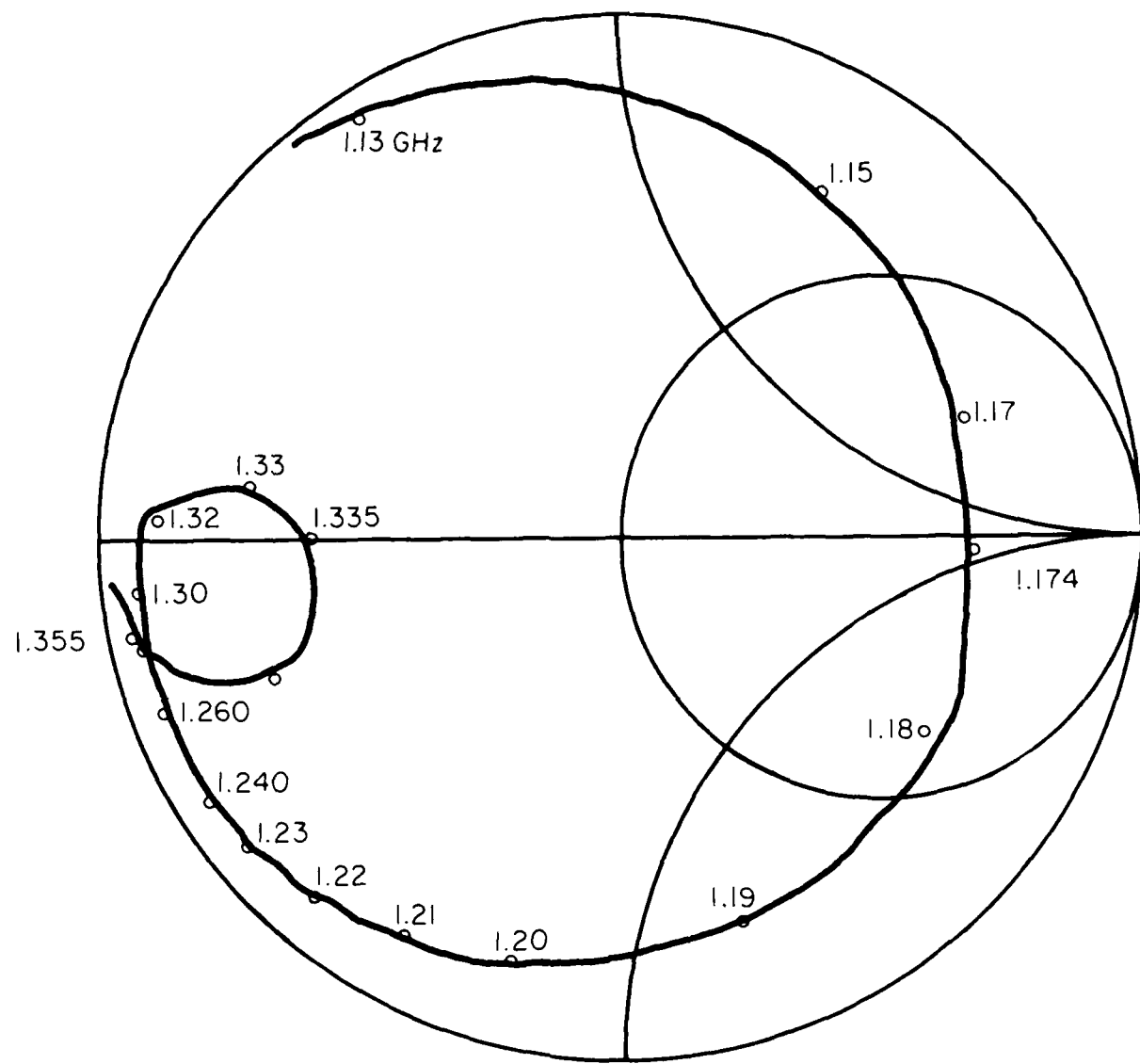


Figure 5. Measured impedance locus of the rectangular microstrip antenna with the c-shaped slot. $a = 99$ mm, $b = 77$ mm, $a_1 = a_2 = b_1 = b_2 = 8$ mm, $\Delta = 2$ mm, $t = 1.58$ mm, $w = 5$ mm. Feed point at $x' = 59.5$ mm, $y' = 10$ mm.

AD-A169 811

A STUDY OF MICROSTRIP ANTENNAS FOR MULTIPLE BAND AND
HIGH FREQUENCY OPERA. (U) ILLINOIS UNIV AT URBANA DEPT
OF ELECTRICAL AND COMPUTER ENGIN. Y T LO ET AL.

4/4

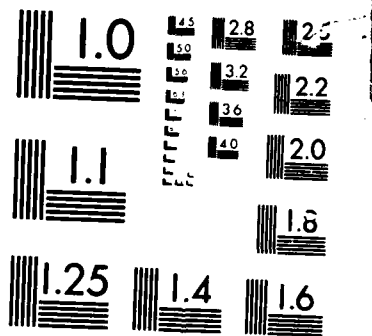
UNCLASSIFIED

MAR 86 UILU-EM-84-15 RADC-TR-86-8

F/B 9/5

ML





MICROCOPY

CHART

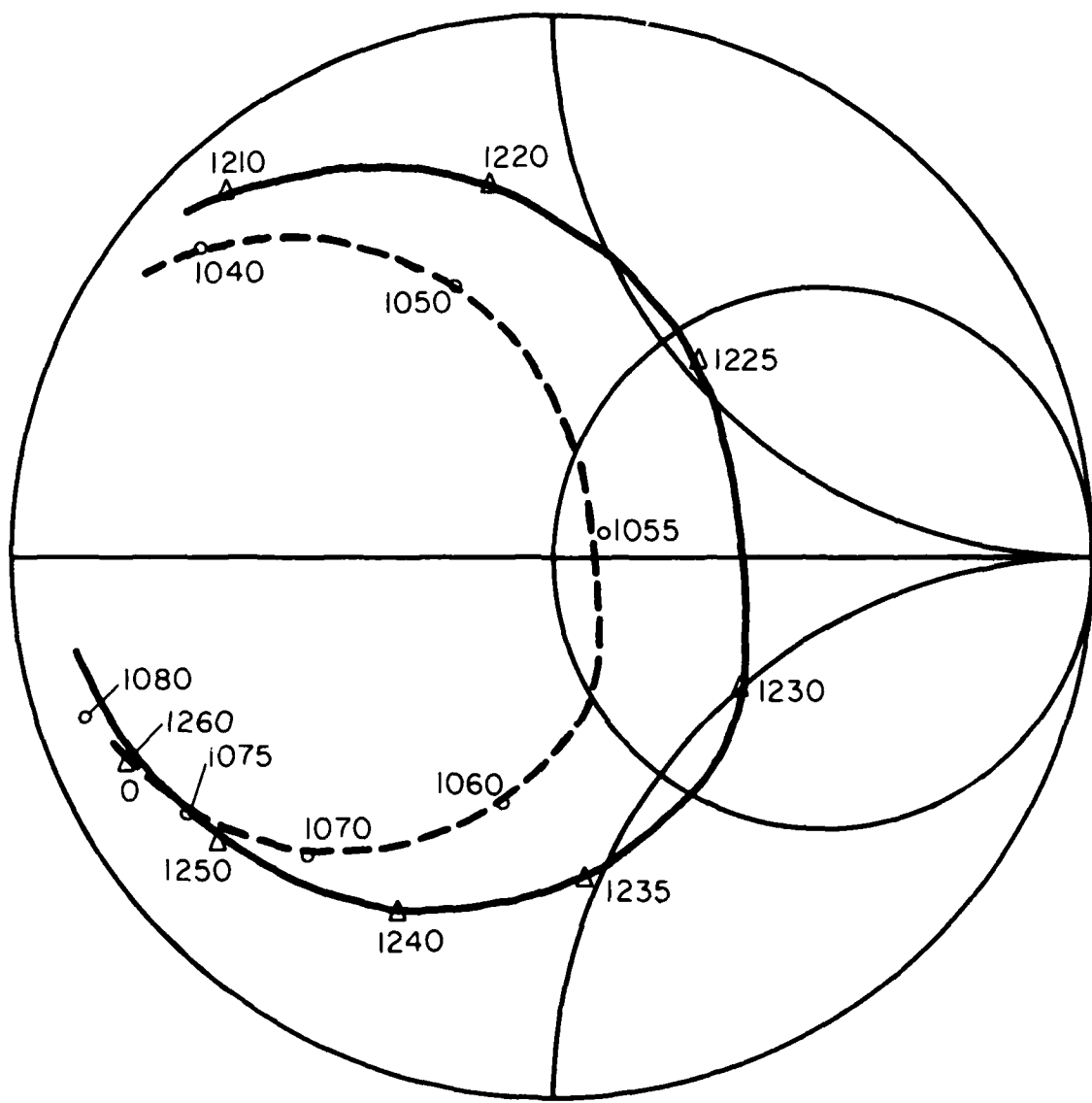


Figure 6. Impedance loci of a microstrip antenna with the c-shaped slot. Dimensions of the antenna are the same as those in Fig. 5 but the feed point is at $x' = 59.5$ mm, $y' = 24$ mm.

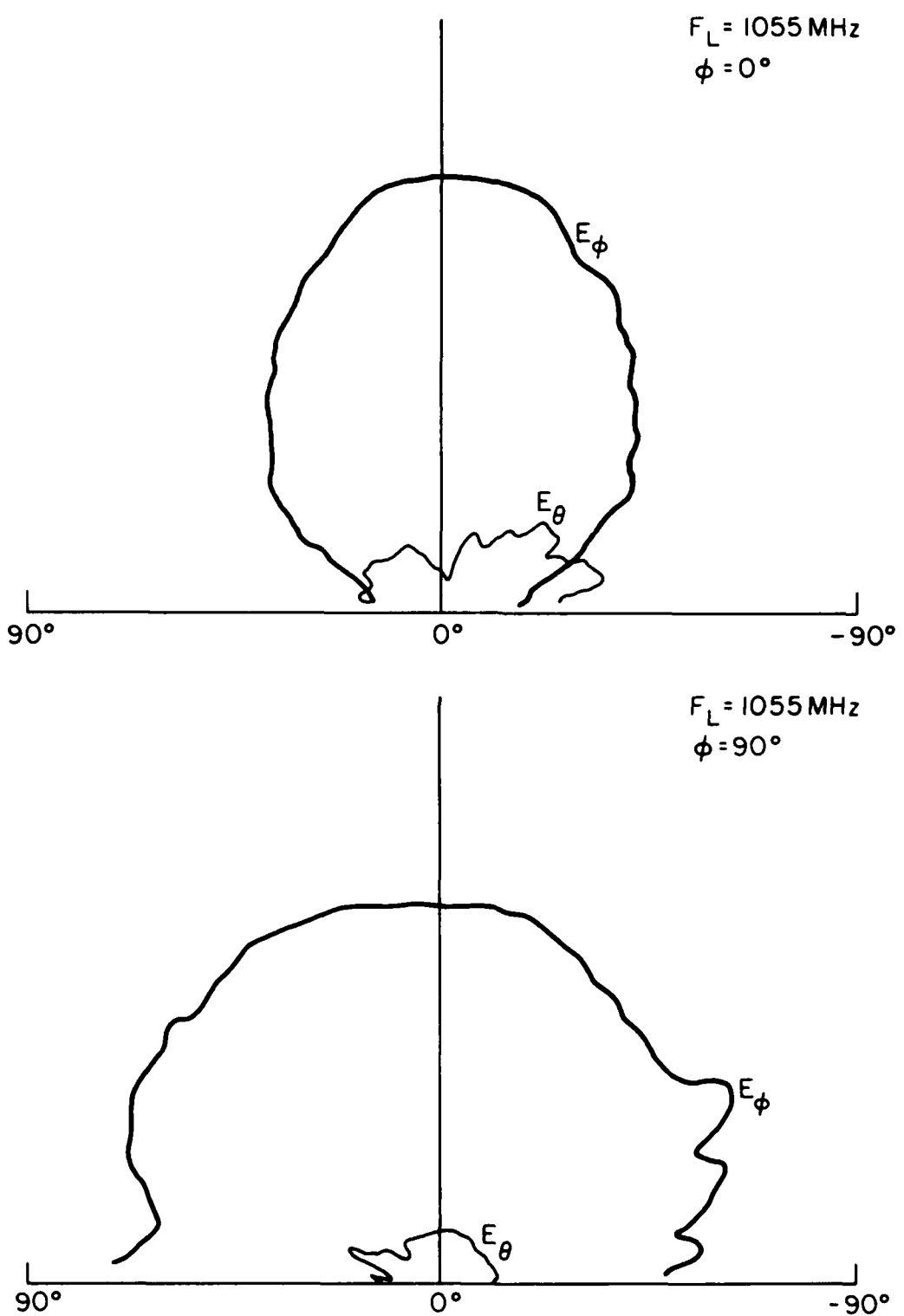


Figure 7. Radiation patterns for the low operating frequency $F_L = 1055 \text{ MHz}$. Dimensions of the antenna are the same as those in Fig. 6.

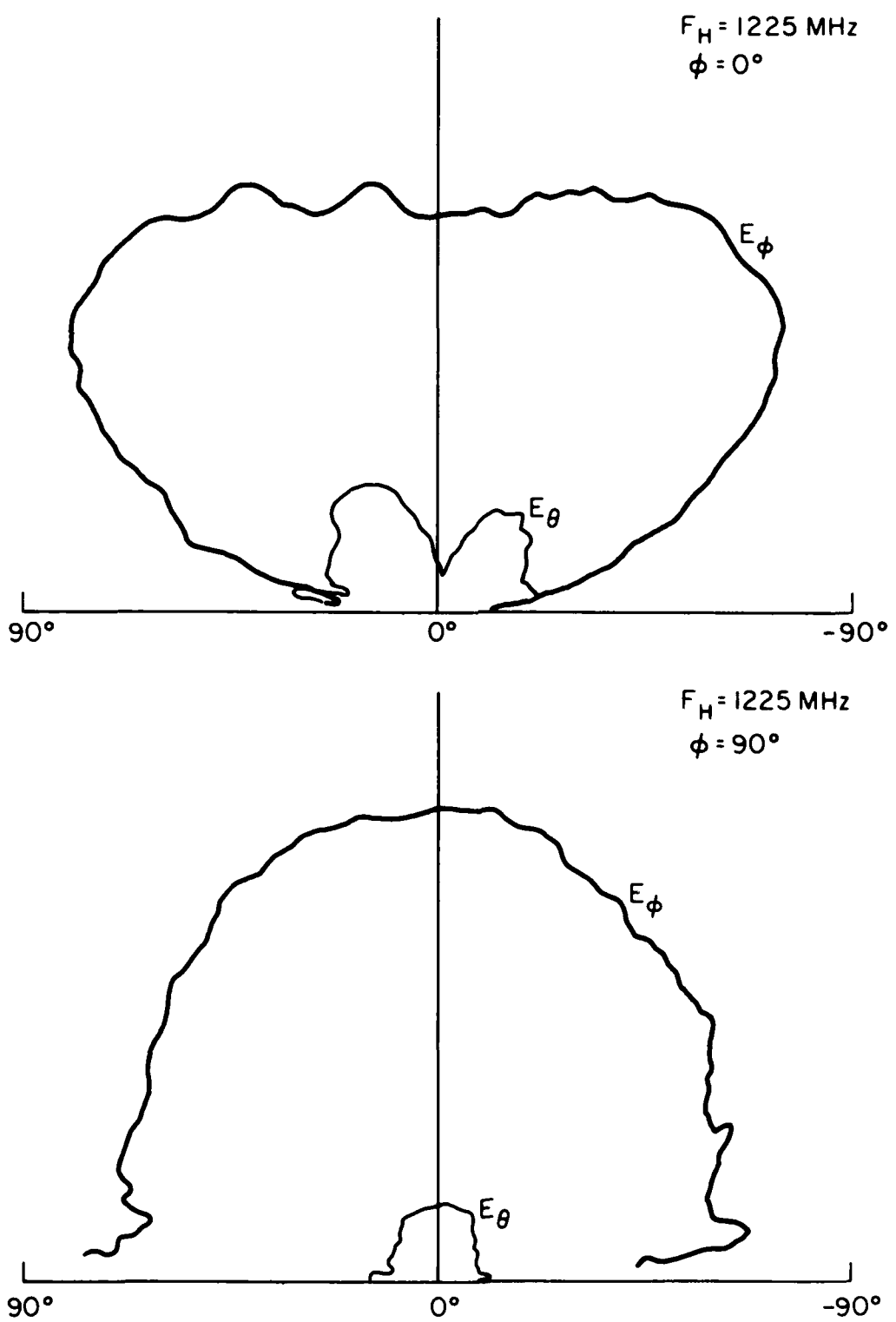


Figure 8. Radiation patterns for high operating frequency $F_H = 1225 \text{ MHz}$. Dimensions of the antenna are the same as those in Fig. 6.

PART V

PERSONNEL

List of participating workers in this project at various times between June 1, 1982 and September 30, 1984: Y. T. Lo, S. M. Wright, W. F. Richards, C. E. Skupien, R. A. Gilbert, S. S. Zhong, M. Davidovitz, B. Engst, B. F. Wang (without pay).

PART VI

OTHER REPORTS RESULTING FROM CONTRACT SPONSORSHIP

- (1) Y. T. Lo, D. D. Harrison, D. Solomon, G. A. Deschamps, and F. R. Ore, "Study of Microstrip Antenna, Microstrip Phased Arrays, and Microstrip Feed Networks," RADC-TR-77-406, Oct. 1977, under AF19628-76-C-0140.
- (2) Y. T. Lo, W. F. Richards, and D. D. Harrison, "An Improved Theory for Microstrip Antennas and Applications - Part I," RADC-TR-79-111, May 1979, under F19628-78-C-0025.
- (3) Y. T. Lo, D. D. Harrison, and W. F. Richards, "An Analysis of the Disk Microstrip Antenna - Part II, RADC-TR-79-132, May 1979, under F19628-78-C-0025.
- (4) Y. T. Lo, W. F. Richards, and J. E. Brewer, "Evaluation of Losses in Microstrip Antenna Materials," RADC-TR-80-85, April, 1980, under F19628-78-C-0025.
- (5) Y. T. Lo, W. F. Richards, P. Simon, "A Study of Microstrip Antenna Elements and Arrays," RADC-TR-80-363, Dec. 1980 under F19628-78-C-0025.
- (6) Y. T. Lo, W. F. Richards, P. S. Simon, J. E. Brewer, and C. P. Yuan, "Study of Microstrip Antenna Elements, Arrays, Feeds, Losses, and Applications," RADC-TR-81-98, June 1981, under F19628-78-C-0025.
- (7) W. F. Richards and Y. T. Lo, "A Fortran Program for Rectangular Microstrip Antennas," RADC-TR-82-78, April 1982, under AFOSR Grant-81-0234.
- (8) Y. T. Lo, C. E. Skupien, and S. S. Zhong, "A Study of Microstrip Antennas for Multiple Band Operation," RADC-TR-82-236, Sept. 1982, under AFOSR 81-0234.

PUBLICATIONS RESULTING FROM CONTRACT SPONSORSHIP

Y. T. Lo, D. Solomon, and W. F. Richards, "Theory and Experiment on Microstrip Antenna," 1978 International Symposium on Antennas and Propagation, Sendai, Japan, pp. 53-56, August 1978.

Y. T. Lo, D. Solomon, and W. F. Richards, "Theory and Experiment on Microstrip Antennas," IEEE Transactions on Antennas and Propagation, AP-27, 2:137-145, March, 1979.

Y. T. Lo, W. F. Richards, and D. D. Harrison, "Improved Theory for Microstrip Antennas," Electronics Letters, 15, 2:42-44, January 1979.

Y. T. Lo and R. F. Richards, "An Improved Theory for Microstrip Antennas and Application," IEEE AP-S 1979 International Symposium Digest, 113-116, June 1979.

Y. T. Lo, R. F. Richards, and P. Simon, "Design and Theory of Circularly Polarized Microstrip Antennas," IEEE AP-S 1979 International Symposium Digest, 117-120, June 1979.

Y. T. Lo, W. F. Richards, P. Simon, and D. D. Harrison, "Theory and Applications for Microstrip Antennas," Proceedings of the Printed Circuit Antenna Technology Workshop, 8.1 to 8.23, Oct. 1979.

Y. T. Lo, W. F. Richards, and J. Brewer, "A Simple Experimental Method for Separating Loss Parameters of a Microstrip Antenna," IEEE Transactions on Antennas and Propagation, AP-29, 1:150-151, January 1981.

Y. T. Lo, W. F. Richards, and D. D. Harrison, "An Improved Theory for Microstrip Antennas and Applications," IEEE Transactions on Antennas and Propagation, AP-29, 1:38-46, January 1981.

Y. T. Lo and W. F. Richards, "Perturbation Approach to Design of Circularly Polarized Microstrip Antennas," Electronics Letters, 17, 11:383-385, May 1981.

Y. T. Lo, J. D. Ou, and W. F. Richards, "An Analysis of Annular, Annular Sector, and Circular Sector Microstrip Antennas," Proceedings of the 1981 Antenna Applications Symposium, September 1981.

Y. T. Lo, W. F. Richards, J. R. Zinecker, and R. D. Clark, "A Theoretical and Experimental Study of the 'Feed Inductance' of a Microstrip Antennas," URSI Digest, May 1982.

Y. T. Lo and S. S. Zhong, "Single-Element Rectangular Microstrip Antenna for Dual-Frequency Operation," Electronics Letters, 19, 8:298-300, April 1983.

Y. T. Lo and S. M. Wright, "Efficient Analysis for Infinite Microstrip Dipole Arrays," Electronics Letters, 19, 24:1043-1045, November 1983.

Y. T. Lo and W. F. Richards, "Theoretical and Experimental Investigation of a Microstrip Radiator with Multiple Linear Lumped Loads," Electromagnetics, 3:371-385, July-Dec. 1983.

Y. T. Lo and B. F. Wang, "Microstrip Antennas for Dual-Frequency Operation," IEEE AP-S 1984 International Symposium Digest, 551-554, 1984.

Y. T. Lo and Y. L. Chen, "Artificial Reactive Reflectors," IEEE AP-S 1984 International Symposium Digest, 763-766, 1984.

Y. T. Lo, B. Engst, and R. Q. H. Lee, "Circularly Polarized Microstrip Antennas," Antenna Applications Symposium, 1984.

Y. T. Lo, "Microstrip Antennas for Dual-Frequency Operation," IEEE Trans. on Antennas and Propagation, AP-32, 938-943, 1984.

Y. T. Lo and S. M. Wright, "An Efficient Moment Method Analysis of Infinite Microstrip Arrays," URSI Digest, June, 1984.

Y. T. Lo and W. F. Richards, "A Simple Theory for Reactively Loaded Microstrip Antennas," IEEE AP-S 1984 International Symposium Digest, 259-262, 1984.





7 - 86